


Università degli Studi di Cagliari

PHD DEGREE

Chemical Sciences and Technologies

Cycle XXXII

TITLE OF THE PHD THESIS

Novel Supramolecular Architectures based on weak interactions

.

Scientific Disciplinary Sector

Chemistry – Chim/03

PhD Student — Giacomo Picci

Coordinator of the PhD Programme — Prof Stefano Enzo
Supervisor — Prof Claudia Caltagirone

Final exam. Academic Year 2018 – 2019
Thesis defence: January-February 2020 Session

This thesis reports the synthesis and the studies of a new series of supramolecular architectures containing urea, amide, squaramide groups enable to function as selective anion receptors, efficient transmembrane transporters and as low molecular weight gelators (LMWGs).

In Chapter 2 we describe a novel family of bis-selenoureas. Receptors **L1**-**L4**, reported in Figure 1, were synthesised and their affinity towards different anion species by means ^{1}H-NMR titrations in DMSO-d_6 were tested. **L1** and **L3** exhibited a good affinity towards phosphate anions, higher compared to that of the oxoanion species. The presence on the receptor structure of the different chalcogen atom represent by selenium, softer than the sulphur and oxygen that precede it along the IX group of the Periodic Table, makes the NHs of the urea moieties more acid increasing the interaction of the receptors with respect to the anion species. The stability constant calculated, higher compared to the analogous bis-ureas already reported in literature, confirmed our hypothesis.

In Chapter 3 a novel family of amide-based receptor are reported. Specifically, the role of the halogen substituents on the anion binding properties and on the activity as anion transporters of a series of isophthalamides and dipicolineamides (**L5**-**L10**, Figure 2) both in solution and in the solid state was investigated. In particular, we wanted to evaluate the possibility to establish different and combined interactions depending on the substituents on the aromatic rings. Only **L9** and **L10** bearing perfluorophenyl rings as substituents have some affinities for the set of anion studies. In particular, in the case of **L9** an interesting behaviour with the formation of a non-symmetric adduct was hypothesised by ^{1}H- and ^{19}F-NMR spectroscopy studies in solution and confirmed by theoretical calculation. The study of the crystal structures of the receptors demonstrate that the steric hindrance of the halogens influence the accessibility of the isophtalamide or dipicoline amide NHs, thus modulating the affinity towards the anions. Furthermore, **L9** and **L10** are able to function as synthetic anion transporters through lipid vesicles.

With the same aim, a new family of symmetric squaramide- based receptors functionalised with different fluorophores (**L11-L16**, Figure 3) for anion recognition, transport and cell imaging are described in Chapter 4. The anion binding properties of the five receptors towards different anion guests (F^-, CN^-, AcO^-, BzO^-, $H_2PO_4^-$, and Cl^-) were studied by means of ^{1}H-NMR spectroscopy in DMSO-d_6 and UV-Vis and fluorescent spectroscopies in DMSO and MeCN. **L12** exhibited the highest stability constants towards the anion species studied and, in particular, the highest affinity constant for the chloride species ever observed, to the best of our knowledge. The strong affinity of **L12** for all the anion guests tested may be explained considering the cooperative effect between the indole and the squaramide NHs in stabilizing the anion adducts. Vesicle anion transport assays using anion selective electrodes demonstrated that only **L12** is enable to transport chloride across to the phospholipidic membrane. However, although the results revealed **L12** active at low concentration, it was not able to reach the saturation of the chloride efflux. Our hypothesis is that an equilibrium between the chloride species into the internal solution and into the external solution was reached and this made not possible to transport all the chloride species. Finally, we described the ability of **L11** and **L13** as imaging agents towards non-tumoral and tumoral cells as free molecules and when encapsulated inside lipid-based nanoparticles, named cubosomes.

The synthesis, gelation tests and characterization of eight LMWGs (**L17**-**L24** Figure 4) based on the urea moiety scaffold are described in Chapter 5. The bis-urea based gelators **L17**-**L19** are characterised by the presence of three different fluorophores as substituents (quinoline, indole and dansyl derivative for **L17**, **L18**, and **L19**, respectively) in order to design new luminescent materials enable to change their optical properties in the presence of external stimuli or in the presence of other species enable to interact by means non-covalent interactions. Oscillatory stress sweep rheometry results evidenced **L18** in a mixture of DMSO and water as the strongest LMWG. Particularly, the formation of the gel in this medium allowed to perform tests in presence of anion

species enable to affect the self-association properties of the compound estabilishing non-covalent gelator-anion interactions. The presence of BzO^- and F^- inhibits the gelation process. An explanation is proposed on the base of the results of ^{1}H-NMR titrations in DMSO d_6 performed in presence of the different anion species tested. The monourea based receptors **L20**-**L24** are characterised by an alkyl chain of different length and different aryl substituents. Particularly, **L20**-**L22** bear a nitrophenyl ring, while **L23**-**L24** are characterised by a naphtyl aromatic group. In this case, the aim was to understand how the different length of the alkyl chain was able to modulate or change the gelation properties of the gelators and, particularly in the case of **L20**-**L22**, a multicomponent systems was able to affect the capability to form gels, to modulate or increase the gelation process or the strength of the gel at least. **L23**-**L24** formed soft gels in apolar solvents like nitrobenzene and chlorobenzene. Particularly, the materials obtained in nitrobenzene are stronger then in chlorobenzene, as suggested by the rheology analysis performed. **L22** formed gels in a polar-like media as ethanol. Interestingly, changes in the mechanic properties as well as in the morphology of the materials obtained in presence of different species (a metal ion or an anion) were suggested by rheology and SEM analysis. In particular, an increase of the solid-like behaviour was observed moving from the free ligand compound to the three components system (gelator + metal ion + anion).

Finally, a new family of aromatic selenoureas **A1**-**A3** (Figure 5) is reported in Appendix A. The aim was to compare their anion binding properties with those of the corresponding thioureas (**A4**-**A6**) and ureas (**A7**-**A9**) using ^{1}H-NMR spectroscopy in DMSO-d_6, in order to explore the possibility for selenoureas of forming mono-coordinated adducts in solution along with classic bi-coordinated ones and, therefore, the possibility to construct molecular logic gates based on the nature of the adduct formed. Furthermore, in appendix B and C results on a side project carried out during this PhD on hexosomes (Appendix B) and cubosomes(Appendix C) for theranostic application are reported.

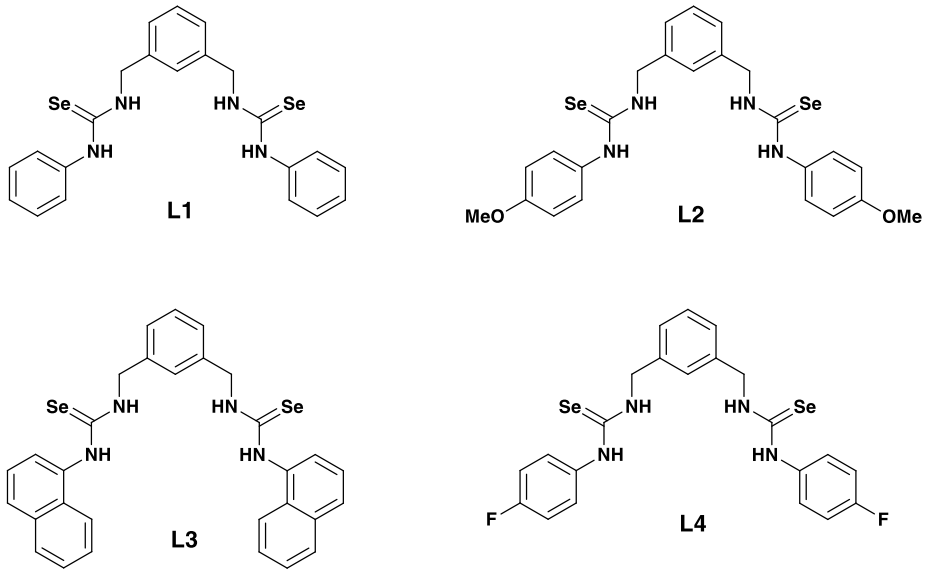

Figure 1 Bis-selenourea-based receptors described in Chapter 2

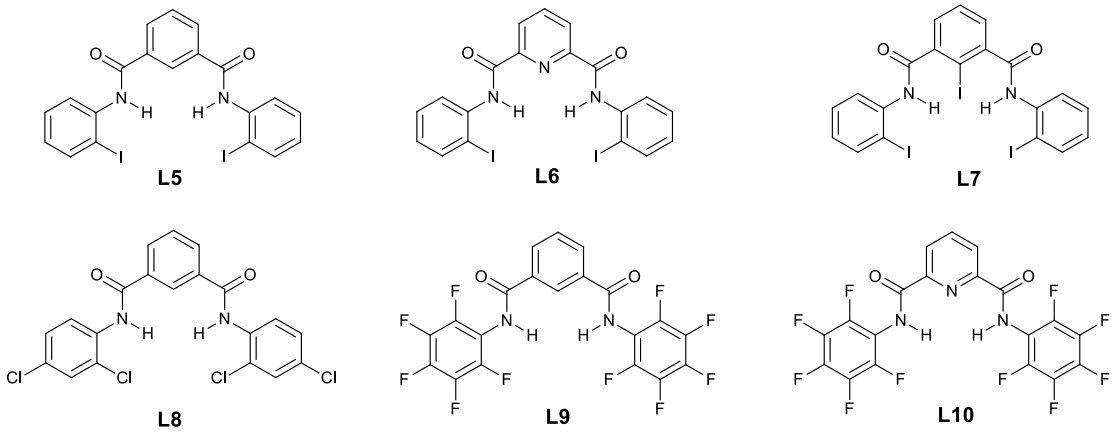

Figure 2 diisophtalamide and dipicolinamide-based receptors synthesised and studies in Chapter 3

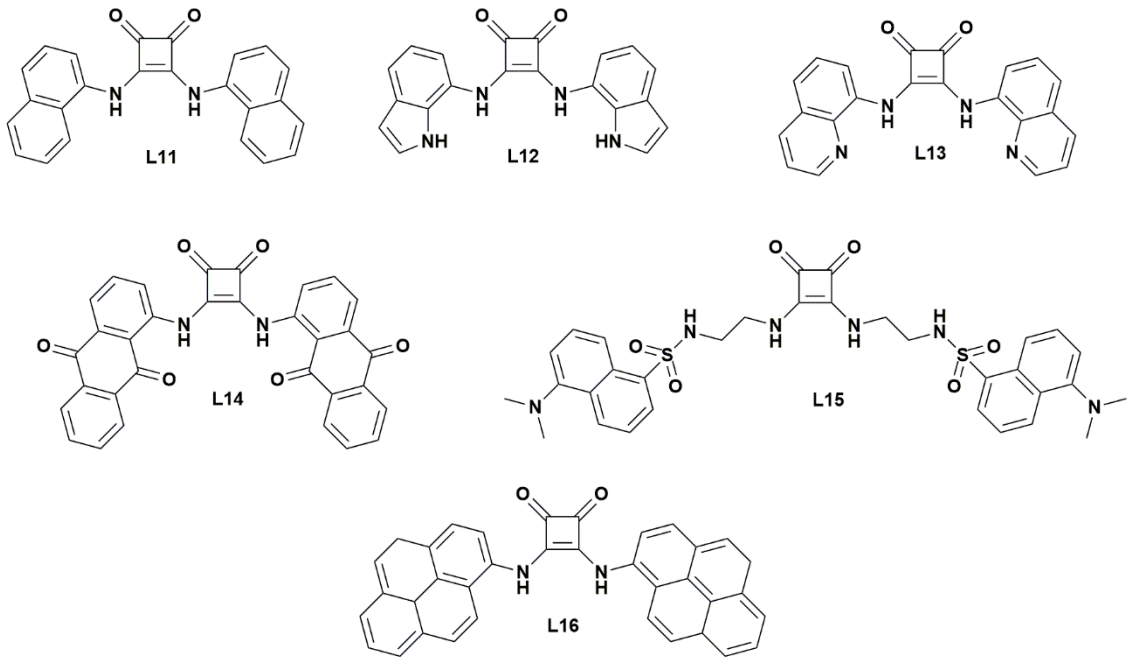

Figure 3 Squaramide-based receptors synthesised and described in Chapter 4

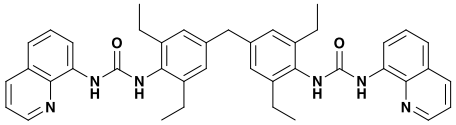

L17

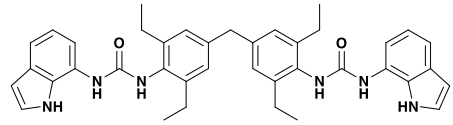

L18

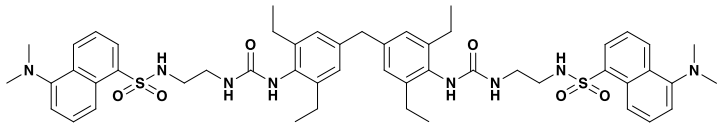

L19

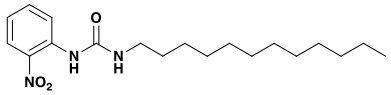

L20

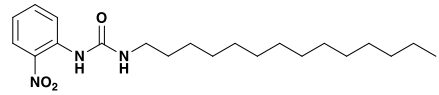

L21

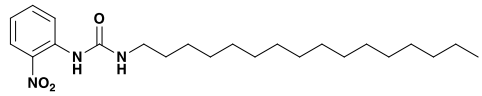

L22

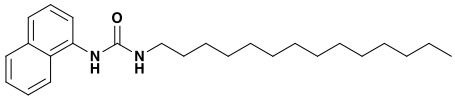

L23

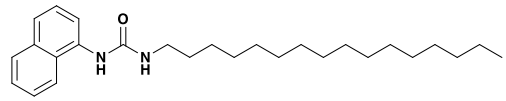

L24

Figure 4 LMWGs described in Chapter 5

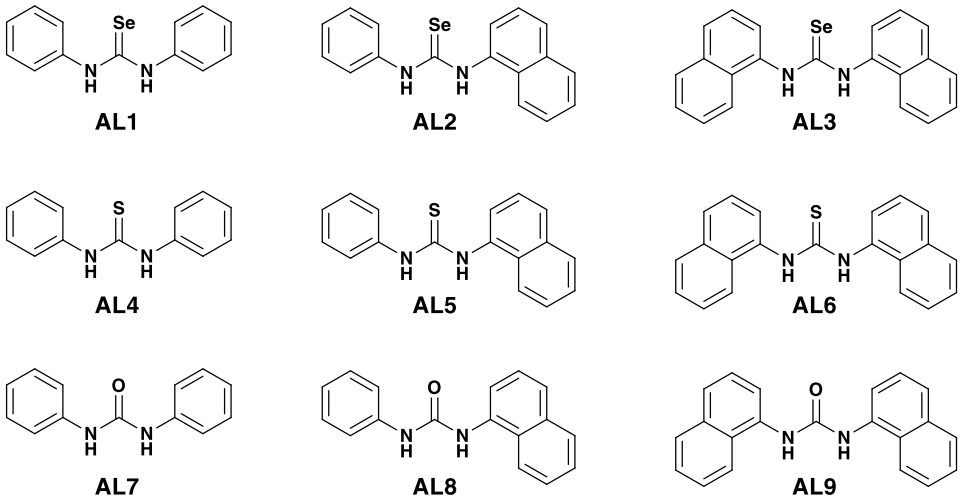

Figure 5 Summary of the receptors described in Appendix A

Chapter 5: Urea-based Low Molecular Weight Gelators

Chapter 1:

Introduction

1 introduction

1.1 Supramolecular Chemistry

Supramolecular Chemistry is a significant area of the modern research that quickly developed in the last decades because of its multidisciplinarity involving chemistry, biology and physics.

The time line of Supramolecular chemistry roots can be collocated in the 19th century when important discoveries were the first signals of the existence of internal non-covalent interactions (Supramolecular interactions) between molecules. In 1893 Alfred Werner (Nobel Prize in 1913) introduced for the first time the concept of Coordination Chemistry [1,2] and in 1894 Emil Fisher (Nobel Prize in 1902) was able to explain the particular and specific interactions between enzyme and substrate with his new "Lock and Key" model.[3] Basically, this principle is based on the perfect complementary in terms of shape, size and geometry between an enzyme and a substrate that leads to a very specific interaction. Paul Ehrlich used this model in 1906 when he introduced the concept of biological receptor [4] and when James Watson and Francis Crick in 1953 discovered the double helix structure of DNA [5] originated from very specific hydrogen bonds connecting two strands of purine and pyrimidine bases, it was clear the importance of intermolecular forces in chemical and biological process.

Following these new discoveries, D.J. Cram,[6] C.J. Pedersen [7] and J.M. Lehn [8] in 1987 won the Nobel Prize for their pioneering job in this new area of chemistry. Furthermore, the Nobel Prize in Chemistry 2016 was awarded jointly to Jean-Pierre Sauvage, Sir J. Fraser Stoddart and Bernard L. Feringa for the design and

synthesis of molecular machines that we can consider another concrete application of the Supramolecular Chemistry principles.[9]

The result of these contribution led to a the first official definition of Supramolecular Chemistry as "the Chemistry of molecular assemblies and of intermolecular bond" [10] as "a chemistry beyond the molecule, bearing on the organised entities of higher complexity that result from the association of two or more chemical species held together by intermolecular forces" [11] such as H-bonding, hydrophobic interactions, π-π stacking and specific coordination properties of metal cations or metal complexes.

The consequence of the selective non-covalent interaction between receptor and substrate (host-guest interaction) is a new species called supramolecule with different structure and physical-chemical properties with respect to the two components.

Therefore, molecular recognition may be defined as the specific binding of a guest molecule with a host compound forming a host-guest complex (supramolecule) through non-covalent interaction.[12]

The key concepts in all fields of development in Supramolecular chemistry can be summarized in:

a) *Host-Guest complexation*: the interaction between host and guest entities required high degree of complementary in terms of shape, size and geometry.[13,14,15] The Host molecule generally presents convergent binding sites (hydrogen bond donor groups, Lewis bases) and cavity or pseudo cavity of adequate dimension and shape to accommodate a small guest molecule that, as opposed, shows divergent binding sites (hydrogen bond acceptor groups, Lewis acids).

b) *Templating, Molecular self-assembly and self-organization*: Templating refers to a synthetically efficient technique that uses a temporary or permanent inorganic or organic "helper" for the stepwise assembly of Supramolecular structures of higher complexity. [16] Self-assembly and self-organization are processes reversible and spontaneous, in which

molecules interact with each other through non-covalent interaction and without external stimuli in order to form the supramolecule.

c) *Crystal engineering:* "the understanding of intermolecular interactions in the context of crystal packing and in the utilisation of such understanding in the design of new solids with desired physical and chemical properties". [17,18]

d) *Supramolecular transport:* it is the process that, taking advantage of host-guest recognition, permits the selective transport of a substrate from an aqueous source phase to an organic phase containing the appropriate receptor through a membrane. [19] In this sense the receptor may act as a mobile carrier for particular substrate target and this fact has a remarkable importance in lot of fields, particularly In biomedicine.

e) *Supramolecular sensors and devices:* they are system composed by a receptor, a possible spacer unit and a photoactive o redox-active group. The molecular recognition between the receptor and a specific substrate leads to a variation in the physical and/or chemical properties of the active unit. Therefore, the molecular sensor can translate the complexation event in a detectable analytical signal (change in pH, fluorescence or UV/Visible variation or electronic distribution). Examples of molecular devices are "molecular machines" [20] able to perform easy mechanical movements and chemosensors. [21]

1.2 Anion recognition

The development of new receptors, sensors and transporters for anionic species results to be a rich area of research in Supramolecular chemistry due the ubiquitous role of the anion species in a lot of fields such as biology, industry, environment and medicine. [22,23]

They are essential for life because they are involved in almost every biochemical processes. Important biological molecules such as DNA or RNA are polyanionic at physiological pH. Phosphates, for example, are constituents of membrane lipids and are involved in many biological processes such as energy storage, gene regulation, muscle contraction, and signal transduction. [24,25] Bicarbonate and chloride take active part in the anion flux across cell membranes and the interruption of this flux can increment disease like cystic fibrosis, Dent's disease or osteoporosis.[26,27,28]

Fluoride plays an important beneficial aspect in dental health (fluoride containing toothpaste), but over exposure to fluoride (fluorosis) can have detrimental effects such as kidney failure and debilitating skeletal defects. [29]

In general, the constant monitoring of the anion cellular concentration is essential for the osmotic pressure regulation, signal transduction pathways activation and in the production of electrical signals.

Many anions, such as chromate, arsenate, nitrate, perchlorate, sulphate and sulphide, are included in the "Priority Pollutant list" reported by the European Community as they cause pollution problems in the environment. Nitrate and phosphate, which are commonly used as fertilizers, can cause the eutrophication of the water while other anions are components of pesticides or they are part of industrial or nuclear fuels.

Because of the importance of the anionic species, it is clear why the development of new receptors, sensors and transporters for anion targets continues to be a research area of constant interest.[30,31,32,33]

However, the design of anion receptors is more complicated with respect to the metal ions analogue due to some of their properties:

a) *Size*: anions are larger than their isoelectronic cations therefore the receptor must be designed to have a cavity suitable for the size of the target anion. (Table 1.1)

Table 1.1 Comparison of the radii of isoelectronic cations and anions

Cation	Radius Å	Anion	Radius Å
Na^+	1.16	F^-	1.19
K^+	1.52	Cl^-	1.67
Rb^+	1.66	Br^-	1.82
Cs^+	1.81	I^-	2.06

b) *Charge*: Generally, they show a low charge to radius ratio that involves in a less functional electrostatic binding interaction than covalent bond established with the cations.

c) *Geometry*: anions have a wide range of shape and geometry that must be considered in the receptor design phase in order to guarantee the high degree of complementary between host and guest. (Figure 1.1)

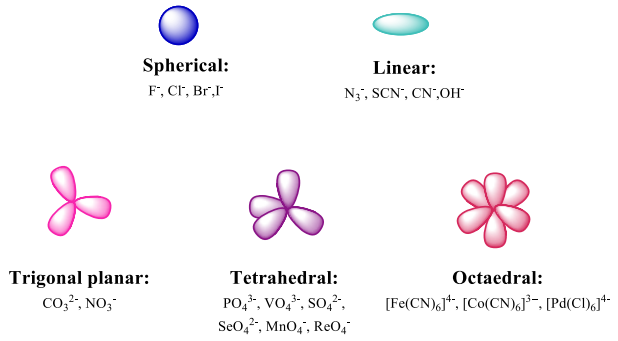

Figure 1.1 Geometries of anions

d) *pH dependence*: the anions negative charge can be influenced by variation of pH (because at low pH they can be protonated). For this reason the receptor must be able to work within the specific pH range of the anion target that they want recognise.

e) *Solvent*: the nature of the solvent plays a central role in the anion recognition. Anion binding is based on electrostatic interactions that occur between the receptor and the anion. However, this type of force can occur also between the solvent and the anion so an ideal receptor must compete with the solvent environment and with the counter cation too. For example, neutral receptor that only bind anion through hydrogen-bond interactions will be more competitive in aprotic organic solvent. In fact, protic solvent can establish strong hydrogen bonds with the anion and the receptor must compete with them to bind the anion and take their place.

f) *Hydrophobicity*: Following the Hofmeister series (Figure 1.2) it is clear that an increase of the anion hydrophobicity corresponds to a decrease of its aqueous solvation. Hydrophobic anions are generally bound more strongly in hydrophobic binding sites with respect to the hydrophilic ones and it is true the opposite combination (Hydrophilic anions in hydrophilic binding sites).

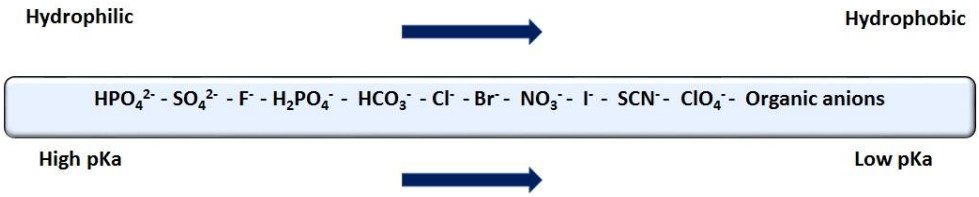

Figure 1.2 Hofmeister series

In order to design and synthesize a selective anion receptor, all the mentioned factors must be taken into account. Therefore, the choice of the noncovalent interaction used to complex the anion results to be very important in the design of the receptor. These interactions include basically electrostatic interactions, hydrogen bonding, halogen bonding, Lewis acids and a combination of these interactions.

The easiest way to bind an anionic species is to introduce one or more positive charge in the receptor structure to bind the anion target through *electrostatic interactions.*

More positive is the charge of the system and, in theory, more strong and effective these interaction should be. However, the fact of introducing lot of charged groups can became a problem if these charges start to repel one other. To avoid this situation, in general, rigid moieties or cyclic units are widely used.

Another common way to complex anion targets is to use the *hydrogen bonds*. Anions can be considered as electron pair donors and they interact with electron pair acceptors such as electron-positive hydrogen atom forming a hydrogen bond. Functional groups with this property are for example N-H or O-H widely employed in urea, amide or alcohol based receptors. If we substitute, as electron pair acceptors, the electron positive hydrogen atom in the hydrogen bond with a halogen atom, the resulting interaction is called *halogen bond.* Both in the case of hydrogen bond and halogen bond, it is very common to design receptor systems that show hydrogen or halogen atoms orientated in a correct, convergent manner to facilitate the complexation of a particular anion target depending on its size and geometry.

Finally, another way to bind anions is to use metal ions, which work as *Lewis acids*. These electro-deficient groups are able to accept electron pairs from an anionic guest into their vacant orbitals.

All these kind of interactions can be used together in a synergic way to produce a very selective and efficient receptor for anions.

1.3 Classification of anion receptors

On the basis of the type of interactions previously mentioned, anion receptors can be divided into three groups:

a) Charged anion receptors*:*

- *Ammonium based receptors*
- *Guanidinium based receptors*
- *Imidazolium and triazolium based receptors*

b) Neutral anion receptors*:*

- *Amide based anion receptors*
- *Urea and thiourea based anion receptors*
- *Alcohol based anion receptors*
- *Indole and pyrrole based anion receptors*

c) Metal and Lewis acid receptors

Selected examples on recent advances in the field, focussing on neutral receptors will be described in the next paragraphs.

1.3.1 Amide-based anion receptors

Amide groups have been extensively used as H-bond donors for the design of anion receptors. Recently a family of (thio)amidebenzimidazoles (**1-4**) or (thio)amideindoles (**5-10**) was synthesised and by reacting them with anions such as fluoride or benzoate authors were able to determine the acid-base half-equivalence point. Indeed, in the presence of fluoride only the deprotonated monomers were obtained in the solid state, while dimers in which one fully deprotonated molecule interacts with a neutral molecule via H-bond or two half-deprotonated molecules share the same proton were isolated in the presence of benzoate.[34, 35]

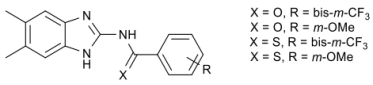

1-4

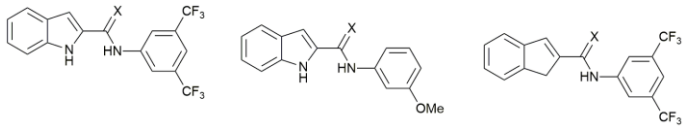

5-10

Caltagirone and co-workers have described the first example of an isophtalamide and dipicolinemide based receptors containing a trypthophan moiety.[36] In the presence of fluoride deprotonation of the carboxylic acids decreases the acidity of amide NHs,

switching on the anion binding ability of the deprotonated receptors with selectivity for HF_2^- and fluoride complexation (Figure 1.3)

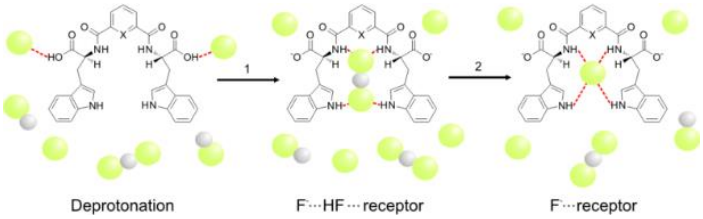

Figure 1.3 Proposed binding mode for the isophtalamide receptors containing tryptophan. Reproduced from Ref. 36.

The proposed systems represent a unique example of anionic receptors able to bind anions *via* H-bonding.

A class of compounds can be considered similar to amides is the squaramide class. A detailed description of the peculiar properties of squaramides is described in Chapter 4. Joliffe and co-workers have recently compared the anion binding properties of deltamides and croconamides with those of ureas and amides.[37]

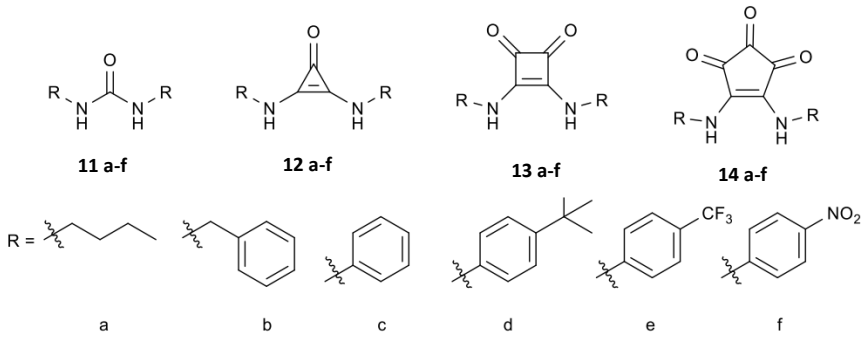

The croconamides **14a-f** were found to be considerably more acidic than the corresponding squaramides **13a-f**, while the deltamides **12a-f** are less acidic than the squaramides **13a-f**, but more acidic than the ureas **11a-f** with identical substituents. In contrast to the trends observed for ureas **11a-f**, deltamides **12a-f** and squaramides **13a-f**, N,N'-dialkylcroconamides **14a-b** have higher affinities for anions than the N,N'-diaryl derivatives **14c-f** in DMSO, presumably due to partial deprotonation of the

N,N'-diarylderivatives at neutral pH. Due to the differences in structure between the three cyclic cores, the deltamides **12a-f** displayed higher affinity for dihydrogenphosphate ions than other oxoanions or halides, in contrast to the ureas **11a-f** and squaramides **13a-f**, where anion binding affinity correlates with anion basicity.

1.3.2 Alcohol-based anion receptors

Hunter and co-workers have used simple OH-containing receptors with different H-bond donor abilities (**15-17**) to evaluate the hydrogen-bond acceptor parameter (β) for various anions (including chloride, bromide, iodide, phosphate diester, acetate, benzoate, perrhenate, nitrate, triflimide, perchlorate, hexafluorophosphate, hydrogen sulfate, methyl sulfonate, triflate, and perfluorobutyl sulfonate) using UV-Vis spectroscopy in acetonitrile and chloroform.[38] The results demonstrated that carboxylates were the strongest hydrogen-bond acceptors studied with β parameters of ≈ 15 while hexafluorophosphate was the weakest in both solvents.

1.3.3 Urea-based anion receptors

Urea-based receptors have been extensively used in the design of anion receptors. It is well known that with respect to ureas, thioureas show an increased acidity of the urea NHs groups. [39] Selenoureas, instead have only been recently studied as anion binding receptors (an example will be reported in Paragraph 1.4.1). In Chapter 2 new examples of selenoureas for anion binding will be discussed.

Selenoureas have been used by Ciancaleoni and co-workers to increase anion-binding strength by a cooperative effect between H-bond and halogen bond.[40] Simple selenourea can simultaneously act as an XB acceptor toward $I(CF_2)_5CF_3$ and as a hydrogen bond donor towards benzoate anion through its NH groups (**18**) Diffusion NMR studies along with NMR titration studies in acetone-d_6 showed that hydrogen

bonding from selenourea NHs to the benzoate anion strongly enhances the strength of the Se···I XB by approximately an order of magnitude. Computational studies confirmed the hydrogen bond to benzoate polarizes the selenourea which increases the partial negative charge on the Se atom. As a result, this hydrogen bond induced polarisation enhances the XB acceptor properties on selenourea which increases the XB bond strength.

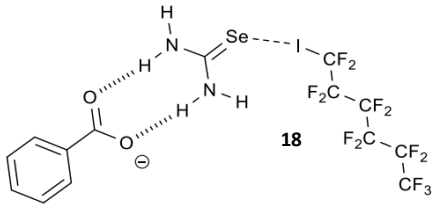

18

Ureas have also been recently used for the development of functional materials such as gels. Various examples of ureas and bis-ureas as low molecular weight gelators (LMWG) will be described in Chapter 5. Steed and co-workers have recently reported that pyridinylmethylureas **19a-e** are able to form strong gels in aromatic solvents such as toluene, 1,3-dichlorobenzene, and nitrobenzene though urea-urea hydrogen bonding.[41] The addition of transition metal ions such as Zn(II), Cu(II) and Co(II) triggered a 'turn off' gelation to varying degrees due to the formation of non-gelator octahedral metal complex. Interestingly, however, gelation recovered upon the addition of bromide, resulting in a gel–sol–gel cascade. Authors hypothesised that bromide causes a change in metal coordination geometry from a non-gelator octahedral complex to a tetrahedral complex which allows self-assembly via urea α-tape formation.

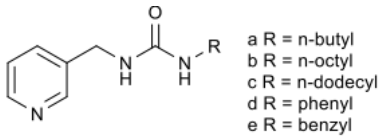

19 a-e

1.4 Applications

Application of anion receptor chemistry include different areas such as organocatalysis, transport, extraction, sensing, self-assembly. In particular, we will focus here on recent examples on sensing and transmembrane anion transport.

1.4.1 Molecular sensors

According to the definition of IUPAC, a chemical sensor is a device that transforms chemical information , ranging from the concentration of a specific sample to total composition analysis into an analytically useful signal (change in pH, light emission or electronic distribution).[42]

On the base of the IUPAC definition, a chemical sensor is a macroscopic device but following the modern principles of supramolecular chemistry, an analogue of chemical sensor can be obtained for the molecular world. [43,44,45]

This approach is well known as “bottom-up” approach where the design starts from the molecular level to reach a resolution unachievable with a classic “top-down” method. The result of these interactions are a supramolecular species that are usually named molecular sensor or chemosensor to distinguish them from chemical sensor. [46,47,48]

Same specific properties must be possessed by a molecular sensor:

- The sensor should be specific and selective to one or to a small number of substrates of interest.
- The interaction between host and guest (receptor and analyte) should be fast and reversible.
- The sensor should be stable over a long time period in order to guarantee the data reproducibility.
- The sensor should be cheap and easy to synthesize.

The molecular sensor is composed of a receptor or binding subunit (which is the unit able to bind the analyte) and an active unit or signalling unit (which is the part that

changes its physical properties after the interaction between the receptor and the substrate, generally separated by a spacer (Figure 1.3).

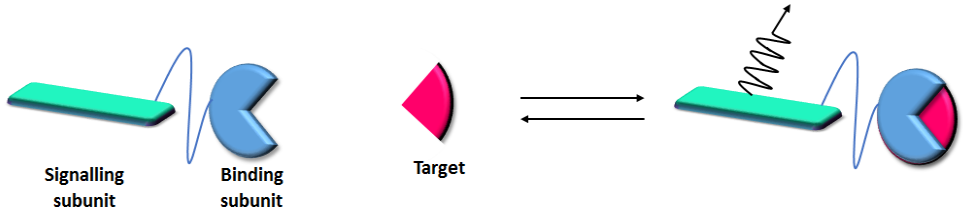

Figure 1.3 General scheme of a molecular sensor

The sensor are classified according to the principles of signal transduction in:

- Optical sensors
- Electrochemical sensors
- Electrical sensors
- Magnetic sensors
- Thermometric sensors

Recently Miljanic *et al*. reported a fluorinated trispyrazole **20** which in the presence of dicarboxylic acid undergoes a selective turn-on fluorescence response. [49] Fluorescence response was attributed to the formation of a dimer bridged by three dicarboxylates guests. An aggregation induced emission (AIE) turn on response was observed depending on the relative position of the two carboxylic groups. Indeed the system was able to discriminate ortho-aromatic dicarboxylic acids over meta-, or para-, dicarboxylic acids, and also, cis-isomers of alkene based dicarboxylic acids and not trans-isomers.

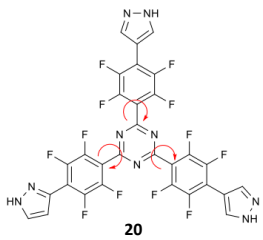

20

A water-soluble selective light-up luminescence sensor for commonly used herbicide glyphosate based on a macrocyclic europium complex (**21**) was described by Parker and co-workers. [50] A shown in Figure 1.5 the guest molecule should interact via H-bond with a protonated NH of one of the pendant arm and the metal centre.

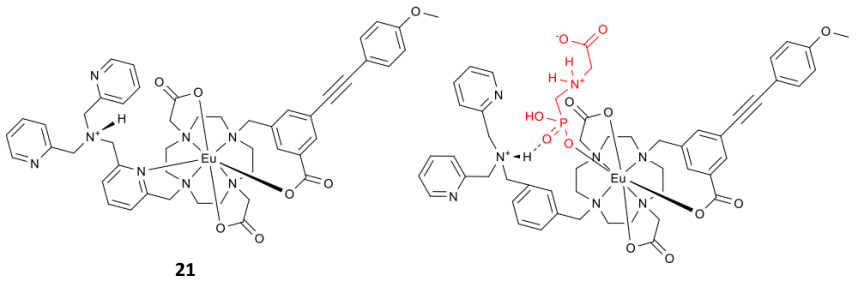

21

Figure 1.5 Structure of compound **21** and proposed binding mode of glyphosate.

The system was able to sense glyphosate in the range operating between 5 and 50μM.

Caltagirone, Martinez-Manez and co-workers described the first example of a chemosensor (**22**) containing a selenourea moiety is here described. **22** is able to colorimetrically sense the presence of CN^- and S^{2-} in H_2O:MeCN (75:25, v/v). Moreover, when it was loaded in functionalised mesoporous silica nanoparticles an increase in the selectivity towards S^{2-} in H_2O occurs *via* a selective fluorescent response (Figure 1.6).[51]

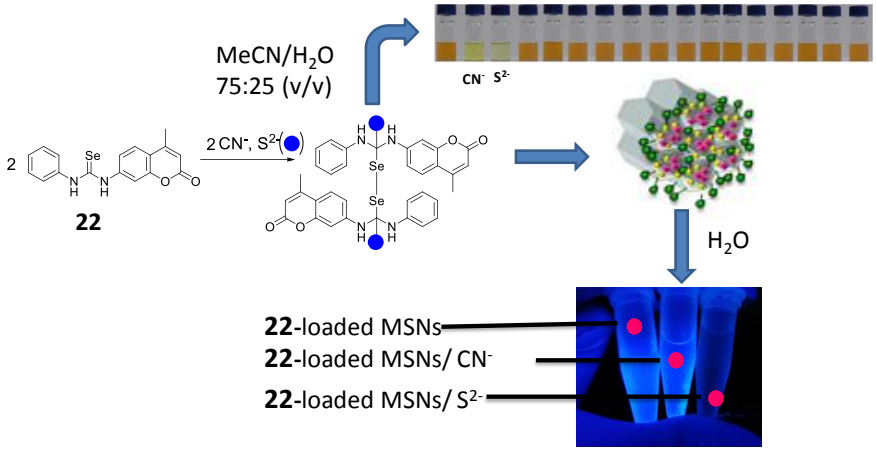

Figure 1.6 Sensing mechanism proposed for fluorescent selenourea **22**.

Long, Huang, Sessler and co-workers have recently proposed a two-layer gel construct that permits the on-site detection of the chloride anion by means of a UV-vis lamp and a smart phone"app".[52] Eight polystyrene gels were prepared a calix[4]pyrrole recognition unit, an imidazolium unit bearing fluoride (**G1**-**G4**) or bromide (**G5**-**G8**) as a counter anion and a fluorophore composed of either a coumarin, BODIPY, rhodamine B or rhodamine B plus Cu^{2+} giving the colours blue, green, red and black respectively (Figure 1.7).

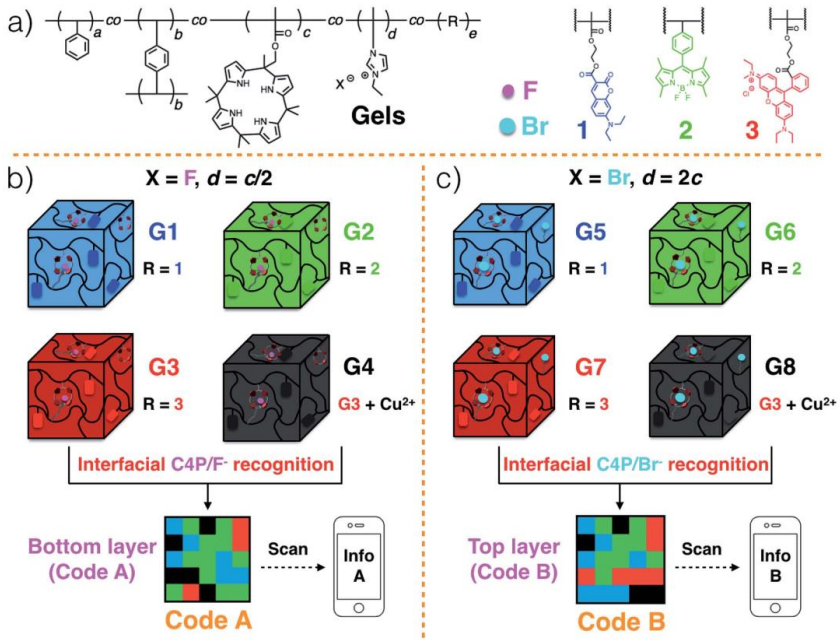

Figure 1.7 a) Chemical structures of the polymeric gels and the incorporated fluorescent elements. Cartoon representations of: (b) **G1**–**G4** and the formation of 3D colour Code A via interfacial C4P/imidazolium-fluoride interactions; (c) **G5**–**G8** and the formation of 3D colour Code B via interfacial C4P/imidazolium-bromide anion interactions. Reproduced from ref. 51 (open access paper).

Treatment with a chloride anion source was found to delaminate the top layer and leave intact the more robust bottom layer, allowing the bottom layer (Code A) to be read out.

1.4.2 Transmembrane anion transport

Anion transport is an expanding research field in Supramolecular Chemistry due to its relevance in biological systems.[53, 54] There are many membrane spanning ion-channels responsible for critical biological processes, such as maintaining cellular pH and volume, and cellular signalling.[55] Defects in these channels can reduce the flux of anions through membranes and lead to serious diseases known as channelopathies;

such as Bartter syndrome and the more commonly known cystic fibrosis.[56, 57] Numerous examples of small molecule acting as anion transporters have been developed in the last 15 years with the aim to restore the transport of anions across membranes.

In Chapter 3 and 4 we will describe the transport activity of some of the receptors studied in this PhD thesis

Squaramides, due to their excellent anion binding properties, have been extensively used as anion transporters. Gale and co-workers have recently described the anion transport activity of a family of squaramides bearing a 1,8-naphtalimide fluorophore (**23 a-d**).[58] The anion transport activity of these compounds in POPC lipid vesciscles, followed the trend **23a**>**23c**>**23b**>**23d** according their anion binding affinities. The most active transporter **23a** was found to have the highest efficiency in fluorescent staining of living A549 cells.

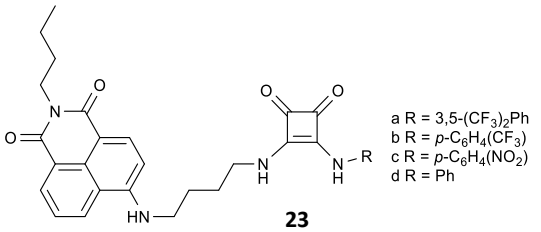

23

Urea containing receptors have also proved to be active compunds as transmembrane anionophores. Davis and co-workers have described the series of anthracene bis-ureas (**24a-d**) which are able to transport chloride at low transporter concentration. [59]

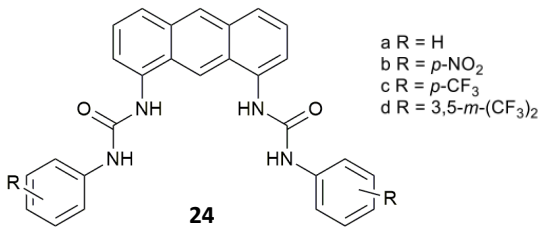

24

The transmembrane anion-transport activities of compounds **24a-d** were studied using a Cl^-/NO_3^- exchange assay in POPC:cholesterol (7:3) vesicles incorporating the carrier in the membrane and with the test anionophore pre-incorporated in the membrane and encapsulating lucigenin within the vesicles. The Nitrophenyl bisurea **24b** was the most powerful even at the lowest transporter to lipid ratio of 1:1000000. The $EC_{50,270s}$ value calculated for **24b** was 0.0003 mol%, which is one of the lowest reported to date for chloride–nitrate exchange and even lower than that of the natural anionophore prodigiosin.

A series of indole-based amide-sulfonamide derivatives 24a-d were described by Talukdar and co-workers.[60] that take advantage of pairs sulfonamide N–H proton acidity The ion transport efficiency directly correlated to the pK_a of the sulfonamide N–H protons. The mechanistic study indicated proton–anion symport across the lipid bilayer membrane.

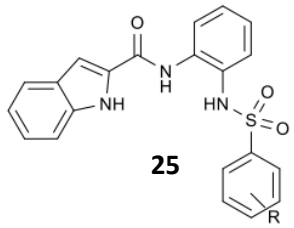

25

a, R = 2,3,4,5,6-Pentafluoro
b, R = *p*-Br
c, R = *p*-NO_2
d, R = *p*-Me
e, R = *p*-CF_3
f, R = *p*-OMe
g, R = 2,4,6-Trifluro

1.5 Aim of the thesis

The receptors that will be discussed in next chapters are reported in Figure 1.8. The importance of Supramolecular Chemistry to build up molecular architectures for anion binding, sensing and transport has been introduced. In the previous paragraphs, the different classification of the scaffold groups mostly used for the anion chemistry applications has been described above. A wide number of receptors based essentially on the hydrogen bond interaction for anion species are constantly designed and

synthesized because of the fundamental interest towards anions. Among them, the urea and amide moieties are the most largely employed due to their easy synthesis and due the presence of NH acid protons able to interact with anions through hydrogen bond.

The work described in this thesis will be focused on the design, the synthesis and the study of a new series of molecules containing different anion binding scaffolds that are able to act as receptors for anions in competitive media, to transport anions through phospholipids membranes or, as building blocks for the development of new materials.

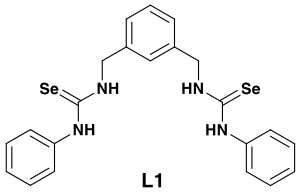

L1

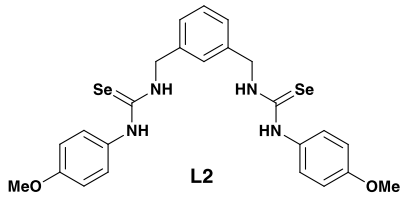

L2

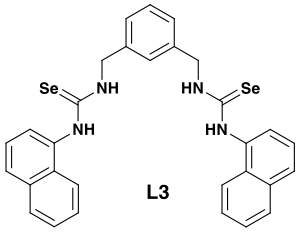

L3

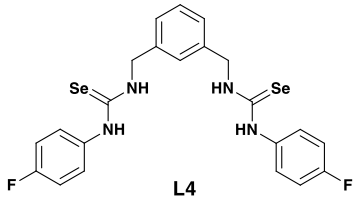

L4

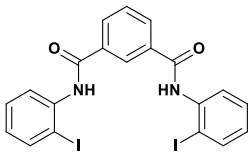

L5

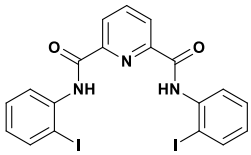

L6

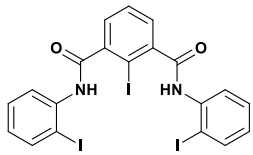

L7

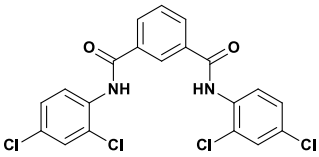

L8

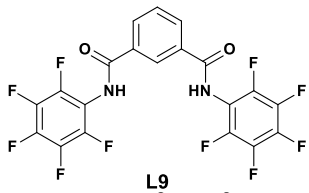

L9

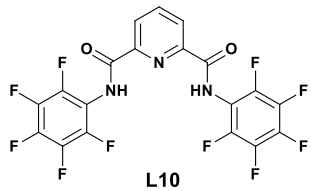

L10

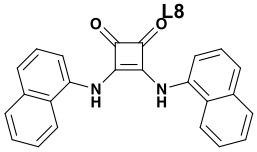

L11

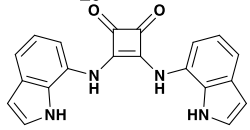

L12

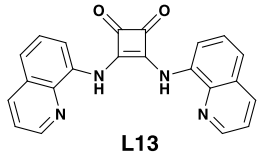

L13

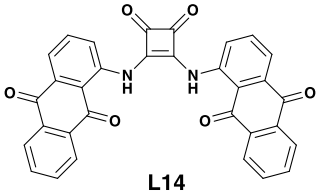

L14

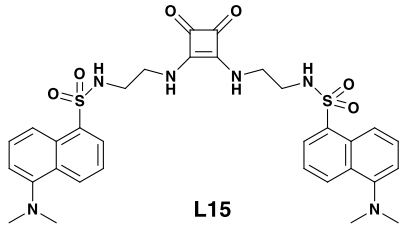

L15

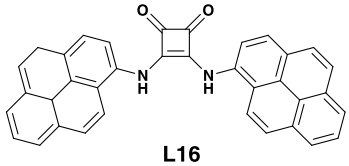

L16

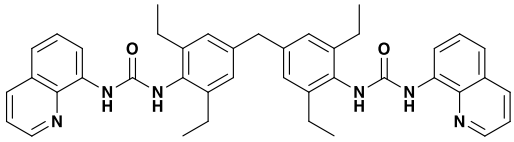

L17

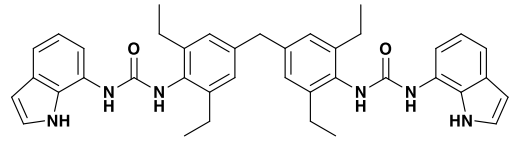

L18

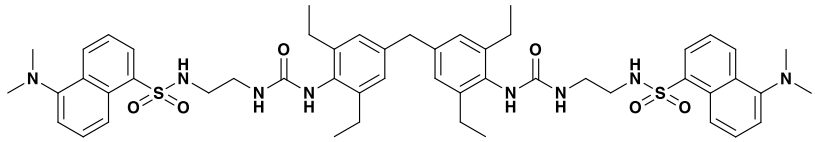

L19

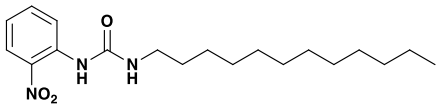

L20

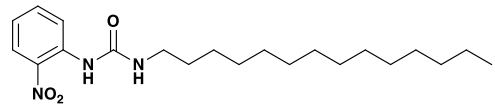

L21

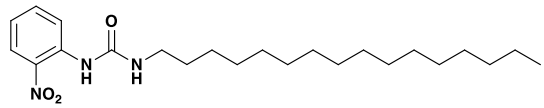

L22

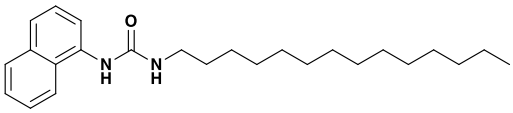

L23

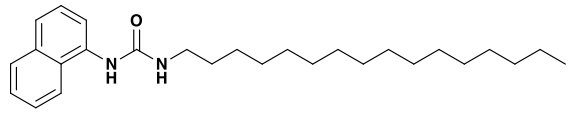

L24

Figure 1.8 Summary of the receptors discussed in this thesis

1.6 References

1. N. L. i. C. A. Werner, 1966,256-269.
2. K. Bowman-James, *Acc. Chem. Res.*, 2005, **38**, 671-678.
3. E. Fischer, *Berichte der deutschen chemischen Gesellschaft*, 1895, **28**, 1429-1438.
4. P. Ehrlich, 1967,Nobel Lecture, Physiol. or Med., 304-320.
5. F. C. J. Watson, Nobel Lecture: Physiology or Medicine, 1962.
6. D. J. Cram, Nobel Lectures in Chemistry (1981–1990). World Scientific Publishing Co, Singapore 1992, 419.
7. C. Pedersen and B. Malmström, World Scientific Publishing Co. Singapore, 1992.
8. J. Lehn, *World Scientific Publishing Co, Singapore*, 1992, 474.
9. J. M. Lehn, *Angew. Chem. Int. Ed. Eng.*, 1988, **27**, 89-112.
10. J.M. Lehn, Pure Appl. Chem., 1978, 50, 871.
11. J. M. L. K.B. Mertes, in Comprehensive Coordination Chemistry, Eds. G. Wilkinson, R.D. Gillard, J.A. McClevety, Pergamon Press, Oxford, 1987, Vol. 2, Ch. 21.3.
12. J.M. Lehn, Nobel Lecture, 1987.
13. N. Curtis and G. Melson, *Plenum Press, New York*, 1979, 230.
14. J. M. Lehn, *Acc. Chem. Res.*, 1978, **11**, 49-57.
15. B. Dietrich, J. Lehn, J. Sauvage and J. Blanzat, *Tetrahedron*, 1973, **29**, 1629-1645.
16. J.-M. Lehn, *Supramolecular chemistry*, Vch, Weinheim, 1995.
17. G. R. Desiraju and G. W. Parshall, *Materials science monographs*, 1989, **54**.
18. G. R. Desiraju, *Angew. Chem. Int. Ed.*, 2007, **46**, 8342-8356.
19. J.M. Lehn, Supram. Chem., 1985, 227, 849.
20. J. F. S. J.P. Sauvage, B.L. Feringa, Nobel Lecture, Chemistry, 2016.
21. J. M. Engle, C. N. Carroll, D. W. Johnson and M. M. Haley, *Chem. Sci.*, 2012, **3**, 1105-1110.
22. P. A. Gale, S. E. Garcia-Garrido and J. Garric, *Chem. Soc. Rev.*, 2008, **37**, 151-190.
23. P. A. Gale and R. Quesada, *Coord. Chem. Rev.*, 2006, **250**, 3219-3244.

24. R. L. P. K. Adams, J.T.;Leader,D.P.TheBiochemistryof the Nucleic Acids, 10th ed.; Chapman and Hall: New York, 1986.

25. M. Egli and W. Saenger, *Principles of nucleic acid structure*, Springer Science & Business Media, 2013.

26. M. P. Anderson and R. J. Gregory, *Science*, 1991, **253**, 202.

27. O. Devuyst, P. T. Christie, P. J. Courtoy, R. Beauwens and R. V. Thakker, *Human molecular genetics*, 1999, **8**, 247-257.

28. U. Kornak, D. Kasper, M. R. Bösl, E. Kaiser, M. Schweizer, A. Schulz, W. Friedrich, G. Delling and T. J. Jentsch, *Cell*, 2001, **104**, 205-215.

29. L. S. Kaminsky, M. C. Mahoney, J. Leach, J. Melius and M. J. Miller, *bone*, 1990, **14**, 17.

30. P. A. Gale, S. E. García-Garrido and J. Garric, *Chem.Soc. Rev.*, 2008, **37**, 151-190.

31. P. A. Gale and R. Quesada, *Coord. Chem. Rev.*, 2006, **250**, 3219-3244.

32. J. L. Sessler, P. A. Gale and W.-S. Cho, *Anion receptor chemistry*, Royal Society of Chemistry, 2006.

33. A. Bianchi, K. Bowman-James and E. García-España, *Supramolecular chemistry of anions*, Wiley-vch New York, 1997.

34. S. Koeller, M. H. Lescure, C. Davies, J. P. Desvergne, S. Massip and B. Bibal, *Eur. Org. Chem.*, 2017, **2017**, 5627-5631.

35. S. Koeller, M. H. Lescure, C. Davies, J. P. Desvergne, S. Massip and B. Bibal, *Org. Biomol. Chem.*, 2017, **15**, 7263-7266.

36. R. Montis, A. Bencini, S. J. Coles, L. Conti, L. Fusaro, P. A. Gale, C. Giorgi, P. N. Horton, V. Lippolis, L. K. Mapp and C. Caltagirone, *Chem. Comm.*, 2019, **55**, 2745-2748.

37. V. E. Zwicker, K. K. Y. Yuen, D. G. Smith, J. Ho, L. Qin, P. Turner and K. A. Jolliffe, *Chem. - Eur. J.*, 2018, **24**, 1140-1150.

38. S. J. Pike, J. J. Hutchinson and C. A. Hunter, *J. Am. Chem. Soc.*, 2017, **139**, 6700-6706.

39. C. Caltagirone, G. W. Bates, P. A. Gale and M. E. Light, *Chem. Comm.*, 2008, 61-63.

40. G. Ciancaleoni, *Phys. Chem. Chem. Phys.*, 2018, **20**, 8506-8514.

41. C. A. Offiler, C. D. Jones and J. W. Steed, *Chem. Comm.*, 2017, **53**, 2024-2027.

42. H. Adam, G. Stanislaw and I. Folke, *Pure Appl. Chem*, 1991, **63**, 1274-1250.

43. R. Pinalli, F. F. Nachtigall, F. Ugozzoli and E. Dalcanale, *Angew. Chem. Int. Ed.*, 1999, **38**, 2377-2380.

44. J. L. Atwood and J.-M. Lehn, *Comprehensive supramolecular chemistry*, Pergamon, 1996.

45. L. Fabrizzi, *Coord. Chem. Rev*, 2000, **205**, 1-232.

46. J. Janata, M. Josowicz, P. Vanýsek and D. M. DeVaney, *Anal. Chem-*, 1998, **70**, 179-208.

47. E. Bakker, P. Bühlmann and E. Pretsch, *Chem. Rev.*, 1997, **97**, 3083-3132.

48. P. Bühlmann, E. Pretsch and E. Bakker, *Chem. Rev.*, 1998, **98**, 1593-1688.

49. Z. Zhang, M. I. Hashim, C. H. Wu, J. I. Wu and O. Š. Miljanić, *Chem. Comm.*, 2018, **54**, 11578-11581.

50. L. B. Jennings, S. Shuvaev, M. A. Fox, R. Pal and D. Parker, *Dalton Trans.*, 2018, **47**, 16145-16154.

51. A. Casula, A. Llopis-Lorente, A. Garau, F. Isaia, M. Kubicki, V. Lippolis, F. Sancenón, R. Martínez-Máñez, A. Owczarzak, C. Santi, M. Andrea Scorciapino and C. Caltagirone, *Chem. Comm.*, 2017, **53**, 3729-3732.

52. X. Ji, W. Chen, L. Long, F. Huang and J. Sessler, *Chem. Sci.*, 2018, **9**, 7746-7752.

53. N. Busschaert and P. A. Gale, *Angew. Chem. Int. Ed.*, 2013, **52**, 1374-1382.

54. P. A. Gale, R. Pérez-Tomás and R. Quesada, *Acc. Chem. Res.*, 2013, **46**, 2801-2813.

55. D. C. Gadsby, *Nat. Rev. Mol. Cell Biol.*, 2009, **10**, 344-352.

56. F. M. Ashcroft, *Nature*, 2006, **440**, 440-447.

57. N. Miyamura, K. Matsumoto, T. Taguchi, H. Tokunaga, T. Nishikawa, K. Nishida, T. Toyonaga, M. Sakakida and E. Araki, *J. Clin. Endocrinol. Metab.*, 2003, **88**, 781-786.

58. X. Bao, X. Wu, S. N. Berry, E. N. W. Howe, Y. T. Chang and P. A. Gale, *Chem. Comm.*, 2018, **54**, 1363-1366.

59. C. M. Dias, H. Valkenier and A. P. Davis, *Chemistry - Eur. J.*, 2018, **24**, 6262-6268.

60. S. V. Shinde and P. Talukdar, *Chem. Comm.*, 2018, **54**, 10351-10354.

Chapter 2

Bis-Selenourea-based receptors for anion recognition: an NMR study

2 Bis-Selenourea-based receptors for anion recognition: an NMR study

In this chapter we describe a novel family of bis-selenoureas. Receptors **L1**-**L4**, were synthesised and their affinity towards different anion species by means ^{1}H-NMR titrations in DMSO-d_6 were tested. **L1** and **L3** exhibited a good affinity towards phosphate anions, higher compared to that of the oxoanion species. The presence on the receptor structure of the different chalcogen atom represent by selenium, softer than the sulphur and oxygen that precede it along the IX group of the Periodic Table, makes the NHs of the urea moieties more acid increasing the interaction of the receptors with respect to the anion species. The stability constant calculated, higher compared to the analogous bis-ureas already reported in literature, confirmed our hypothesis.

2.1 Introduction

Selenium is a controversial element. In the past, it was described as a highly toxic element for the biological system causing poisoning. However, in the last years it has been discovered that Selenium is an essential nutrient for the correct physiological processes in the human organism. [1] At this purpose, a very important role in the self-defence mechanism against oxidative stress is played by some selenoproteins such as glutathione peroxidase, [2,3 in] which the presence of Selenium have an active centre where important redox reactions with ROS species (Reactive Oxygen Species) take place. [4] Alterations in the equilibrium between the oxidative stress and the Selenium levels lead to a large number of

diseases such as rheumatoid arthritis,[5] pancreatitis, diabetes[6] and cardiovascular complications. Recent studies have highlighted the anticancer ability of many Selenium derivatives to induce apoptosis of tumor cells and reduce cancerous metastasis in animals.[7,8,9,10] Moreover, a wide range of Selenium compounds show anti-inflammatory, antihypertensive, antiviral, antibacterial, and antifungal properties. [11,12,13] Due to these significant properties, the interest towards Selenium compounds has quickly developed. Organoselenium derivatives have been extensively used as key synthetic intermediates [14,15,16,17] and ligands in asymmetric synthesis. [18,19,20] Also Selenium-containing derivatives such as isoselenocyanates, [21,22,23,] selenocarbamates, [24,25] selenoheterocycles [26,27,28] and selenoureas [29] are quite popular.

Currently, the most common use of selenourea compounds is in the antioxidant activity field.[30,31,32, 33] Reactive Oxygen Species (ROS) and Reactive Nitrogen Species (RNS), such as free radicals, superoxide anion, hydroperoxides, organic peroxides, nitric oxide (NO), are involved in very important biological process such as intra- and inter-cellular redox signalling,[34] gene transcription,[35] neurotransmitter activity and immune response.[35] However when the equilibrium between ROS/RNS species and natural antioxidant defences is disrupted, there is an evidence of oxidative stress.[36] This phenomenon has been associated with different diseases like cancer,[37] or neurodegenerative disorder.[38]

Fernández-Bolaños *et al.* reported the synthesis and a biological study of different families of lipophilic organoselenium compounds including selenoureas, with *in vitro* antioxidant activity.[30] These compounds were evaluated as ROS scavengers against free radicals and hydrogen peroxide, in particular.

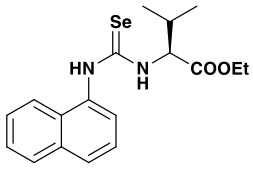

1

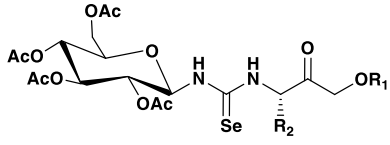

2 R_1 = Et; R_2 = H

3 R_1 = Et; R_2 = CH_2Ph

4 R_1 = Et; R_2 = CH_2OH

5 R_1 = Et; R_2 = iPr

6 R_1 = Me; R_2 = 

Among the selenocompounds studied, the remarkable results in terms of anti-radical capacity (reported in EC_{50}, effective concentration for scavenging 50% of the initial DPPH, stable free radical commonly used for the anti-radical activity studies [39] were found for the naphthyl and sugar-based selenoureas.

Compound **1** acted as the best free radical scavenger with an EC_{50} of 19.3± 3 μM (the well-known anti-oxidant ascorbic acid presents a scavenging activity of 13.3± 3 μM). Interesting, the anti-hydrogen peroxide activity of these selenourea is very low compared with the other seleno-based compound like selenocarbamate and selenohydantois that instead, can be considered as a good candidate as H_2O_2 scavengers.

Lopez and colleagues reported another application of selenourea species as antioxidant agents.[40] They designed and synthesised compound **7** that can be defined as a concrete example of dual multitarget drugs for the cure of the Gaucher disease and its side effects. The Gaucher pathology is a recessively inherited disease caused by a mutation of the GBA1 gene (glucocerebrosidase) that leads to the misfolding of the β-glucosidase. In addition, the loss of the cognitive function associated to the neurological complications of Gaucher disease involves the levels of acetylcholinesterase (AChE) that, in turn, is involved in some of the physiological manifestations of dementia-type diseases. Furthermore, an oxidative cellular stress condition, commonly associated with neurological pathologies, is observed in these conditions.[41,42] Structure **7** has been designed for inhibiting simultaneously β-glucosidase, responsible for the Gaucher disease, and acetylcholinesterease, connected with its effects, with an antioxidant activity at the same time due the presence of three specific moieties able to act selectively for each aspect above mentioned.

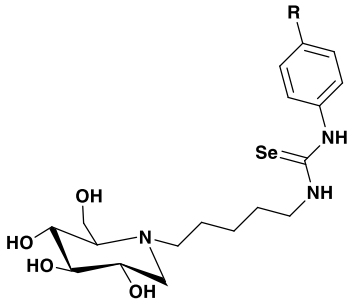

7a R = Br

7b R = OMe

7c R = Me

7

The presence of polyhydroxilate piperidines guarantees a glycosidase inhibitor site [43,44, 45] and the incorporation of an arylalkyl fragment on the nitrogen increases the selectivity for this process. The presence of Selenium in C=Se bond leads to an increase in the antioxidant activity with respect to the ROS species while the deoxynojirimycin residue of **7**, partially protonated at physiological pH values, can mimic the iminium cation of acetylcoline. All the synthesized compounds, in particular compound **7a**, were found to be strong competitive β-glucosidase (*Ki* in 1.6-5.5 μM range) and AChE inhibitors. The antiproliferative properties of compounds **7a-c** were tested on six solid human tumor cell lines with good results in the case of **6a** with respect to A549,HBL-100 and T47D cell lines (GI_{50} 7.0-12.0 μM).

Moving down along the chalcogen group, in the Periodic Table, interesting trends in binding properties can be put in evidence. In compounds containing chalcogen atoms, the absorption and emission maxima shift to longer wavelengths changing the atom from Oxygen to Sulfur to Selenium and also their softness increases. On this purpose, Selenium shows a borderline hard/soft nature that can be tuned as required to recognize specific analyte targets. Due to the low oxidation potential of Selenium and its capacity to change its valance state, organoselenium derivatives are very sensitive in

oxidizing species such as thiols and ROS.[45] Moreover, the high reactivity of selenoderivatives, in particular Se-P, Se-N and Se-O bonds, makes these compounds very attractive for fluorescence detection via chemical reactions.

For these reasons, nowadays, selenoderivatives sensing probes able to recognize neutral and ionic species through economic techniques such as fluorescence and UV-Visible spectroscopies are developing in the supramolecular chemistry.[47]

Recently, organoselenium compounds were studied as supramolecular scaffolds for anion recognition and for the transmembrane transport of chloride species.[46]

As already mentioned in Paragraph 1.4.1 Caltagirone, Martinez-Manez *at al*. reported the first example of fluorescent bis-selenoureas based receptors for anion binding. [47]

Caltagirone *et al* in 2013 reported the study of a new family of bis-ureidic anion receptors based on the 1,3-bis(aminomethyl)-benzene platform **8-10**. They demonstrated how different substituents in the pendant urea moieties both a colorimetric and a fluorimetric selective sensing of hydrogen pyrophosphate, even to the naked eye, can be achieved in DMSO.[48]

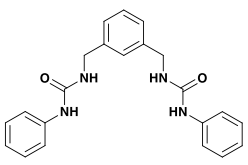

8

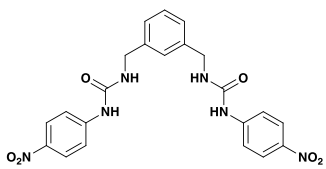

9

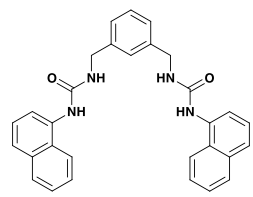

10

Encouraged by these previous results obtained in this field we report here the synthesis of a new family of functionalised bis-selenourea based receptors **L1-L4** reported in Figure 2.1 for anion recognition. The four receptor bears a phenyl, a *p*-MeO phenyl (electro-donating group), a naphthyl (fluorescent group), and a *p*-fluorophenyl (electro withdrawing group) substituents for **L1**, **L2**, **L3**, and **L4** respectively. Our aim was to determine how the presence of the selenium as chalcogen on the molecular skeleton was able to increase the affinity towards anion species. In order to prove our hypothesis ^{1}H –NMR titrations in DMSO-d_6 in presence of different anion species ($HPpi^{3-}$, BzO^{-}, $H_2PO_4^{-}$ and AcO^{-} added as tetrabutylammonium salts) were conducted and the results were compared with the analogous bis-ureas.

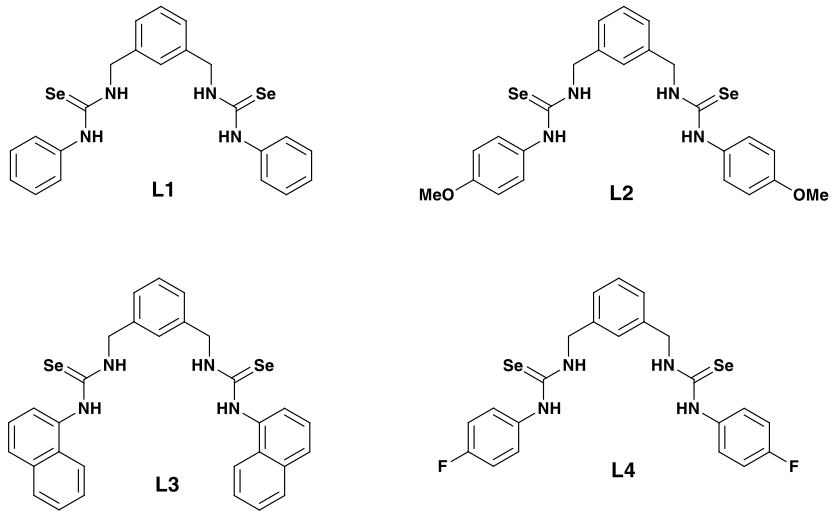

Figure 2.1 Structures of the bis-selenourea-based receptors studied in this chapter

2.2 Synthesis

The synthesis of receptors **L1**-**L4** was carried out following the synthetic procedures reported in Scheme 2.2 by reacting the 1,3-bis(aminomethyl)-benzene with the corresponding isoselenocyanate previously synthesised following the synthetic procedure reported in Scheme 2.1. All receptors were obtained in moderate yields(from 40% to 60%). Synthetic details are reported in the Experimental Part (Paragraph 2.4**)**

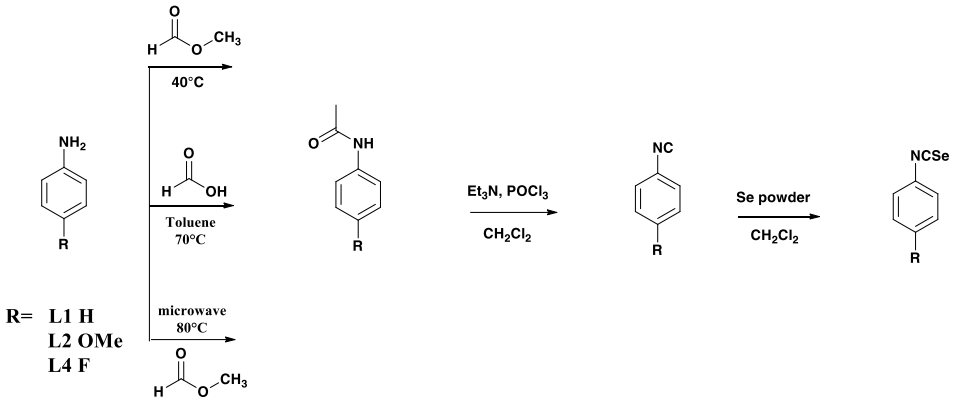

Scheme 2.1 Synthetic procedure for the synthesis of isoselenocyanate precursors

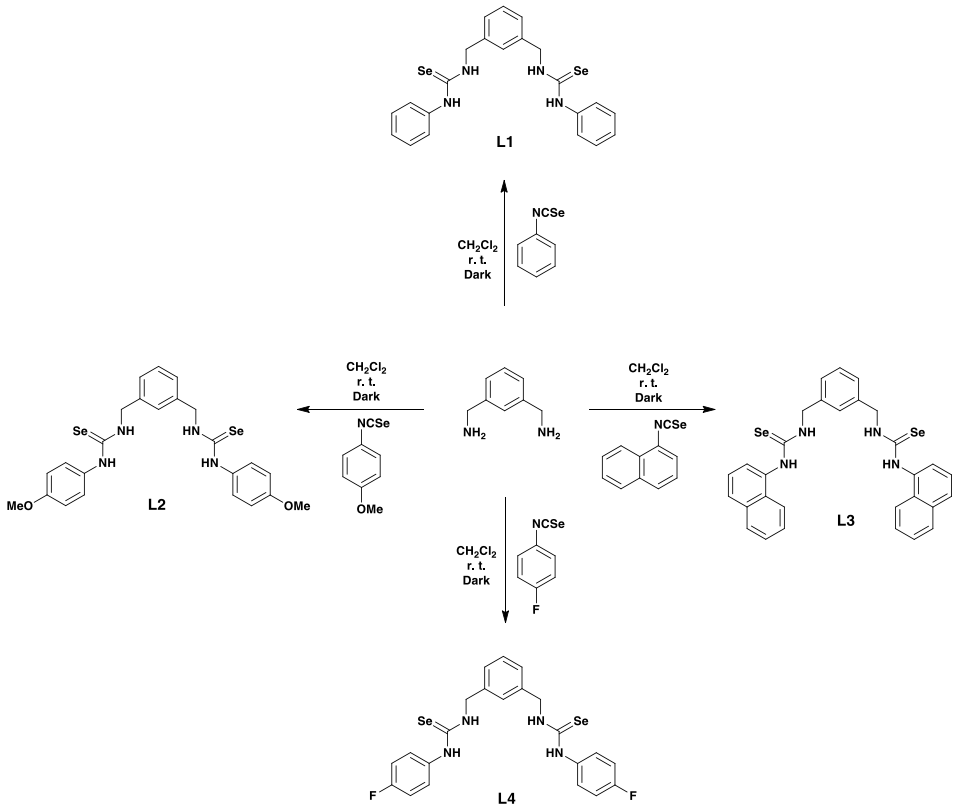

Scheme 2.2 Synthetic procedure for the synthesis of **L1**-**L4**

2.3 Solution studies

Anion-binding studies were conducted by means of ^{1}H-NMR titrations using DMSO-d_6/0.5% water as a solvent. Stability constants from the obtained ^{1}H-NMR titration curves (see Paragraph 2.4) were calculated by fitting the data to a 1:1 binding model using WinEQNMR[49] as shown in Table 2.1.

Table2.1 Association constants (K_a/M^{-1}) for the formation of adducts of **L1-L4** with anions added as tetrabutylammonium salts in DMSO-d_6/0.5% water at 300 K. All errors estimated to be≤14%

	$HPPi^{3-}$	$H_2PO_4^-$	BzO^-	AcO^-	Cl^-
L1	**Deprot**	**1941**	**515**	**nd**	**25**
L2	**Deprot**	**315**	**80**	**nd**	**16**
L3	**Deprot**	**1219**	**277**	**nd**	**<10**
L4	[a]	[a]	[a]	[a]	[a]

[a]**:** association constants for **L4** were not calculated as the compound was unstable to light and air Black selenium precipitate was observed before the addition of anion species.

As reported in Table 2.1, a precipitate of black selenium powder with **L4** was observed, suggesting a degradation of the receptor to the corresponding bis-urea when exposed to light and air. Furthermore, a splitting of the signals attributed to the NHs of the urea moiety was observed before the addition of anion seemed to confirm the hypothesis.

Under the experimental conditions in the presence of pyrophosphate the disappearance of the signal attributed to the selenourea NHs was observed already upon the addition of 0.2 equiv. of anionic guest, suggesting a deprotonation for all the receptors with this anion.

Interestingly, **L1**-**L3** showed a stronger affinity towards the dihydrogen phosphate compared to the benzoate, as already described for the analogous bis-ureas.[48] As shown in Table 2.1 and in the stack plot reported in paragraph 2.4, the broadening and then the disappearance of both the signals attributed

to the NHs protons during the titration with the AcO^- was observed, suggesting a deprotonation of all the bis-selenoureas studied with this anion.

As shown in Table 2.1, for receptor **L1** in the presence of $H_2PO_4^-$, following the downfield shift of the signals attributed to the selenourea NH protons we observed the disappearance of the signal attributed to the NH proton in green (Figure 2.2) and a dramatic downfield shift of the signal attributed to the NH proton in blue (Figure 2.2).

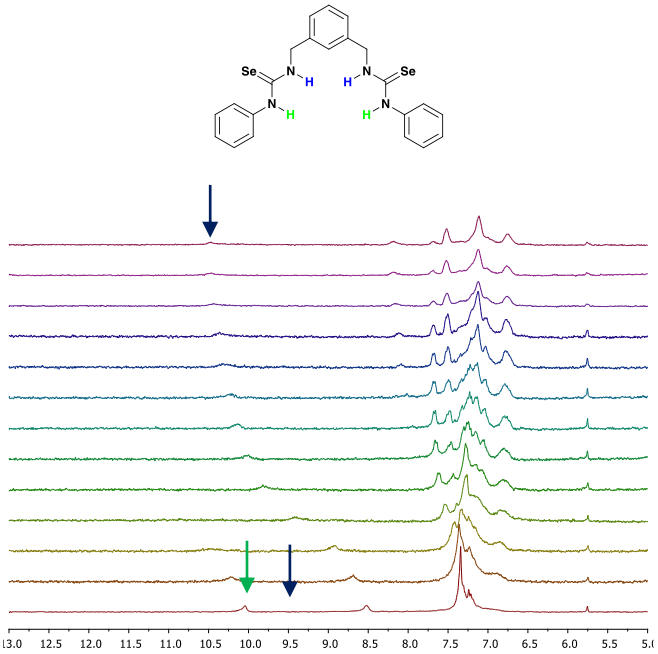

Figure 2.2 Stack-plot of the ^{1}H-NMR titration in DMSO-d_6 at 300 K of **L1** (0.005M) with dihydrogen phosphate added as tetrabutylammonium salt(0.075M).

L1-**L3** showed the highest stability constant with dihydrogen phosphate following the order **L1**>**L3**>**L2**.

By comparing the behaviour observed in the presence of $H_2PO_4^-$ and $HPPi^{3-}$ with **L1** and **L3** and their analogous bis-ureas **8** and **10** already reported in the

literature (Table 2.2), an increase in the anion affinity can be immediately pointed out. As reported in Table 2.2,a deprotonation of **L1** and **L3** in presence of the hydrogenpyrophosphate was observed, suggesting a higher acidity of the NHs of the selenourea moieties compared to the analogous ureas. Moreover, the values of the stability constants calculated for **L1** and **L3**, in the presence of $H_2PO_4^-$ are more than one order of magnitude higher than the corresponding bis-ureas **8** and **10** suggesting a stronger affinity of the bis-selenourea scaffolds compared to the analogous bis-urea with this anion.

Table 2.2 Association constants (*Ka*/M^{-1}) for the formation of adducts of **L1** and **L3** and the analogous bis-ureas **8** and **10** with pyrophosphate and dihydrogen phosphate added as tetrabutylammonium salts in DMSO-d_6/0.5% water at 300 *K*.[48] All errors estimated to be≤14%

	$HPPi^{3-}$	**$H_2PO_4^-$**
L1	**Deprot**	**1941**
8	**5480**	**484**
L3	**Deprot**	**1219**
10	**$>10^4$**	**435**

The steric hindrance exerted by the presence of selenium, softer and bigger than oxygen and sulphur in **L1**-**L3** increase the interaction with particular anion species, in this case represent by dihydrogen phosphate.

These results are supported by the work reported in Appendix A in which we described how, when compared to ureas and thioureas, selenoureas appear to be more versatile receptors for anion binding.[50]

2.4 Conclusions

In conclusion we have developed a new family of bis-selenourea-based receptors bearing different aryl substituents. The results obtained in the solution studies by ^{1}H-NMR spectroscopy show that **L1** and **L3** bearing phenyl and naphthyl groups as substituents, respectively, strongly interact with dihydrogen phosphate. In particular, the higher affinity compared to the analogous bis-ureas previously reported, has been highlighted in this work. In our hypothesis, this behaviour could be caused by the steric hindrance exerted by the presence of selenium on the receptor structure.

2.5 Experimental part

All reactions were performed in oven-dried glassware under a slight positive pressure of nitrogen. ^{1}H-NMR (300 MHz) and ^{13}C NMR (75 MHz, 125MHz) spectra were determined on a 300 MHz Bruker. Chemical shifts for ^{1}H NMR are reported in parts per million (ppm), calibrated to the residual solvent peak set, with coupling constants reported in Hertz (Hz). The following abbreviations are used for spin multiplicity: s = singlet, d = doublet, t = triplet, m = multiplet . Chemical shifts for ^{13}C NMR are reported in ppm, relative to the central line of a septet at δ = 39.52 ppm for deuteriodimethylsulfoxide. Infrared (IR) spectra were recorded on a NICOLET 5700 FT-IR spectrophotometer and reported in wavenumbers (cm^{-1}). Microanalytical data were obtained using a Fisons EA CHNS-O instrument (T = 1000 °C). All solvents and starting materials were

purchased from commercial sources where available. Proton NMR titrations were performed by adding aliquots of the putative anionic guest (as the TBA salt, 0.075 M) in a solution of the receptor (0.005M) in DMSO-d_6/0.5% water.

2.5.1 Synthesis

General procedure for the synthesis of the arylformamides (A)

The aryl amine was dissolved in a solution of ethyl formate. The mixture was kept stirring vigorously under argon atmosphere at 40°C monitoring the progress of the reaction by TLC. Once the reaction was complete, a precipitate was observed. The solid was filtrated and dried under reduced pressure.

General procedure for the synthesis of the arylformamides (B)

To a solution of aniline in 5 mL of toluene, 2 mL di formic acid were added. The mixture was kept at 70°C under vigorously stirring for 24 hs. Then, the solvent was removed under reduced pressure, washed with water and extracted with dichloromethane(3x10mL). The organic phase was dried with Na_2SO_4 and then the solvent was removed under reduced pressure collecting the product as a crude solid.

General procedure for the synthesis of the arylformamides (C)

In a microwave tube the aryl amine was dissolved in a solution of ethyl formate. The mixture was kept in a microwave equipment at 90°C for 2hs. After that time a precipitate was observed. The mixture was filtrated and the solid was dried and collected as a crude solid.

General procedure for the synthesis of the isoselenocyanate

To a solution of the arylformamide (1 equiv) in dry dichloromethane (10 mL) under vigorously stirring triethylamine (6 equiv) and $POCl_3$(0.8 equiv) were added slowly. The reaction was kept at room temperature under argon

atmosphere for 24 hs. The progress of the reaction was monitored by TLC. After that time 40 mL of a $NaHCO_3$ saturated solution was added dropwise (development of gas was observed) and kept stirring for 2hs (till the gas development stopped). Then the mixture was repeatedly extracted with dichloromethane(4x10mL) and the organic phases were combined and then dried over Na_2SO_4 and concentrated under reduced pressure. The product obtained was then dissolved in dry dichloromethane (5mL) and kept under argon atmosphere at 40°C. Selenium powder (3equiv) was then added. The reaction was kept stirring at dark for 24hs and the reaction progress monitored by TLC. After that time, the mixture was filtrated over celite to remove the selenium powder in excess and washed repeatedly with dichloromethane. The solvent was then removed under *vacuo* and the residue purified by flash chromatography on silica gel(eluent depending by the different substrate used).

General procedure for the synthesis of the bis-selenoureas compounds (**L1**-**L4**)

To a solution of 1,3-bis(aminomethyl)-benzene in dry dichloromethane (4 mL) a solution of the relative isoselocyanate in 2mL of dry dichloromethane was added. The mixture was kept stirring at room temperature under argon atmosphere for 24 hs. The progress of the reaction was monitored by TLC. After that time a precipitate was observed. Then the mixture was filtrated and the solid dried collecting the product as a crude solid.

1,1'-(1,3-phenylenebis(methylene))bis(3-phenylselenourea) (**L1**)

Yield 62% ^{1}H NMR (400 MHz, DMSO-d_6) δ 10.05 (s, 1H), 8.50 (s, 1H), 7.28 (m, 8H), 6.91 (d, 1H), 4.81(s, 2H) ^{13}C NMR (125 MHz, DMSO-d_6) δ 140.80, 138.12, 127.99, 127.69, 126.05, 125.35, 122.86, 120.33, 47.85.

1,1'-(1,3-phenylenebis(methylene))bis(3-(4-methoxyphenyl)selenourea) (**L2**)

Yield 66% ^{1}H NMR (400 MHz, DMSO-d_6) δ 9.85 (s, 1H), 8.22 (s, 1H), 7.16 (m, 4H), 6.90 (d, 1H), 4.79(s, 2H) ^{13}C NMR (125 MHz, DMSO-d_6) δ 162.50, 144.29, 133.27, 132.12, 130.99, 120.11, 60.49.

1,1'-(1,3-phenylenebis(methylene))bis(3-(naphthalen-1-yl)selenourea) (**L3**)

Yield 42% ^{1}H NMR (400 MHz, DMSO-d_6) δ 10.20 (s, 1H), 8.17 (s, 1H), 7.98 (d, 1H), 7.92 (t, 2H), 7.55 (m, 4H) 7.48 (t, 1H), 7.20 (d, 2H), 7.11 (s, 1H), 4.76(s, 2H) ^{13}C NMR (125 MHz, DMSO-d_6) δ 140.79, 137.80, 135.29, 129.25, 127.98, 126.87, 126.14, 126.06, 125.44, 125.35, 123.44, 121.56, 112.5, 47.85.

1,1'-(1,3-phenylenebis(methylene))bis(3-(4-fluorophenyl)selenourea) (**L4**)

Yield 54% ^{1}H NMR (400 MHz, DMSO-d_6) δ 10.14 (s, 1H), 8.57 (s, 1H), 7.34 (m, 3H), 7.24 (s, 1H), 7.14 (m, 4H), 4.80(s, 2H) ^{13}C NMR (125 MHz, DMSO-d_6) δ 158.22, 140.82, 136.18, 127.97, 126.05, 125.35, 121.46, 115.78, 47.97.

2.5.2 ^{1}H-NMR titrations

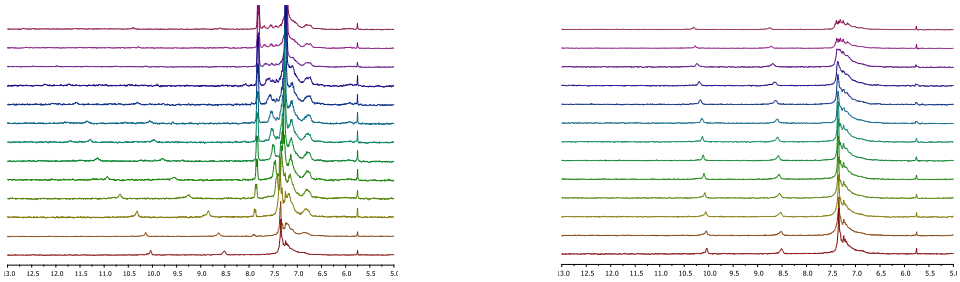

(a) (b)

Figure 2.3 Stack plots of the ^{1}H-NMR spectra of **L1** (0.005 M) upon addition of increasing amount of (a) TBABzO and(b) TBACl (0.075 M) in DMSO-d_6.

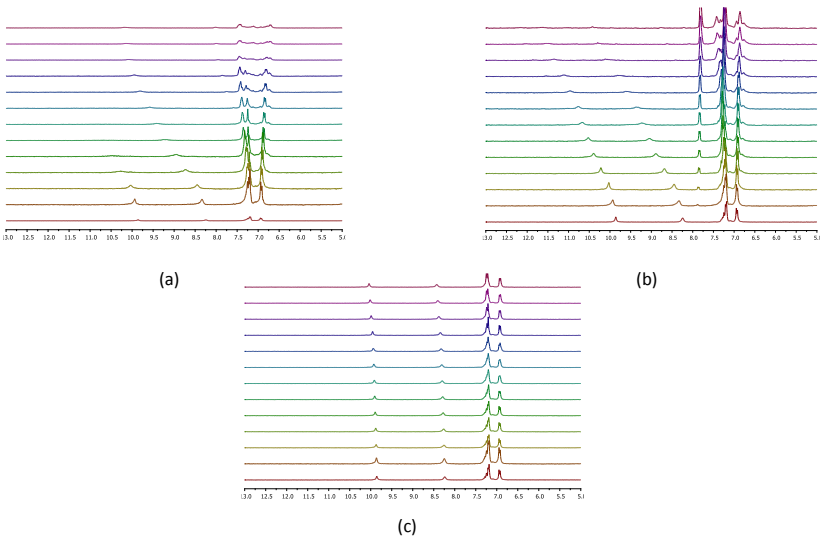

Figure 2.4 Stack plots of the ^{1}H-NMR spectra of **L2** (0.005 M) upon addition of increasing amount of (a) $TBAH_2PO_4$, (b) TBABzO, (c) TBACl (0.075 M) in DMSO-d_6.

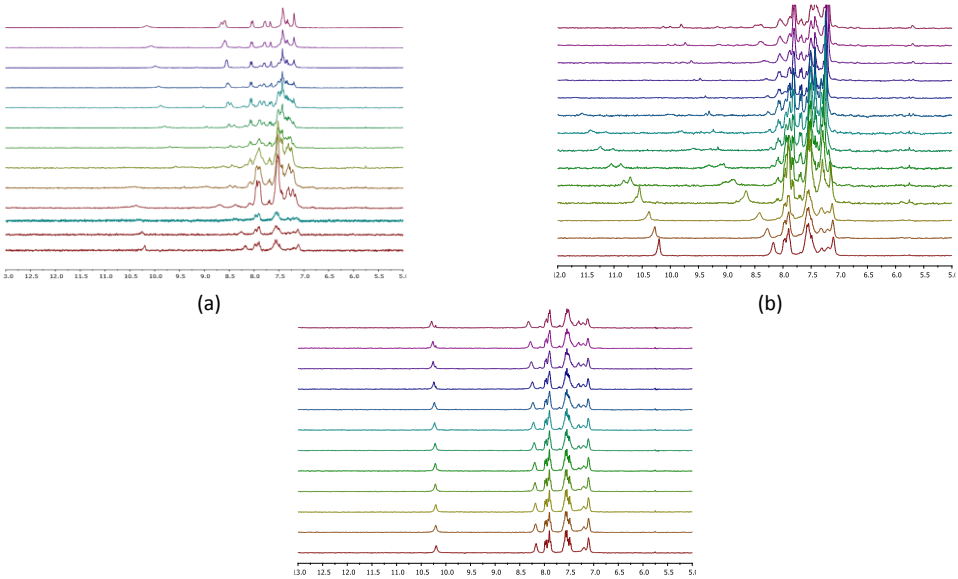

Figure 2.5 Stack plots of the ^{1}H-NMR spectra of **L3** (0.005 M) upon addition of increasing amount of (a) $TBAH_2PO_4$, (b) TBABzO, (c) TBACl (0.075 M) in DMSO-d_6.

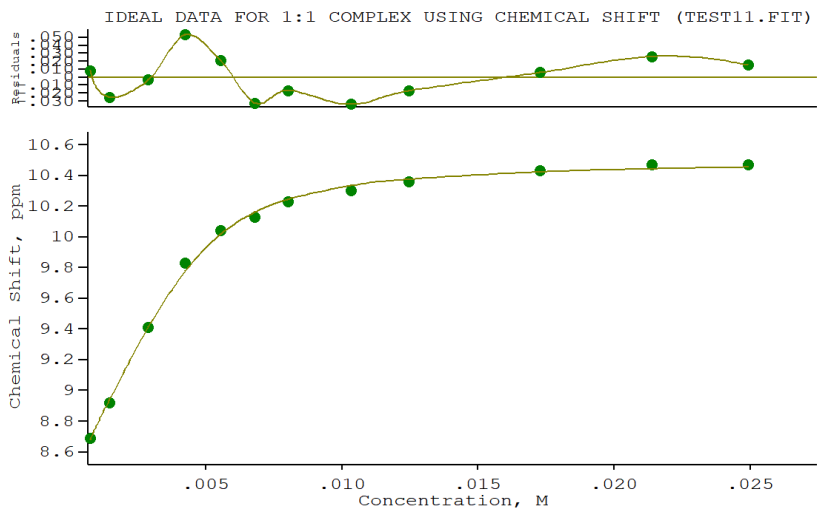

Calculations by WinEQNMR2 Version 2.00 by Michael J. Hynes

Program run at 14:06:11 on 05/31/2019

IDEAL DATA FOR 1:1 COMPLEX USING CHEMICAL SHIFT (TEST11.FIT)

Reaction: Sn + L = Sn(L)

FILE: TEST11.FIT (Measured shift is on 119Sn)

IDEAL DATA: K1 = 63.091; DELTA M = 20.0; DELTA ML = 120.0

File prepared by M. J. Hynes, October 22 2000

Equilibrium constants are floating point numbers

NO.	A	PARAMETER	DELTA	ERROR	CONDITION	DESCRIPTION
1	1	1.94132E+03	2.000E-01	2.221E+02	4.600E+00	K1
2	1	8.40321E+00	2.000E-01	2.583E-02	1.412E+00	SHIFT Sn
3	1	1.05065E+01	1.000E+00	2.148E-02	3.936E+00	SHIFT Sn(L)

Figure 2.6 ^{1}H-NMR titration of **L1** with $TBAH_2PO_4$ in DMSO-*d_6-0.5%*

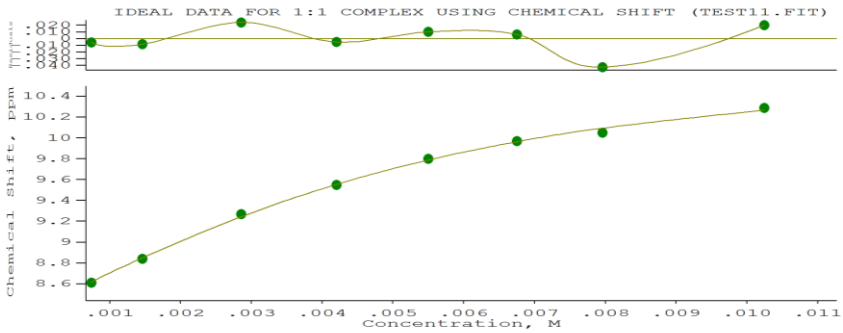

Calculations by WinEQNMR2 Version 2.00 by Michael J. Hynes

Program run at 19:49:20 on 10/26/2019

IDEAL DATA FOR 1:1 COMPLEX USING CHEMICAL SHIFT (TEST11.FIT)

Reaction: Sn + L = Sn(L)

FILE: TEST11.FIT (Measured shift is on 119Sn)

IDEAL DATA: K1 = 63.091; DELTA M = 20.0; DELTA ML = 120.0

File prepared by M. J. Hynes, October 22 2000

Equilibrium constants are floating point numbers

NO.	A	PARAMETER	DELTA	ERROR	CONDITION	DESCRIPTION
1	1	5.15488E+02	2.000E-01	1.068E+02	6.600E+01	K1
2	1	8.36076E+00	2.000E-01	2.390E-02	2.400E+00	SHIFT Sn
3	1	1.08439E+01	1.000E+00	1.273E-01	5.835E+01	SHIFT Sn(L)

0RMS ERROR = 2.48E-02 MAX ERROR = 4.25E-02 AT OBS.NO. 7

RESIDUALS SQUARED = 3.08E-03

RFACTOR = 0.2053 PERCENT

Figure 2.7 ^{1}H-NMR titration of **L1** with TBABzO in DMSO-*d_6-0.5%*

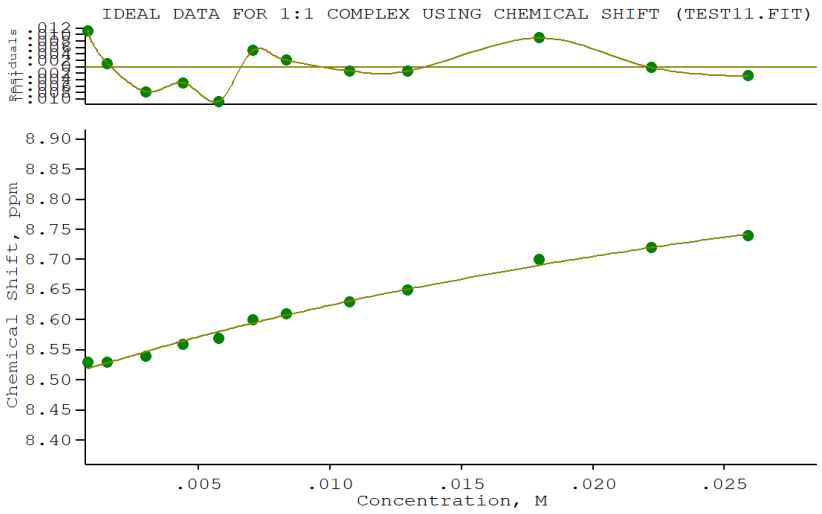

Calculations by WinEQNMR2 Version 2.00 by Michael J. Hynes

Program run at 19:19:58 on 10/26/2019

IDEAL DATA FOR 1:1 COMPLEX USING CHEMICAL SHIFT (TEST11.FIT)

Reaction: Sn + L = Sn(L)

FILE: TEST11.FIT (Measured shift is on 119Sn)

IDEAL DATA: K1 = 63.091; DELTA M = 20.0; DELTA ML = 120.0

File prepared by M. J. Hynes, October 22 2000

Equilibrium constants are floating point numbers

NO.	A	PARAMETER	DELTA	ERROR	CONDITION	DESCRIPTION
1	1	2.49784E+01	2.000E-01	7.808E+00	1.668E+02	K1
2	1	8.50826E+00	2.000E-01	5.399E-03	4.940E+00	SHIFT Sn
3	1	9.13028E+00	1.000E+00	1.152E-01	1.371E+02	SHIFT Sn(L)

0RMS ERROR = 7.03E-03 MAX ERROR = 1.12E-02 AT OBS.NO. 1

RESIDUALS SQUARED = 4.45E-04

RFACTOR = 0.0707 PERCENT

Figure 2.8 ^{1}H-NMR titration of **L1** with TBACl in DMSO-*d_6-0.5%*

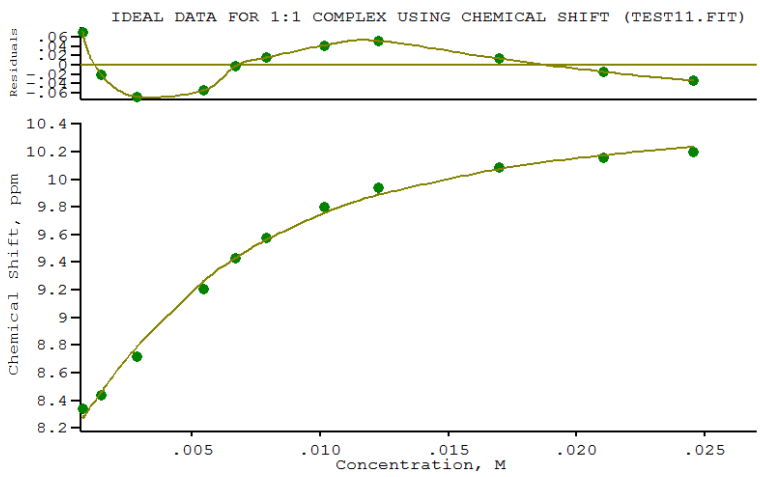

Calculations by WinEQNMR2 Version 2.00 by Michael J. Hynes

Program run at 14:11:22 on 10/27/2019

IDEAL DATA FOR 1:1 COMPLEX USING CHEMICAL SHIFT (TEST11.FIT)

Reaction: Sn + L = Sn(L)

FILE: TEST11.FIT (Measured shift is on 119Sn)

IDEAL DATA: K1 = 63.091; DELTA M = 20.0; DELTA ML = 120.0

File prepared by M. J. Hynes, October 22 2000

Equilibrium constants are floating point numbers

NO.	A	PARAMETER	DELTA	ERROR	CONDITION	DESCRIPTION
1	1	3.15247E+02	2.000E-01	4.552E+01	1.434E+01	K1
2	1	8.06170E+00	2.000E-01	4.269E-02	2.307E+00	SHIFT Sn
3	1	1.05780E+01	1.000E+00	8.020E-02	1.085E+01	SHIFT Sn(L)

0RMS ERROR = 4.87E-02 MAX ERROR = 7.03E-02 AT OBS.NO. 1

RESIDUALS SQUARED = 1.90E-02

RFACTOR = 0.4388 PERCENT

Figure 2.9 ^{1}H-NMR titration of **L2** with $TBAH_2PO_4$ in DMSO-*d_6-0.5%*

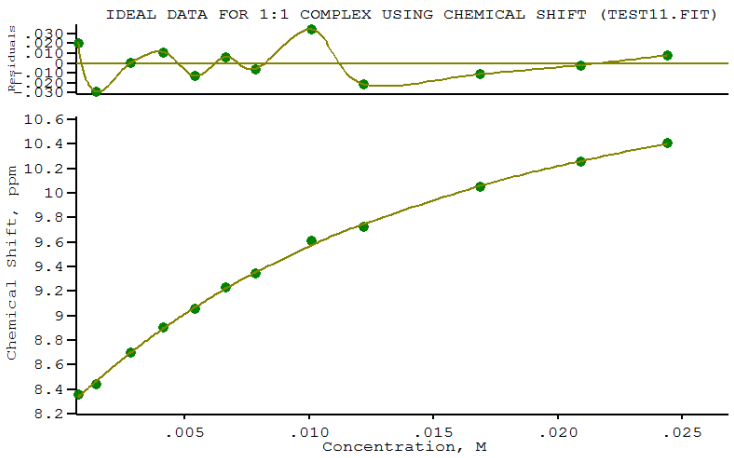

Calculations by WinEQNMR2 Version 2.00 by Michael J. Hynes

Program run at 14:16:25 on 10/27/2019

IDEAL DATA FOR 1:1 COMPLEX USING CHEMICAL SHIFT (TEST11.FIT)

Reaction: Sn + L = Sn(L)

FILE: TEST11.FIT (Measured shift is on 119Sn)

IDEAL DATA: K1 = 63.091; DELTA M = 20.0; DELTA ML = 120.0

File prepared by M. J. Hynes, October 22 2000

Equilibrium constants are floating point numbers

NO.	A	PARAMETER	DELTA	ERROR	CONDITION	DESCRIPTION
1	1	8.05357E+01	2.000E-01	5.513E+00	5.432E+01	K1
2	1	8.19979E+00	2.000E-01	1.638E-02	4.162E+00	SHIFT Sn
3	1	1.16949E+01	1.000E+00	9.443E-02	4.024E+01	SHIFT Sn(L)

0RMS ERROR = 1.94E-02 MAX ERROR = 3.42E-02 AT OBS.NO. 8

RESIDUALS SQUARED = 3.40E-03

RFACTOR = 0.1798 PERCENT

Figure 2.10 ^{1}H-NMR titration of **L2** with TBABzO in DMSO-*d_6-0.5%*

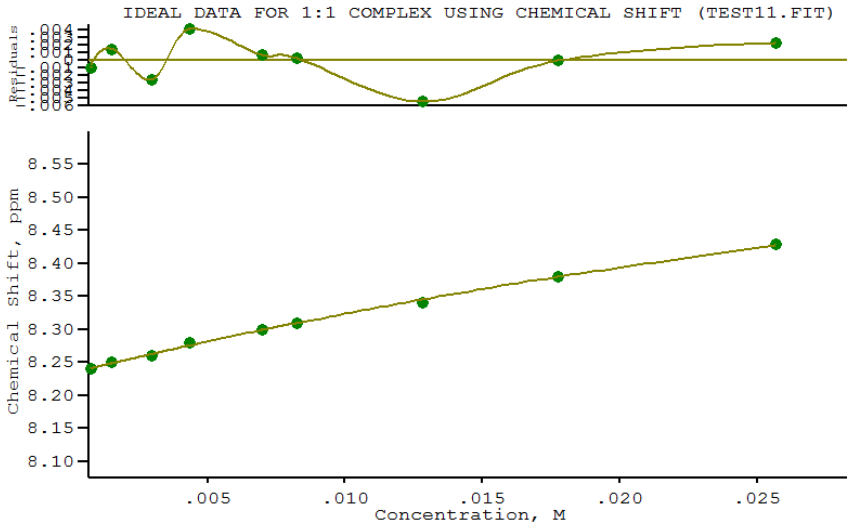

Calculations by WinEQNMR2 Version 2.00 by Michael J. Hynes

Program run at 14:13:54 on 10/27/2019

IDEAL DATA FOR 1:1 COMPLEX USING CHEMICAL SHIFT (TEST11.FIT)

Reaction: Sn + L = Sn(L)

FILE: TEST11.FIT (Measured shift is on 119Sn)

IDEAL DATA: K1 = 63.091; DELTA M = 20.0; DELTA ML = 120.0

File prepared by M. J. Hynes, October 22 2000

Equilibrium constants are floating point numbers

NO.	A	PARAMETER	DELTA	ERROR	CONDITION	DESCRIPTION
1	1	1.59252E+01	2.000E-01	4.372E+00	3.388E+02	K1
2	1	8.23320E+00	2.000E-01	2.500E-03	4.272E+00	SHIFT Sn
3	1	8.93014E+00	1.000E+00	1.349E-01	3.009E+02	SHIFT Sn(L)

0RMS ERROR = 3.25E-03 MAX ERROR = 5.47E-03 AT OBS.NO. 7

RESIDUALS SQUARED = 6.32E-05

RFACTOR = 0.0319 PERCENT

Figure 2.11 ^{1}H-NMR titration of **L2** with TBACl in DMSO-*d_6-0.5%*

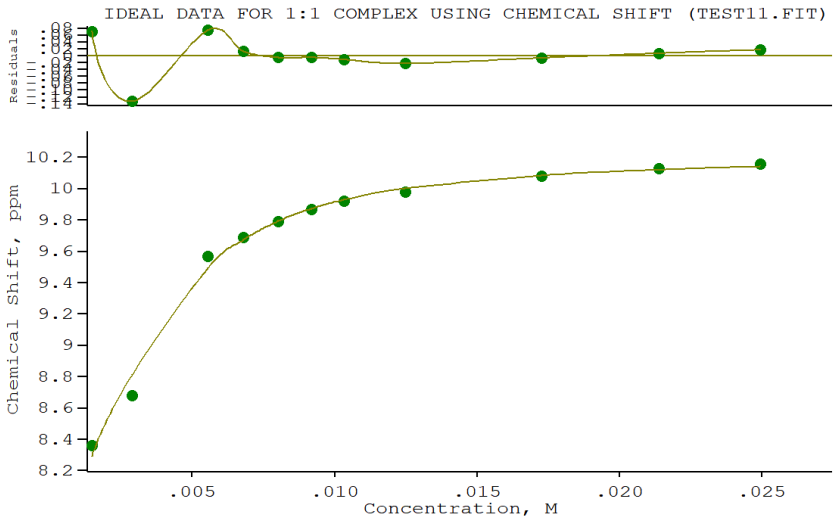

Calculations by WinEQNMR2 Version 2.00 by Michael J. Hynes

Program run at 13:39:53 on 05/31/2019

IDEAL DATA FOR 1:1 COMPLEX USING CHEMICAL SHIFT (TEST11.FIT)

Reaction: Sn + L = Sn(L)

FILE: TEST11.FIT (Measured shift is on 119Sn)

IDEAL DATA: K1 = 63.091; DELTA M = 20.0; DELTA ML = 120.0

File prepared by M. J. Hynes, October 22 2000

Equilibrium constants are floating point numbers

NO.	A	PARAMETER	DELTA	ERROR	CONDITION	DESCRIPTION
1	1	1.21928E+03	2.000E-01	2.369E+02	7.120E+00	K1
2	1	7.66845E+00	2.000E-01	7.867E-02	1.873E+00	SHIFT Sn
3	1	1.02425E+01	1.000E+00	5.338E-02	5.454E+00	SHIFT Sn(L)

Figure 2.12 ^{1}H-NMR titration of **L3** with $TBAH_2PO_4$ in DMSO-*d_6-0.5%*

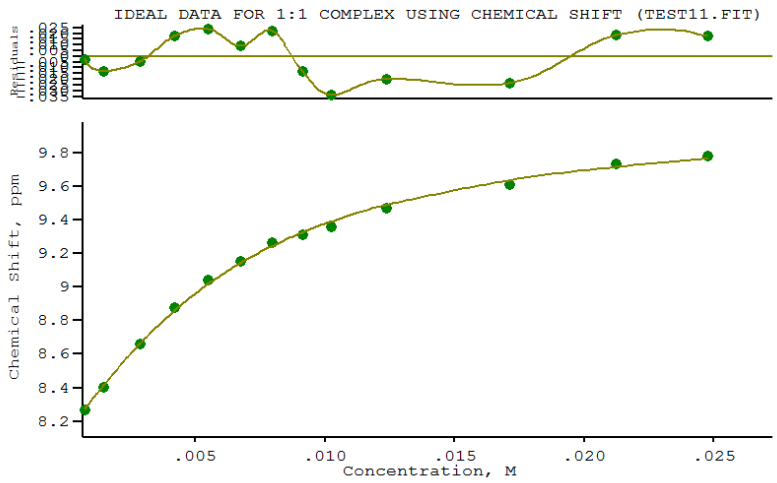

Calculations by WinEQNMR2 Version 2.00 by Michael J. Hynes

Program run at 12:05:50 on 10/27/2019

IDEAL DATA FOR 1:1 COMPLEX USING CHEMICAL SHIFT (TEST11.FIT)

Reaction: Sn + L = Sn(L)

FILE: TEST11.FIT (Measured shift is on 119Sn)

IDEAL DATA: K1 = 63.091; DELTA M = 20.0; DELTA ML = 120.0

File prepared by M. J. Hynes, October 22 2000

Equilibrium constants are floating point numbers

NO.	A	PARAMETER	DELTA	ERROR	CONDITION	DESCRIPTION
1	1	2.77218E+02	2.000E-01	2.182E+01	1.648E+01	K1
2	1	8.11278E+00	2.000E-01	1.891E-02	2.777E+00	SHIFT Sn
3	1	1.00527E+01	1.000E+00	3.482E-02	1.176E+01	SHIFT Sn(L)

0RMS ERROR = 2.14E-02 MAX ERROR = 3.39E-02 AT OBS.NO. 9

RESIDUALS SQUARED = 4.59E-03

RFACTOR = 0.2050 PERCENT

Figure 2.13 ^{1}H-NMR titration of **L3** with TBABzO in DMSO-*d_6-0.5%*

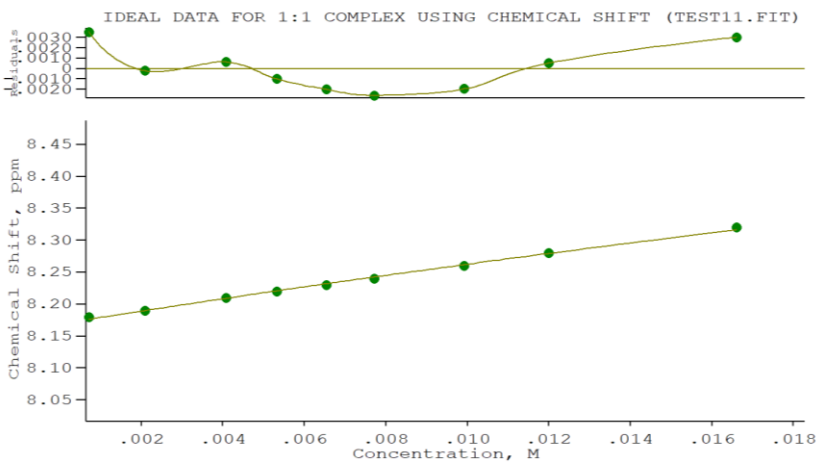

Calculations by WinEQNMR2 Version 2.00 by Michael J. Hynes

Program run at 19:14:20 on 10/26/2019

IDEAL DATA FOR 1:1 COMPLEX USING CHEMICAL SHIFT (TEST11.FIT)

Reaction: Sn + L = Sn(L)

FILE: TEST11.FIT (Measured shift is on 119Sn)

IDEAL DATA: K1 = 63.091; DELTA M = 20.0; DELTA ML = 120.0

File prepared by M. J. Hynes, October 22 2000

Equilibrium constants are floating point numbers

NO. A PARAMETER DELTA ERROR CONDITION DESCRIPTION

1 1 7.86736E+00 2.000E-01 4.076E+00 1.904E+03 K1

2 1 8.16933E+00 2.000E-01 2.055E-03 5.436E+00 SHIFT Sn

3 1 9.46845E+00 1.000E+00 5.849E-01 1.799E+03 SHIFT Sn(L)

0RMS ERROR = 2.51E-03 MAX ERROR = 3.50E-03 AT OBS.NO. 1

RESIDUALS SQUARED = 3.78E-05

RFACTOR = 0.0249 PERCENT

Figure 2.14 ^{1}H-NMR titration of **L3** with TBACl in DMSO-*d_6-0.5%*

2.6 References

1. R. Naithani, *Mini reviews in medicinal chemistry*, 2008, **8**, 657-668.
2. L. A. Wessjohann, A. Schneider, M. Abbas and W. Brandt, *Biol. Chem.*, 2007, **388**, 997-1006.
3. L. Pire, G. Deby-Dupont, T. Lemineur and J.-C. Preiser, *Current Nutrition & Food Science*, 2007, **3**, 222-235.
4. E. E. Battin and J. L. Brumaghim, *Cell biochemistry bioph*, 2009, **55**, 1-23.
5. U. H Gandhi, T. P Nagaraja and K. Sandeep Prabhu, *Curr. Chem.l Biol.*, 2013, **7**, 65-73.
6. T. Xu, Y. Liu, J. Meng, J. Zeng, X. Xu and M. Mi, *Xi bao yu fen zi mian yi xue za zhi= Chinese journal of cellular and molecular immunology*, 2013, **29**, 1245-1250.
7. S. V. Madhunapantula, D. Desai, A. Sharma, S. J. Huh, S. Amin and G. P. Robertson, *Mol,* 2008, **7**, 1297-1308.
8. J.-H. Lee, S. H. Shin, S. Kang, Y.-S. Lee and S. Bae, *Int. J. Mol. Med.*, 2008, **21**, 91.
9. H. K. Rooprai, I. Kyriazis, R. K. Nuttall, D. R. Edwards, D. Zicha, D. Aubyn, D. Davies, R. Gullan and G. J. Pilkington, *Int. J. Onc.*, 2007, **30**, 1263-1272.
10. D. Li, G. L. Graef, J. A. Yee and L. Yan, *J. Nutr.*, 2004, **134**, 1536-1540.
11. N. T. Akbaraly, J. Arnaud, I. Hininger-Favier, V. Gourlet, A.-M. Roussel and C. Berr, *Clin. Chem.*, 2005, **51**, 2117-2123.
12. T. Balasankar, M. Gopalakrishnan and S. Nagarajan, *J. enzyme inhib med chem*, 2007, **22**, 171-175.
13. M. Soriano-Garcia, *Curr. Med. Chem.*, 2004, **11**, 1657-1669.
14. C. Santi, S. Santoro, L. Testaferri and M. Tiecco, *Synlett*, 2008, **2008**, 1471-1474.
15. M. Tiecco, L. Testaferri, L. Bagnoli, C. Scarponi, A. Temperini, F. Marini and C. Santi, *Tetrahedron: Asymmetry*, 2007, **18**, 2758-2767.

16. S. Valerio, A. Iadonisi, M. Adinolfi and A. Ravidà, *J. Org. Chem.*, 2007, **72**, 6097-6106.

17. Z. J. Witczak and S. Czernecki, *Adv carbohyd chem bi*, 1998, **53**, 143-199.

18. E. M. McGarrigle, E. L. Myers, O. Illa, M. A. Shaw, S. L. Riches and V. K. Aggarwal, *Chem. Rev*, 2007, **107**, 5841-5883.

19. A. L. Braga, D. S. Ludtke and F. Vargas, *Curr. Org. Chem.*, 2006, **10**, 1921-1938.

20. M. Tiecco, L. Testaferri, L. Bagnoli, C. Scarponi, A. Temperini, F. Marini and C. Santi, *Tetrahedron: Asymmetry*, 2006, **17**, 2768-2774.

21. S. Braverman, M. Cherkinsky, M. Birsa, S. Ley, R. Noyori and J. Knight, Thieme: Stuttgart, 2005.

22. M. Petrov and N. Zmitrovich, *Russ J gen*, 1999, **69**, 245-256.

23. T. G. Back, *Organoselenium chemistry: a practical approach*, OUP Oxford, 1999.

24. D. R. Garud, M. Makimura, H. Ando, H. Ishihara and M. Koketsu, *Tetrahedron Lett.*, 2007, **48**, 7764-7768.

25. D. H. Barton, S. I. Parekh, M. Tajbakhsh, E. A. Theodorakis and T. Chi-Lam, *Tetrahedron*, 1994, **50**, 639-654.

26. H. Heimgartner, Y. Zhou, P. K. Atanassov and G. L. Sommen, *Phosphorus, Sulfur, and Silicon*, 2008, **183**, 840-855.

27. G. L. Sommen, A. Linden and H. Heimgartner, *Helv. Chim. Acta*, 2008, **91**, 209-219.

28. D. R. Garud, M. Koketsu and H. Ishihara, *Molecules*, 2007, **12**, 504-535.

29. M. Koketsu and H. Ishihara, *Curr. Org. Synth.*, 2006, **3**, 439-455.

30. P. Merino-Montiel, S. Maza, S. Martos, Ó. López, I. Maya and J. G. Fernández-Bolaños, *Eur. J. Pharm. Sci.*, 2013, **48**, 582-592.

31. B. Mishra, P. Hassan, K. Priyadarsini and H. Mohan, *J. Phys. Chem. B*, 2005, **109**, 12718-12723.

32. M. V. Bhaskara Reddy, D. Srinivasulu, K. Peddanna, C. Apparao and P. Ramesh, *Synt. Comm.*, 2015, **45**, 2592-2600.

33. A. P. Fernandes and V. Gandin, *Biochim Biophys Acta -General Subjects*, 2015, **1850**, 1642-1660.

34. V. J. Thannickal and B. L. Fanburg, *Am. J. Physiology-Lung Cell. Mol. Phys.*, 2000, **279**, L1005-L1028.

35. Y.-Z. Fang, S. Yang and G. Wu, *Nutrition*, 2002, **18**, 872-879.

36. R. Kohen and A. Nyska, *Tox. pathology*, 2002, **30**, 620-650.

37. C. L. Grek and K. D. Tew, *Curr. opinion pharm.*, 2010, **10**, 362-368.

38. D. A. Butterfield, M. Perluigi and R. Sultana, *Eur. j. pharmacol.*, 2006, **545**, 39-50.

39. O. P. Sharma and T. K. Bhat, *Food chem*, 2009, **113**, 1202-1205.

40. J. I. Olsen, G. B. Plata, J. M. Padrón, Ó. López, M. Bols and J. G. Fernández-Bolaños, *Eur. J. Med. Chem.*, 2016, **123**, 155-160.

41. E. Niedzielska, I. Smaga, M. Gawlik, A. Moniczewski, P. Stankowicz, J. Pera and M. Filip, *Mol. neurobiol.*, 2015, 1-32.

42. Y.-J. Lee, S.-J. Kim and T.-H. Heo, *Biochem. biophys. res. comm.*, 2011, **413**, 254-258.

43. M. Yagi, T. Kouno, Y. Aoyagi and H. Murai, *J. Agr. Chem. Soc. Jap.*, 1976.

44. T. Butters, L. Van den Broek, G. Fleet, T. Krulle, M. Wormald, R. Dwek and F. Platt, *Tetrahedron: Asymmetry*, 2000, **11**, 113-124.

45. R. H. Lachmann, 2005.

46. M. J. Spooner and P. A. Gale, *Supramol. Chem.*, 2018, **30**, 514-519.

47. A. Casula, A. Llopis-Lorente, A. Garau, F. Isaia, M. Kubicki, V. Lippolis, F. Sancenón, R. Martínez-Máñez, A. Owczarzak, C. Santi, M. Andrea Scorciapino and C. Caltagirone, *Chem. Comm.*, 2017, **53**, 3729-3732.

48. C. Caltagirone, C. Bazzicalupi, F. Isaia, M. E. Light, V. Lippolis, R. Montis, S. Murgia, M. Olivari and G. Picci, *Org. Biomol. Chem.*, 2013, **11**, 2445-2451.

49. M. J. Hynes, *J. Chem. Soc., Dalton Trans.*, 1993, 311-312.

50. A. Casula, P. Begines, A. Bettoschi, J. G. Fernandez-Bolaños, F. Isaia, V. Lippolis, Ó. López, G. Picci, M. Andrea Scorciapino and C. Caltagirone, *Chem. Comm.*, 2017, **53**, 11869-11872.

Chapter 3:

Halogenated isophthalamides and dipicolinamides: the role of the halogen substituent on the anion binding properties and transport

3 Halogenated *isophthalamides* and dipicolinamides: the role of the halogen substituent on the anion binding properties and transport

In this chapter a novel family of amide-based receptor are reported. Specifically, the role of the halogen substituents on the anion binding properties and on the activity as anion transporters of a series of isophthalamides and dipicolineamides (**L5**-**L10**) both in solution and in the solid state was investigated. In particular, we wanted to evaluate the possibility to establish different and combined interactions depending on the substituents on the aromatic rings. Only **L9** and **L10** bearing perfluorophenyl rings as substituents have some affinities for the set of anion studies. In particular, in the case of **L9** an interesting behaviour with the formation of a non-symmetric adduct was hypothesised by ^{1}H- and ^{19}F-NMR spectroscopy studies in solution and confirmed by theoretical calculation. The study of the crystal structures of the receptors demonstrate that the steric hindrance of the halogens influence the accessibility of the isophtalamide or dipicoline amide NHs, thus modulating the affinity towards the anions. Furthermore, **L9** and **L10** are able to function as synthetic anion transporters through lipid vesicles.

3.1 Introduction

The development of neutral receptors for anion recognition has been a fundamental topic in the field of Supramolecular Chemistry in the last 20 years.[1-5] It is well known that in Nature proteins can bind anions through their amide linkages that can work both as hydrogen bond donors (*via* the NH groups) and hydrogen bond acceptors (*via* the C=O groups). Therefore, among the various classes of neutral receptors, those containing one or more amide moieties have attracted great attention. In particular, the pioneering work of Crabtree and Smith at the end of the '90s demonstrated that isophthalamides are an important class of receptors which are able to bind anions both in solution and in the solid state when adopting a *syn-syn* conformation.[6,7] Since

then, the isophthalamide motif and its pyridine analogous have been adopted in the design of both acyclic and macrocyclic systems for anion binding and transport and for the development of H-bond based architectures.[8-17] Along with H-bonds, other interactions are of great importance for the stabilization of anion adducts with neutral receptors. Halogen bonds (XB), highly directional supramolecular interaction between an electrophilic species (XB donor) and a Lewis base (XB acceptor), are particularly attractive interactions for the electron-rich nature of anions and the formation of halogen bonds between anion guests and synthetic receptors have been demonstrated both in solution and in the solid state.[18-20]

Aromatic interactions, such as π-π stacking, CH- π, cation- π, lone-pair- π are also important of the stabilization of molecular architectures, particularly in biology.[21] In the early 2000s' the possibility to establish anion- π interactions have been demonstrated for the first time by Frontera, Deya and co-workers who described the interactions with anions and hexafluorobenzene in the solid state.[22] It is indeed well established that the introduction of fluorine atoms in the benzene ring (i.e. moving from C_6H_6 to C_6F_6) causes an inversion in the value of quadripole moment *Q* (from Q_{C6H6} =^-29.0 x10^{-40} to Q_{C6F6} = 31.7x10^{-40} C m^{-2}),[23] thus favouring aromatic interactions.

In this Chapter we investigate the role of the halogen substituents on the anion binding properties of a series of isophthalamides and dipicolinamides (**L5**-**L10**, Figure 3.1) both in solution and in the solid state. In particular, we wanted to evaluate the possibility to establish different and combined interactions depending on the substituents on the aromatic rings. Theoretical calculations helped us to get a deeper understanding of the interactions involved in the proposed systems.

Examples of isophthalamide and isophthalamide-like molecules have also been studied as transmembrane carriers.[24,25] Although simple isophthalamides have been proven ineffective as transmembrane anion carriers,[26]decoration of this motif with hydroxyl groups in the 4 and 6 positions of the aromatic group resulted in the stabilization of the appropriate conformation of the anion binding motif and

polarization of the N-H groups, activating transmembrane anion transport.[27] Likewise, preorganization of the binding cleft in dipicolylamides also proved useful in terms of transmembrane chloride transport.[28] Polarization of the hydrogen-bond donor groups to enhance the anion binding is frequently used to increase the anion transport properties of anionophores. In this regard, introducing fluorinated substituents is particularly effective since, in addition to the electron-withdrawing effect of these substituents, an increase of the lipophilicity of the molecule is obtained.[29] Indeed, lipophilicity is a key parameter to tune the transmembrane activity of these compounds.[30,31] For these reasons we have also studied the transport abilities of these family of compounds.

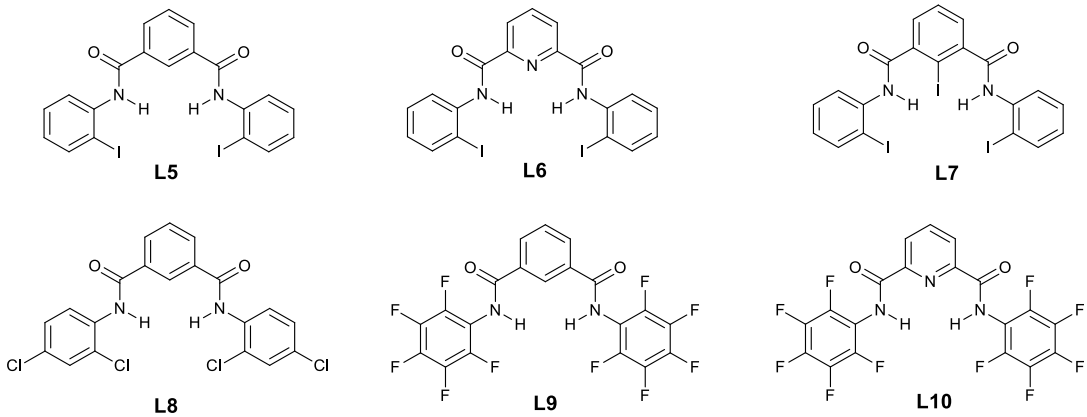

Figure 3.1 Receptors discussed in this chapter.

3.2 Synthesis

The synthesis of receptors **L5**-**L6** and **L8** was carried out in MeCN by reacting commercially available isophthaloyl chloride or pyridine-2,6-dicarbonyl dichloride with the suitable halogenated aniline in the presence of KOH. In the case of **L7** the acyl chloride was synthesised by reacting the 2-iodoisophthalic acid with thionyl chloride. The synthesis of receptor **L9** has already been reported elsewhere.[32] **L10** was obtained by the reaction of pyridine-2,6-dicarbonyl dichloride with pentafluoroaniline

in DCM. All receptors were obtained in high yields (from 57% to 97%). Reaction schemes are reported in Scheme 3.1 and 3.2. Synthetic details are reported in the Experimental Part (Paragraph 3.8)

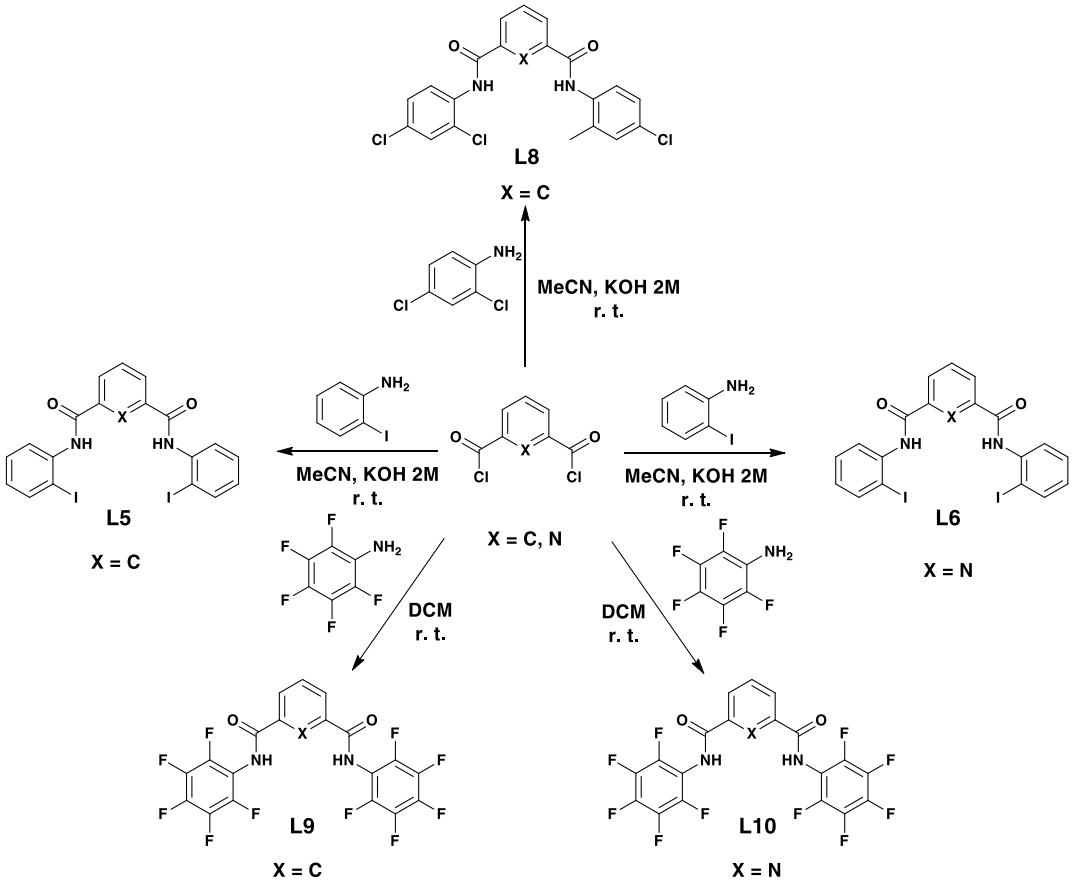

Scheme 3.1 Synthetic procedure for receptors **L5**, **L6**, **L8**, **L9** and **L10**

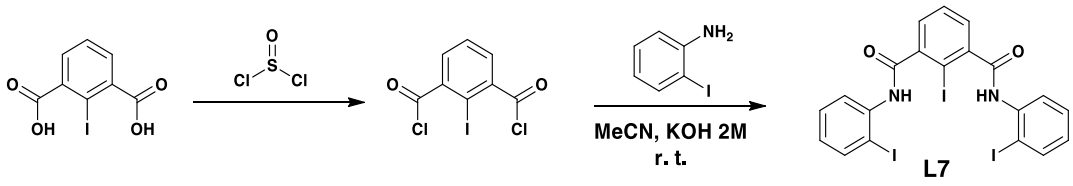

Scheme 3.2 Synthetic procedure for receptors **L7.**

3.3 Solution studies

The anion binding properties of **L5**-**L10** was evaluated in solution by means of ^{1}H-NMR titrations in DMSO-d_6 towards a set of anion guests (F^-, CN^-, BzO^-, $H_2PO_4^-$, and Cl^-) as their tetrabutylammonium salts. Stability constants for the formation of the 1:1 adducts (Table 3.1) were calculated using WinEQNMR.[33]

Table 3.1 Stability constants (Ka, M^{-1}) for the 1:1 adducts of **L5**-**L10** with the anions in DMSO-d_6. In the case of **L9** stability constants were determined following the downfield shift of the CH signal. In the case of **L5**-**L8**, and **L10** stability constants were determined following the downfield shift of the NH signal. All errors are estimated <25%.

Receptors	Anions				
	F^-	**CN^-**	**BzO^-**	**$H_2PO_4^-$**	**Cl^-**
L5	No interaction[a]	Deprot.[b]	No interaction[a]	No interaction[a]	No interaction[a]
L6	Deprot.[b]	Deprot.[b]	No interaction[a]	No interaction[a]	No interaction[a]
L7	No interaction[a]	Deprot.[b]	No interaction[a]	No interaction[a]	No interaction[a]
L8	Deprot.[b]	Deprot.[b]	224	n.d.[c]	No interaction[a]
L9	Deprot.[b]	Deprot.[b]	537	638	22
L10	Deprot.[b]	Deprot.[b]	258	n.d.[c]	47

[a] None of the signals shifted upon addition of the tested anions; [b] the amide NH signal disappeared upon addition of the tested anions; [c] we were not able to fit the experimental data.

The results reported in Table 3.1 show that basic anions such as fluoride and cyanide caused, in most of the cases, the disappearance of the signal attribute to the amide

NH suggesting a deprotonation of the receptor. Indeed, in the attempt to crystallize the 1:1 adduct of **L10** with TBAF in DMSO we obtained instead the crystal structure of the bis-deprotonated form of the receptor with two TBA units as the countercations (see Paragraph 3.5).

L5, **L6**, and **L7**, all containing iodine atoms, were not able to interact with any of the anions considered, probably because of the steric hindrance of the substituents which did not allow the formation of H-bonds between the amide NHs and the anion guests (see below). The most interesting results were obtained for **L9** and **L10**. In the case of **L10** the classic downfield shift of the signal attributed to the amide NH was observed upon addition of BzO^-, $H_2PO_4^-$, and, to a less extent, Cl^- (Figure 3.2a-c).

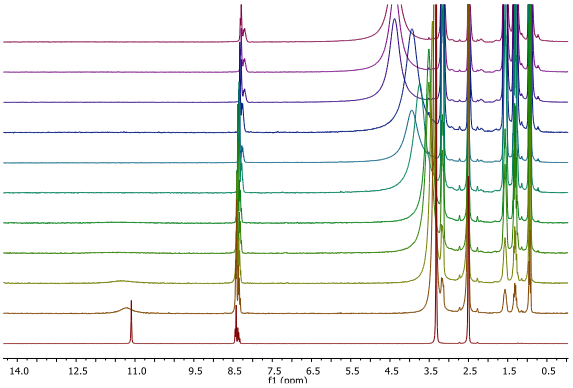

(a)

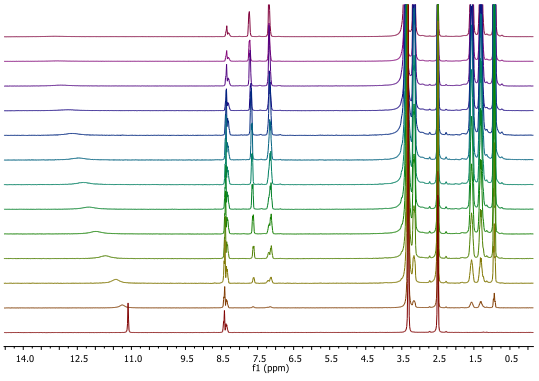

(b)

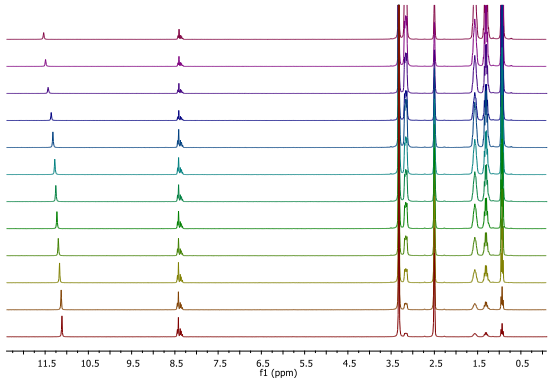

(c)

Figure 3.2 Stack plots of the ^{1}H-NMR spectra of **L10** (0.005 M) upon addition of increasing amount of (a) $TBAH_2PO_4$, (b) TBABzO, (c) TBACl (0.075 M) in DMSO-d_6.

In the case of **L9** a more peculiar behaviour was observed when the receptor was titrated with TBABzO (Figure 3.3) and $TBAH_2PO_4$ (Figure 3.4a). Upon addition of increasing amounts of BzO^- a progressive decrease in the intensity of the signal at 10.82 ppm (green star in Figure 3.3) attributed to the isophtalamide NHs and the concomitant formation of a new signal at 5.84 ppm (red star in Figure 3.3) was observed. Moreover, the singlet signal at 8.63 ppm (blue star in Figure 3.3) attributed to the phenyl CH pointing towards the pseudo-cavity of the receptor dramatically shifted downfield during the titration. Interestingly, also the chemical shifts of the proton signals of BzO^- (black stars in Figure 3.3) were affected by the interaction with the host and shifted upfield. These observations suggest that upon addition of the anion guest the two isophtalamide protons lose their chemical equivalency with the one (at 10.82 ppm) interacting with the anion that experiences slow exchange and disappears, and the other (at 5.84 ppm) that is not affected by the guest presence.[34]

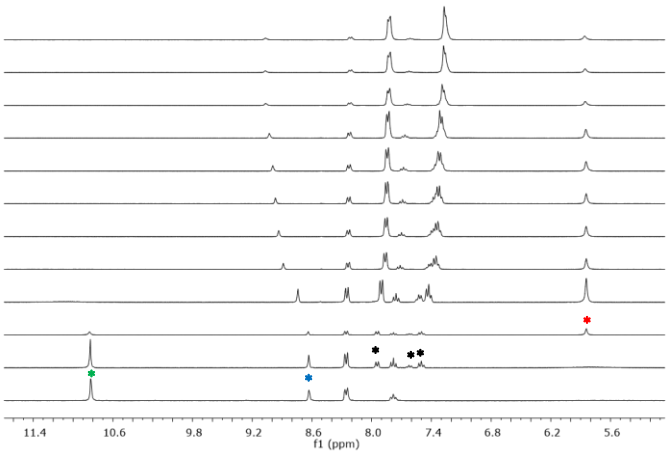

Figure 3.3 Stack plot of the ^{1}H-NMR spectra of **L9** (0.005 M) upon addition of increasing amount of TBABzO (0.075 M) in DMSO-d_6. Green star (isophtalamide NH), blue star (phenyl CH), black stars (BzO- signals), red star (new signal).

We could then hypothesise the formation of a mono-cooordinated adduct assisted by the formation of a CH---$^{-}$OBz hydrogen bond, i.e. receptor **L9** coordinates BzO^{-} in a *syn anti* conformation. The fact that receptor **L9** adopts this conformation was also suggested by Hunter and co-workers.[32] The chemical shift of the BzO^{-} signals might suggest the formation of π-π interactions between the benzoate ring and the pentafluorophenyl ring. A similar behaviour was observed when titrating receptor **L9** with $TBAH_2PO_4$ (Figure 3.4a). In the case of chloride, as the interaction is weaker compared to the other anions considered, we were not able to observe the formation of the mono-coordinated adduct as the preponderant species (Figure 3.4b).

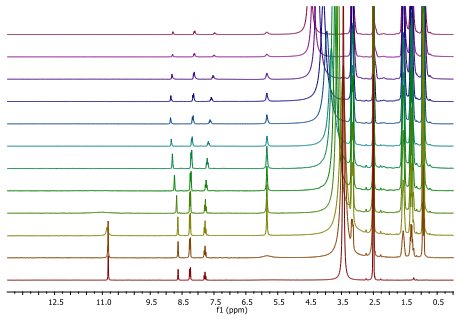

(a)

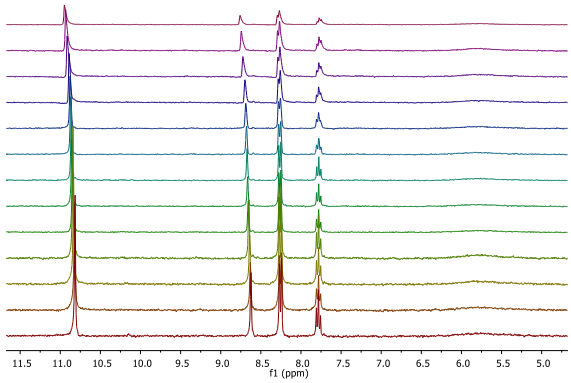

(b)

Figure 3.4. Stack plots of the ^{1}H-NMR spectra of **L9** (0.005 M) upon addition of increasing amount of (a) $TBAH_2PO_4$, (b) TBACl (0.075 M) in DMSO-d_6.

In order to get a better insight into the nature of the adducts between receptor **L9** and anions we also performed ^{19}F-NMR titrations (Figure 3.5a and b for the titrations with $H_2PO_4^-$ and Cl^-, respectively) in DMSO-d_6.

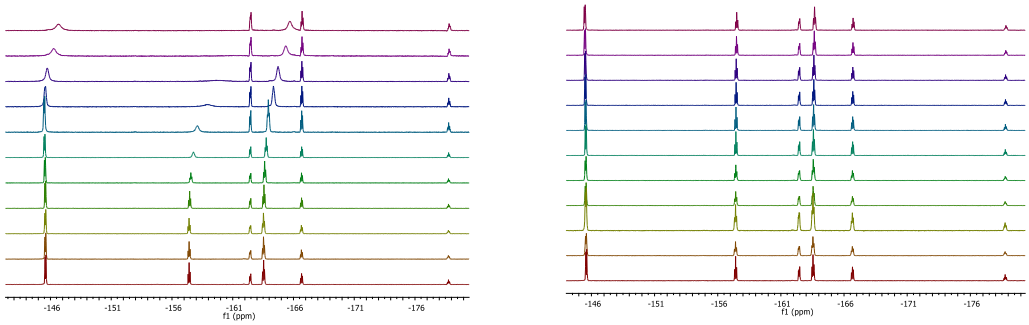

(a) (b)

Figure 3.5 Stack plot of the ^{19}F-NMR spectra of **L9** (0.005 M) upon addition of increasing amount of $TBAH_2PO_4$ (a) and TBACl (b) (0.075 M) in DMSO-d_6.

As shown in Figures 3.5 and 3.6, the free receptor present six distinct signals in the ^{19}F-NMR spectrum, demonstrating that in solution the two pentafluorophenyl rings

are not chemically equivalent. Upon addition of increasing amounts of benzoate (Figure 3.5) only three signals were affected by the presence of the anion guest and, in particular, the triplet at -157.41 ppm shifted upfield and broadened. The triplet at -162.42 and the doublet centred at -145.58 also upfield shifted and broaden to a less extent. These results corroborate the hypothesis reported above on the basis of the ^{1}H-NMR titration, i.e. the non-equivalence of the two half of the receptors and the possibility to have multiple host-guest interactions.

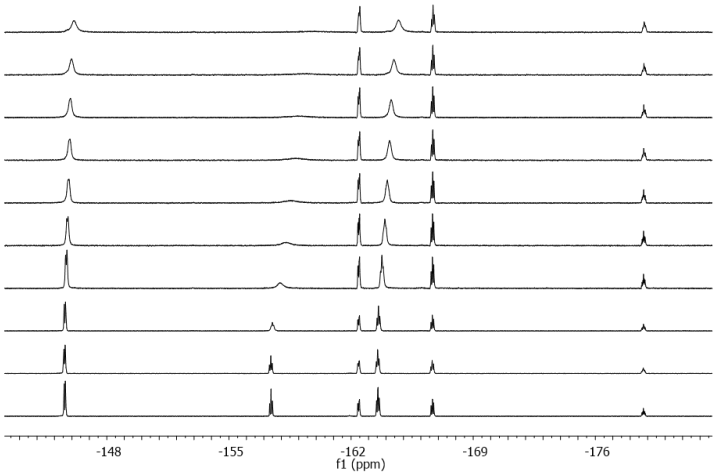

Figure 3.6 Stack plot of the ^{19}F-NMR spectra of **L9** (0.005 M) upon addition of increasing amount of TBABzO (0.075 M) in DMSO-d_6.

3.4 Theoretical calculations

Theoretical calculations were carried out to understand the nature of the adducts formed in solution. 20 ns long metadynamics was used to explore the structural (conformational) dynamics of the two interacting systems (**L9** and **L10** receptors with benzoate and $H_2PO_4^-$ anions) and to enhance the sampling of the conformational space of receptor/anion adducts. A principal component analysis (PCA) was carried out on the frames from the metadynamic trajectories to highlight the prevalent conformations occurring between the interacting structures (receptor/anion

systems). To this aim, the frames from the metadynamic trajectories were characterized by the H-bond distances and angles computed on the two interacting systems. In addition, the centroid-centroid distances separating the aromatic groups of **L9** or **L10** and benzoate anion were measured in order to evidence the possible presence of π-stacking interactions. Plotting the MetaD frames (about 400 for each adduct trajectory) into the space defined by the principal components PCs allows the snapshots to be grouped into distinct conformational classes based on conformers' conformational similarity. In all the studied systems the amide hydrogens play a vital role in forming H-bond interactions with the substrate. Ligands can use both the amide hydrogens to bind the substrate, or only one of them, giving conformations which in the following will be defined as symmetric or non-symmetric, respectively. Notably, the non-symmetric conformation (only one amide hydrogen used in H-bond formation) are dominant for both adduct formed by **L9**, while the symmetric ones are the most important in the **L10**/benzoate system (see Paragraph 3.5 for further discussion), confirming the results observed experimentally. Performing a PC analysis and plotting the trajectory snapshots into the PC1 vs PC2 space (71% of the overall variance explained) revealed three distinct clusters for the system **L9**/benzoate (Figure 3.7).

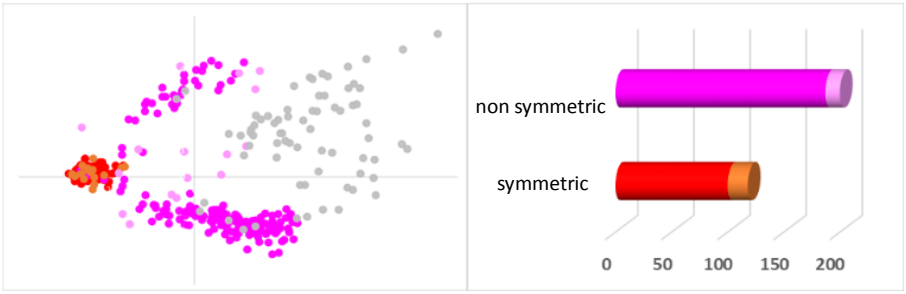

Figure 3.7 Results from PCA analysis of frames from metadynamic trajectory: (a) PC1 vs PC2 score plot; (b) counting of the symmetric and non-symmetric frames classified on the basis of the ligand/substrate H-bonds. (magenta: 1 H-bond; light pink: 1 H-

bond and π-stacking interaction; red: 2 H-bond; brown: 2 H-bond and π-stacking interaction; grey: no interaction)

Cluster 1 (grey points) refers to conformers where no interactions occur between **L9** and benzoate; cluster 2 (magenta and light pink points) refers to conformers where one H-bond is formed between the ligand **L9** and the anion and cluster 3 (red and brown points) describes the situation where two H-bonds are formed. In some symmetric (brown points) and non-symmetric (light pink points) conformers, π- π interactions reinforce the H-bond ones, contributing to stabilize the adduct. Representative structures for these clusters are shown in Figure 3.8.

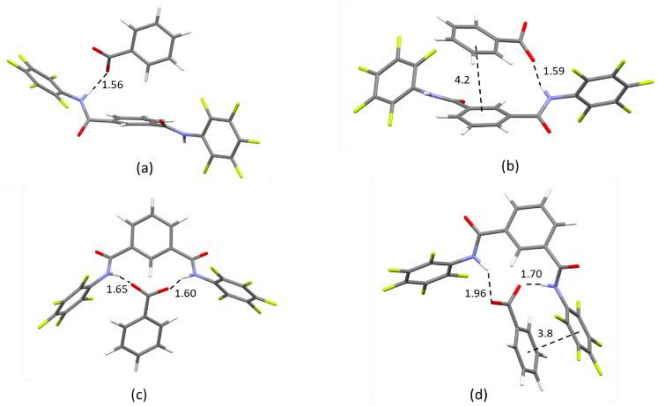

Figure 3.8 Representative structures for the adduct **L9**/BzO^- for the magenta (a), light pink (b), red (c) and brown (d) clusters.

3.5 Solid state studies

In order to study the anion binding in solid state we crystallised **L5**-**L10** by slow evaporation from solutions of the receptor, in presence of TBA salts of the suitable anion species. Unfortunately, despite many attempts we were not able to obtain crystals suitable for X-ray diffraction analysis, but the adducts precipitate as powders. In general, we obtained good quality crystals only for receptors **L5**, **L6**, **L8**, **L9** and **L10**.

Crystallizations of **L7** (even in the presence of anionic species), only resulted in precipitation of fine powders.

The results of the crystal structure determination show that, apart the case of **L10** in the presence of TBAF, that produced a TBA salt of the deprotonated receptor, all the other receptors crystallised as their neutral form, even in presence of excess of different anion species. This is in some way consistent with the results from solution studies, that suggested no particular affinities between receptors **L5**-**L10** and the set of anions chosen for this study. The analysis of the molecular conformation in the solid state shows that, in most of the structures, the molecules adopt a *syn-syn* conformation, with the NH-donors oriented toward the same side of the aromatic spacer. This is observed in the case of **L5**, **L8** and **L9** (Figure 3.9a-c). For **L5** and **L8** all the double-substituted phenyl rings lye coplanar to the central aromatic spacer (Figure 3.9 a-b, on the left), while, in the case of **L9**, these are oriented perpendicular to the plane of the aromatic spacer (Figure 3.9 c, on the left). The common molecular conformation observed in **L5**, **L8** and **L9** is reflected in common structural features. In all the structures, adjacent receptor molecules interact each other via N-H…O hydrogen bond to form infinite chains (Figure 3.9a-c, on the right). These are then differently packed along the remaining two directions of the packing, generating different crystal structures (see Paragraph 3.8).

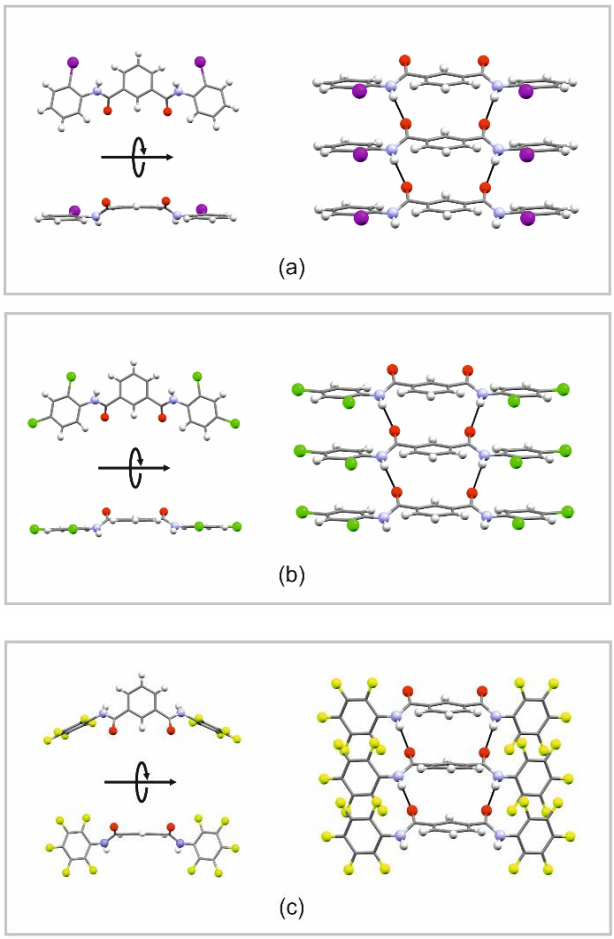

Figure 3.9 Crystal structure of **L5** (a), **L8** (b) and **L9** (c) view along the *b* axes and their crystal packing.

In the case of **L6** and deprotonated **L10**, the receptor molecule adopts a conformation with the amide NHs (or the deprotonated N^- in the case of deprotonated **L10**) oriented towards the centre of a pseudo-cavity (Figure 3.10a-b). In the case of **L6**, the cavity is locked by the presence of the iodo-substituents (Figure 3.10 a). Conversely, in the deprotonated receptor **L10** this is accessible and occupied by a water molecule (Figure 3.10 b). Similarly to what observed for **L9**, in deprotonated **L10**, the conformation adopted in solid state show the fluorinated phenyl rings oriented

approximately perpendicular with respect to the central pyridine ring. The orientation of the substituents could be the key factor to understand the affinity of the receptors towards the anion guests observed in solution.

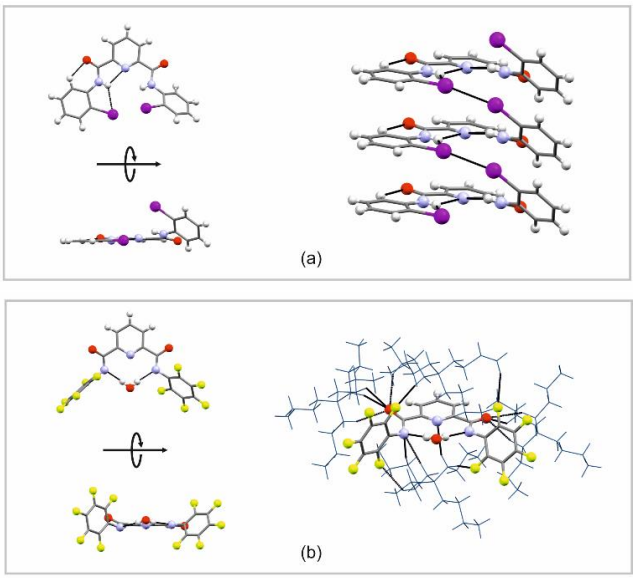

Figure 3.10 Crystal structure of **L6** (a), and deprotonated **L10** (b) view along the *b* axes and their crystal packing. In the deprotonated form of **L10** TBA countercations have been omitted for clarity in the representation of the conformation of the molecule.

3.6 Transport studies

The transport properties of the compounds were first evaluated in model phospholipid vesicles using a chloride-selective electrode.[35] In these assays chloride-containing liposomes composed of POPC are suspended in an isotonic solution and the studied compounds are added as an aliquot of DMSO solution (see paragraph 3.8 for details). The experiments are repeated at least in triplicate using different batches of vesicles and the results obtained using different concentrations of the compound are analysed employing the Hill equation. As input, the chloride efflux observed after 300 s of the experiment is used. The concentration of compound needed to release 50% of the encapsulated chloride corresponds to EC_{50}. The lower the value of this

parameter, the more efficient the compound is (Table 3.2). Chloride/nitrate and chloride/bicarbonate exchanges were studied (Figures 3.11-3.12), the EC_{50} values for the latter being, in most of the cases, between one and two orders of magnitude higher than those obtained for the former. This is the commonly observed trend and it is in line with the Gibbs free energy of hydration of both anions (ΔG_{hyd} = -335 and -300 kJ·mol^{-1} for bicarbonate and nitrate, respectively);[36] nitrate is more lipophilic than bicarbonate and, consequently, easier to extract into the membrane.

Table 3.2 Transport activities expressed as EC_{50} (nM) and Hill parameter for compounds **L5**-**L10**

Compound	EC_{50} (μM) NO_3^-/Cl^-	Hill parameter, *n* NO_3^-/Cl^-	EC_{50} (μM) HCO_3^-/Cl^-	Hill parameter, *n* HCO_3^-/Cl^-	Lipophilicity (logP)[c]
L5	[a]	[a]	[a]	[a]	5.11
L6	[a]	[a]	[a]	[a]	4.42
L7	[a]	[a]	[a]	[a]	4.80
L8	[a]	[a]	[a]	[a]	5.94
L9	3.05	2.22 ± 0.2	10.3	2.06±0.1	4.35
L10	2.2	1.93 ± 0.2	6.03	1.92±0.08	4.21

[a] No significant chloride efflux was detected with compound added up to 5%.

The data reported in Table 3.2 show that compounds **L5**-**L8** are not active as anion carriers. This result is in agreement with their inability to bind chloride in solution. On the other hand, electron-withdrawing perfluorophenyl substituents proved successful to improve the transport activity with compound **L10** more active than **L9**. In order to support the chloride-selective electrode transport studies, emission spectroscopy experiments were conducted.

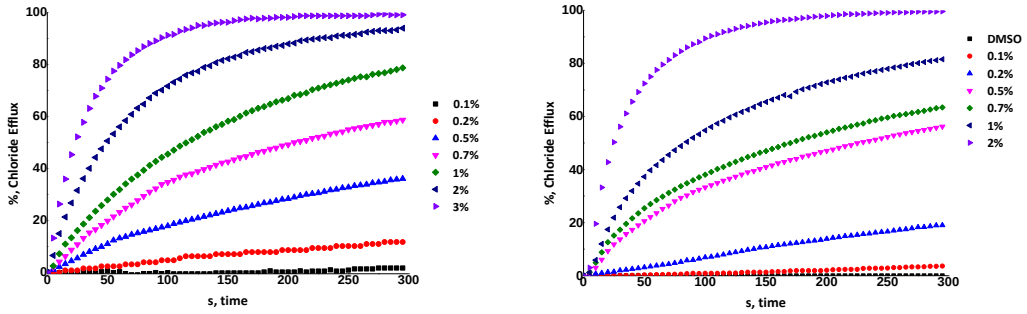

(a) **(b)**

Figure 3.11 Chloride efflux promoted by **L9** (a) and **L10** (b) at different concentrations in unilamellar POPC vesicles. Vesicles loaded with 489 mM NaCl were buffered at pH 7.2 with 5 mM phosphate and dispersed in 489 mM $NaNO_3$ buffered at pH 7.2. Each trace represents the average of at least three trials.

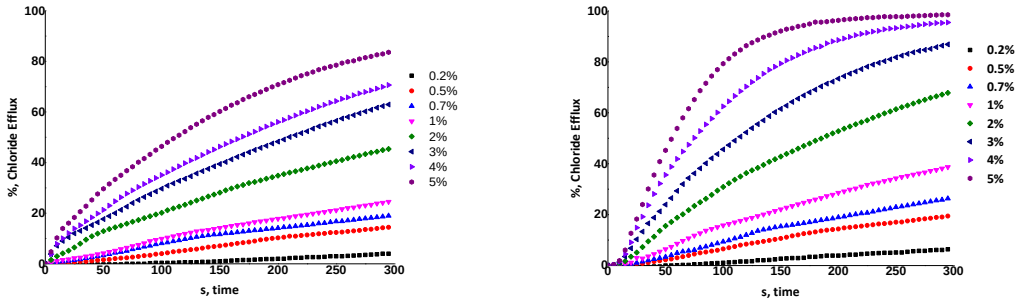

(a) **(b)**

Figure 3.12 Chloride efflux promoted by **L9** (a) and **L10** (b) at different concentrations (40 µM, black; 25 µM, red; 10 µM, blue; 5 µM, magenta) in unilamellar POPC vesicles. Vesicles, which contained NaCl (451 mM NaCl and 20 mM phosphate buffer, pH 7.2), were immersed in Na_2SO_4 (150 mM Na_2SO_4, 40 mM HCO_3^- and 20 mM phosphate buffer, pH 7.2). Each trace represents an average of at least three different experiments.

To confirm the lack of detergent effect exerted by these compounds, the well-established carboxyfluorescein-based assay was performed.

In this experiment chloride- and carboxyfluorescein-loaded liposomes are suspended in an isotonic sodium sulfate aqueous solution. After one minute the corresponding carrier is added to the suspension and the emission changes monitored for five minutes. At the end of the experiment, a detergent is added to lyse the vesicles and release the entrapped carboxyfluorescein (see paragraph 3.8 for further details). Carboxyfluorescein is encapsulated at self-quenching concentrations and its release is signaled by an increase of the fluorescence as a result of the dilution of the dye. The results showed almost no fluorescence changes upon addition of compounds until the surfactant is added, thus ruling out the formation of large non-selective pores in the lipid membrane (Figure 3.13).

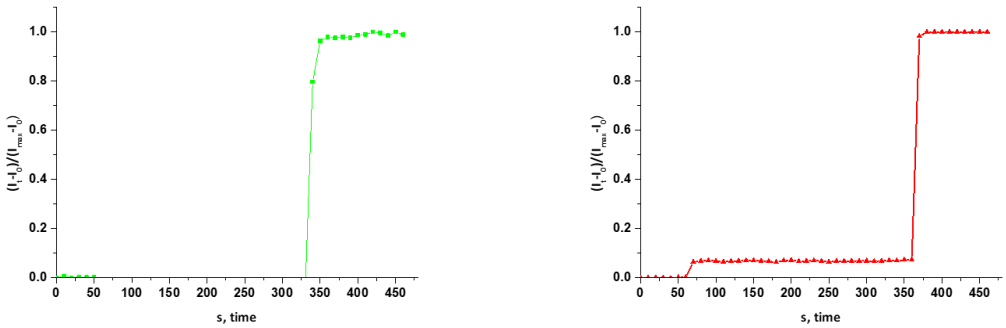

(a) (b)

Figure 3.13 Carboxyfluorescein leakage upon addition of **L9** (a) and **L10** (b) at 1% mol to POPC vesicles, 0.05 mM.

Finally, pH gradient discharge mediated by these compounds was evaluated using pH sensitive dye pyranine (HPTS). Ionophoric activity correlates with the ability of anion transporters to facilitate the balance of the internal pH of vesicles upon imposing a pH gradient with the external solution. First of all, a calibration curve matching I_{460}/I_{403}, (corresponding to the excitation wavelengths of the probe's deprotonated and

protonated forms, respectively) of an HPTS aqueous solution and the pH was built (see SI for details). In this way, the emission values obtained from the HPTS assay can be converted into pH values. In order to perform the experiments, chloride- and HPTS-containing liposomes composed of a 7:3 POPC:cholesterol mixture are suspended in an isotonic sodium nitrate solution (see SI for details). At t = 30 s an aliquot of a sodium hydroxide aqueous solution is added, followed by the addition, at t = 60 s, of an aliquot of the corresponding carrier in DMSO. The graphical representations are shown in Figure 3.14.

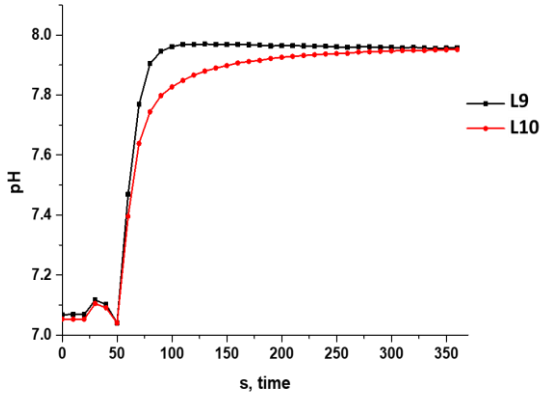

Figure 3.14 Variation of the pH upon addition of **L9** and **L10** at 1% mol to POPC:Cholesterol 7:3 vesicles, 0.5 mM.

At 1 mol% carrier to lipid concentration the response in the assay is quite similar for the two compounds although the activity of the compounds is concentration dependent.

3.7 Conclusions

In conclusion we have developed a new family of isophthalamides and dipicolinepamides receptors bearing various halogenated aromatic substituents. The results obtained in the solution studies by NMR show that only receptors **L9** and **L10** bearing perfluorophenyl rings as substituents have some affinities for the set of anion

studies. In particular, in the case of **L9** an interesting behaviour with the formation of a non-symmetric adduct was hypothesised and confirmed by theoretical calculation. The study of the crystal structures of the receptors demonstrate that the steric hindrance of the halogens influence the accessibility of the isophtalamide or dipicoline amide NHs, thus modulating the affinity towards the anions. We have also shown that only **L9** and **L10** which are able to bind anions can work as synthetic anion transporters through lipid vesicles.

3.8 Experimental part

All reactions were performed in oven-dried glassware under a slight positive pressure of nitrogen. ^{1}H-NMR (300 MHz) and ^{13}C NMR (100 MHz, 125MHz) spectra were determined on a (---------). Chemical shifts for ^{1}H-NMR are reported in parts per million (ppm), calibrated to the residual solvent peak set, with coupling constants reported in Hertz (Hz). The following abbreviations are used for spin multiplicity: s = singlet, d = doublet, t = triplet, m = multiplet . Chemical shifts for ^{13}C NMR are reported in ppm, relative to the central line of a septet at δ = 39.52 ppm for deuteriodimethylsulfoxide. Infrared (IR) spectra were recorded on a NICOLET 5700 FT-IR spectrophotometer and reported in wavenumbers (cm−1). Microanalytical data were obtained using a Fisons EA CHNS-O instrument (T = 1000 °C). Fluorescence spectra were recorded on a Cary Eclypse spectrofluorimeter. All solvents and starting materials were purchased from commercial sources where available. Proton NMR titrations were performed by adding aliquots of the putative anionic guest (as the TBA salt, 0.075 M) in a solution of the receptor (0.005M) in DMSO-d_6/0.5% water to a solution of the receptor (0.005M).

3.8.1 Synthesis

Synthesis of N,N'-bis(2-iodophenyl)isophthalamide (L5)

To a solution of 2-iodoaniline (0.108 g, 0.50 mmol) in 7 mL of MeCN, 247 µL di KOH 2M were added. Then a solution of isophthaloyl chloride (0.050 g, 0.245 mmol) in 5 mL of MeCN was added dropwise to the reaction mixture. The solution was stirred at room temperature for 2 h. After that time the desired product was obtained as a white precipitate which was filtered off and washed with DCM. Yield= 72% (0.073 g, 0.12 mmol), M.p. = 220°C with decomposition. ^{1}H-NMR (400 MHz, DMSO-d_6, 298 K), δ_H: 10.25 (s, NH, 2H), 8.64 (s, 1H), 8.23 (d, J = 4 Hz, 2H), 7.95 (d, J = 8 Hz, 1H), 7.73 (t, J = 8Hz, 1H), 7.51-7.43 (m, 4H), 7.08 (t, J = 8Hz, 2H). ^{13}C-NMR (100 MHz, DMSO-d_6, 298 K), δ_C: 164.80, 139.74, 138.91, 134.60, 130.66, 128.85, 128.76, 128.59, 128.42, 127.30, 98.33. IR (KBr disk), ν_{NH} = 3257 cm^{-1},ν_{CO} = 1656 cm^{-1}. Elemental Analysis % experimental (%calculated): C 42.35 (42.28), H 2.42 (2.48), N 4.90 (4.93).

N,N'-bis(2-iodophenyl)pyridine-2,6-dicarboxamide (L6)

To a solution of 2-iodoaniline (0.103 g, 0.47 mmol) in 10 mL of MeCN, 250 µL di KOH 2M were added. Then a solution of 2,6-pyridine-dicarbonyl dichloride (0.050 g, 0.245 mmol) in 3 mL of MeCN was added dropwise to the reaction mixture. The solution was stirred at room temperature overnight. After that time the desired product was obtained as a white precipitate which was filtered off and washed with MeCN. Yield= 72% (0.101 g, 0.18 mmol), M.p. = 182°C. ^{1}H-NMR (400 MHz, DMSO-d_6, 298 K), δ_H: 10.94 (s, NH, 2H), 8.39 (d, J = 8 Hz, 2H), 8.32 (t, J = 8 Hz, 1H), 7.98 (d, J = 8 Hz, 2H), 7.56 (d, J = 8 Hz, 2H), 7.49 (t, J = 8 Hz, 2H), 7.11 (t, J = 8Hz, 2H). ^{13}C-NMR (100 MHz, DMSO-d_6, 298 K), δ_C: 161.80, 148.44, 140.20, 139.31, 138.94, 128.90, 128.62, 128.43, 125.23, 127.30, 98.80. IR (KBr disk), ν_{NH} = 3317 cm^{-1},ν_{CO} = 1692 cm^{-1}. Elemental Analysis % experimental (%calculated): C 40.06 (40.10), H 2.36 (2.30), N 7.41 (7.38).

2-iodobenzene-1,3-dicarbonyl dichloride (A)

In a round bottom flask 2-iodo-1,3-benzenedicarboxylic acid (0.155 g, 0.53 mmol) and 2 mL of thionyl chloride were stirred under nitrogen atmosphere for 2h30 min at 80°C. The solvent was then evaporated to give a yellow crystalline solid which used without further purification. Yield=90% (0.154 g, 0.470 mmol).

2-iodo-N,N'-bis(2-iodophenyl)isophthalamide (L7)

To a solution of 2-iodoaniline (0.235 g, 1.071 mmol) in 10 mL of dry MeCN, 535 µL di KOH 2M were added. Then a solution of **1** (0.154 g, 0.470 mmol) in 10 mL of MeCN was added dropwise to the reaction mixture. The solution was stirred at room temperature overnight. After that time the desired product was obtained as a brown precipitate which was filtered off and washed with MeCN to yield a white solid. Yield= 57% (0.185 g, 0.266 mmol), M.p. = 250°C. ^{1}H-NMR (100 MHz, DMSO-d_6, 298 K), δ_H: 10.15 (s, NH, 2H), 7.94 (d, J = 8 Hz, 2H), 7.66-7.44 (m, 7H), 7.09 (t, J = 8 Hz, 2H). ^{13}C-NMR (100 MHz, DMSO-d_6, 298 K), δ_C: 167.72, 144.06, 139.16, 139.03, 129.42, 129.04, 128.79, 128.43, 128.03, 97.79, 92.32. IR (KBr disk), ν_{NH} = 3231 cm^{-1},ν_{CO} = 1663 cm^{-1}. Elemental Analysis % experimental (%calculated): C 34.58 (34.51), H 1.93 (1.89), N 3.99 (4.04).

N,N'-bis(2,4-dichlorophenyl)isophthalamide (L8)

To a solution of 2,4-dichloroaniline (0.150 g, 0.923 mmol) in 9 mL of MeCN, 450 µL di KOH 2M were added. Then a solution of isophtaloyl dichloride (0.090 g, 0.4453 mmol) in 9 mL of MeCN was added dropwise to the reaction mixture. The solution was stirred at room temperature overnight. After that time the desired product was obtained as a white precipitate which was filtered off. Yield= 97% (0.194 g, 0.426 mmol), M.p. = 230°C with decomposition. ^{1}H-NMR (400 MHz, DMSO-d_6, 298 K), δ_H: 10.40 (s, NH, 2H), 8.62 (s, 1H), 8.21 (d, J = 8 Hz, 2H), 7.73-7.68 (m, 3H), 7.51 (d, J = 4 Hz, 2H), 7.49 (d, J = 4 Hz, 2H). ^{13}C-NMR (100 MHz, DMSO-d_6, 298 K), δ_C: 168.06,

137.36, 137.16, 134.07, 138.94, 133.82, 132.77, 132.21, 131.96, 130.78, 130.51. IR (KBr disk), ν_{NH} = 3279 cm^{-1},ν_{CO} = 1662 cm^{-1}. Elemental Analysis % experimental (%calculated): C 52.87 (52.90), H 2.62 (2.66), N 6.21 (6.17).

N,N'-bis(perfluorophenyl)isophthalamide (L9)

To a solution of pentafluoroaniline (1.806 g, 9.851 mmol) in 10 mL of DCM a solution of isophtaloyl dichloride (0.600 g, 2.463 mmol) in 10 mL of DCM was added. The solution was stirred at room temperature for 72 h. The formation of a white precipitate was observed. The reaction mixture was diluted with further 20 mL of DCM and washed with NaOH 1 M (3x 10 mL). The white precipitate was dissolved. Then the organic phase was washed with HCl 1M (3 x 10 mL) and dried over Na_2SO_4. The solvent was removed at reduced pressure to give the desired product as a white solid. Yield = 90% (1.094 g, 2.198 mmol). M.p. = 263°C. ^{1}H-NMR (300 MHz, DMSO-d_6, 298 K), δ_H: 10.82 (s, NH, 2H), 8.63 (s, 1H), 8.26 (d, J = 8 Hz, 2H), 7.78 (t, J = 9Hz, 1H). ^{13}C-NMR (125 MHz, DMSO-d_6, 298 K), δ_C: 167.98, 135.99, 134.86, 132.40, 130.86. ^{19}F-NMR (282 MHz, DMSO-d_6, 298 K), δ_F: -145.62 (d, J = 18.91 Hz), -157.41 (t, J = 22.36 Hz), -162.42 (q, J = 9.40 Hz), -163.54 (t, J = 21.05 Hz), -166.67 (t, J = 20.63 Hz), -178.75 (m). IR (KBr disk), ν_{NH} = 3244 cm^{-1},ν_{CO} = 1674 cm^{-1}. Elemental Analysis % experimental (%calculated): C 48.39 (48.41), H 1.25 (1.22), N 5.59 (5.64).

N,N'-bis(perfluorophenyl)pyridine-2,6-dicarboxamide (L10)

To a solution of pentafluoroaniline (1.800 g, 9.831 mmol) in 10 mL of DCM a solution of isophtaloyl dichloride (0.502 g, 2.467 mmol) in 10 mL of DCM was added. The solution was stirred at room temperature for 24 h. The formation of a pink precipitate was observed. The precipitate was filtered off and the filtrate was evaporated to yield a pink oil which was purified with flash chromatography using DCM as eluent. The desired product was obtained as a white microcrystalline solid. Yield = 75% (0.912 g,

1.834 mmol). M.p. = 253°C. ^{1}H-NMR (300 MHz, DMSO-d_6, 298 K), δ_H: 11.09 (s, NH, 2H), 8.44 (d, J = 8.4 Hz, 2H), 8.37 (d, J = 8.4 Hz, 1H). ^{13}C-NMR (125 MHz, DMSO-d_6, 298 K), δ_C: 165.09, 150.36, 143.74, 130.12. ^{19}F-NMR (282 MHz, DMSO-d_6, 298 K), δ_F: -145.62 (d, J = 18.91 Hz), -157.41 (t, J = 22.36 Hz), -162.42 (q, J = 9.40 Hz), -163.54 (t, J = 21.05 Hz), -166.67 (t, J = 20.63 Hz), -178.75 (m). IR (KBr disk), ν_{NH} = 3297 cm^{-1},ν_{CO} = 1688 cm^{-1}. Elemental Analysis % experimental (%calculated): C 45.94 (45.89), H 1.10 (1.01), N 8.41 (8.45).

3.8.2 ^{1}H-NMR titrations

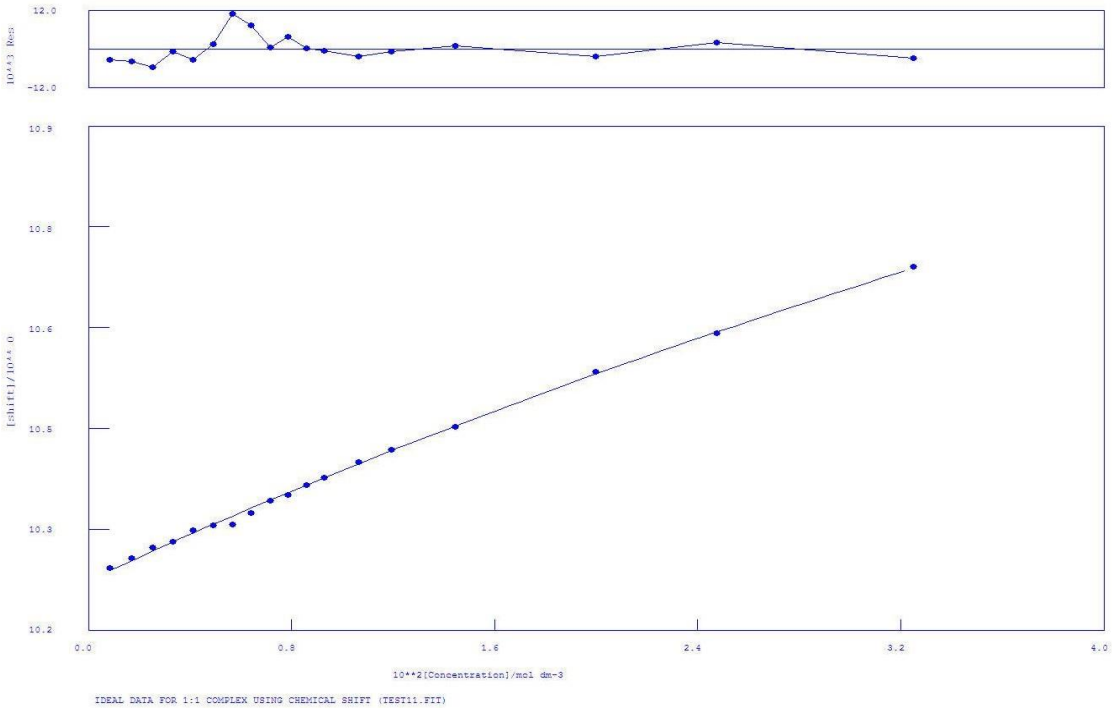

Calculations by WinEQNMR Version 1.20 by Michael J. Hynes Program run at 17:55:24 on 03/11/2015

IDEAL DATA FOR 1:1 COMPLEX USING CHEMICAL SHIFT (TEST11.FIT)

Reaction: M + L = ML FILE: TEST11.FIT

IDEAL DATA: K1 = 63.091; DELTA M = 20.0; DELTA ML = 120.0

File prepared by M. J. Hynes, October 22 2000

NO. A PARAMETER DELTA ERROR CONDITION DESCRIPTION 1 1 7.13281E+00 2.000E-01 1.316E+00 7.560E+02 K1

2 1 1.02687E+01 2.000E-01 2.562E-03 5.417E+00 SHIFT M

3 1 1.26245E+01 1.000E+00 3.528E-01 6.851E+02 SHIFT ML

0RMS ERROR = 4.39E-03 MAX ERROR = 1.09E-02 AT OBS.NO. 7 RESIDUALS SQUARED = 2.89E-04

RFACTOR = 0.0385 PERCENT

Figure 3.15 ^{1}H-NMR titration of **L5** with TBABzO in DMSO-d_6.

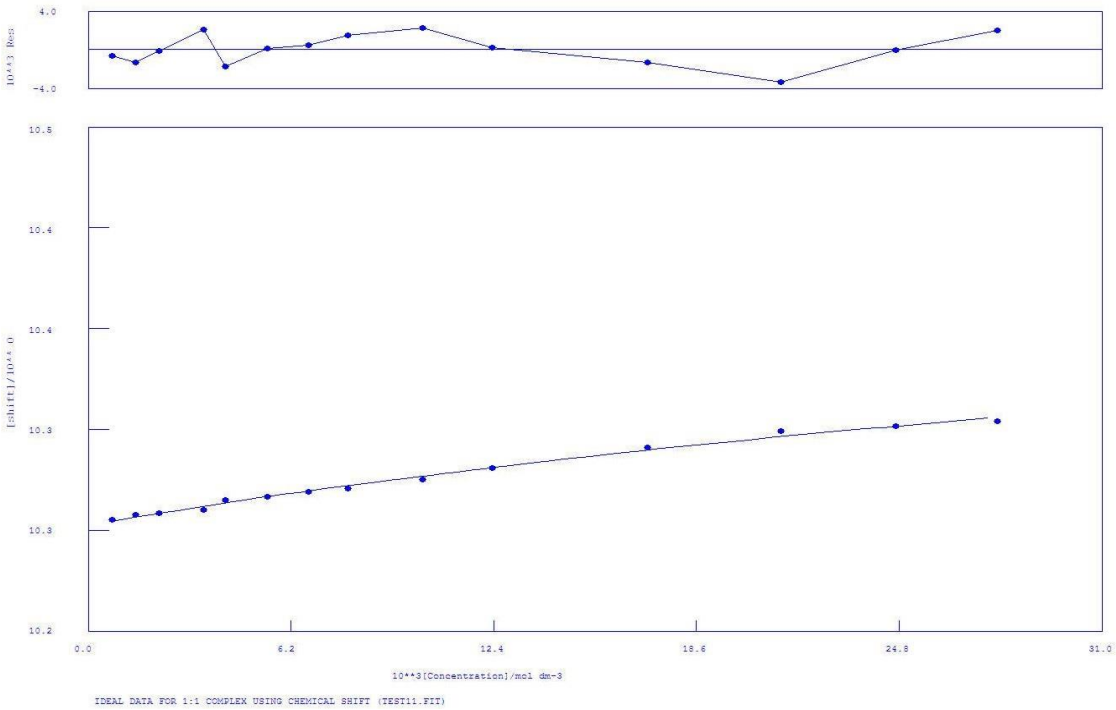

Calculations by WinEQNMR Version 1.20 by Michael J. Hynes Program run at 17:27:41 on 03/11/2015

IDEAL DATA FOR 1:1 COMPLEX USING CHEMICAL SHIFT (TEST11.FIT)

Reaction: M + L = ML FILE: TEST11.FIT

IDEAL DATA: K1 = 63.091; DELTA M = 20.0; DELTA ML = 120.0

File prepared by M. J. Hynes, October 22 2000

NO. A PARAMETER DELTA ERROR CONDITION DESCRIPTION 1 1 1.64609E+01 2.000E-01 2.118E+00 4.218E+01 K1

2 1 1.02630E+01 2.000E-01 8.523E-04 2.536E+00 SHIFT M

3 1 1.04724E+01 1.000E+00 1.825E-02 3.788E+01 SHIFT ML

0RMS ERROR = 1.76E-03 MAX ERROR = 3.36E-03 AT OBS.NO. 12 RESIDUALS SQUARED = 3.40E-05

RFACTOR = 0.0151 PERCENT

Figure 3.16 ^{1}H-NMR titration of **L5** with TBACl in DMSO-d_6

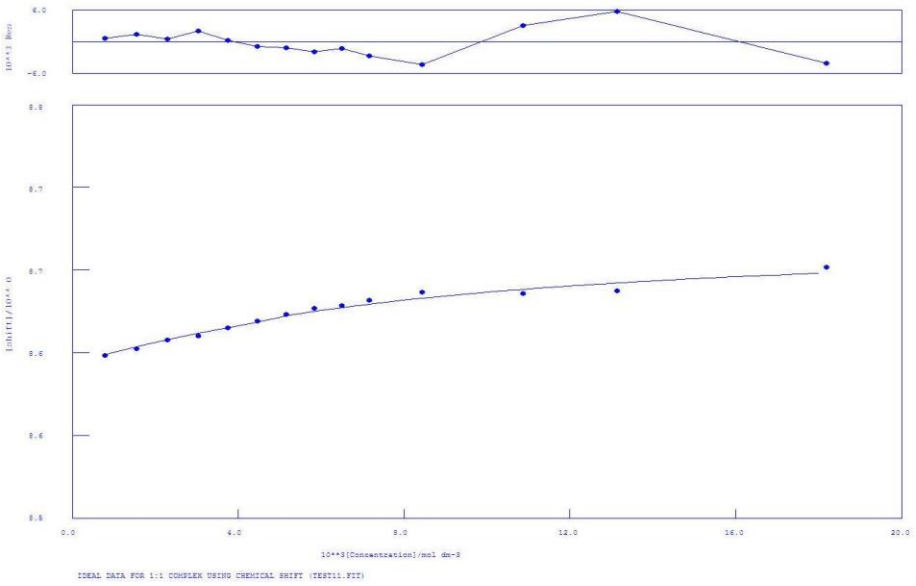

Calculations by WinEQNMR Version 1.20 by Michael J. Hynes Program run at 17:14:47 on 03/11/2015

IDEAL DATA FOR 1:1 COMPLEX USING CHEMICAL SHIFT (TEST11.FIT)

Reaction: M + L = ML FILE: TEST11.FIT

IDEAL DATA: K1 = 63.091; DELTA M = 20.0; DELTA ML = 120.0

File prepared by M. J. Hynes, October 22 2000

NO. A PARAMETER DELTA ERROR CONDITION DESCRIPTION 1 1 1.85323E+02 2.000E-01 6.179E+00 1.560E+00 K1

2 1 8.61241E+00 2.000E-01 2.039E-03 2.586E+00 SHIFT M

3 1 8.70098E+00 1.000E+00 2.752E-03 2.233E+00 SHIFT ML

0RMS ERROR = 3.00E-03 MAX ERROR = 5.64E-03 AT OBS.NO. 13 RESIDUALS SQUARED = 9.93E-05

RFACTOR = 0.0308 PERCENT

Figure 3.17 ^{1}H-NMR titration of **L8** with TBAF in DMSO-d_6

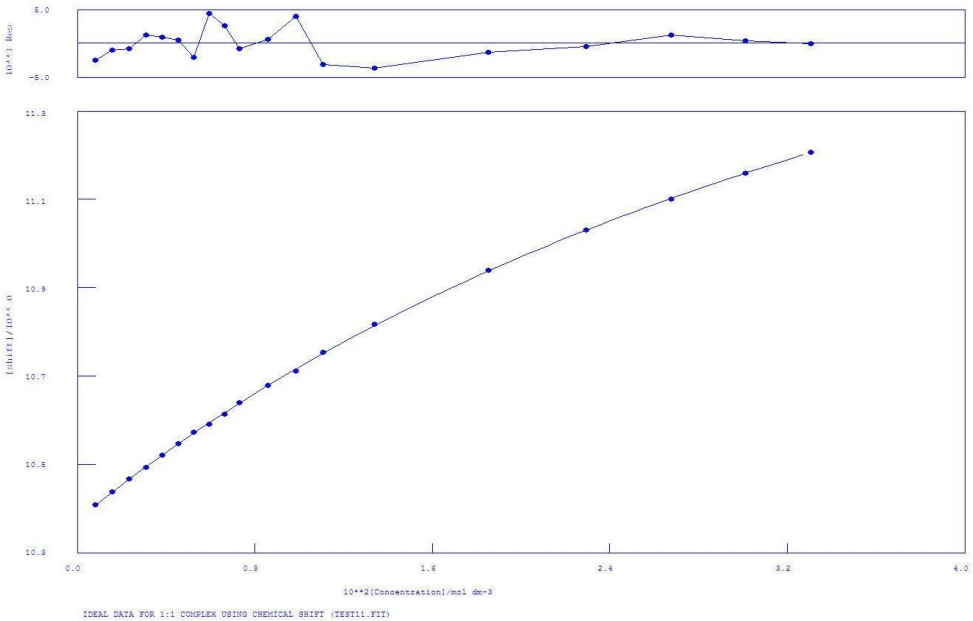

Calculations by WinEQNMR Version 1.20 by Michael J. Hynes Program run at 18:01:15 on 03/11/2015

IDEAL DATA FOR 1:1 COMPLEX USING CHEMICAL SHIFT (TEST11.FIT)

Reaction: M + L = ML FILE: TEST11.FIT

IDEAL DATA: K1 = 63.091; DELTA M = 20.0; DELTA ML = 120.0

File prepared by M. J. Hynes, October 22 2000

NO. A PARAMETER DELTA ERROR CONDITION DESCRIPTION 1 1 2.24508E+01 2.000E-01 5.669E-01 1.760E+02K1

2 1 1.03744E+01 2.000E-01 1.494E-03 5.608E+00 SHIFT M

3 1 1.23976E+01 1.000E+00 3.005E-02 1.416E+02 SHIFT ML

0RMS ERROR = 2.31E-03 MAX ERROR = 4.40E-03 AT OBS.NO. 8 RESIDUALS SQUARED = 8.50E-05

RFACTOR = 0.0197 PERCENT

Figure 3.18 ^{1}H-NMR titration of **L8** with TBABzO in DMSO-d_6

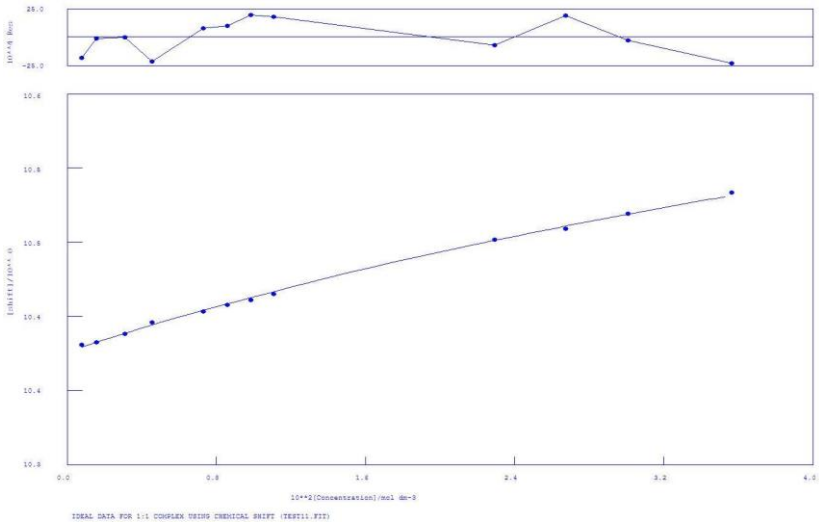

Calculations by WinEQNMR Version 1.20 by Michael J. Hynes Program run at 17:38:14 on 03/11/2015

IDEAL DATA FOR 1:1 COMPLEX USING CHEMICAL SHIFT (TEST11.FIT)

Reaction: M + L = ML FILE: TEST11.FIT

IDEAL DATA: K1 = 63.091; DELTA M = 20.0; DELTA ML = 120.0

File prepared by M. J. Hynes, October 22 2000

NO. A PARAMETER DELTA ERROR CONDITION DESCRIPTION 1 1 1.09150E+01 2.000E-01 1.840E+00 2.979E+02 K1

2 1 1.03913E+01 2.000E-01 1.149E-03 4.335E+00 SHIFT M

3 1 1.08522E+01 1.000E+00 5.479E-02 2.619E+02 SHIFT ML

0RMS ERROR = 1.70E-03 MAX ERROR = 2.30E-03 AT OBS.NO. 12 RESIDUALS SQUARED = 2.60E-05

RFACTOR = 0.0141 PERCENT

Figure 3.19 ^{1}H-NMR titration of **L8** with TBACl in DMSO-d_6

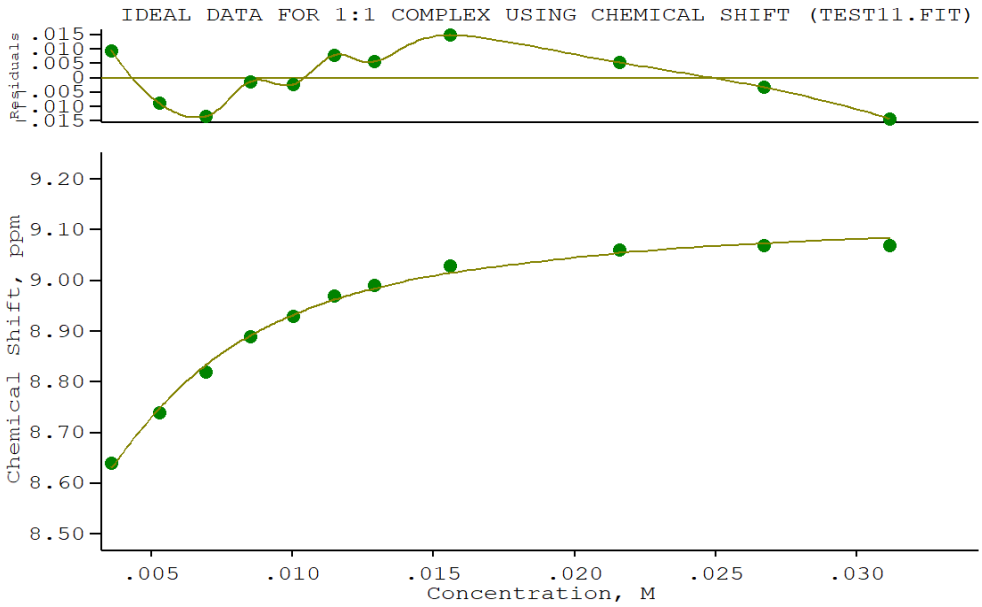

Calculations by WinEQNMR2 Version 2.00 by Michael J. Hynes

Program run at 13:03:17 on 10/09/2018

IDEAL DATA FOR 1:1 COMPLEX USING CHEMICAL SHIFT (TEST11.FIT)

Reaction: Sn + L = Sn(L)

FILE: TEST11.FIT (Measured shift is on 119Sn)

IDEAL DATA: K1 = 63.091; DELTA M = 20.0; DELTA ML = 120.0

File prepared by M. J. Hynes, October 22 2000

Equilibrium constants are floating point numbers

NO. A PARAMETER DELTA ERROR CONDITION DESCRIPTION

1 1 5.36975E+02 2.000E-01 6.586E+01 1.937E+01 K1

2 1 8.26540E+00 2.000E-01 2.907E-02 6.824E+00 SHIFT Sn

3 1 9.14158E+00 1.000E+00 1.182E-02 8.037E+00 SHIFT Sn(L)

0RMS ERROR = 1.07E-02 MAX ERROR = 1.49E-02 AT OBS.NO. 8

RESIDUALS SQUARED = 9.11E-04

RFACTOR = 0.1019 PERCENT

Figure 3.20 ^{1}H-NMR titration of **L9** with TBABzO in DMSO-d_6

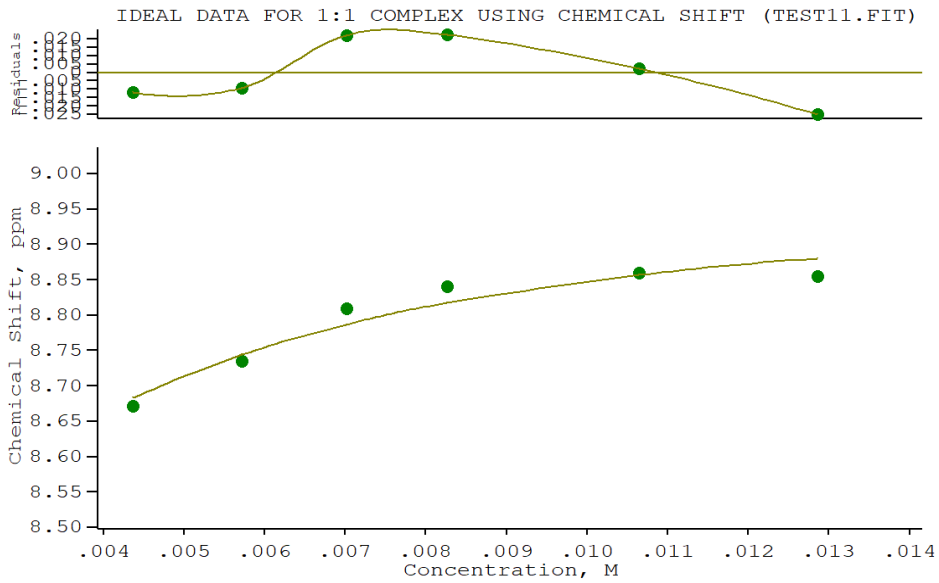

Calculations by WinEQNMR2 Version 2.00 by Michael J. Hynes

Program run at 17:33:25 on 11/22/2018

IDEAL DATA FOR 1:1 COMPLEX USING CHEMICAL SHIFT (TEST11.FIT)

Reaction: Sn + L = Sn(L)

FILE: TEST11.FIT (Measured shift is on 119Sn)

IDEAL DATA: K1 = 63.091; DELTA M = 20.0; DELTA ML = 120.0

File prepared by M. J. Hynes, October 22 2000

Equilibrium constants are floating point numbers

NO.	A	PARAMETER	DELTA	ERROR	CONDITION	DESCRIPTION
1	1	6.38163E+02	2.000E-01	1.373E+02	3.048E+00	K1
2	1	8.36498E+00	2.000E-01	6.839E-02	4.443E+00	SHIFT Sn
3	1	8.97297E+00	1.000E+00	3.254E-02	5.213E+00	SHIFT Sn(L)

0RMS ERROR = 2.49E-02 MAX ERROR = 2.51E-02 AT OBS.NO. 6

RESIDUALS SQUARED = 1.87E-03

RFACTOR = 0.2005 PERCENT

Figure 3.21 ^{1}H-NMR titration of **L9** with $TBAH_2PO_4$ in DMSO-d_6

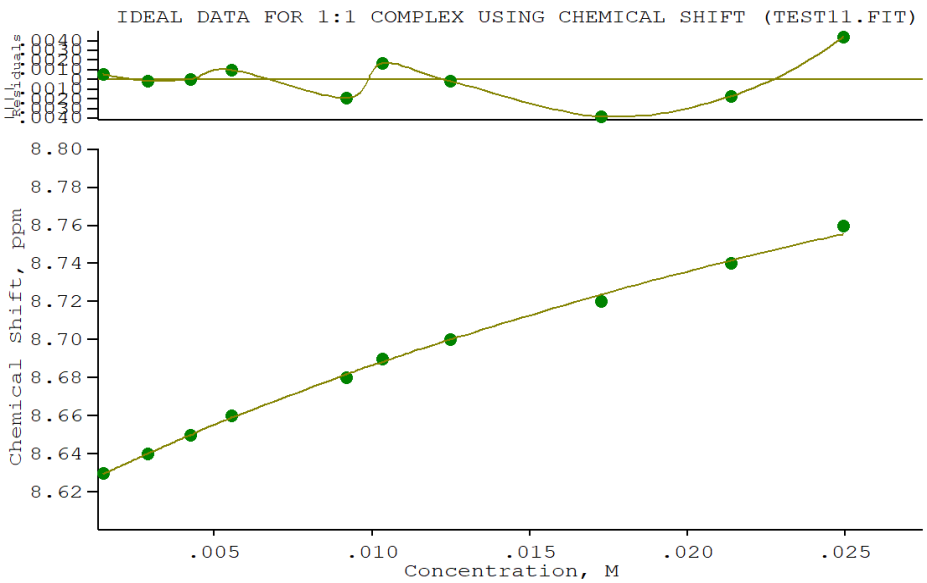

Calculations by WinEQNMR2 Version 2.00 by Michael J. Hynes

Program run at 13:20:36 on 10/09/2018

IDEAL DATA FOR 1:1 COMPLEX USING CHEMICAL SHIFT (TEST11.FIT)

Reaction: Sn + L = Sn(L)

FILE: TEST11.FIT (Measured shift is on 119Sn)

IDEAL DATA: K1 = 63.091; DELTA M = 20.0; DELTA ML = 120.0

File prepared by M. J. Hynes, October 22 2000

Equilibrium constants are floating point numbers

NO. A PARAMETER DELTA ERROR CONDITION DESCRIPTION

1 1 2.20801E+01 2.000E-01 4.468E+00 1.923E+02 K1

2 1 8.61786E+00 2.000E-01 2.233E-03 5.464E+00 SHIFT Sn

3 1 9.02173E+00 1.000E+00 5.088E-02 1.582E+02 SHIFT Sn(L)

0RMS ERROR = 2.53E-03 MAX ERROR = 4.44E-03 AT OBS.NO. 10

RESIDUALS SQUARED = 4.47E-05

RFACTOR = 0.0243 PERCENT

Figure 3.22 ^{1}H-NMR titration of **L9** with TBACl in DMSO-d_6

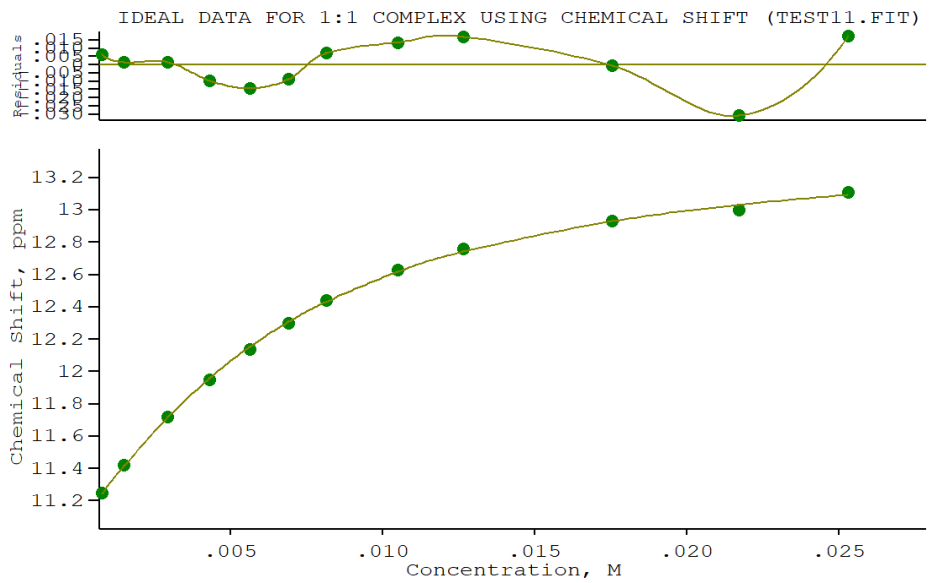

Calculations by WinEQNMR2 Version 2.00 by Michael J. Hynes

Program run at 15:45:01 on 11/22/2018

IDEAL DATA FOR 1:1 COMPLEX USING CHEMICAL SHIFT (TEST11.FIT)

Reaction: Sn + L = Sn(L)

FILE: TEST11.FIT (Measured shift is on 119Sn)

IDEAL DATA: K1 = 63.091; DELTA M = 20.0; DELTA ML = 120.0

File prepared by M. J. Hynes, October 22 2000

Equilibrium constants are floating point numbers

NO.	A	PARAMETER	DELTA	ERROR	CONDITION	DESCRIPTION
1	1	2.58384E+02	2.000E-01	1.257E+01	1.636E+01	K1
2	1	1.10516E+01	2.000E-01	1.377E-02	2.753E+00	SHIFT Sn
3	1	1.34692E+01	1.000E+00	2.669E-02	1.163E+01	SHIFT Sn(L)

0RMS ERROR = 1.55E-02 MAX ERROR = 3.06E-02 AT OBS.NO. 11

RESIDUALS SQUARED = 2.18E-03

RFACTOR = 0.1093 PERCENT

Figure 3.23 ^{1}H-NMR titration of **L9** with TBABzO in DMSO-d_6

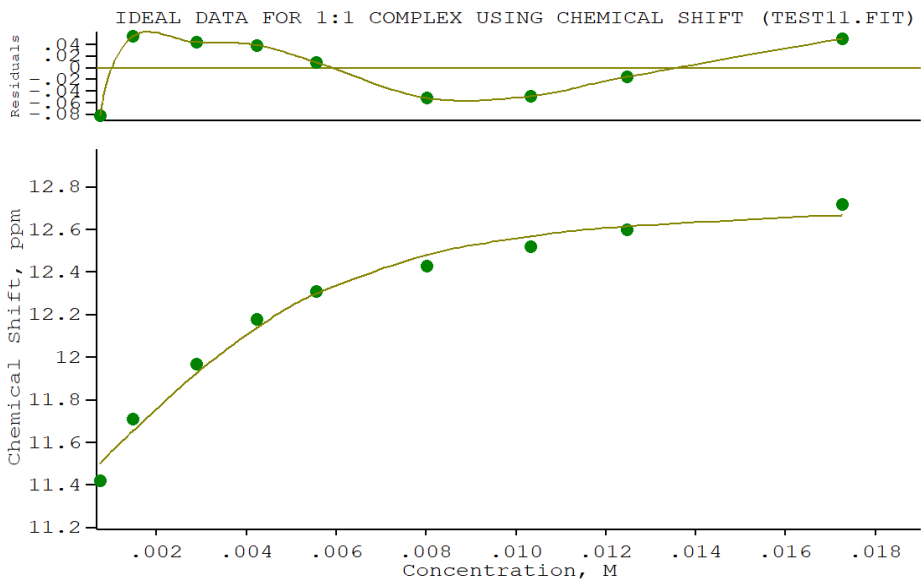

Calculations by WinEQNMR2 Version 2.00 by Michael J. Hynes

Program run at 17:54:00 on 11/22/2018

IDEAL DATA FOR 1:1 COMPLEX USING CHEMICAL SHIFT (TEST11.FIT)

Reaction: Sn + L = Sn(L)

FILE: TEST11.FIT (Measured shift is on 119Sn)

IDEAL DATA: K1 = 63.091; DELTA M = 20.0; DELTA ML = 120.0

File prepared by M. J. Hynes, October 22 2000

Equilibrium constants are floating point numbers

NO.	A	PARAMETER	DELTA	ERROR	CONDITION	DESCRIPTION
1	1	1.07465E+03	2.000E-01	2.166E+02	3.611E+00	K1
2	1	1.13394E+01	2.000E-01	4.960E-02	1.479E+00	SHIFT Sn
3	1	1.27692E+01	1.000E+00	5.336E-02	3.224E+00	SHIFT Sn(L)

0RMS ERROR = 5.95E-02 MAX ERROR = 8.24E-02 AT OBS.NO. 1

RESIDUALS SQUARED = 2.12E-02

RFACTOR = 0.3976 PERCENT

Figure 3.24 ^{1}H-NMR titration of **L10** with $TBAH_2PO_4$ in DMSO-d_6

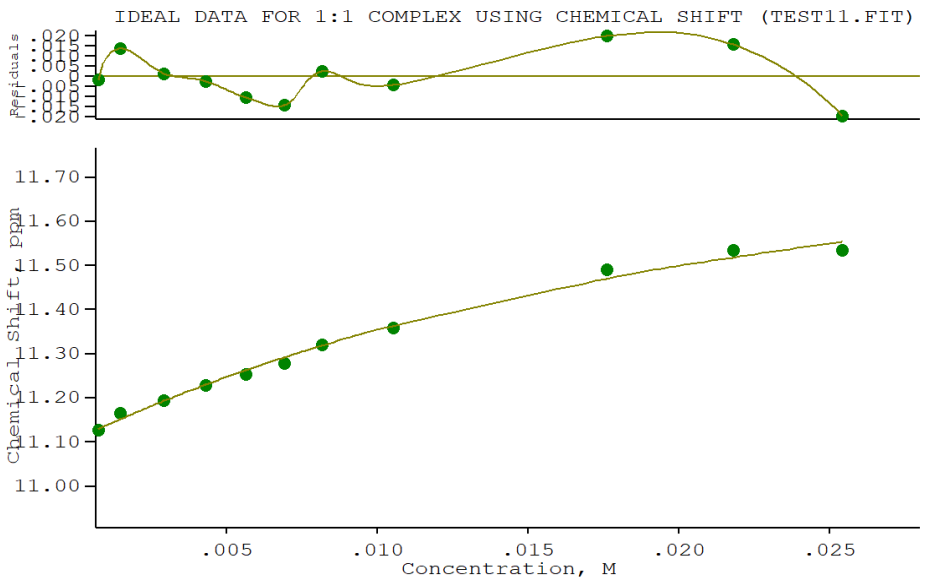

Calculations by WinEQNMR2 Version 2.00 by Michael J. Hynes

Program run at 16:05:59 on 11/22/2018

IDEAL DATA FOR 1:1 COMPLEX USING CHEMICAL SHIFT (TEST11.FIT)

Reaction: Sn + L = Sn(L)

FILE: TEST11.FIT (Measured shift is on 119Sn)

IDEAL DATA: K1 = 63.091; DELTA M = 20.0; DELTA ML = 120.0

File prepared by M. J. Hynes, October 22 2000

Equilibrium constants are floating point numbers

NO.	A	PARAMETER	DELTA	ERROR	CONDITION	DESCRIPTION
1	1	4.68057E+01	2.000E-01	1.151E+01	6.088E+01	K1
2	1	1.11055E+01	2.000E-01	1.124E-02	4.233E+00	SHIFT Sn
3	1	1.19704E+01	1.000E+00	9.705E-02	4.566E+01	SHIFT Sn(L)

0RMS ERROR = 1.40E-02 MAX ERROR = 2.00E-02 AT OBS.NO. 9

RESIDUALS SQUARED = 1.56E-03

RFACTOR = 0.1053 PERCENT

Figure 3.25 ^{1}H-NMR titration of **L10** with TBACl in DMSO-d_6

3.8.3 Transport studies

Preparation of 1-palmitoyl -2-oleoyl-sn-glycero-3-phosphocholine vesicles

A lipid film of 1-palmitoyl -2-oleoyl-sn-glycero-3-phosphocholine (POPC) was formed from a chloroform solution (20 mg/mL). The solvent was removed under reduced pressure and dried under vacuum for at least 2 hours. The lipid film was rehydrated by vortexing with an internal solution of NaCl 489 mM buffered at pH 7.2 with NaH2PO4 5 mM. The lipid suspension was then subjected to seven freeze-thaw cycles and allowed to age for 15 min at room temperature before extruding 27 times throwgh a 200 nm polycarbonate membrane. The resulting unilamellar vesicles were dialyzed against the external solution (two cycles of 40 min) to remove unencapsulated NaCl salts. The vesicles were then diluited to 10 mL with the external solution to obtain a stock solution of lipid.

Antiport Cl^-/NO_3^-

Sample for assay was prepared in a vial by diluting to 5 mL lipid stock solution with the external solution to give a solution of 0.5 mM of lipid. Chloride efflux was monitored using an ion selective electrode (Hach, ISE F-9655C) for chloride, calibrated against sodium chloride solutions of known concentration before starting the measurements. To initiate the experiment, at t= 60 s the carrier compound was added to the sample as DMSO solution and the chloride efflux was monitored during 6 min. At the end of the experiment, detergent was added to lyse the phospholipidic vesicles and detected the 100 % of the chloride efflux. Experiments were repeated in duplicate and all traces presented are the average of three trials.

Antiport Cl^-/HCO_3^-

Unilamellar POPC vesicles containing 451 mM NaCl solution buffered to 7.2 with 20 mM sodium dihydrogen phosphate salts, prepared as described in the Cl-/NO3-

antiport test, were suspended in 150 mM Na2SO4 solution buffered to pH 7.2 with sodium dihydrogen phosphate salts.

Sample for assay was prepared in a vial by diluting to 5 mL lipid stock solution with the external solution to give a solution of 0.5 mM of lipid. Chloride efflux was monitored using an ion selective electrode (Hach, ISE F-9655C) for chloride, calibrated against sodium chloride solutions of known concentration before starting the measurements. At t = 50 s, $NaHCO_3$ solution (0.5 M in 150 mM Na2SO4 solution buffered to pH 7.2 with sodium dihydrogen phosphate salts) was added so that the external solution contained 40mM $NaHCO_3$. At t = 60 s, a DMSO solution of the carrier compound was added to start the measurement and chloride efflux was monitored during 6 min. At the end of the experiment, detergent was added to lyse the phospholipidic vesicles and detected the 100 % of the chloride efflux. Experiments were repeated in triplicate and all traces presented are the average of three trials.

Carboxyfluorescein assay:

Unilamellar POPC vesicles containing a 50 mM solution of carboxyfluorescein (CF) dissolved in a 451 mM NaCl solution buffered to 7.2 with 20 mM sodium dihydrogen phosphate salts, were suspended in 150 mM Na2SO4 solution buffered to pH 7.2 with sodium dihydrogen phosphate salts 20 mM. The unencapsulated CF was removed by means exclusion chromatography column, using Sephadex G-25 as stationary phase and the external solution as mobile phase. Sample for assay was prepared in a disposable plastic cuvette by diluting to 2.5 mL lipid stock solution with the external solution to give a solution of 0.05 mM of lipid. The CF emission was monitored using a fluorimeter (HITACHI F-7000 Fluorescence Spectrophotometer). To initiate the experiment, at t = 60 s the carrier compound was added as DMSO solution and the emission was monitored during 6 min. At the end of the experiment, detergent was added to lyse the phospholipidic vesicles and recorded the maximum intensity of the

CF emission band. Experiments were repeated in duplicate and all traces presented are the average of two trials.

HPTS assay

Unilamellar POPC:Cholesterol 7:3 vesicles containing 10 µM HPTS dissolved in a 126.2 mM NaCl solution buffered to 7.2 with 10 mM sodium dihydrogen phosphate salts, were suspended in 126.2 mM $NaNO_3$ solution buffered to pH 7.2 with sodium dihydrogen phosphate salts 10 mM. The unencapsulated HPTS was removed by means exclusion chromatography column, using Sephadex G-25 as stationary phase and the external solution as mobile phase.

Sample for assay was prepared in a disposable plastic cuvette by diluting to 2.5 mL lipid stock solution with the external solution to give a solution of 0.5 mM of lipid. The I460nm/I403nm ratio was monitored using a fluorimeter (HITACHI F-7000 Fluorescence Spectrophotometer). At t = 30 s a 0.5 M NaOH solution was added to create a pH gradient between the internal and external solution and then, to initiate the experiment the carrier compound was added as DMSO solution and the I460nm/I403nm ratio was monitored during 6 min. Experiments were repeated in triplicate and all traces presented are the average of three trials. At the end of the experiment, detergent was not added to lyse the phospholipidic vesicles.

HPTS assay calibration

The system was calibrated monitoring the I460nm/I403nm ratio of a 10 mM solution of HPTS dissolved in a 126.2 mM NaCl solution buffered to 7.2 with 10 mM sodium dihydrogen phosphate salts upon the addition of increasing aliquots of a 0.5 M NaOH solution. We plotted the pH values starting from 5.5 until 9.5 against the I460nm/I403nm ratio. Hence, fitting the data by means a sigmoidal or polynomial

fitting, we were able to obtain the equation curve which allowed to convert the photometric data in pH values.

Antiport Cl^-/NO_3^-

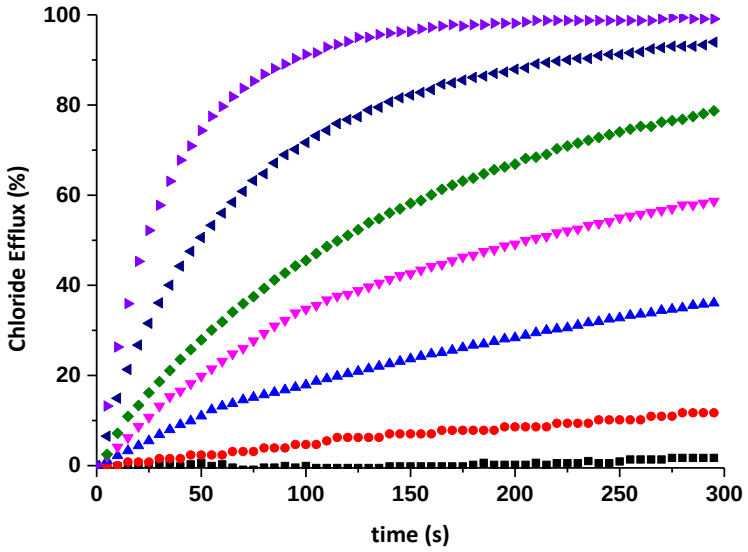

Figure 3.26. Chloride efflux promoted by **L9** at different concentrations (0.5 µM black,; 1 µM, red; 2.5 µM, light blue; 3.5 µM, magenta; 5 µM, green; 10 µM, blue; 15 µM, violet) in unilamellar POPC vesicles. Vesicles loaded with 489 mM NaCl were buffered at pH 7.2 with 5 mM phosphate and dispersed in 489 mM $NaNO_3$ buffered at pH 7.2. Each trace represents the average of at least three trials.

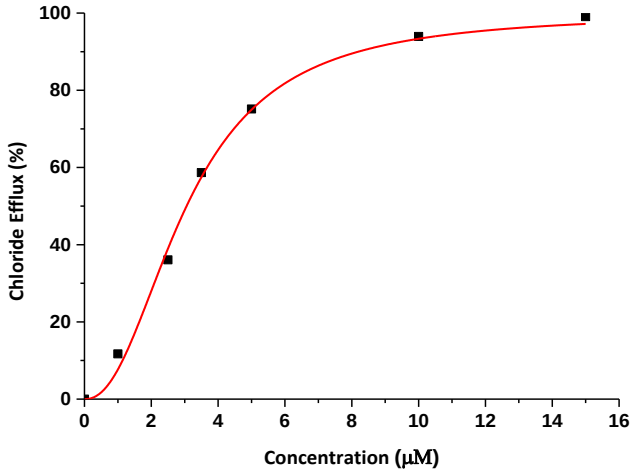

Figure 3.27 Normalised chloride efflux at 300 s plotted against the concentration of compound **L9**. Data have been plotted with Hill equation (continuous line)

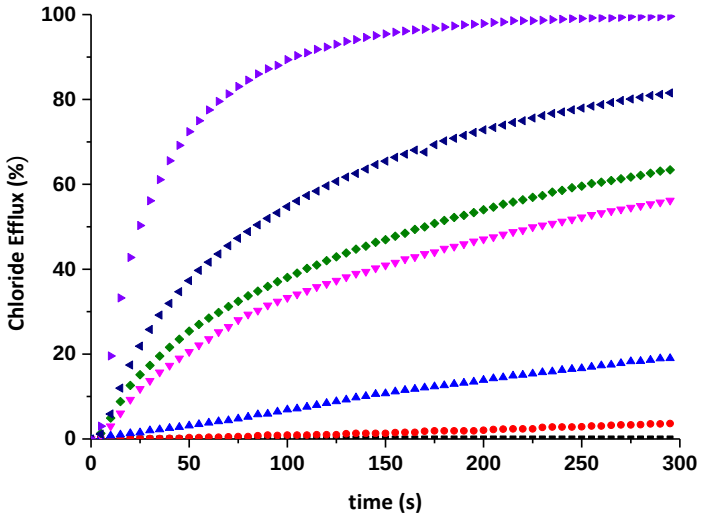

Figure 3.28 Chloride efflux promoted by **L10** at different concentrations (DMSO(blank), black,0.5 μM, red; 1 μM, light blue; 2.5 μM, magenta; 3.5 μM, green; 5 μM, blue; 10 μM, violet) in unilamellar POPC vesicles. Vesicles loaded with 489 mM

NaCl were buffered at pH 7.2 with 5 mM phosphate and dispersed in 489 mM $NaNO_3$ buffered at pH 7.2. Each trace represents the average of at least three trials.

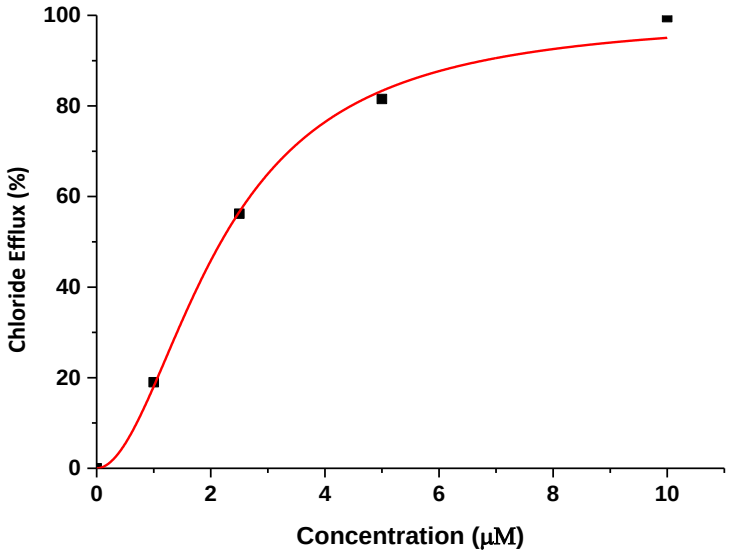

Figure 3.29 Normalised chloride efflux at 300 s plotted against the concentration of compound **L10**. Data have been plotted with Hill equation (continuous line)

Antiport Cl^-/HCO_3^-

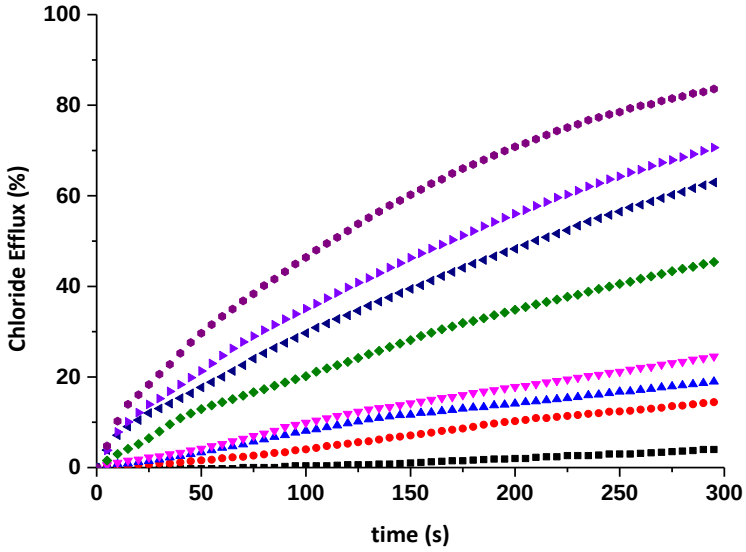

Figure 3.30 Chloride efflux promoted by **L9** at different concentrations (1 μM black,; 2.5 μM, red; 3.5 μM, light blue; 5 μM, magenta; 10 μM, green; 15 μM, blue; 20 μM, violet; 25 μM, fuchsia) in unilamellar POPC vesicles. Vesicles, which contained NaCl (451 mM NaCl and 20 mM phosphate buffer, pH 7.2), were immersed in Na_2SO_4 (150 mM Na_2SO_4, 40 mM HCO_3^- and 20 mM phosphate buffer, pH 7.2). Each trace represents an average of at least three different experiments.

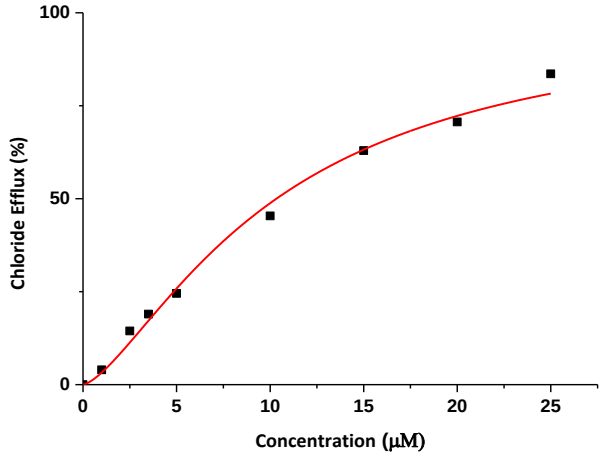

Figure 3.31 Normalised chloride efflux at 300 s plotted against the concentration of compound **L9**. Data have been plotted with Hill equation (continuous line)

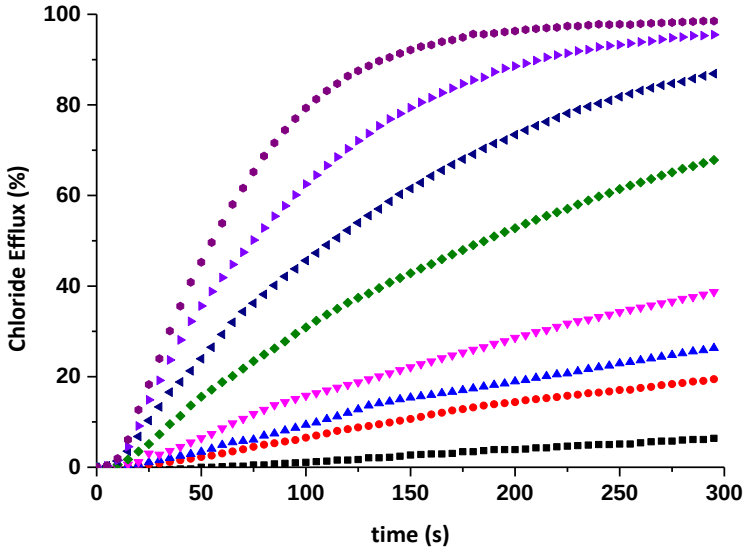

Figure 3.32 Chloride efflux promoted by **L10** at different concentrations (1 μM black,; 2.5 μM, red; 3.5 μM, light blue; 5 μM, magenta; 10 μM, green; 15 μM, blue; 20 μM, violet; 25 μM, fuchsia) in unilamellar POPC vesicles. Vesicles, which contained NaCl (451 mM NaCl and 20 mM phosphate buffer, pH 7.2), were immersed in Na_2SO_4 (150

mM Na_2SO_4, 40 mM HCO_3^- and 20 mM phosphate buffer, pH 7.2). Each trace represents an average of at least three different experiments.

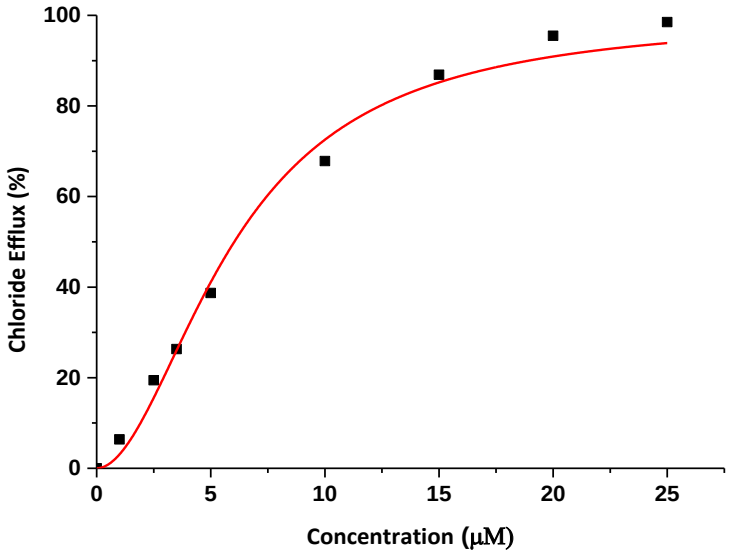

Figure 3.33. Normalised chloride efflux at 300 s plotted against the concentration of compound **L10**. Data have been plotted with Hill equation (continuous line)

3.8.4 Crystallography

Crystals suitable for X-ray diffraction analysis was selected and mounted on a MITIGEN holder with perfluoroether oil then aligned upon a Rigaku 007HF diffractometer, equipped with Varimax confocal mirrors and an AFC11 goniometer and HyPix 6000 detector. The crystal was kept at a steady T = 100(2) K during data collection. The structure was solved with the ShelXT (Sheldrick, 2015) structure solution program using the Intrinsic Phasing solution method and by using Olex2 (Dolomanov et al., 2009) as the graphical interface. The model was refined with version 2018/3 of ShelXL (Sheldrick, 2015) using Least Squares minimisation.

Table 3.3 Crystallographic data.

	L5	**L6**	**L8**
Formula	C20H14O2N2I2	C19H13O2N3I2	C20H12O2N3Cl4
M.w.	568.15	569.14	454.13
Crystal system	monoclinic	monoclinic	monoclinic
Space group	P21/c	P21/n	P21/n
a /Å	19.3172(8) Å	4.2221(2)	19.0305(14)
b /Å	4.75900(13) Å	16.2083(10) Å	4.7498(4)
c /Å	22.0316(8) Å	26.3584(17)	21.7414(16)
α / º	90.00	90.00	90.00
β / º	115.395(5)	93.3100(10)	104.946(3)
γ / º	90.00	90.00	90.00
V /Å^3	1829.67(14)	1800.78(18)	1898.7(3)
T / K	100(2)	100(2)	170(2)
Crystal shape	needle	needle	needle
Crystal size / mm^3	0.22 x 0.025 x 0.001	0.37 x 0.04 x 0.02	0.231x 0.061 x 0.053

Colour	light brown	colourless	colourless
Z	2	4	4
All reflns	6317	24002	18757
Un. reflns	6317	4125	4371
Rint	-	0.0387	0.0941
R1obs[I>2σ(I)]	0.0385	0.0190	0.0440
R1all_	0.0440	0.0206	0.0988
wR2(obs)	0.1087	0.0463	0.0804
wR2 (all)	0.1112	0.0473	0.0966

	L9	**L10 (deprotonated)**
Formula	C20H6F10N2O2	$[(C32H41F10N3O2)\cdot(H2O)]^{2-}$ $2(NC16H36)^{+}$
M.w.	496.26	998.17
Crystal system	monoclinic	Trigonal
Space group	P21/m	*P*31*c*
a /Å	6.9136(2)	40.28774(8)
b /Å	35.5239(12)	40.29774(8)
c /Å	7.4234(2)	17.08786(4)
α / º	90.00	90.00
β / º	96.837(3)	90.00
γ / º	90.00	120.00
V /Å^3	1810.21	24031.42(11)
T / K	100(2)	100(2)
Crystal shape	needle	Cut block
Crystal size / mm^3	--- x --- x ----	0.368 x 0.219 x 0.175
Colour	colourless	colourless
Z	4	18

All reflns	---	396211
Un. reflns	---	28906
Rint	---	0.0318
R1obs[I>2σ(I)]	---	28521
R1all_	---	0.0276
wR2(obs)	---	0.0754
wR2 (all)	---	0.0756

3.9 References

1. V. Amendola, L. Fabbrizzi and L. Mosca, *Chem. Soc. Rev.*, 2010, **39**, 3889-3915.

2. P. A. Gale, E. N. W. Howe and X. Wu, *Chem*, 2016, **1**, 351-422.

3. P. A. Gale, E. N. W. Howe, X. Wu and M. J. Spooner, *Coord. Chem. Rev.*, 2018, **375**, 333-372.

4. Q. He, P. Tu and J. L. Sessler, *Chem*, 2018, **4**, 46-93.

5. M. J. Langton, C. J. Serpell and P. D. Beer, *Angew. Chem. - Int. Ed.*, 2016, **55**, 1974-1987.

6. M. P. Hughes and B. D. Smith, *J. Org. Chem.*, 1997, **62**, 4492-4499.

7. K. Kavallieratos, S. R. De Gala, D. J. Austin and R. H. Crabtree, *J. Am. Chem. Soc.*, 1997, **119**, 2325-2326.

8. G. W. Bates, P. A. Gale and M. E. Light, *Chem. Comm.*, 2007, 2121-2123.

9. I. J. Bazany-Rodríguez, D. Martínez-Otero, J. Barroso-Flores, A. K. Yatsimirsky and A. Dorazco-González, *Sensors and Actuators, B: Chemical*, 2015, **221**, 1348-1355.

10. S. N. Berry, N. Busschaert, C. L. Frankling, D. Salter and P. A. Gale, *Org. Biomol. Chem.*, 2015, **13**, 3136-3143.

11. I. A. Carasel, C. R. Yamnitz, R. K. Winter and G. W. Gokel, *J. Org. Chem.*, 2010, **75**, 8112-8116.

12. S. J. Coles, J. G. Frey, P. A. Gale, M. B. Hursthouse, M. E. Light, K. Navakhun and G. L. Thomas, *Chem. Comm.*, 2003, **5**, 568-569.

13. J. Eckelmann, V. Saggiomo, S. Fischmann and U. Lüning, *Beilstein J. Org. Chem.*, 2012, **8**, 11-17.

14. N. Łukasik and E. Wagner-Wysiecka, *Photochem. Photob. Sci.*, 2017, **16**, 1570-1579.

15. L. Mao, W. Pan, Y. Fu, L. Chen, M. Xu, Y. Ren, W. Feng and L. Yuan, *Org. Lett.*, 2017, **19**, 18-21.

16. X. Wu, R. Liu, B. Sathyamoorthy, K. Yamato, G. Liang, L. Shen, S. Ma, D. K. Sukumaran, T. Szyperski, W. Fang, L. He, X. Chen and B. Gong, *J. Am. Chem. Soc.*, 2015, **137**, 5879-5882.

17. Y. Zhang, R. Cao, J. Shen, C. S. F. Detchou, Y. Zhong, H. Wang, S. Zou, Q. Huang, C. Lian, Q. Wang, J. Zhu and B. Gong, *Org. Lett.*, 2018, **20**, 1555-1558.

18. G. Cavallo, P. Metrangolo, R. Milani, T. Pilati, A. Priimagi, G. Resnati and G. Terraneo, *Chem. Rev.*, 2016, **116**, 2478-2601.

19. L. C. Gilday, S. W. Robinson, T. A. Barendt, M. J. Langton, B. R. Mullaney and P. D. Beer, *Chem. Rev.*, 2015, **115**, 7118-7195.

20. R. Tepper and U. S. Schubert, *Angew. Chem. - Int. Ed.*, 2018, **57**, 6004-6016.

21. M. Giese, M. Albrecht and K. Rissanen, *Chem. Rev.*, 2015, **115**, 8867-8895.

22. D. Quiñonero, C. Garau, C. Rotger, A. Frontera, P. Ballester, A. Costa and P. M. Deyà, *Angew. Chem. Int. Ed.*, 2002, **41**, 3389-3392.

23. M. R. Battaglia, A. D. Buckingham, D. Neumark, R. K. Pierens and J. H. Williams, *Mol. Physics*, 1981, **43**, 1015-1020.

24 S. N.Berry, N.Busschaert, C. L.Frankling, D.Salter, P. A. Gale, *Org. Biomol. Chem.* 2015, ***13***, 3136-3143.

25 C. R.Yamnitz, S.Negin, I. A.Carasel, R. K. Winter, G. W. Gokel, *Chem. Commun.* 2010, ***46***, 2838-2840.

26 P. A Gale, J.Garric, M. E. Light, B. A.McNally, B. D. Smith, *Chem. Commun.* 2007, 1736-1738.

27 P. V. Santacroce, J. T. Davis, M. E. Light, P. A. Gale, J. C. Iglesias-Sánchez, P. Prados, R. Quesada, *J. Am. Chem. Soc.* 2007, ***129***, 1886-1887.

28 P.-Y. Liu, S.-T. Li, F.-F. Shen, W.-H. Ko, X.-Q. Yao, D. Yang, *Chem. Commun.* 2016, ***52***, 7380-7383.

29 M. J. Spooner, H. Li, I. Marques, P. M. R. Costa, X. Wu, E. N. W. Howe, N. Busschaert, S. J. Moore, M. E. Light, D. N. Sheppard, V. Félix, P. A. Gale, *Chem. Sci.* 2019, ***10***, 1976-1985.

30 N. J. Knight, E. Hernando, C. J. E.Haynes, N. Busschaert, H. J. Clarke, K. Takimoto, V. García-Valverde, J. G. Frey, R. Quesada, P. A. Gale, *Chem. Sci.* 2016, ***7***, 1600-1608.

31 Z. Li, W.-H. Chen, *Mini-Rev. Med. Chem.* 2017, ***17***, 1398-1405.

32 H. Adams, J. L. Jimenez Blanco, G. Chessari, C. A. Hunter, C. M. R. Low, J. M. Sanderson and J. G. Vinter, *Chem. Eur. J.*, 2001, **7**, 3494-3503.

33 M. J. Hynes, *J. Chem. Soc., Dalton Trans.*, 1993, 311-312.

34 A. Casula, P. Begines, A. Bettoschi, J. G. Fernandez-Bolaños, F. Isaia, V. Lippolis, Ó. López, G. Picci, M. Andrea Scorciapino and C. Caltagirone, *Chem. Commun.*, 2017, **53**, 11869-11872.

35 L. A.Jowett, P. A. Gale, *Supramol. Chem.* 2019, ***31***, 297-312.

36 Y. *J.* Marcus, *Chem. Soc. Faraday Trans.* 1991, ***87***, 2995-2999.

Chapter 4

Highly efficient squaramide receptors for anion binding, cell imaging and transmembrane transport

4 High efficient squaramide receptors for anion binding, cell imaging and transmembrane transport

In this chapter a new family of symmetric squaramide- based receptors functionalised with different fluorophores (**L11-L16**) for anion recognition, transport and cell imaging are described. The anion binding properties of the five receptors towards different anion guests (F^-, CN^-, AcO^-, BzO^-, $H_2PO_4^-$, and Cl^-) were studied by means of ^{1}H-NMR spectroscopy in DMSO-d_6 and UV-Vis and fluorescent spectroscopies in DMSO and MeCN. **L12** exhibited the highest stability constants towards the anion species studied and, in particular, the highest affinity constant for the chloride species ever observed, to the best of our knowledge. The strong affinity of **L12** for all the anion guests tested may be explained considering the cooperative effect between the indole and the squaramide NHs in stabilizing the anion adducts. Vesicle anion transport assays using anion selective electrodes demonstrated that only **L12** is enable to transport chloride across to the phospholipidic membrane. However, although the results revealed **L12** active at low concentration, it was not able to reach the saturation of the chloride efflux. Our hypothesis is that an equilibrium between the chloride species into the internal solution and into the external solution was reached and this made not possible to transport all the chloride species. Finally, we described the ability of **L11** and **L13** as imaging agents towards non-tumoral and tumoral cells as free molecules and when encapsulated inside lipid-based nanoparticles, named cubosomes.

4.1 Introduction

Anions are ubiquitous in Nature and play fundamental roles in environmental and biological systems. Their toxicity for the environment and for the health of human bodies, as well as their recognition and monitoring, are important topics of scientific debate.[1-5] For this purpose, during the past decades a wide range of synthetic neutral

anion receptors able to interact *via* hydrogen bonds formation with anion species have been reported. Amides, sulfonamides, ureas, thioureas and, more recently selenoureas[6-7] are all examples of receptors that exert their host-guest properties towards anions by forming hydrogen bonds through their NH moieties.[8] Squaramides represent an important family of synthetic neutral anion receptors that have been studied recently.[9] Membered ring that, along with the hydrogen-bond donor and acceptor ability, confers them interesting features, which can be applied to the design of anion receptors. Indeed, compared with the analogous ureas and thioureas, squaramides exhibit a greater acidity as well as structural convergence of their NH bonds that make them more suitable for anion binding, in particular halides.[10] During the last decade several examples of squaramide receptors for applications in different fields, such as medicinal chemistry, catalysis, liquid crystalline self-assembly, anion recognition have been reported.[11-13] Squaramides have also been successfully employed as scaffolds for the construction of polymers and gels,[9] and for the development of synthetic anion transporters across membranes.[9, 14] Surprisingly, few examples of fluorescent squaramides for anion sensing have been reported in the literature so far. In particular, Jolliffe *et al.* described four squaramide based fluorescent anion sensors with selectivity for chloride with concomitant changes in both their UV/visible and fluorescence properties, signalled by a colour change.[15] Muthyala *et al*. also described a fluorescent squaramide derivative that works as a chloride sensor, with an increase of the emission upon chloride binding.[16] Recently, Gale and co-workers developed a series of squaramide-based anion transporters functionalised with the 1,8-naphtalimide fluorophore for improved ionophoric activity and fluorescent imaging in cells.[17]

In this chapter we will describe a new family of symmetric squaramide- based receptors functionalised with different fluorophores (**L11-L16**, Figure 4.1) for anion recognition, transport and cell imaging. The fluorophores were chosen with the aim to explore the possibility to tune the binding/recognition event depending on the heteroatoms in the squaramide substituents. The anion binding properties of the five

receptors towards different anion guests (F^-, CN^-, AcO^-, BzO^-, $H_2PO_4^-$, and Cl^-) were studied by means of ^{1}H-NMR spectroscopy in DMSO-d_6 and UV-Vis and fluorescent spectroscopies in DMSO and MeCN.

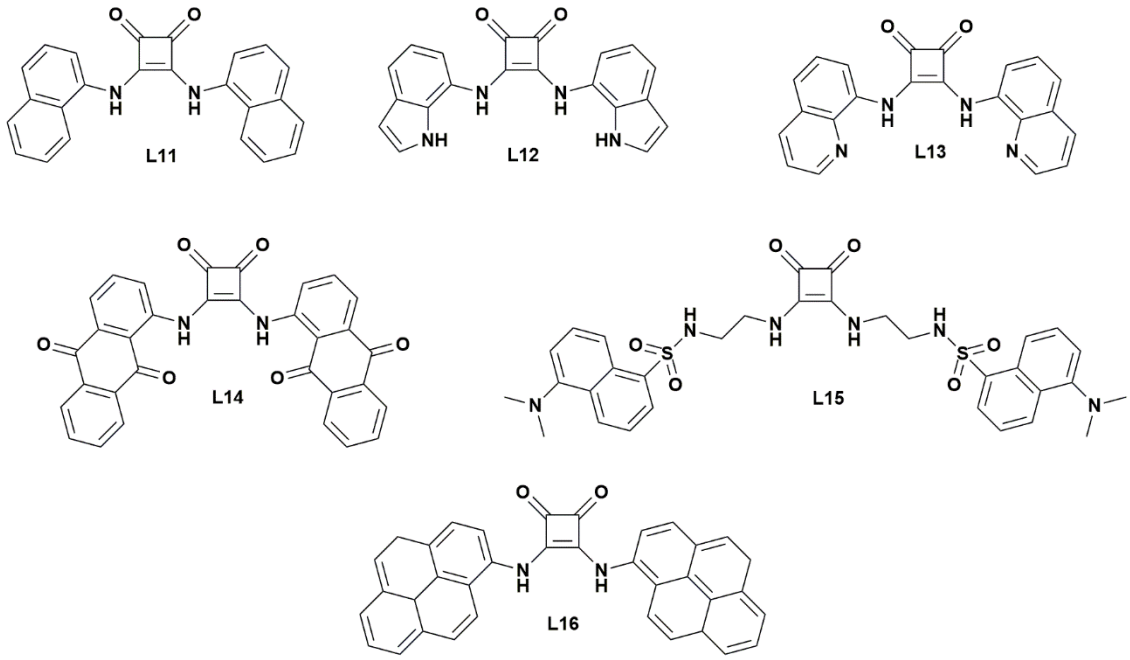

Figure 4.1 Receptors described in the present chapter.

Moreover, in order to test the capability of **L11**-**L16** to mediate chloride transport across membranes, we investigated their transmembrane anion transport activity. Finally we will describe the ability of **L11** and **L13** as imaging agents towards non-tumoral and tumoral cells as free molecules and when encapsulated inside cubosomes.[18]

4.2 Synthesis

Receptors **L11**-**L16** were synthesised by reacting squarate esters (methyl or ethyl) with the appropriate amine in a mixture of DMF/Toluene (1:19 v/v) for **L11**, **L12**, **L14**,

L15 and **L16** or MeOH (**L13**) using $Zn(OTf)_2$ as a Lewis acid catalyst from adapted literature procedure.[19]

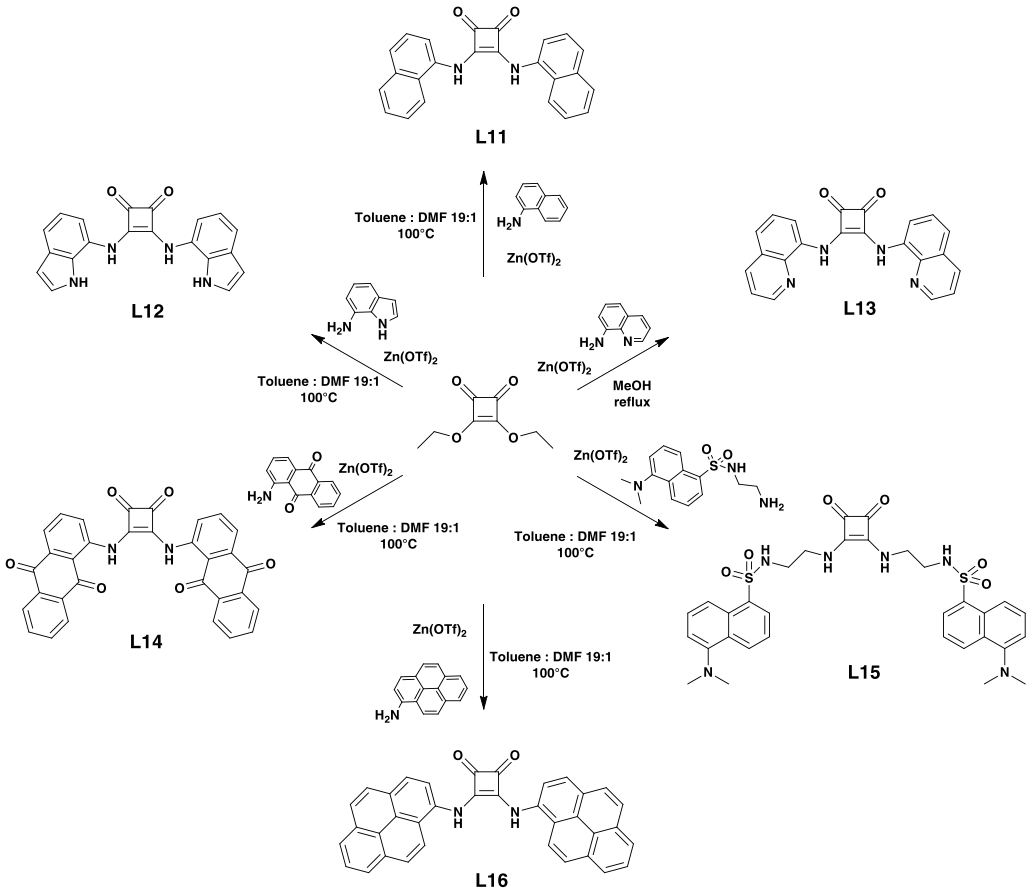

Scheme 4.1 Synthetic procedure for receptors **L11**-**L16**

4.3 Solution studies

Anion-binding studies were conducted by means of ^{1}H-NMR titrations using DMSO-d_6/0.5% water as a solvent. Stability constants from the obtained ^{1}H-NMR titration curves (see paragraph 4.8) were calculated by fitting the data to a 1:1 binding model using WinEQNMR[20] as shown in Table 4.1.

Table 4.1 Association constants (Ka/M^{-1}) for the formation of adducts of **L11–L16** with anions added as tetrabutylammonium salts in DMSO-d_6/0.5% water at 300 *K*. All errors estimated to be≤14%

Receptors	**Anions**					
	F^-	CN^-	AcO^-	BzO^-	$H_2PO_4^-$	Cl^-
L11	Deprot.[a]	Deprot.[a]	406	607	1434	156
L12	Deprot.[a]	Deprot.[a]	$>10^4$	n.d.[c]	$>10^4$	1199
L13	Deprot.[a]	Deprot[a]	No interaction[b]	No interaction[b]	No interaction[b]	No interaction[b]
L14	Deprot.[a]	Deprot.[a]	No interaction[b]	No interaction[b]	No interaction[b]	No interaction[b]
L15	Deprot.[a]	Deprot[a]	3678	1703	5483	n.d.[d]
L16	Deprot.[a]	Deprot[a]	Deprot.[a]	Deprot[a]	Deprot.[a]	164

[a] The squaramide NH signal disappeared upon addition of the tested anions; [b]none of the signals shifted upon addition of the tested anions; [c]we were not able to fit the experimental data; [d]the NH signal attributed to the squaramide slightly downfield shifted under the other aromatic signal and did not emerged. No other signals shifted during the titration. For this reason, the association constant could not be calculated.

Under the experimental conditions in the presence of fluoride and cyanide the disappearance of the signal attributed to the squaramide NHs was observed already upon the addition of 0.2 equiv. of anionic guest, accompanied by a dramatic colour

change of the solution, suggesting a deprotonation for all the receptors with these anions.

Interestingly, as shown in Table 4.1, in the case of **L13** and **L14** we did not observe any relevant changes in the resonances of the NH protons in the presence of the tested anion guests.

To explain this behaviour, ^{1}H-NMR experiments at different temperature were conducted and we could observe a high-field shift of the signals attributed to the NHs squaramide protons with the temperature increase (Figures 4.2a-b). This is probably due to the presence of an intramolecular H-bond between the squaramide NHs and the heteroatoms in the quinoline and anthraquinone moieties in **L13**and **L14**, respectively.

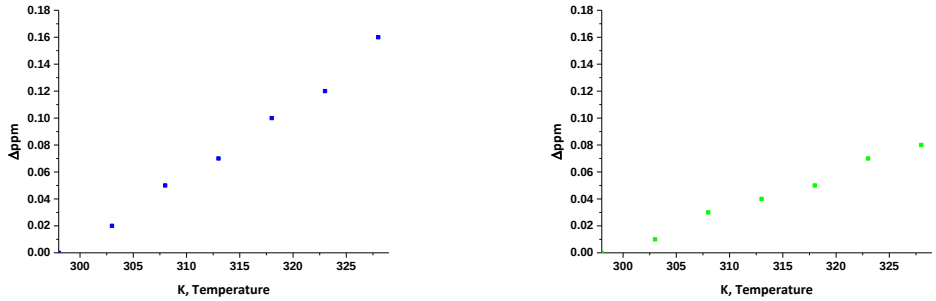

Figure 4.2 Plot of the Δppm vs temperature for **L13** (a) and **L14** (b).

The presence of the intramolecular H-bond in the case of **L13** was also confirmed by the solid state results. Crystals of **L13** (structure **3** in Table 4.4) were obtained by slow evaporation from MeOH solution. **L13** crystallizes as a hydrate, and it should be stressed that in solution studies water was always present, so the effect of water might be present for all the receptors studied. However, in none of other crystal structures water was present, in particular not in such a well-defined and structurally

crucial position. Figure 4.3 shows that water molecule accepts two strong NH···O hydrogen bonds, while at the same time serves as a donor for two OH···N hydrogen bonds with the same **L13** molecule (see paragraph 4.3, Table 4.4).

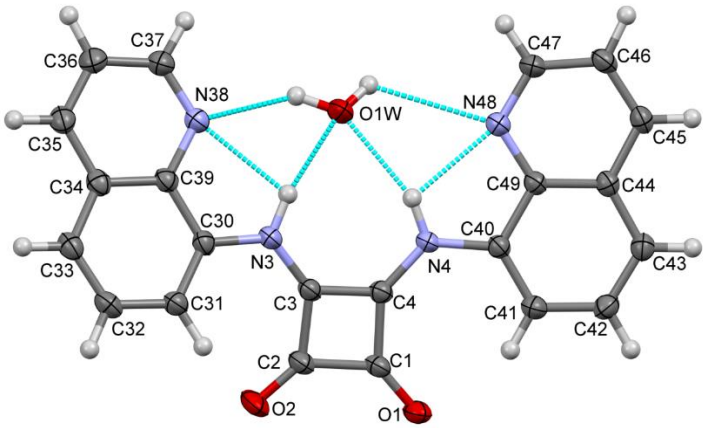

Figure 4.3 A perspective view of the hydrate of **L13** ·H_2O as seen in its crystal structure with the adopted numbering scheme. Ellipsoids are drawn at the 50% probability level, hydrogen atoms are shown as spheres of arbitrary radii. Dashed blue lines show the hydrogen bonds.

Indeed, these bonds are in principle intramolecular, together with weaker intramolecular NH···N contacts. It can be noted that in this case water molecule helps in attaining better hydrogen bond geometry as compared with sole intramolecular NH···N ones. So, the complexation of anion might be highly because of both structural (hydrogen bonding) and steric factors and - in effect - improbable. Similar arguments could be applied for **L14** – the only change is carbonyl oxygen as an acceptor instead of nitrogen atom.

L11, L12 and **L15** coordinate the oxo-anions (i.e. AcO-, BzO-, and $H_2PO_4^-$) with stability constants following the order **L12**>**L15**>**L11**.

In the case of receptor **L15** the signal attributed to the sulphonamide NHs (8.06 ppm) broadened and then disappeared during the titration with the above-mentioned anions suggesting a slow exchange in the NMR timescale, while the signal attributed

to the squaramide NHs (7.39 ppm) shifted downfield upon addition of the guests (Figure 4.4 a-d).

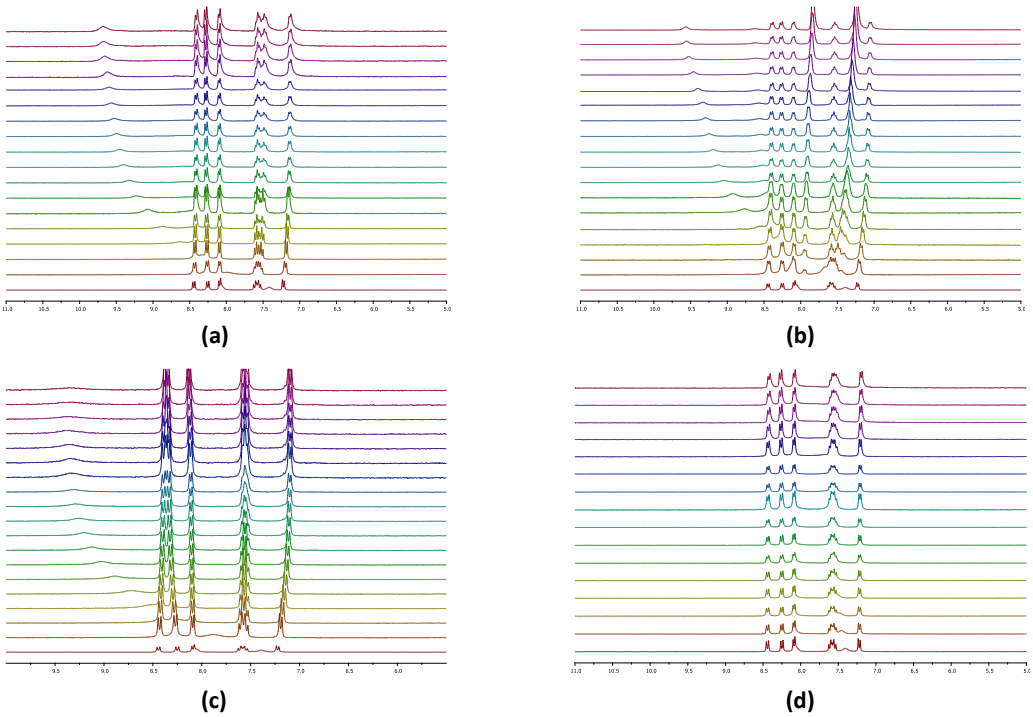

Figure 4.4 Stack plots of the ^{1}H-NMR spectra of **L15** (0.005 M) upon addition of increasing amount of (a) TBaAcO, (b) TBABzO, (c) $TBAH_2PO_4$ d) TBACl (0.075 M) in DMSO-d_6.

As reported in Table 4.1, only **L11** and **L12** and **L16** were able to bind chloride.

The strong affinity of **L12** for all the anion guests tested may be explained considering the cooperative effect between the indole and the squaramide NHs in stabilizing the anion adducts. Indeed, as shown in the stack-plot of the ^{1}H NMR titration in the case of Cl^- (Figure 4.5) the signal attributed to the squaramide NHs dramatically downfield shifted (Δppm = 0.97) upon addition of the guest. Less pronounced downfield shifts of the signals attributed to the indole NH protons (Δppm = 0.15) and of the CH protons adjacent to the squaramide NH protons (Δppm = 0.46) were observed.

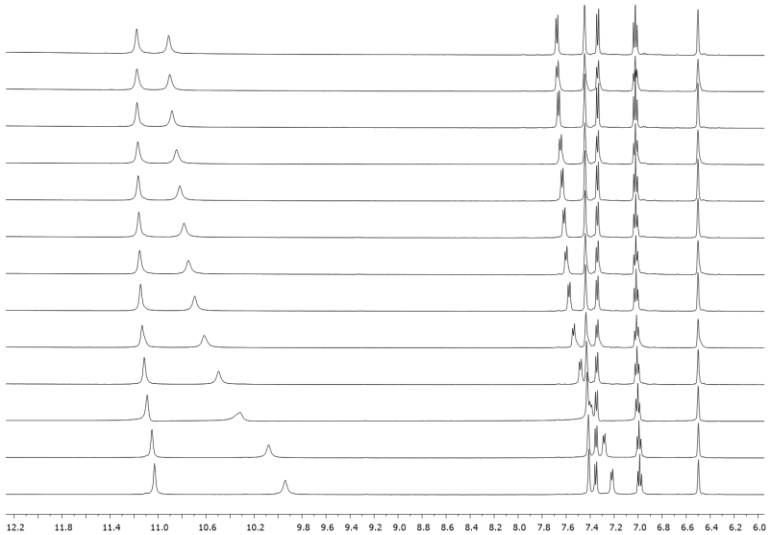

Figure 4.5 Stack plots of the ^{1}H-NMR spectra of **L12** (0.005 M) upon addition of increasing amount of TBACl (0.075 M) in DMSO-d_6.

A similar behaviour was observed in the presence of the other anions (see Figures 4.6a-c for AcO^-, BzO^-, and $H_2PO_4^-$, respectively).

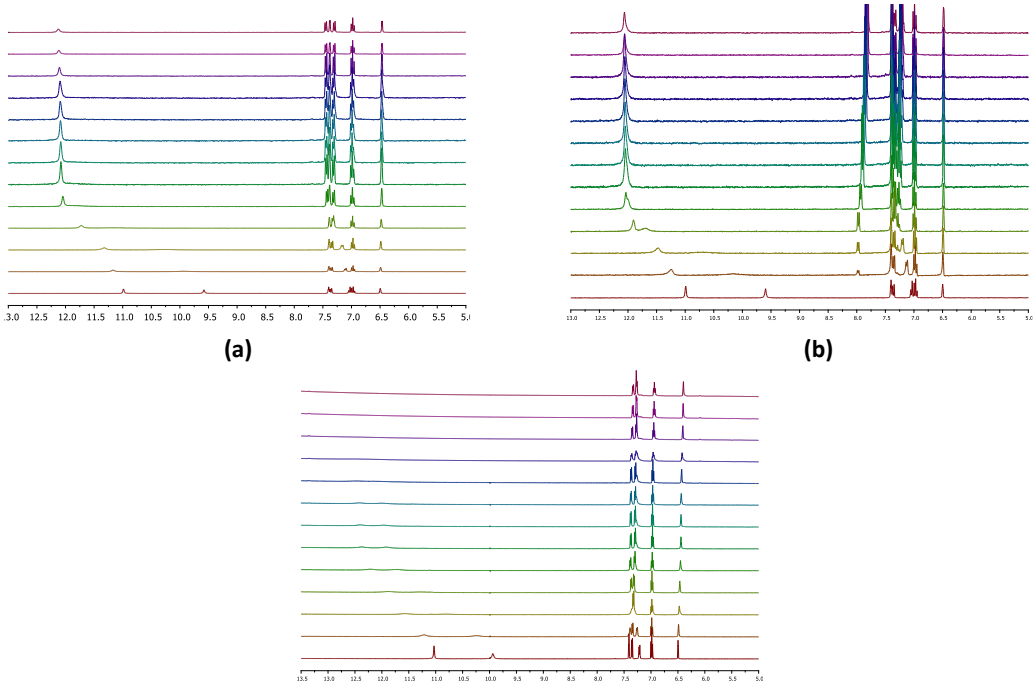

Figure 4.6 Stack plots of the ^{1}H-NMR spectra of **L12** (0.005 M) upon addition of increasing amount of (a) TBaAcO, (b) TBABzO, (c) $TBAH_2PO_4$ (0.075 M) in DMSO-d_6.

Encouraged by the high affinity of **L12** observed in DMSO-d_6/0.5% water, we decided to perform anion binding studies with **L12** in more competitive solvent mixtures (i.e. DMSO-d_6 with 10% and 25% water). The results reported in Table 4.2 points out the remarkable high affinity for the oxo-anions as well as a significant affinity for chloride in these conditions, with a stability constant $>10^3$ for the oxo-anions and $>10^2$ for chloride at 10% water. When the experiments were carried out at 25% water/DMSO-d_6 mixture the formation of the 1:1 adduct with both oxoanions and chloride was still detected. When comparing the results reported with **L12** with those of Gale and co-workers for 1,3-diindolylureas,[6] stability constants of an order of magnitude higher were obtained with the former in 25% water, demonstrating the remarkable binding properties of the diindolyl squaramide **L12** compared to the analogous urea. It is interesting to note that the obtained results demonstrate that **L12** showed the

highest stability constants with respect to the other squaramide receptors reported so far in the literature for the set of anions tested, to the best of our knowledge.

Table 4.2 A comparison of **(i)** the stability constants (M^{-1}) of compound **L12** with a variety of putative anionic guests (added as tetrabutylammonium salts) at 298 K in DMSO-d_6–0.5% water with **(ii)** in DMSO-d_6/10% water and **(iii)** in DMSO-d_6/25% water. In all cases 1:1 receptor: anion stoichiometry was observed. Errors estimated to be no more than 15%.

Anionic species	Stability Constant /M^{-1}		
	i	ii	iii
$H_2PO_4^-$	$>10^4$	2000	1743
AcO^-	$>10^4$	1876	217
BzO^-	nd*	3770	121
Cl^-	1999	114	21

***We were not able to fit the experimental data

Time resolved luminescence (TRPL) measurements on the receptors **L11**-**L15** were performed using an optical parametric oscillator with a frequency doubler device exciting the samples at 250 nm in backscattering configuration. As shown in Table 4.3, in which the emission peak position of receptors and their respective time decay are reported, only in the case of receptor **L15** we have achieved a remarkable value of time decay (19.3 ns) in the solid state.

Table 4.3 Time resolved luminescence (TRPL) measurements of **L11**-**L16** receptors exciting the samples at 250 nm in backscattering configuration.

	L11	L12	L13	L14	L15	L16
Peak position (nm)	470	495	430	410	467	464
Time decay (ns)	<5	<5	<5	<5	19.3	<5

Only in the case of **L15** an emission band at 522 nm upon excitation at 370 nm was observed in solution both in MeCN (Φ = 0.18) and DMSO (Φ = 0.26) (Figure 4.7a-f)). Upon addition of all the anion tested (F^-, CN^-, AcO^-, $H_2PO_4^-$ and BzO^-) a quenching of the fluorescence emission was observed. No interaction with Cl^- was observed.

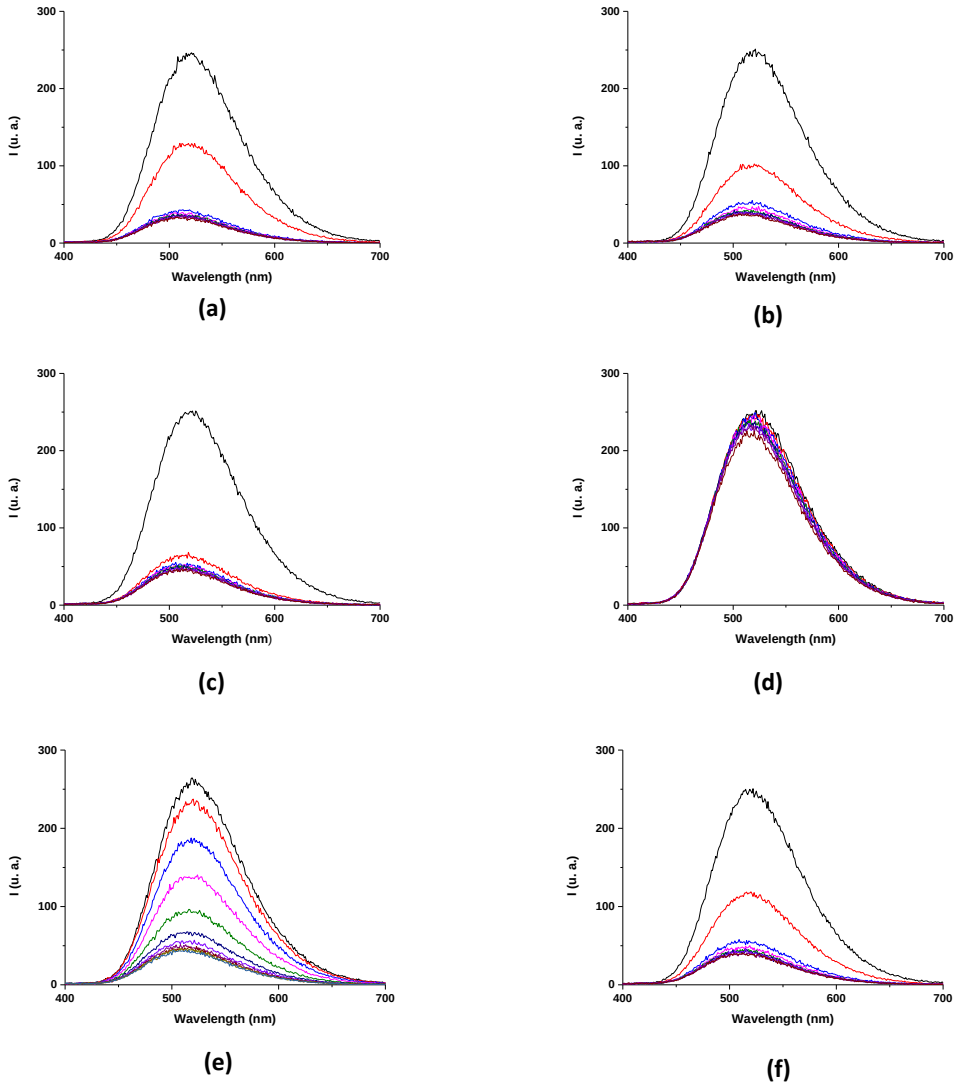

Figure 4.7 Fluorescence titration of **L15** with TBAAcO (a), $TBAH_2PO_4$ (b) TBABzO (c), TBACl (d), TBAF (e) and TBACN (f) in CH_3CN.

Receptors **L11**-**L14** did not show any appreciable fluorescent emission as free receptors and in the presence of anion guests no changes in the absorption and emission properties of the receptors were observed in DMSO. However, it is worth noticing that in the case of **L13**, when UV-Vis spectroscopic studies were performed in MeCN upon addition of the oxoanions some changes in the UV-Vis spectrum of the free receptors were observed (i.e. a slight blue shift of the absorption band at 372 nm and the concomitant increase of absorption band at 443 nm upon the addition of 4 equivalents of anion guest (Figure 4.8a-f), suggesting that the polarity of the solvent could affect the strength of the intramolecular hydrogen bond described above.

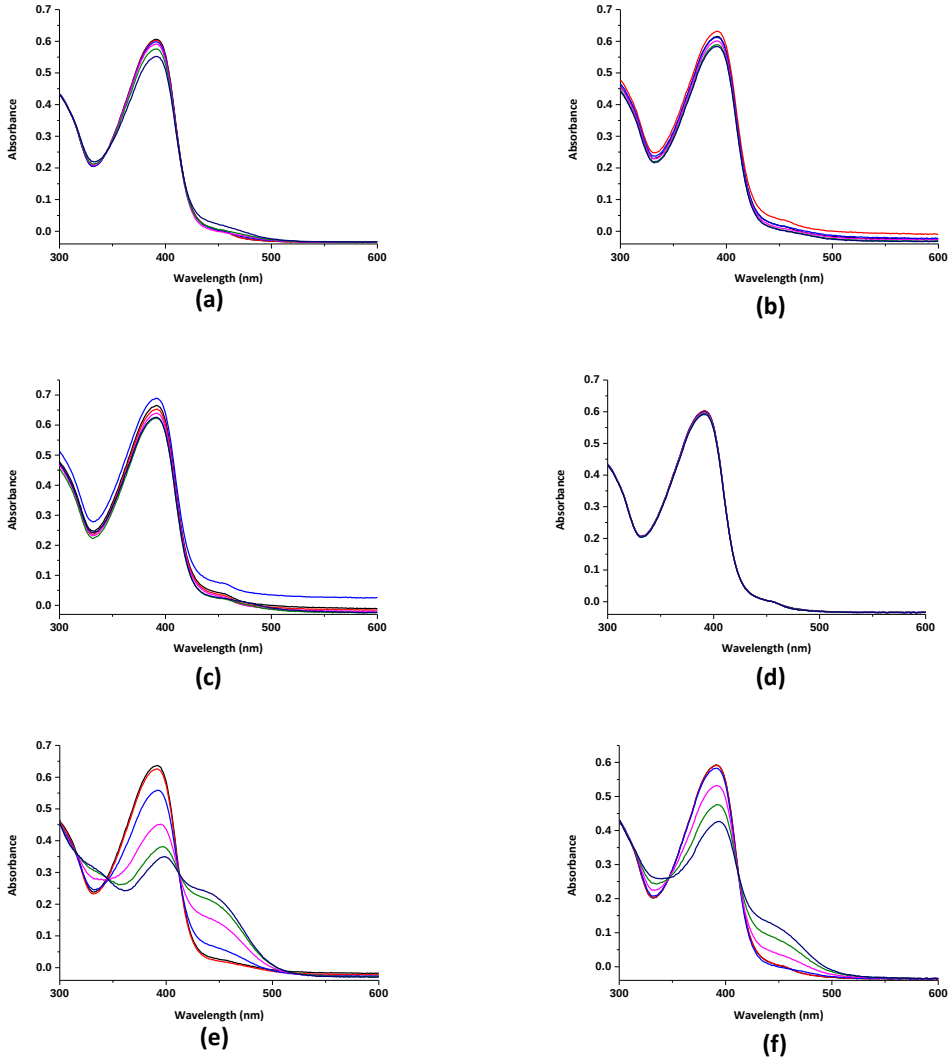

Figure 4.8 Fluorescence titration of **L13** with TBAAcO (a), $TBAH_2PO_4$ (b) TBABzO (c), TBACl (d), TBAF (e) and TBACN (f) in CH_3CN.

Receptor **L16** although showing an emission band in CH_3CN solution centred at 464 nm but did not show any change in the presence of the anions studied.

4.4 Solid state studies

Crystals structure of the 1:1 adducts of **L11** with TBABzO [(**L11**BzO)TBA)] (**1**) and of **L12** with TBACl [(**L12**Cl)TBA)] (**2**) were obtained by slow evaporation of a solution of the receptors in the presence of an excess of anions in DMSO (Figure 4.9a-b, for structures **1** and **2**, respectively).

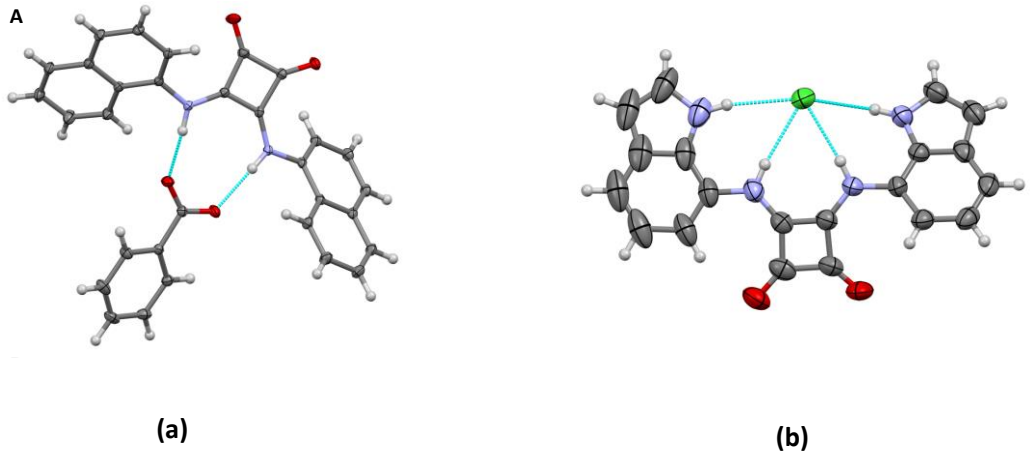

Figure 4.9 Perspective views of the hydrogen-bonded adducts of A) [(**L11**BzO)TBA)] (**1**) and of B) [(**L12**Cl)TBA)] (**2**) as seen in their crystal structures. Ellipsoids are drawn at the 50% probability level; hydrogen atoms are shown as spheres of arbitrary radii. Dashed blue lines show the hydrogen bonds. TBA counter cations are omitted for clarity.

Both **1** and **2** crystallize with multiple, symmetry-independent moieties in the asymmetric part of the unit cell (2 in case of **1**, 4 for **2**). In general, such situation is regarded as an effect of some kind of packing conflicts. For **1** and **2** such a conflict can be related to the packing of well-defined molecules of ligand and anions on one hand, and bulky tetrabutylammonium cations on the other. The general features–bond lengths and angles-of the receptor molecules (seven symmetry independent cases) are quite similar and consistent with the formulae. However, the overall conformations differ quite significantly, as can be seen from the values of dihedral

angles between planes of central C_4 ring and the planes of aryl substituents. In both structures the receptors form hydrogen-bonded adducts with the anions (Hydrogen bond data are listed in Table 4.4). It might be noted that the chloride anion fits perfectly to the cavity in **2** and this can be an explanation of almost 8-fold increase in the association constant compared to the receptor **L11**. In the crystal structures these complexes are the main building blocks, connected by much weaker CH···O and other interactions. In the voids of such created structures the TBA cations are located.

Table 4.4 Hydrogen bond data (Å, °) for crystal structures **1**, **2**, and **3**.

D	H	A	D-H	H···A	D···A	D-H···A
1						
N3A	H3A	O2C	0.88	1.89	2.6814(16)	149
N4A	H4A	O1C	0.88	1.92	2.7478(15)	155
N3B	H3B	O1D^{i}	0.88	1.90	2.7395(15)	159
N4B	H4B	O2D^{i}	0.88	1.91	2.7075(15)	151
C1E	H1EB	O1C	0.99	2.23	3.1813(19)	162
C13E	H13A	O2C^{ii}	0.99	2.29	3.269(2)	170
C13F	H13C	O1D^{ii}	0.99	2.39	3.3276(18)	157
C14F	H14B	O2A	0.99	2.31	3.2946(19)	177
2						
N3A	H3A	CL1J	0.88	2.39	3.257(4)	170
N4A	H4A	Cl1J	0.88	2.28	3.143(4)	165
N38A	H38A	Cl1J	0.88	2.39	3.250(5)	167
N48A	H48A	Cl1J	0.88	2.54	3.328(4)	150
N3B	H3B	Cl1L	0.88	2.38	3.245(3)	167
N4B	H4B	Cl1L	0.88	2.33	3.204(4)	172
N38B	H38B	Cl1L	0.88	2.38	3.223(4)	161
N48B	H48B	Cl1L	0.88	2.38	3.224(4)	161
N3C	H3C	Cl1K	0.88	2.33	3.200(4)	172
N4C	H4C	Cl1K	0.88	2.31	3.184(4)	170
N38C	H38C	Cl1K	0.88	2.41	3.238(4)	157
N48C	H48C	Cl1K	0.88	2.38	3.215(4)	159
N3D	H3D	Cl1I	0.88	2.36	3.229(4)	172
N4D	H4D	Cl1I	0.88	2.26	3.136(3)	174
N38D	H38D	Cl1I	0.88	2.39	3.246(4)	165
N48D	H48D	Cl1I	0.88	2.43	3.241(4)	153
C32A	H32A	O2A	0.95	2.31	3.148(8)	147
C32B	H32B	O2B	0.95	2.24	3.128(6)	155
C42B	H42B	O1B	0.95	2.32	3.107(6)	139
C32C	H32C	O2C	0.95	2.30	3.141(6)	147

C42C	H42C	O1C	0.95	2.24	3.103(6)	150
C32D	H32D	O2D	0.95	2.27	3.144(7)	152
C42D	H42D	O1D	0.95	2.36	3.108(6)	135
3						
N3	H3	O1W	0.918(16)	1.994(17)	2.8864(13)	163.4(15)
N4	H4	O1W	0.913(16)	2.205(16)	3.0625(13)	156.2(13)
O1W	H1W1	N38	0.91(2)	2.21(2)	2.9446(14)	137(2)
O1W	H1W2	O1^{iii}	0.87(2)	2.12(2)	2.9636(13)	161.3(18)
C41	H41	O1	0.952(16)	2.224(16)	3.0961(15)	151.7(13)

4.5 Cell imaging

The potential use of **L11** and **L13** for live cell imaging application on human line cells both tumoral (Caco-2) and non-tumoral (293 T), as free molecules and when encapsulated inside lipid-based nanoparticles (namely cubosomes) was explored. Cubosomes are nanosized carriers formulated exploiting the self-assembling properties of several lipids in water. They differ from analogous nanoparticles because of their unique honeycomb-like internal structure, consisting in a lipid bilayer arranged in three dimensions to form two disjoined water channels and describing an Infinite Periodic Minimal Surface belonging to a cubic space group (Pn3m, Ia3d, or Im3m).[21] *In vitro* and *in vivo* studies demonstrated that these nanoparticles could be successfully used at a non-toxic concentration as imaging/theranostic agents.[22, 23]

L11 and **L13** were incubated with tumoral Caco-2, and non-tumoral 293T cell lines. As shown in Figure 4.10 and Figure 4.11 (ESI), **L13** rapidly passed cell membranes of the examined cell. Cell penetration of **L13** was already observed after 10 min incubation with the probe at the lowest concentration tested (10 μM, Figure 4.10), suggesting that cellular internalization is an effective and rapid process.

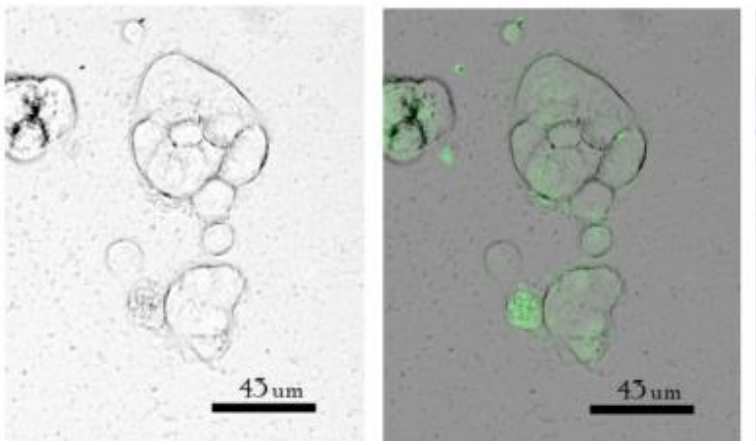

(a) (b)

Figure 4.10 Caco-2 cells incubated for 10 min with **L13** 10 μM. (a) Bright field image; (b) merge image of bright and green field Green channel λ_{Ex} 480 ± 17 λ_{Em} 517 ± 23.

Remarkably, even at the highest ligand concentration (200 μM, Figure 4.11), the morphology of the examined cells did not change after 10 min exposition to the probe. This finding suggests that **L13** could be used for potential fast clinical cell imaging at short exposition time, exploiting the high sensitivity and contrast achieved using higher **L13** concentrations. However, it is important to note that **L13** enters both in Caco-2 (Figure 4.10) and 293T cells (Figure 4.11), without selectivity.

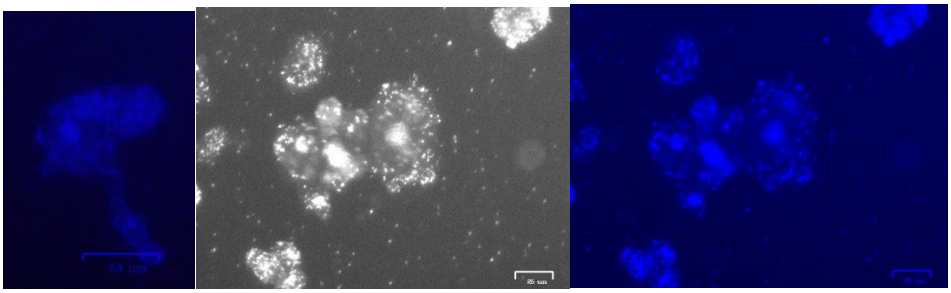

(a) (b) (c)

Figure 4.11. 293T (a) and Caco-2 cells (b and c) incubated for 10 min with **L13** 200 μM.

When **L11** was incubated with Caco-2 cells, at 10 μM concentration, after an incubation time of 10 min, a green fluorescence was observed on the cells membrane (Figure 4.12 b).

Short incubation time and low concentration of **L11** ligand were chosen for proper visualization of membrane in comparative staining with PKH26, a commercially available cell membrane marker. It can be observed in Figure 4.12b that **L11** interacts rapidly with the cell membrane. The subsequent staining with PKH26 (Figure 4.12c) showed the imposition of red signal (PKH26) over green signal (**L11**) in most regions. Moreover, it can be observed that at the same concentration and incubation time **L11** is more efficient for membrane staining than PKH26. The affinity of **L11** for cell membrane could be explained considering its affinity for oxo-anions such as phosphates.

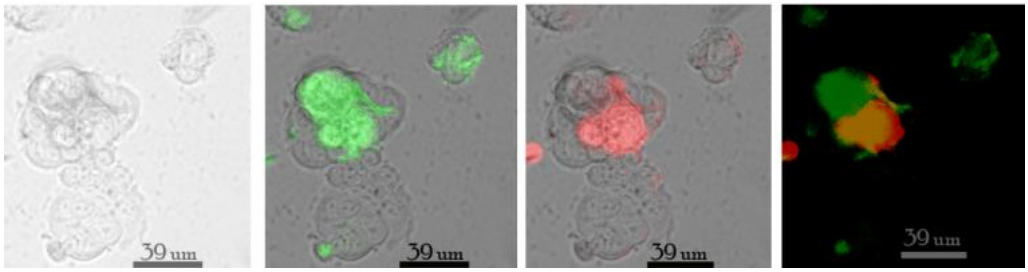

(a) (b) (c) (d)

Figure 4.12 Caco-2 cells treated with 10 µM **L11** solution for 10 min. (a) Bright field image; (b) merge image of bright field in green; (c) Caco-2 cells treated successively with 10 µM PKH26 marker as a merge image of bright field in red, C) merge image of bright field in red; (d) Caco-2 cells treated successively with 10 µM PKH26 marker as a merge image of bright field in red merge image of green and red field. Green channel λ_{Ex} 480 ± 17 λ_{Em} 517 ± 23; Red channel λ_{Ex} 556 ± 20 λ_{Em} 615 ± 61.

Indeed, an increase in the fluorescent emission was observed upon addition of one equivalent of $H_2PO_4^-$ (as its tetrabutylammonium salt) into a DMSO/H_2O (1:25 v/v) solution of **L11** , suggesting a ligand-anion interaction (Figure 4.13).

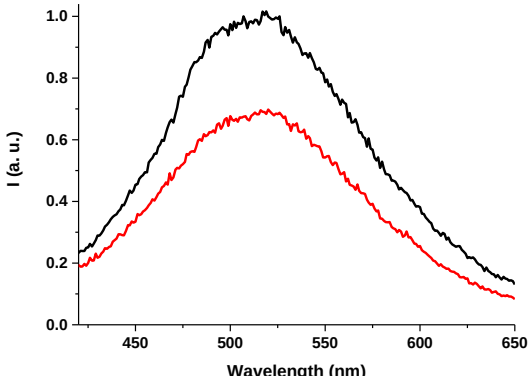

Figure 4.13 Normalized emissions of **L11** (red) and **L11** in the presence of 1 eq of $TBAH_2PO_4$ (black) of a DMSO solution (1 mM) diluted in water (25 µM). λ_{Ex} 480 nm.

The toxicity and IC_{50} value of **L11** and **L13** were determined in the non-tumoral human kidney cells 293T (more susceptible with respect to tumoral cell lines) in triplicated experiments, with the use of Luna^{FL} automated method. Compare to MTT assay, which is limited in cell viability testing[24] the trypan blue staining permits to obtain more accurate data. IC50 dose of **L13** was found at 12.0 µM concentration and it is comparable with the toxicity of other squaramide derivatives.[25,26] **L11** showed lower toxicity respect to **L13**, with IC_{50} dose of 400 µM.

L13 cell uptake and localization studies in 293T cells were examined as a function of the exposure time, using an initial concentration five times lower than IC_{50} (2.5 µM), to avoid cellular death and the subsequent possible changes of localization. As shown in Figure 4.14, at low ligand concentration, **L13** associated fluorescence was observed only in few cells after 1 h of incubation, while after 2 h it was present inside almost all the cells. The maximum fluorescence intensity was obtained after 3 h. Remarkably, cell loaded with **L13** showed a diffused emission coming from the cytoplasm region, and an emission coming from a more specific granulated accumulation in the perinuclear region.

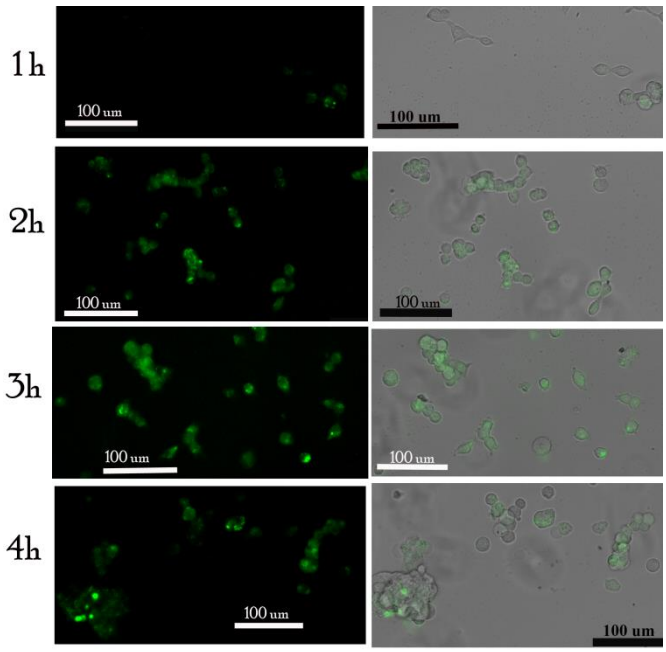

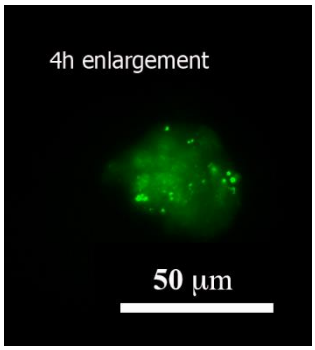

Figure 4.14 The cell uptake studies of **L13** in the 293T cells after 0, 1, 2, 3 and 4 h of incubation, [**L13**] = 2.5 μM. Green fluorescence filed (left) and merge of bright and green filed (right). Enlargement 60x.

Previous studies on squaramide-based fluorescent probes[27] suggested that the internalization into cells takes place through endocytic receptor-mediated mechanisms and that the internalized probes are sequestered in late endosomes arising from the maturation of early endosomes, which in turn are formed by an endocytosis process.[28] Therefore, although the detailed morphological and biochemical studies of endocytosis process are beyond the scope of this chapter an endocytic receptor-mediated mechanism for the cellular internalization of **L13** can be reasonably hypothesized. Particularly, the endocytosis process finished after 5-6 h and a diffuse low intensity green fluorescence was observed only in cytoplasm suggesting that after this time **L13** might be released by endosomes.

Considering the possible use of **L11** and **L13** as *in vivo* imaging probe, they were then encapsulated within monoolein-based cubosomes. This formulation should allow the administration of the apolar **L11** and **L13** in the bloodstream**,** simultaneously offering the possibility to selectively address the fluorescent ligand by properly decorating the cubosome surface with targeting agents. In previous papers[29] fluorescent cubosomes formulations were investigated *in vitro* in HeLa cell lines. The optical images showed the lipid droplets (LDs) accumulation in HeLA cells as a result of cubosomes internalization. Moreover, it was demonstrated that the uptake of cubosomes

induced modifications of the cell lipid profile, lipid droplets accumulation, mitochondrial hyperpolarization and mitochondrial ROS generation.

Cubosomes formulations loaded with **L11** and **L13** were, at first, physicochemically characterized for their inner structure, size, and surface charge. The two SAXS patterns for samples containing **L11** and **L13**, shown in Figure 4.15a, share common features in the entire *q*-range. At high *q* values, diffraction peaks appear between 0.04 and 0.3 $Å^{-1}$, while in the medium-*q* region, a q^{-4} slope in the log I(q)/log q plot indicates a smooth interface between dispersed particles and bulk solvent. This is followed, at lower q values, by a correlation peak indicating the center-to-center distance between nearest-neighbor particles in dispersion. Such peak is centered at slightly different q values for each sample, corresponding to the following real-space distances (calculated as $d = 2\pi/q$): 187 nm for cubosomes containing **L13** and 193 nm for those loaded with **L11**.

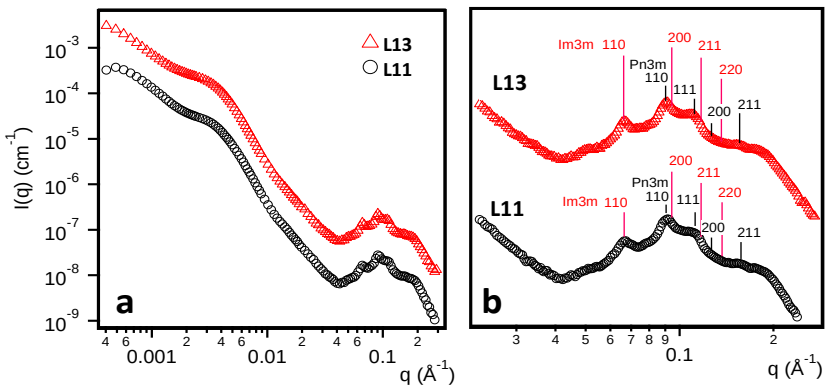

Figure 4.15 SAXS patterns obtained for cubosome samples loaded with **L13** (red triangles) and **L11** (black circles): (a) full *q*-range patterns; (b) high-*q* zoom enhancing the cubic phase diffraction peaks. The first four reflections of the Im3m and Pn3m lattices are evidenced, in red and in black, respectively, for both SAXS patterns. The curve in the case of **L13** was offset by 1 log unit uniquely for presentation purposes.

The diffraction peaks in the high-*q* region can be indexed as pertaining to two coexisting bicontinuous cubic lyotropic phases, namely Im3m and Pn3m, as shown in Figure 4.15b. The lattice parameters for the Im3m phases are essentially identical for cubosome samples containing **L13** and **L11** (around 12.7 nm); conversely, the Pn3m lattice parameter is slightly smaller in the case of **L13** (9.8 nm) than in the case of **L11** (10 nm). These data, summarized in Table 4.5, basically confirm that the inclusion of squaramide receptors within the lipid bilayer does not alter the inner structure of these nanoparticles. Furthermore, measured hydrodynamic diameters and ζ - potentials, respectively, 139 nm (PDI = 0.234) and −25 mV for cubosomes loaded with **L13**, and 138 nm (PDI = 0.124) and −26 mV for cubosomes loaded with **L11**, are in the range typically found for empty cubosomes.

Table 4.5 Crystallographic space group and corresponding lattice parameters for the liquid crystalline phases found in cubosome samples loaded with **L11** and **L13**.

Sample	Space group	Lattice parameter (nm)
L13	Im3m	12.8
	Pn3m	10.0
L11	Im3m	12.7
	Pn3m	9.8

The Caco-2 cell lines used for *in vitro* experiments with the molecularly dispersed imaging probe were treated with empty cubosomes or cubosomes containing **L11** (Figure 4.17b and c) and **L13** (Figure 4.18b and c) at 0.035 μM concentration, corresponding to a 200 times dilution of the fresh prepared cubosome formulation, well below their cytotoxic concentration (see below). The presence of LDs (as grainy structures), characteristic for the incubation with cubosomes, was observed after 30 min inside the cells (Figure 4.17B and 4.18B), while, the green fluorescence emission

inside the cell is associated to the presence of the ligand. In addition, the experiment was repeated with 293T cell line and cubosomes containing **L13** ligand (Figure 4.19).

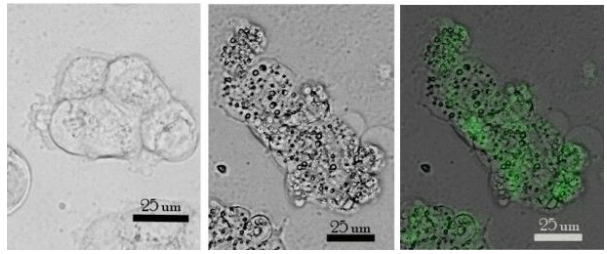

(a) (b) (c)

Figure 4.16 Caco-2 cells (a) control sample without any treatment; (b) treated for 30 min with cubosomes loaded with **L11**, bright field image; (c) treated for 30 min with cubosomes loaded with **L11**, merge of bright and green field image.

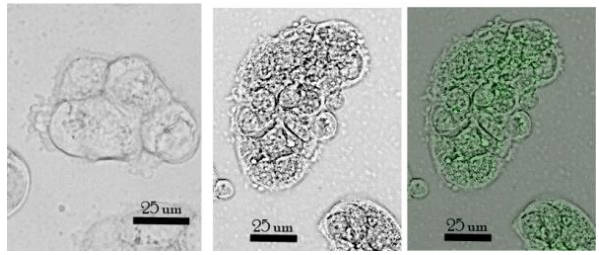

(a) (b) (c)

Figure 4.17 Caco-2 cells (a) control sample without any treatment; (b) treated for 30 min with cubosomes loaded with **L13**, bright field image (LDs are observed as grainy structures in cytoplasm); (c) treated for 30 min with cubosomes loaded with **L13**, merge of bright and green field image

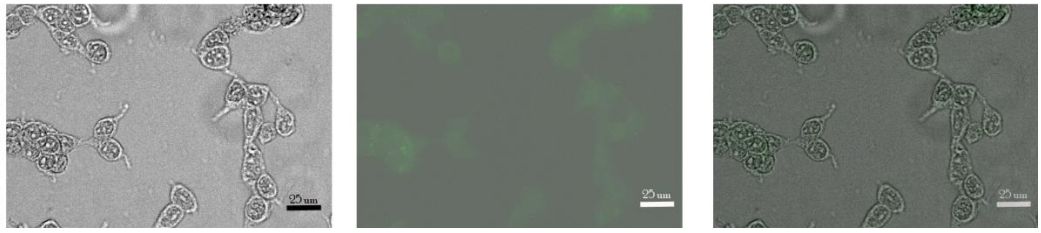

(a) (b) (c)

Figure 4.18 293T cells incubated for 30 min with cubosomes containing **L13** ligand 0.035 µM.(a) Bright field; (b) Green field; (c) merge image of bright and green field.

The cytotoxic effect of the cubosome formulation loaded with **L13** was studied with 293T cells and compared with an analogous experiment conducted with empty cubosomes. The cells were incubated with different quantities of cubosomes for 24 h and stained with 0.1 % Trypan Blue both manually and with LunaFL automated system. The IC_{50} of empty cubosomes measured was 246 µg mL^{-1} (to be compared with the IC50 value in HeLa cells of 165 µg mL^{-1}),[29] and addition of **L13** into the cubosomes do not change their cytotoxicity.

4.6 Transport studies

The transport properties of the compounds **L11**-**L16** were first evaluated in model phospholipid vesicles using a chloride-selective electrode. In these assays chloride-containing liposomes composed of POPC are suspended in an isotonic solution and the studied compounds are added as an aliquot of DMSO solution (see paragraph 4.8 for details). The experiments are repeated at least in triplicate using different batches of vesicles and the results obtained using different concentrations of the compound are analysed employing the Hill equation. As input, the chloride efflux observed after 300 s of the experiment is used. The concentration of compound needed to release 50% of the encapsulated chloride corresponds to EC_{50}. The lower the value of this parameter, the more efficient the compound is (Table 4.6). Chloride/nitrate and chloride/bicarbonate exchanges were studied (Figures 4.20-4.21), the EC_{50} values for the latter being, in most of the cases, between one and two orders of magnitude higher than those obtained for the former. This is the commonly observed trend and it is in line with the Gibbs free energy of hydration of both anions (ΔG_{hyd} = -335 and -300 kJ·mol^{-1} for bicarbonate and nitrate, respectively);[36] nitrate is more lipophilic than bicarbonate and, consequently, easier to extract into the membrane.

Table 4.6 Transport activities expressed as EC_{50} (nM) and Hill parameter for compounds **(L11-L16)**.

Receptor	EC_{50} (nM) NO_3^-/Cl^-	EC_{50} (%) NO_3^-/Cl^-	Hill parameter n NO_3^-/Cl^-	EC_{50} (nM) HCO_3^-/Cl^-	EC_{50} (%) HCO_3^-/Cl^-	Hill parameter. n HCO_3^-/Cl^-	Log P
L11	-*1	-*1	-*1	-*1	-*1	-*1	4.82
L12	60	0.12	0.68±0.03	1492	2.98	0.67±0.03	2.84
L13	-*1	-*1	-*1	-*1	-*1	-*1	2.98
L14	-*1	-*1	-*1	-*1	-*1	-*1	4.41
L15	-*1	-*1	-*1	-*1	-*1	-*1	2.61
L16	-*1	-*1	-*1	-*1	-*1	-*1	4.35

***1**: No significant chloride efflux was detected with compound added up to 5%.

The data reported in Table 4.6 show that compounds **L11** and **L13-L16** are not active as anion carriers. This result is in agreement with their scarce ability to bind chloride in solution. Particularly, chloride transport assays demonstrates that only **L12** is active as anion transporter, as suggested by the low value of the EC50 for the chloride/nitrate antiport assay. This results, instead, seems to be in agreement with the strong affinity of **L12** towards chloride already discussed in the previous paragraphs.

However, even though a good activity for **L12** was revealed, we did not detect the saturation of chloride efflux. Indeed, as shown in Figure 4.20, the 82% of the chloride efflux has been promoted by the carrier at 1% mol respect to the POPC. This result could be explained considering two different aspects: firstly, the strong affinity towards chloride of **L12** that could affect the multiple equilibria between the different species within the double layer of the phospholipic membrane during the transport process. Moreover, another aspect that could affect the transport process is the lipophilicity of the carrier. The different lipophilicity degree of the free/complexed carrier can influence the double layer crossing pathway, thus decreasing the activity of the transporter. In order to support the chloride-selective electrode transport

studies, emission spectroscopy exeperiments were conducted.

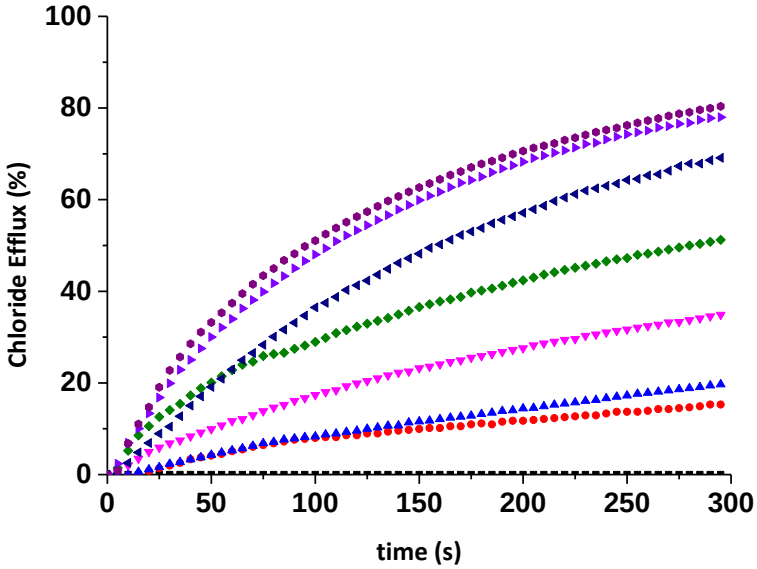

Figure 4.19 Chloride efflux promoted by **L12** at different concentrations (DMSO black; 0.05 µM, red; 0.1 µM, light blue; 0.25 µM, magenta; 0.5 µM, green; 2 µM, blue; 3.5 µM, violet; 5 µM, fuchsia) in unilamellar POPC vesicles. Vesicles loaded with 489 mM NaCl were buffered at pH 7.2 with 5 mM phosphate and dispersed in 489 mM $NaNO_3$ buffered at pH 7.2. Each trace represents the average of at least three trials.

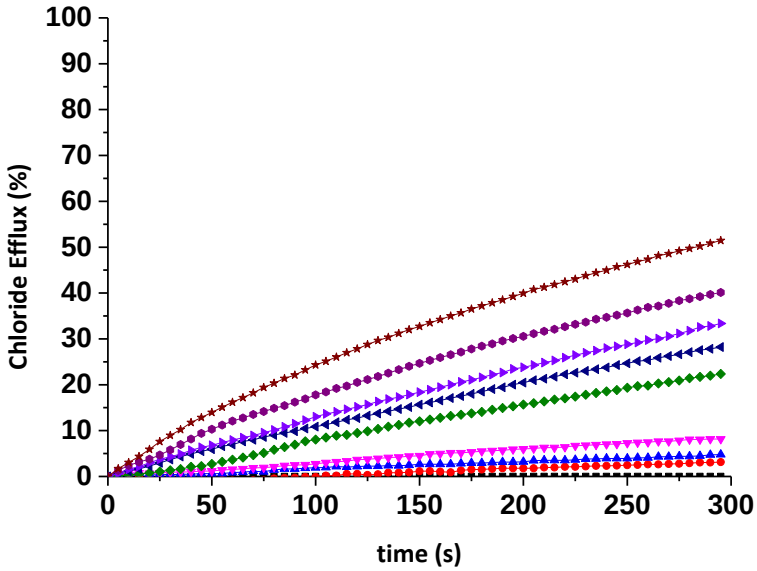

Figure 4.20 Chloride efflux promoted by **L12** at different concentrations (DMSO black; 0.1 µM red; 0.25 µM, light blue; 0.5 µM, magenta; 2 µM, green; 3.5 µM blue; 5 µM,violet;10 µM, fuchsia; 15 µM, bordeaux) in unilamellar POPC vesicles. Vesicles, which contained NaCl (451 mM NaCl and 20 mM phosphate buffer, pH 7.2), were immersed in Na_2SO_4 (150 mM Na_2SO_4, 40 mM HCO_3^- and 20 mM phosphate buffer, pH 7.2). Each trace represents an average of at least three different experiments.

To confirm the lack of detergent effect exerted by **L12**, the well-established carboxyfluorescein-based assay was performed. In this experiment sodium chloride and carboxyfluorescein-loaded liposomes are suspended in an isotonic sodium sulfate aqueous solution. After one minute the corresponding carrier is added to the suspension and the emission changes monitored for five minutes. At the end of the experiment, a detergent is added to lyse the vesicles and release the entrapped carboxyfluorescein (see paragraph 4.8 for further details). Carboxyfluorescein is encapsulated at self-quenching concentrations and its release is signaled by an

increase of the fluorescence as a result of the dilution of the dye. The results showed almost no fluorescence changes upon addition of compounds until the surfactant is added, thus ruling out the formation of large non-selective pores in the lipid membrane (Figure 4.22).

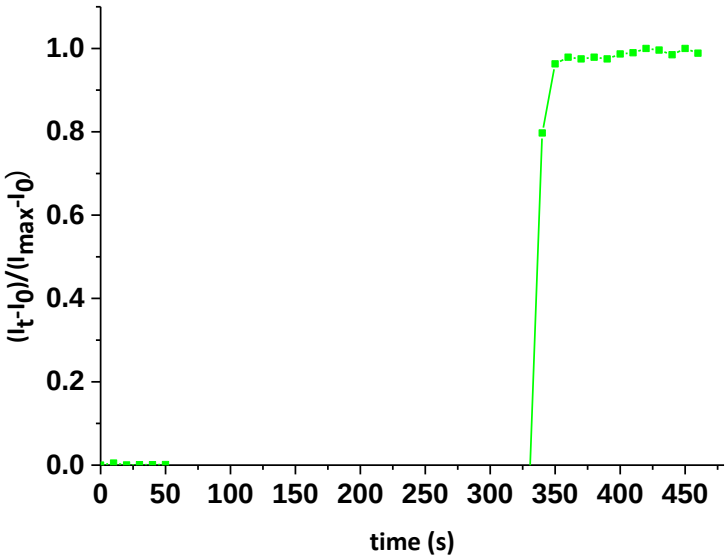

Figure 4.21 Carboxyfluorescein leakage upon addition of **L12** at 1% mol to POPC vesicles, 0.05 mM.

Finally, pH gradient discharge mediated by these compounds was evaluated using pH sensitive dye pyranine (HPTS). Ionophoric activity correlates with the ability of anion transporters to facilitate the balance of the internal pH of vesicles upon imposing a pH gradient with the external solution. First of all, a calibration curve matching I_{460}/I_{403}, (corresponding to the excitation wavelengths of the probe's deprotonated and protonated forms, respectively) of an HPTS aqueous solution and the pH was built (see paragraph 4.8). In this way, the emission values obtained from the HPTS assay can be converted into pH values. In order to perform the experiments, chloride- and HPTS-containing liposomes composed of a 7:3 POPC:cholesterol mixture are

suspended in an isotonic sodium nitrate solution (see SI for details). At t = 30 s an aliquot of a sodium hydroxide aqueous solution is added, followed by the addition, at t = 60 s, of an aliquot of the corresponding carrier in DMSO. The graphical representations are shown in Figure 4.24

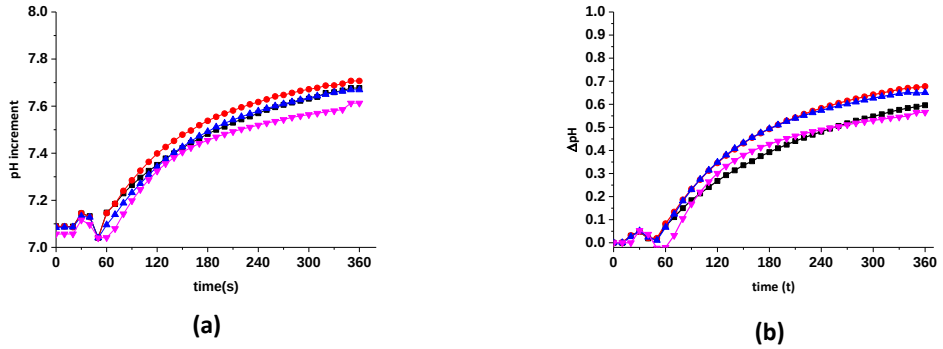

Figure 4.22 (a) Variation of the pH upon addition of **L12** at different concentration(0.5 µM black,; 1 µM, red; 2 µM, light blue; 5 µM, magenta) to POPC:Cholesterol 7:3 vesicles, 0.5 mM; (b) normalised pH variation upon addition of **L12** at different concentration(0.5 µM black,; 1 µM, red; 2 µM, light blue; 5 µM, magenta) to POPC:Cholesterol 7:3 vesicles, 0.5 mM.

As shown in Figure 4.22, a certain pH dependence of the transport was observed. Interestingly, we observed an higher pH dependence at low concentration of the carrier, wheares the higher the concentration of the carrier the smaller the pH dependence of the transport process, suggesting different transport mechanisms involved, depending by the concentration of the carrier and by the different condition of the system.

4.7 Conclusions

In conclusion, a new family of symmetric squaramides (**L11-L16**) were synthesised and their anion binding properties were studied both in solution and in the solid state. The results demonstrate that receptor **L12** exhibits excellent anion binding properties also in aqueous media. Transport studies showed that **L12** is able to mediate chloride efflux through phospholipidic membranes with a low EC_{50} value. The presence of fluorescent substituents on the receptors allow us also to test their properties as cell imaging agents in the case of **L11** and **L13** both in cancer and non-cancer cells.

4.8 Experimental part

All reactions were performed in oven-dried glassware under a slight positive pressure of nitrogen. ^{1}H-NMR (300 MHz) and ^{13}C NMR (75 MHz, 125MHz) spectra were determined on a 300 MHz Bruker. Chemical shifts for ^{1}H NMR are reported in parts per million (ppm), calibrated to the residual solvent peak set, with coupling constants reported in Hertz (Hz). The following abbreviations are used for spin multiplicity: s = singlet, d = doublet, t = triplet, m = multiplet . Chemical shifts for 13C NMR are reported in ppm, relative to the central line of a septet at δ = 39.52 ppm for deuteriodimethylsulfoxide. Infrared (IR) spectra were recorded on a NICOLET 5700 FT-IR spectrophotometer and reported in wavenumbers (cm^{-1}). Microanalytical data were obtained using a Fisons EA CHNS-O instrument (T = 1000 °C). Fluorescence spectra were recorded on a Cary Eclypse spectrofluorimeter. All solvents and starting materials were purchased from commercial sources where available. Proton NMR titrations were performed by adding aliquots of the putative anionic guest (as the TBA salt, 0.075 M) in a solution of the receptor (0.005M) in DMSO-d_6/0.5% water

4.8.1 Synthesis

General procedure for squaramides synthesis A(**L11**, **L12**, **L14**, **L15**, **L16**)

To a stirred solution of 3, 4-diethoxycyclobut-3-ene-1, 2-dione (1.0 equiv) and zinc trifluoromethanesulfonate (20 mol %) in toluene/DMF (19:1 v/v, 4 mL) the amine (2.1 equiv) was added. The solution was heated to 100°C and stirred for 12 h. When the solution was cooled to room temperature, a precipitate was observed and isolated by filtration. The solid was further washed with methanol (3x5 mL), and dried under reduced pressure to remove the residual methanol obtaining the product as crude solid.

General procedure for squaramides synthesis B (**L13**)

To a stirred solution of 3, 4-diethoxycyclobut-3-ene-1, 2-dione (1.2 equiv) and zinc trifluoromethanesulfonate (20 mol %) in methanol (20 mL) at room temperature the amine (2.0 equiv) was added. The solution was stirred for 1 h at room temperature and after that time a precipitate was formed, which was isolated by filtration and washed several times with an excess of methanol. The solid was dried under reduced pressure to remove the residual ethanol yielding the product as crude solid.

3,4-bis(naphthalen-1-ylamino)cyclobut-3-ene-1,2-dione (L11)

Yield 57% M.p.: 170 °C; ^{1}H NMR (600 MHz, DMSO-d_6, 298 K) δH: 7.50 (m, Ar-H, 2H), 7.62 (t, J = 6 Hz Ar-H, 1H), 7.70 (t, J = 6 Hz, Ar-H, 1 H), 7.75 (d, J = 6 Hz, Ar-H, 1 H), 8.01 (d, J = 6 Hz, Ar-H, 1 H), 8.27 (d, J = 6 Hz, Ar-H, 1 H), 10.21 (s, N-H, 1 H).^{13}C NMR (100 MHz, DMSO-d_6, 298 K) δ_{ArC}: 119.14, 122.56, 125.08, 126.11, 126.39, 126.82, 126.92, 128.89, 167.54 $\delta_{C=O}$: 181.24 IR: 3400 cm^{-1} (stretching N-H), 1780 cm^{-1} (stretching C=O)

3,4-bis((1H-indol-7-yl)amino)cyclobut-3-ene-1,2-dione (L12)

Yield 50% M.p.: > 250 °C; ^{1}H NMR (500 MHz, DMSO-d_6) δ 10.96 (s, 1H), 9.54 (s, 1H), 7.40 (t, J = 2.6 Hz, 1H), 7.36 (d, J = 7.8 Hz, 1H), 7.04 (d, J = 7.4 Hz, 1H), 6.97 (t, J = 7.7 Hz, 1H), 6.51 – 6.47 (m, 1H) ^{13}C NMR (126 MHz, DMSO-d_6) δ 183.5, 166.4, 129.2, 128.5, 125.6, 122.8, 119.1, 116.8, 113.7, 101.9, 39.5, 36.7. IR: 3400 cm^{-1} (stretching N-H), 1780 cm^{-1} (stretching C=O).

3,4-bis(quinolin-8-ylamino)cyclobut-3-ene-1,2-dione (L13)

Yield 90% M.p.: > 250 °C; ^{1}H NMR (600 MHz, DMSO-d_6, 298 K) δH: 7.66 (t, J = 6 Hz, Ar-H, 1H), 7.70 (d, J = 6 Hz, Ar-H, 1H), 7.75 (d, J = 6 Hz, Ar-H, 1H), 7.76 (d, J = 6 Hz, Ar-H, 1H), 8.11 (d, J = 6 Hz, Ar-H, 1 H), 8.46 (d J = 6 Hz, Ar-H, 1 H), 9.05 (d, J = 6 Hz, Ar-H, 1 H), 11.46 (s, N-H, 1 H).^{13}C NMR (100 MHz, DMSO-d_6, 298 K) 119.05, 122.68, 123.27, 127.16, 128.89, 135.13, 137.13, 139.67, 149.70, 167.43 δ_{ArC}: $\delta_{C=O}$: 183.56 IR: 3400 cm^{-1} (stretching N-H), 1780 cm^{-1} (stretching C=O).

5,5'-((3,4-dioxocyclobut-1-ene-1,2-diyl)bis(azanediyl))bis(anthracene-9,10(4aH,9aH)-dione) (L14)

Yield: 70%, M.p.:> 250°C, ^{1}H-NMR (300 MHz, DMSO-d_6, 298 K): δH: 7.69-7.84(m,2H), 7.86-8.00 (m,2H), 8.18 (d, J=3 Hz, 1H), 8.28 (d, J=3Hz, 1H), 8.91 (d, J=3Hz, 1 H), 11.92 (s, 1H, NH). ^{13}C-NMR (75 MHz, DMSO-d_6, 298 K): 117.23, 117.80, 119.52, 125.75, 126.50, 126.91, 128.74, 134.33, 134.80, 135.52, 153.59, 154.30, 167.46, 167.75. IR: 3400 cm^{-1} (stretching N-H), 1780 cm^{-1} (stretching C=O).

***N*,N'-(((3,4-dioxocyclobut-1-ene-1,2-diyl)bis(azanediyl))bis(ethane-2,1 diyl))bis(5(dimethylamino)naphthalene-1-sulfonamide) (L15)**

Yield: 51%, M.p.: 226°C ^{1}H-NMR (300 MHz, DMSO-d6, 298 K): δH: 2.81(s,2H), 2.88-2.98(m,2H), 7.23 (d, J= 9 Hz, 1H), 7.39 (s, br,1H, NH), 7.52-7.64 (m,2H), 8.06(s, br,1H, NH), 8.09(d, J=6Hz,1H), 8.25(d, J=6Hz,1H), 8.45(d, J=6Hz,1H) ^{13}C-NMR (75 MHz, DMSO-d6, 298 K): δC: 43.03, 45.09, 47.47, 115.22, 119.08, 123.61, 127.91, 128.38, 129.05, 129.50, 135.56, 151.23, 167.73, 182.42. IR: 3400 cm^{-1} (stretching N-H), 1780 cm^{-1} (stretching C=O).

3,4-bis(pyren-1-ylamino)cyclobut-3-ene-1,2-dione (L16)

Yield: 61%, M.p.: 160°C ^{1}H-NMR (300 MHz, DMSO-d6, 298 K): δH: 7.90-8.40 (m, 13H), 8.47 (d, J = 9, 2H), 10.69 (s, br , 1H), ^{13}C-NMR (75 MHz, DMSO-d6, 298 K): δC: 115.26, 121.20, 126.25, 127.23, 131.78, 137.18, 156.08, 184.02 IR: 3400 cm^{-1} (stretching N-H), 1780 cm^{-1} (stretching C=O).

4.8.2 ^{1}H-NMR titrations

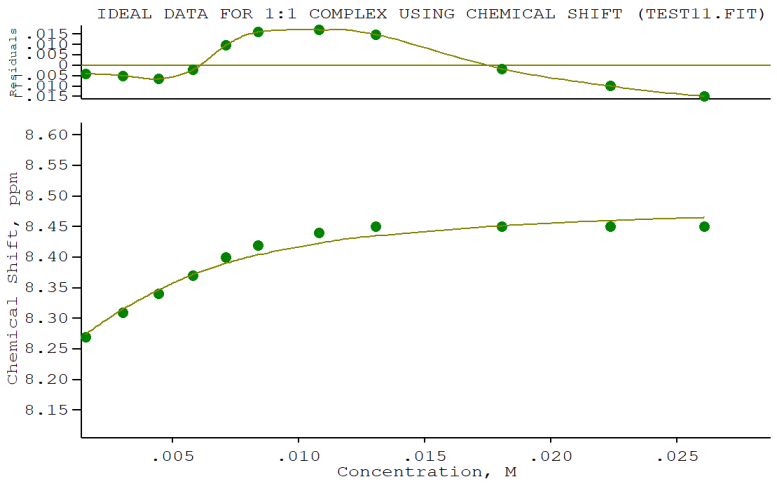

IDEAL DATA: K1 = 63.091; DELTA M = 20.0; DELTA ML = 120.0

File prepared by M. J. Hynes, October 22 2000

Equilibrium constants are floating point numbers

NO. A PARAMETER DELTA ERROR CONDITION DESCRIPTION

1 1 4.05719E+02 2.000E-01 5.244E+01 1.945E+00 K1

2 1 8.22332E+00 2.000E-01 1.248E-02 1.957E+00 SHIFT Sn

3 1 8.49144E+00 1.000E+00 7.998E-03 2.017E+00 SHIFT Sn(L)

0RMS ERROR = 1.26E-02 MAX ERROR = 1.69E-02 AT OBS.NO. 7

RESIDUALS SQUARED = 1.26E-03

RFACTOR = 0.1277 PERCENT

Figure 4.23 ^{1}H-NMR titration of **L11** with TBAAcO in DMSO-d_6.

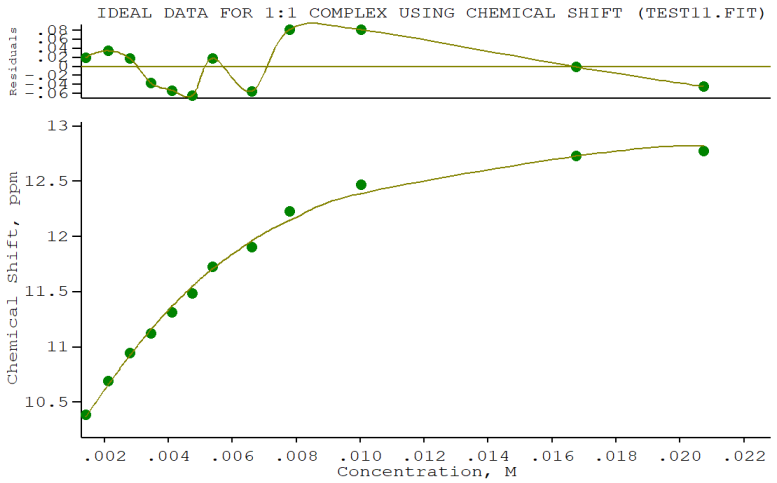

Calculations by WinEQNMR2 Version 2.00 by Michael J. Hynes

Program run at 12:02:30 on 03/29/2018

IDEAL DATA FOR 1:1 COMPLEX USING CHEMICAL SHIFT (TEST11.FIT)

Reaction: Sn + L = Sn(L)

FILE: TEST11.FIT (Measured shift is on 119Sn)

IDEAL DATA: K1 = 63.091; DELTA M = 20.0; DELTA ML = 120.0

File prepared by M. J. Hynes, October 22 2000

Equilibrium constants are floating point numbers

NO.	A	PARAMETER	DELTA	ERROR	CONDITION	DESCRIPTION
1	1	6.07003E+02	2.000E-01	8.789E+01	1.433E+01	K1
2	1	9.69189E+00	2.000E-01	6.076E-02	3.242E+00	SHIFT Sn
3	1	1.31399E+01	1.000E+00	8.160E-02	9.306E+00	SHIFT Sn(L)

0RMS ERROR = 5.65E-02 MAX ERROR = 8.20E-02 AT OBS.NO. 10

RESIDUALS SQUARED = 2.88E-02

RFACTOR = 0.4195 PERCENT

Figure 4.24 ^{1}H-NMR titration of **L11** with TBABzO in DMSO-d_6.

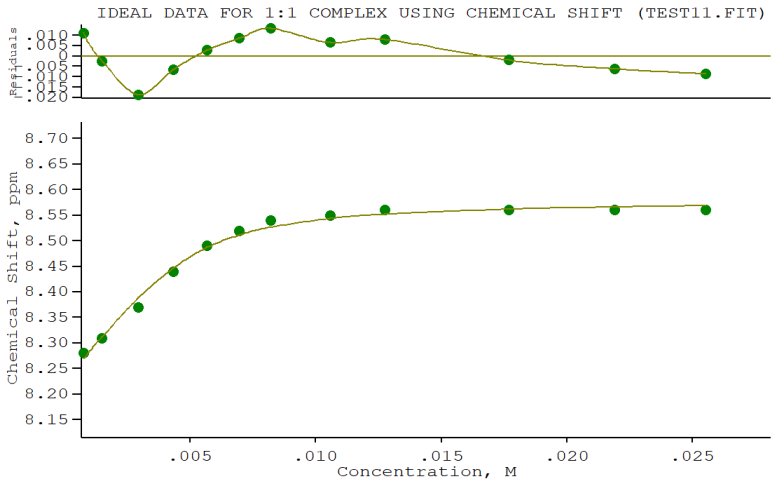

Calculations by WinEQNMR2 Version 2.00 by Michael J. Hynes

Program run at 15:07:15 on 09/05/2018

IDEAL DATA FOR 1:1 COMPLEX USING CHEMICAL SHIFT (TEST11.FIT)

Reaction: Sn + L = Sn(L)

FILE: TEST11.FIT (Measured shift is on 119Sn)

IDEAL DATA: K1 = 63.091; DELTA M = 20.0; DELTA ML = 120.0

File prepared by M. J. Hynes, October 22 2000

Equilibrium constants are floating point numbers

NO.	A	PARAMETER	DELTA	ERROR	CONDITION	DESCRIPTION
1	1	1.43378E+03	2.000E-01	6.509E+01	1.021E+00	K1
2	1	8.22256E+00	2.000E-01	8.528E-03	1.241E+00	SHIFT Sn
3	1	8.57936E+00	1.000E+00	4.376E-03	1.219E+00	SHIFT Sn(L)

0RMS ERROR = 1.05E-02 MAX ERROR = 1.86E-02 AT OBS.NO. 3

RESIDUALS SQUARED = 9.94E-04

RFACTOR = 0.1073 PERCENT

Figure 4.25 ^{1}H-NMR titration of **L11** with $TBAH_2PO_4$ in DMSO-d_6.

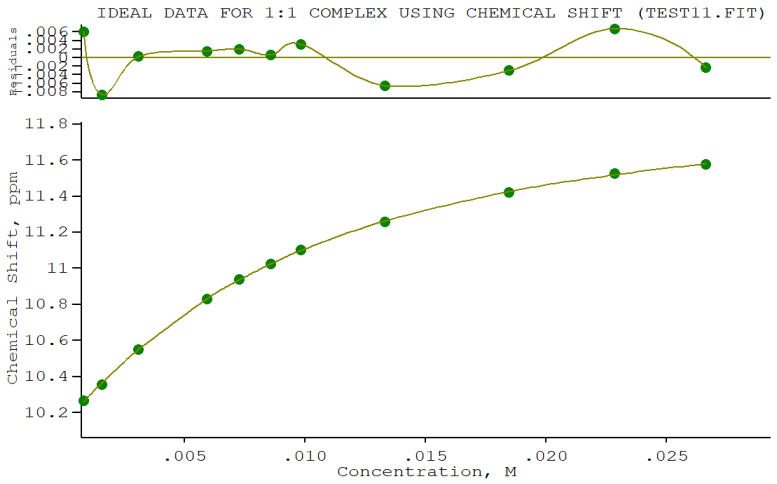

Calculations by WinEQNMR2 Version 2.00 by Michael J. Hynes

Program run at 14:15:33 on 09/18/2018

IDEAL DATA FOR 1:1 COMPLEX USING CHEMICAL SHIFT (TEST11.FIT)

Reaction: Sn + L = Sn(L)

FILE: TEST11.FIT (Measured shift is on 119Sn)

IDEAL DATA: K1 = 63.091; DELTA M = 20.0; DELTA ML = 120.0

File prepared by M. J. Hynes, October 22 2000

Equilibrium constants are floating point numbers

NO. A PARAMETER DELTA ERROR CONDITION DESCRIPTION

1 1 1.56135E+02 2.000E-01 3.970E+00 2.367E+01 K1

2 1 1.01442E+01 2.000E-01 4.692E-03 2.932E+00 SHIFT Sn

3 1 1.19915E+01 1.000E+00 1.325E-02 1.746E+01 SHIFT Sn(L)

0RMS ERROR = 5.38E-03 MAX ERROR = 8.66E-03 AT OBS.NO. 2

RESIDUALS SQUARED = 2.32E-04

RFACTOR = 0.0418 PERCENT

Figure 4.26 ^{1}H-NMR titration of **L11** with TBACl in DMSO-d_6.

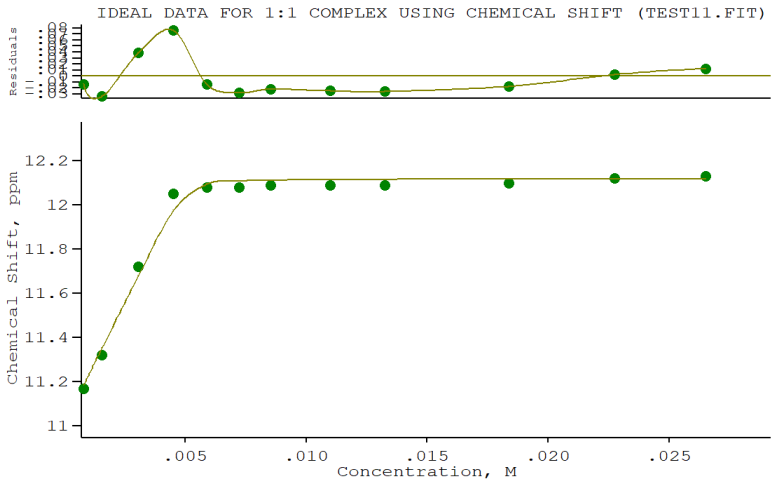

Calculations by WinEQNMR2 Version 2.00 by Michael J. Hynes

Program run at 12:56:01 on 03/29/2018

IDEAL DATA FOR 1:1 COMPLEX USING CHEMICAL SHIFT (TEST11.FIT)

Reaction: Sn + L = Sn(L)

FILE: TEST11.FIT (Measured shift is on 119Sn)

IDEAL DATA: K1 = 63.091; DELTA M = 20.0; DELTA ML = 120.0

File prepared by M. J. Hynes, October 22 2000

Equilibrium constants are floating point numbers

NO.	A	PARAMETER	DELTA	ERROR	CONDITION	DESCRIPTION
1	1	4.30449E+04	2.000E-01	8.976E+03	1.037E+00	K1
2	1	1.10110E+01	2.000E-01	3.196E-02	1.048E+00	SHIFT Sn
3	1	1.21180E+01	1.000E+00	1.254E-02	1.085E+00	SHIFT Sn(L)

0RMS ERROR = 3.64E-02 MAX ERROR = 7.62E-02 AT OBS.NO. 4

RESIDUALS SQUARED = 1.19E-02

RFACTOR = 0.2644 PERCENT

Figure 4.27 ^{1}H-NMR titration of **L12** with TBAAcO in DMSO-d_6.

Calculations by WinEQNMR2 Version 2.00 by Michael J. Hynes

Program run at 12:12:17 on 03/29/2018

IDEAL DATA FOR 1:1 COMPLEX USING CHEMICAL SHIFT (TEST11.FIT)

Reaction: Sn + L = Sn(L)

FILE: TEST11.FIT (Measured shift is on 119Sn)

IDEAL DATA: K1 = 63.091; DELTA M = 20.0; DELTA ML = 120.0

File prepared by M. J. Hynes, October 22 2000

Equilibrium constants are floating point numbers

NO.	A	PARAMETER	DELTA	ERROR	CONDITION	DESCRIPTION
1	1	1.07909E+04	2.000E-01	1.692E+03	2.766E+00	K1
2	1	9.98073E+00	2.000E-01	1.463E-02	1.070E+00	SHIFT Sn
3	1	1.20346E+01	1.000E+00	1.038E-02	2.801E+00	SHIFT Sn(L)

0RMS ERROR = 1.48E-02 MAX ERROR = 1.83E-02 AT OBS.NO. 3

RESIDUALS SQUARED = 1.09E-03

RFACTOR = 0.1005 PERCENT

Figure 4.28 ^{1}H-NMR titration of **L12** with $TBAH_2PO_4$ in DMSO-d_6.

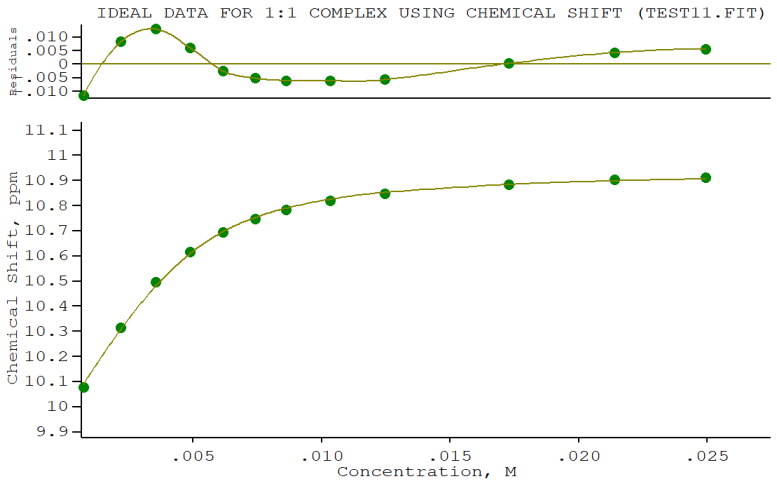

Calculations by WinEQNMR2 Version 2.00 by Michael J. Hynes

Program run at 12:18:19 on 03/29/2018

IDEAL DATA FOR 1:1 COMPLEX USING CHEMICAL SHIFT (TEST11.FIT)

Reaction: Sn + L = Sn(L)

FILE: TEST11.FIT (Measured shift is on 119Sn)

IDEAL DATA: K1 = 63.091; DELTA M = 20.0; DELTA ML = 120.0

File prepared by M. J. Hynes, October 22 2000

Equilibrium constants are floating point numbers

NO.	A	PARAMETER	DELTA	ERROR	CONDITION	DESCRIPTION
1	1	1.19908E+03	2.000E-01	7.447E+01	6.073E+00	K1
2	1	9.96824E+00	2.000E-01	7.988E-03	1.637E+00	SHIFT Sn
3	1	1.09443E+01	1.000E+00	6.795E-03	4.938E+00	SHIFT Sn(L)

0RMS ERROR = 8.12E-03 MAX ERROR = 1.29E-02 AT OBS.NO. 3

RESIDUALS SQUARED = 5.94E-04

RFACTOR = 0.0659 PERCENT

Figure 4.29 ^{1}H-NMR titration of **L12** with TBACl in DMSO-d_6

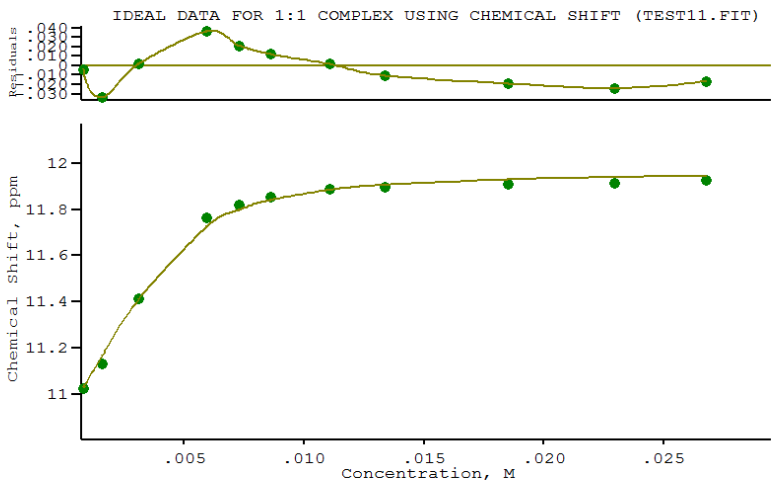

Calculations by WinEQNMR2 Version 2.00 by Michael J. Hynes

Program run at 17:19:00 on 11/25/2018

IDEAL DATA FOR 1:1 COMPLEX USING CHEMICAL SHIFT (TEST11.FIT)

Reaction: Sn + L = Sn(L)

FILE: TEST11.FIT (Measured shift is on 119Sn)

IDEAL DATA: K1 = 63.091; DELTA M = 20.0; DELTA ML = 120.0

File prepared by M. J. Hynes, October 22 2000

Equilibrium constants are floating point numbers

NO. A PARAMETER DELTA ERROR CONDITION DESCRIPTION

1 1 1.87604E+03 2.000E-01 1.552E+02 1.155E+00 K1

2 1 1.08812E+01 2.000E-01 1.949E-02 1.144E+00 SHIFT Sn

3 1 1.19695E+01 1.000E+00 1.002E-02 1.271E+00 SHIFT Sn(L)

0RMS ERROR = 2.35E-02 MAX ERROR = 3.66E-02 AT OBS.NO. 4

RESIDUALS SQUARED = 4.40E-03

RFACTOR = 0.1711 PERCENT

Figure 4.30 ^{1}H-NMR titration of **L12** with TBAAcO in DMSO-*d_6-10%*

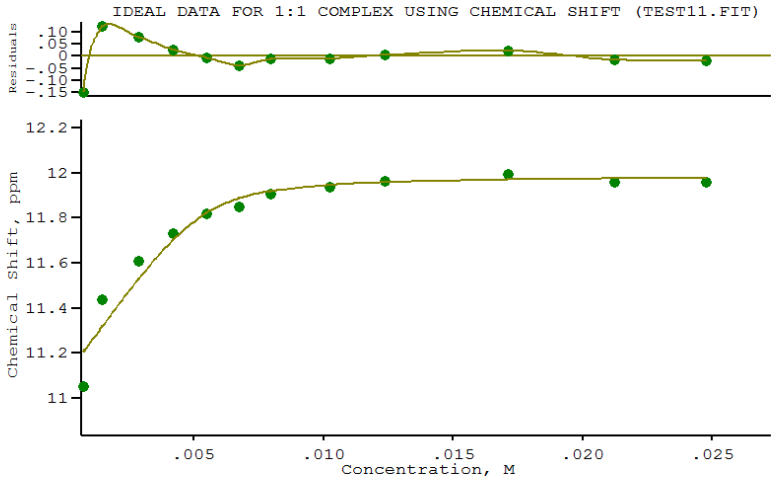

Calculations by WinEQNMR2 Version 2.00 by Michael J. Hynes

Program run at 17:35:41 on 11/25/2018

IDEAL DATA FOR 1:1 COMPLEX USING CHEMICAL SHIFT (TEST11.FIT)

Reaction: Sn + L = Sn(L)

FILE: TEST11.FIT (Measured shift is on 119Sn)

IDEAL DATA: K1 = 63.091; DELTA M = 20.0; DELTA ML = 120.0

File prepared by M. J. Hynes, October 22 2000

Equilibrium constants are floating point numbers

NO.	A	PARAMETER	DELTA	ERROR	CONDITION	DESCRIPTION
1	1	3.77034E+03	2.000E-01	5.929E+02	1.003E+00	K1
2	1	1.10874E+01	2.000E-01	5.836E-02	1.126E+00	SHIFT Sn
3	1	1.19895E+01	1.000E+00	2.741E-02	1.129E+00	SHIFT Sn(L)

0RMS ERROR = 7.22E-02 MAX ERROR = 1.51E-01 AT OBS.NO. 1

RESIDUALS SQUARED = 4.69E-02

RFACTOR = 0.5308 PERCENT

Figure 4.31 ^{1}H-NMR titration of **L12** with TBABzO in DMSO-*d_6-10%*

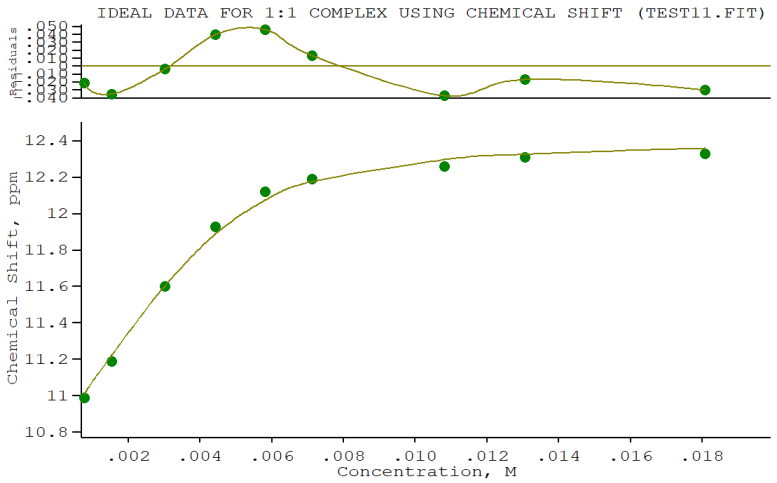

Calculations by WinEQNMR2 Version 2.00 by Michael J. Hynes

Program run at 15:04:12 on 11/14/2018

IDEAL DATA FOR 1:1 COMPLEX USING CHEMICAL SHIFT (TEST11.FIT)

Reaction: Sn + L = Sn(L)

FILE: TEST11.FIT (Measured shift is on 119Sn)

IDEAL DATA: K1 = 63.091; DELTA M = 20.0; DELTA ML = 120.0

File prepared by M. J. Hynes, October 22 2000

Equilibrium constants are floating point numbers

NO.	A	PARAMETER	DELTA	ERROR	CONDITION	DESCRIPTION
1	1	2.00464E+03	2.000E-01	2.429E+02	1.440E+00	K1
2	1	1.07838E+01	2.000E-01	3.168E-02	1.260E+00	SHIFT Sn
3	1	1.24177E+01	1.000E+00	2.087E-02	1.551E+00	SHIFT Sn(L)

0RMS ERROR = 3.68E-02 MAX ERROR = 4.65E-02 AT OBS.NO. 5

RESIDUALS SQUARED = 8.14E-03

RFACTOR = 0.2529 PERCENT

Figure 4.32 ^{1}H-NMR titration of **L12** with $TBAH_2PO_4$ in DMSO-*d_6-10%*

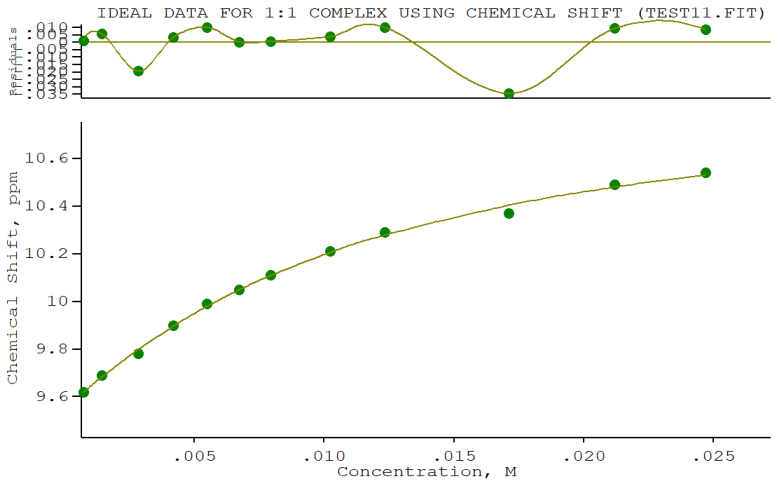

Calculations by WinEQNMR2 Version 2.00 by Michael J. Hynes

Program run at 15:18:04 on 11/14/2018

IDEAL DATA FOR 1:1 COMPLEX USING CHEMICAL SHIFT (TEST11.FIT)

Reaction: Sn + L = Sn(L)

FILE: TEST11.FIT (Measured shift is on 119Sn)

IDEAL DATA: K1 = 63.091; DELTA M = 20.0; DELTA ML = 120.0

File prepared by M. J. Hynes, October 22 2000

Equilibrium constants are floating point numbers

NO.	A	PARAMETER	DELTA	ERROR	CONDITION	DESCRIPTION
1	1	1.14466E+02	2.000E-01	1.208E+01	3.553E+01	K1
2	1	9.54732E+00	2.000E-01	1.278E-02	3.724E+00	SHIFT Sn
3	1	1.09365E+01	1.000E+00	4.894E-02	2.549E+01	SHIFT Sn(L)

0RMS ERROR = 1.48E-02 MAX ERROR = 3.42E-02 AT OBS.NO. 10

RESIDUALS SQUARED = 1.98E-03

RFACTOR = 0.1272 PERCENT

Figure 4.33 ^{1}H-NMR titration of **L12** with TBACl in DMSO-*d*$_6$-*10%*

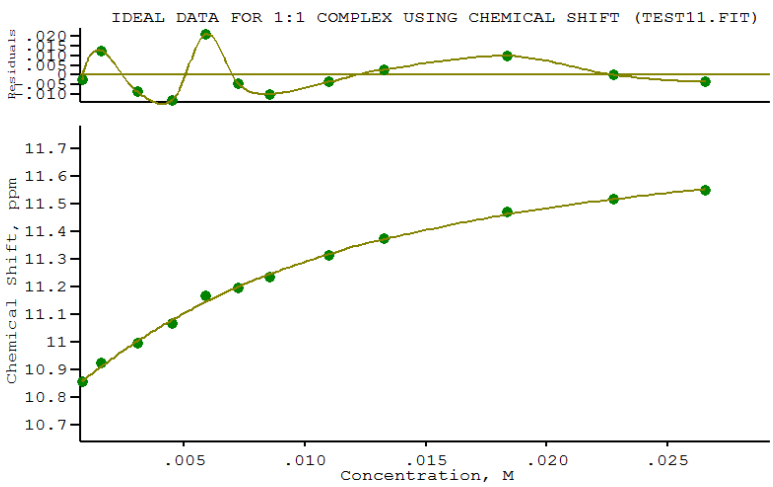

Calculations by WinEQNMR2 Version 2.00 by Michael J. Hynes

Program run at 16:19:35 on 12/01/2018

IDEAL DATA FOR 1:1 COMPLEX USING CHEMICAL SHIFT (TEST11.FIT)

Reaction: Sn + L = Sn(L)

FILE: TEST11.FIT (Measured shift is on 119Sn)

IDEAL DATA: K1 = 63.091; DELTA M = 20.0; DELTA ML = 120.0

File prepared by M. J. Hynes, October 22 2000

Equilibrium constants are floating point numbers

NO.	A	PARAMETER	DELTA	ERROR	CONDITION	DESCRIPTION
1	1	1.21409E+02	2.000E-01	1.254E+01	3.186E+01	K1
2	1	1.07989E+01	2.000E-01	9.802E-03	3.624E+00	SHIFT Sn
3	1	1.18214E+01	1.000E+00	3.290E-02	2.265E+01	SHIFT Sn(L)

0RMS ERROR = 1.12E-02 MAX ERROR = 2.14E-02 AT OBS.NO. 5

RESIDUALS SQUARED = 1.12E-03

RFACTOR = 0.0861 PERCENT

Figure 4.34 ^{1}H-NMR titration of **L12** with TBAAcO in DMSO-*d_6-25%*

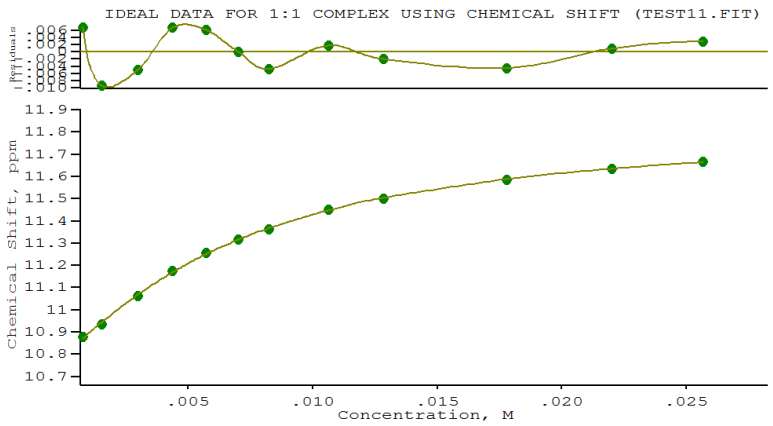

Calculations by WinEQNMR2 Version 2.00 by Michael J. Hynes

Program run at 16:02:57 on 12/01/2018

IDEAL DATA FOR 1:1 COMPLEX USING CHEMICAL SHIFT (TEST11.FIT)

Reaction: Sn + L = Sn(L)

FILE: TEST11.FIT (Measured shift is on 119Sn)

IDEAL DATA: K1 = 63.091; DELTA M = 20.0; DELTA ML = 120.0

File prepared by M. J. Hynes, October 22 2000

Equilibrium constants are floating point numbers

NO.	A	PARAMETER	DELTA	ERROR	CONDITION	DESCRIPTION
1	1	2.16967E+02	2.000E-01	8.930E+00	1.846E+01	K1
2	1	1.07896E+01	2.000E-01	5.137E-03	2.961E+00	SHIFT Sn
3	1	1.18499E+01	1.000E+00	1.081E-02	1.296E+01	SHIFT Sn(L)

0RMS ERROR = 5.75E-03 MAX ERROR = 9.25E-03 AT OBS.NO. 2

RESIDUALS SQUARED = 2.98E-04

RFACTOR = 0.0440 PERCENT

Figure 4.35 ^{1}H-NMR titration of **L12** with TBABzO in DMSO-*d*$_6$-*25%*

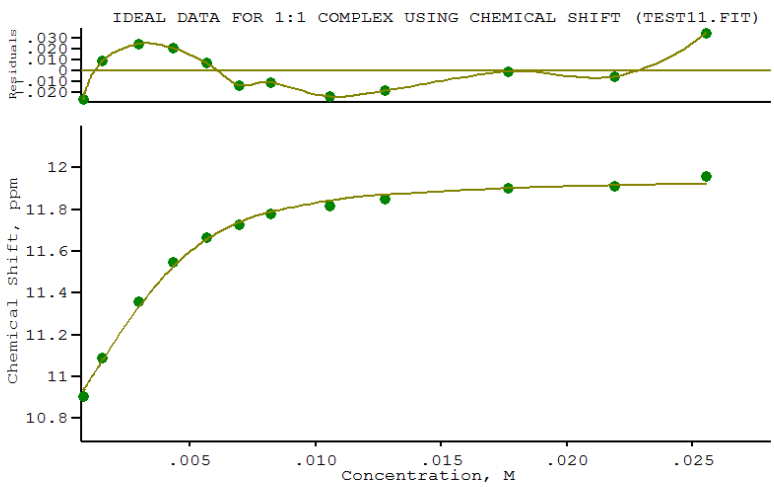

Calculations by WinEQNMR2 Version 2.00 by Michael J. Hynes

Program run at 01:37:14 on 12/01/2018

IDEAL DATA FOR 1:1 COMPLEX USING CHEMICAL SHIFT (TEST11.FIT)

Reaction: Sn + L = Sn(L)

FILE: TEST11.FIT (Measured shift is on 119Sn)

IDEAL DATA: K1 = 63.091; DELTA M = 20.0; DELTA ML = 120.0

File prepared by M. J. Hynes, October 22 2000

Equilibrium constants are floating point numbers

NO.	A	PARAMETER	DELTA	ERROR	CONDITION	DESCRIPTION
1	1	1.50193E+03	2.000E-01	2.100E+02	4.838E+00	K1
2	1	1.07783E+01	2.000E-01	1.936E-02	1.483E+00	SHIFT Sn
3	1	1.19581E+01	1.000E+00	1.641E-02	4.049E+00	SHIFT Sn(L)

0RMS ERROR = 2.17E-02 MAX ERROR = 3.45E-02 AT OBS.NO. 12

RESIDUALS SQUARED = 4.24E-03

RFACTOR = 0.1617 PERCENT

Figure 4.36 ^{1}H-NMR titration of **L12** with $TBAH_2PO_4$ in DMSO-*d_6-25%*

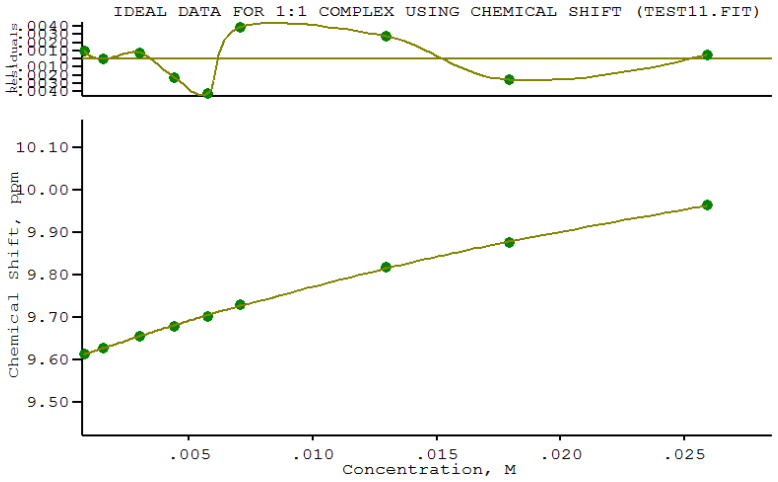

Calculations by WinEQNMR2 Version 2.00 by Michael J. Hynes

Program run at 14:37:32 on 12/04/2018

IDEAL DATA FOR 1:1 COMPLEX USING CHEMICAL SHIFT (TEST11.FIT)

Reaction: Sn + L = Sn(L)

FILE: TEST11.FIT (Measured shift is on 119Sn)

IDEAL DATA: K1 = 63.091; DELTA M = 20.0; DELTA ML = 120.0

File prepared by M. J. Hynes, October 22 2000

Equilibrium constants are floating point numbers

NO.	A	PARAMETER	DELTA	ERROR	CONDITION	DESCRIPTION
1	1	2.13260E+01	2.000E-01	2.559E+00	2.249E+02	K1
2	1	9.59623E+00	2.000E-01	2.459E-03	4.551E+00	SHIFT Sn
3	1	1.06753E+01	1.000E+00	8.228E-02	1.922E+02	SHIFT Sn(L)

0RMS ERROR = 3.02E-03 MAX ERROR = 4.20E-03 AT OBS.NO. 5

RESIDUALS SQUARED = 5.47E-05

RFACTOR = 0.0253 PERCENT

Figure 4.37 ^{1}H-NMR titration of **L12** with TBACl in DMSO-*d*$_6$-*25%*

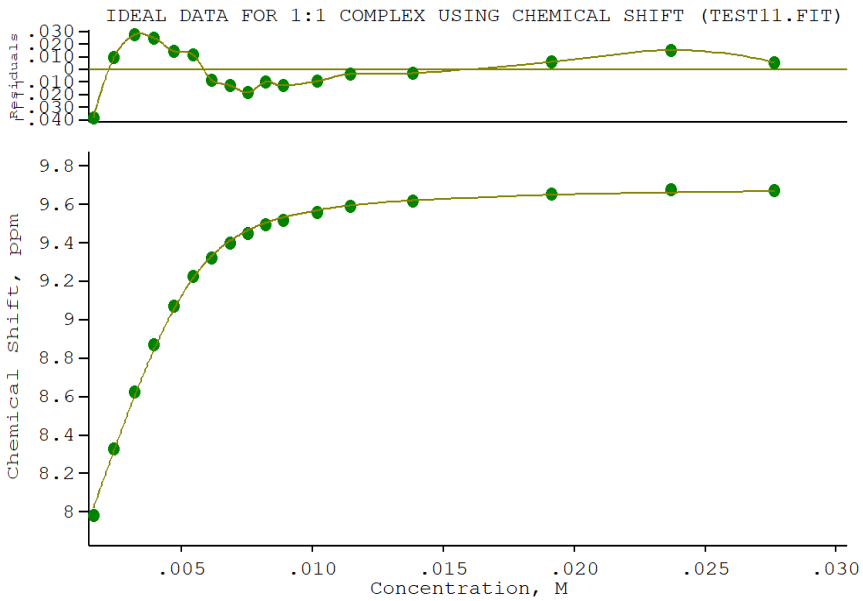

Calculations by WinEQNMR2 Version 2.00 by Michael J. Hynes

Program run at 14:14:15 on 15/05/2018

IDEAL DATA FOR 1:1 COMPLEX USING CHEMICAL SHIFT (TEST11.FIT)

Reaction: Sn + L = Sn(L)

FILE: TEST11.FIT (Measured shift is on 119Sn)

IDEAL DATA: K1 = 63.091; DELTA M = 20.0; DELTA ML = 120.0

File prepared by M. J. Hynes, October 22 2000

Equilibrium constants are floating point numbers

NO. A PARAMETER DELTA ERROR CONDITION DESCRIPTION

1 1 3.36792E+03 2.000E-01 2.285E+02 4.930E+00 K1

2 1 7.37246E+00 2.000E-01 1.884E-02 1.576E+00 SHIFT Sn

3 1 9.69787E+00 1.000E+00 1.058E-02 4.100E+00 SHIFT Sn(L)

Figure 4.38 ^{1}H-NMR titration of **L15** with TBAAcO in DMSO-*d_6-0.5%*

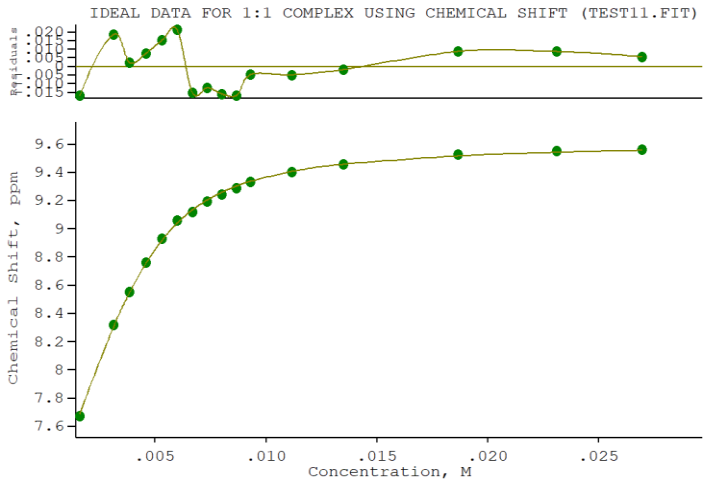

Calculations by WinEQNMR2 Version 2.00 by Michael J. Hynes

Program run at 14:05:39 on 31/05/2018

IDEAL DATA FOR 1:1 COMPLEX USING CHEMICAL SHIFT (TEST11.FIT)

Reaction: Sn + L = Sn(L)

FILE: TEST11.FIT (Measured shift is on 119Sn)

IDEAL DATA: K1 = 63.091; DELTA M = 20.0; DELTA ML = 120.0

File prepared by M. J. Hynes, October 22 2000

Equilibrium constants are floating point numbers

NO.	A	PARAMETER	DELTA	ERROR	CONDITION	DESCRIPTION
1	1	1.70364E+03	2.000E-01	6.717E+01	7.118E+00	K1
2	1	6.96300E+00	2.000E-01	1.832E-02	2.210E+00	SHIFT Sn
3	1	9.62439E+00	1.000E+00	9.678E-03	5.058E+00	SHIFT Sn(L)

Figure 4.39 ^{1}H-NMR titration of **L15** with TBABzO in DMSO-*d_6-0.5%*

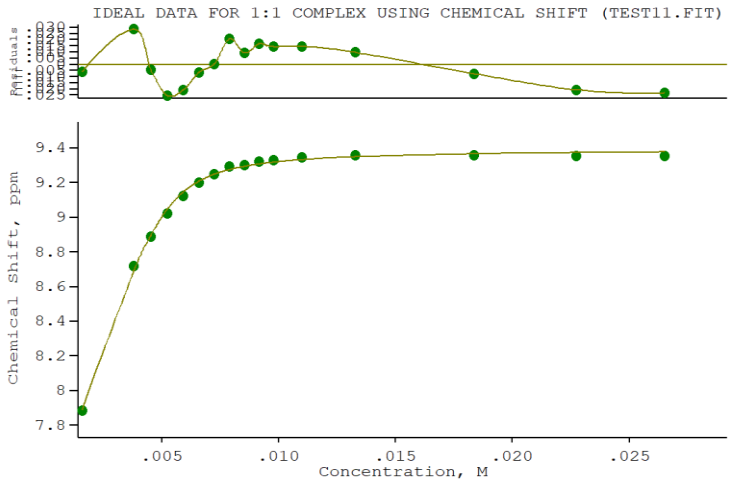

Calculations by WinEQNMR2 Version 2.00 by Michael J. Hynes

Program run at 15:23:42 on 12/06/2018

IDEAL DATA FOR 1:1 COMPLEX USING CHEMICAL SHIFT (TEST11.FIT)

Reaction: Sn + L = Sn(L)

FILE: TEST11.FIT (Measured shift is on 119Sn)

IDEAL DATA: K1 = 63.091; DELTA M = 20.0; DELTA ML = 120.0

File prepared by M. J. Hynes, October 22 2000

Equilibrium constants are floating point numbers

NO. A PARAMETER DELTA ERROR CONDITION DESCRIPTION

1 1 5.42826E+03 2.000E-01 4.852E+02 4.058E+00 K1

2 1 7.27820E+00 2.000E-01 2.488E-02 1.372E+00 SHIFT Sn

3 1 9.39448E+00 1.000E+00 9.623E-03 3.568E+00 SHIFT Sn(L)

Figure 4.40 ^{1}H-NMR titration of **L15** with $TBAH_2PO_4$ in DMSO-*d_6-0.5%*

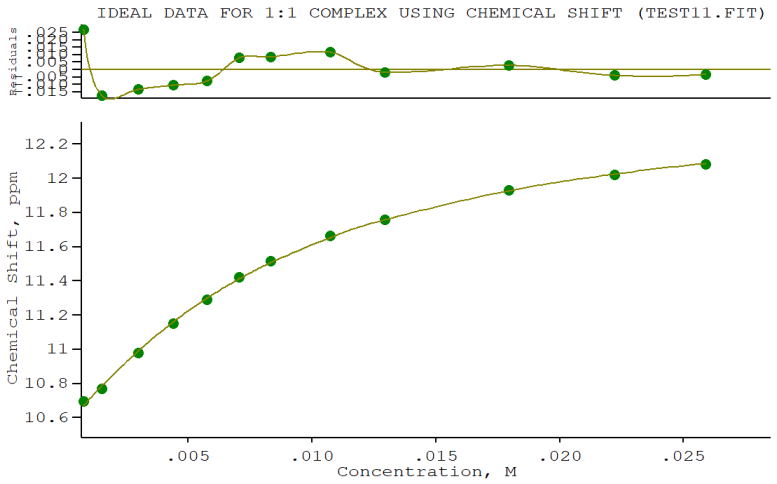

Calculations by WinEQNMR2 Version 2.00 by Michael J. Hynes

Program run at 15:59:15 on 01/31/2019

IDEAL DATA FOR 1:1 COMPLEX USING CHEMICAL SHIFT (TEST11.FIT)

Reaction: Sn + L = Sn(L)

FILE: TEST11.FIT (Measured shift is on 119Sn)

IDEAL DATA: K1 = 63.091; DELTA M = 20.0; DELTA ML = 120.0

File prepared by M. J. Hynes, October 22 2000

Equilibrium constants are floating point numbers

NO.	A	PARAMETER	DELTA	ERROR	CONDITION	DESCRIPTION
1	1	1.63663E+02	2.000E-01	9.369E+00	2.369E+01	K1
2	1	1.05394E+01	2.000E-01	1.217E-02	3.301E+00	SHIFT Sn
3	1	1.25168E+01	1.000E+00	3.164E-02	1.657E+01	SHIFT Sn(L)

0RMS ERROR = 1.37E-02 MAX ERROR = 2.69E-02 AT OBS.NO. 1

RESIDUALS SQUARED = 1.69E-03

RFACTOR = 0.1038 PERCENT

Figure 4.41 ^{1}H-NMR titration of **L16** with TBACl in DMSO-*d_6-0.5%*

4.8.3 Transport studies:

Preparation of 1-palmitoyl -2-oleoyl-sn-glycero-3-phosphocholine vesicles

A lipid film of 1-palmitoyl -2-oleoyl-sn-glycero-3-phosphocholine (POPC) was formed from a chloroform solution (20 mg/mL). The solvent was removed under reduced pressure and dried under vacuum for at least 2 hours. The lipid film was rehydrated by vortexing with an internal solution of NaCl 489 mM buffered at pH 7.2 with NaH_2PO_4 5 mM. The lipid suspension was then subjected to seven freeze-thaw cycles and allowed to age for 15 min at room temperature before extruding 27 times throwgh a 200 nm polycarbonate membrane. The resulting unilamellar vesicles were dialyzed against the external solution (two cycles of 40 min) to remove unencapsulated NaCl salts. The vesicles were then diluited to 10 mL with the external solution to obtain a stock solution of lipid.

Antiport Cl^-/NO_3^-

Sample for assay was prepared in a vial by diluting to 5 mL lipid stock solution with the external solution to give a solution of 0.5 mM of lipid. Chloride efflux was monitored using an ion selective electrode (Hach, ISE F-9655C) for chloride, calibrated against sodium chloride solutions of known concentration before starting the measurements. To initiate the experiment, at t= 60 s the carrier compound was added to the sample as DMSO solution and the chloride efflux was monitored during 6 min. At the end of the experiment, detergent was added to lyse the phospholipidic vesicles and detected the 100 % of the chloride efflux. Experiments were repeated in duplicate and all traces presented are the average of three trials.

Antiport Cl^-/HCO_3^-

Unilamellar POPC vesicles containing 451 mM NaCl solution buffered to 7.2 with 20 mM sodium dihydrogen phosphate salts, prepared as described in the Cl^-/NO_3^- antiport test, were suspended in 150 mM Na2SO4 solution buffered to pH 7.2 with sodium dihydrogen phosphate salts.

Sample for assay was prepared in a vial by diluting to 5 mL lipid stock solution with the external solution to give a solution of 0.5 mM of lipid. Chloride efflux was monitored using an ion selective electrode (Hach, ISE F-9655C) for chloride, calibrated against sodium chloride solutions of known concentration before starting the measurements. At t = 50 s, NaHCO3 solution (0.5 M in 150 mM $Na2SO_4$ solution buffered to pH 7.2 with sodium dihydrogen phosphate salts) was added so that the external solution contained 40mM $NaHCO_3$. At t = 60 s, a DMSO solution of the carrier compound was added to start the measurement and chloride efflux was monitored during 6 min. At the end of the experiment, detergent was added to lyse the phospholipidic vesicles and detected the 100 % of the chloride efflux. Experiments were repeated in triplicate and all traces presented are the average of three trials.

Carboxyfluorescein assay

Unilamellar POPC vesicles containing a 50 mM solution of carboxyfluorescein (CF) dissolved in a 451 mM NaCl solution buffered to 7.2 with 20 mM sodium dihydrogen phosphate salts, were suspended in 150 mM Na_2SO_4 solution buffered to pH 7.2 with sodium dihydrogen phosphate salts 20 mM. The unencapsulated CF was removed by means exclusion chromatography column, using Sephadex G-25 as stationary phase and the external solution as mobile phase. Sample for assay was prepared in a disposable plastic cuvette by diluting to 2.5 mL lipid stock solution with the external solution to give a solution of 0.05 mM of lipid. The CF emission was monitored using a fluorimeter (HITACHI F-7000 Fluorescence Spectrophotometer). To initiate the experiment, at t = 60 s the carrier compound was added as DMSO solution and the emission was monitored during 6 min. At the end of the experiment, detergent was added to lyse the phospholipidic vesicles and recorded the maximum intensity of the CF emission band. Experiments were repeated in duplicate and all traces presented are the average of two trials.

HPTS assay

Unilamellar POPC:Cholesterol 7:3 vesicles containing 10 µM HPTS dissolved in a 126.2 mM NaCl solution buffered to 7.2 with 10 mM sodium dihydrogen phosphate salts, were suspended in 126.2 mM $NaNO_3$ solution buffered to pH 7.2 with sodium dihydrogen phosphate salts 10 mM. The unencapsulated HPTS was removed by means exclusion chromatography column, using Sephadex G-25 as stationary phase and the external solution as mobile phase.

Sample for assay was prepared in a disposable plastic cuvette by diluting to 2.5 mL lipid stock solution with the external solution to give a solution of 0.5 mM of lipid. The I460nm/I403nm ratio was monitored using a fluorimeter (HITACHI F-7000 Fluorescence Spectrophotometer). At t = 30 s a 0.5 M NaOH solution was added to create a pH gradient between the internal and external solution and then, to initiate the experiment the carrier compound was added as DMSO solution and the I460nm/I403nm ratio was monitored during 6 min. Experiments were repeated in triplicate and all traces presented are the average of three trials. At the end of the experiment, detergent was not added to lyse the phospholipidic vesicles.

HPTS assay calibration

The system was calibrated monitoring the I460nm/I403nm ratio of a 10 mM solution of HPTS dissolved in a 126.2 mM NaCl solution buffered to 7.2 with 10 mM sodium dihydrogen phosphate salts upon the addition of increasing aliquots of a 0.5 M NaOH solution. We plotted the pH values starting from 5.5 until 9.5 against the I_{460nm}/I_{403nm} ratio. Hence, fitting the data by means a sigmoidal or polynomial fitting, we were able to obtain the equation curve which allowed to convert the photometric data in pH values.

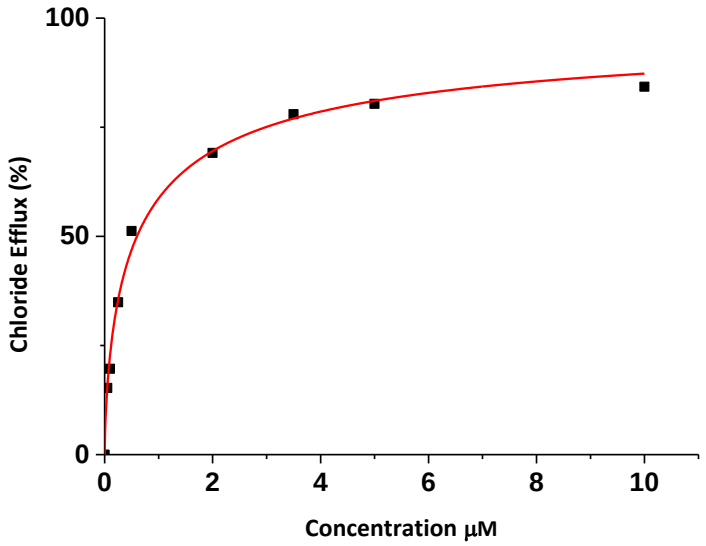

Figure 4.42. Normalised chloride efflux at 300 s plotted against the concentration of compound **L12**. Data have been plotted with Hill equation (continuous line)

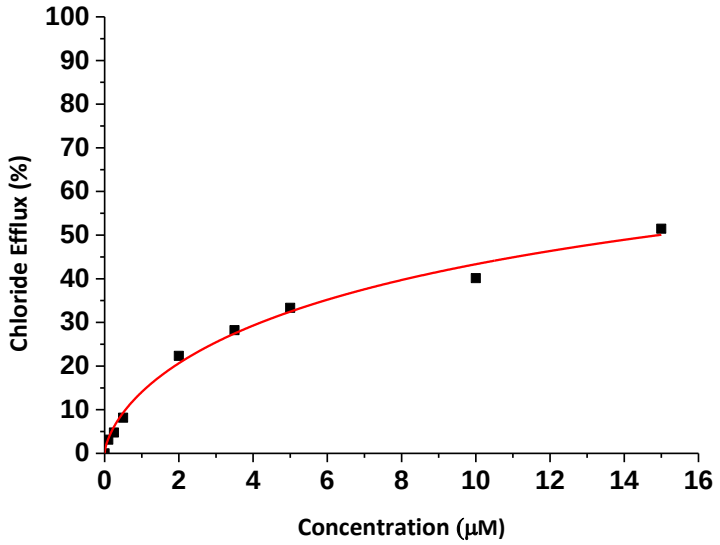

Figure 4.43 Normalised chloride efflux at 300 s plotted against the concentration of compound **L12**. Data have been plotted with Hill equation (continuous line)

4.8.4 Crystallography

Diffraction data were collected by the ω-scan technique at 130(1) K on Rigaku SuperNova four-circle diffractometer with Atlas CCD detector and mirror-monochromated CuK_α radiation (λ=1.54178 Å). The data were corrected for Lorentz-polarization as well as for absorption effects [1]. Precise unit-cell parameters were determined by a least-squares fit of 24399 (**1**), 13684 (**2**) and 8549 (**3**) reflections of the highest intensity, chosen from the whole experiment. The structures were solved with SHELXT-2013 [2] and refined with the full-matrix least-squares procedure on F^2 by SHELXL-2013 [2]. All non-hydrogen atoms were refined anisotropically, hydrogen atoms in **3** were freely, isotropically refined, in **1** and **2** were placed in idealized positions and refined as 'riding model' with isotropic displacement parameters set at 1.2 (1.5 for methyl groups) times U_{eq} of appropriate carrier atoms. In the structure of **1** one of the arms of one of the NBu_4 cations disordered was found, and two alternative positions of this group were found with site occupation factors of 53.7(6)%/46.3(6)%. For this group, weak restraints were applied to its geometry as well as to the shapes of displacement ellipsoids. In **2**, in turn, relatively high residual density far from the rest of the structure, probably caused by heavily disordered water molecule, was taken into model by means of SQUEEZE procedure. Table x lists the details of crystal structures and refinement results.

Table 4.7 Crystal data, data collection and structure refinement

Compound	**1**	**2**	**3**
Formula	$C_{24}H_{16}N_2O_2 \cdot C_{16}H_{36}N \cdot C_7H_5O_2$	$C_{20}H_{14}N_4O_2 \cdot C_{16}H_{36}N \cdot Cl$	$C_{22}H_{14}N_4O_2 \cdot H_2O$
Formula weight	727.95	620.26	384.39
Crystal system	monoclinic	monoclinic	monoclinic
Space group	$P2_1/c$	I2/a	$P2_1/n$
a(Å)	20.61410(15)	33.3689(8)	12.60987(13)

b(Å)	16.28811(11)	22.8121(4)	10.80108(11)
c(Å)	24.27716(18)	38.3244(9)	13.03058(13)
β(º)	96.8619(7)	107.400(2)	102.3166(10)
V(Å^3)	8093.02(10)	27838.1(11)	1733.92(3)
Z	8	32	4
D_x(g cm^{-3})	1.195	1.184	1.472
F(000)	3136	10688	800
μ(mm^{-1})	0.593	1.262	0.829
Θ range (^{0})	2.16 – 76.62	2.28 – 67.50	4.43 – 76.30
Reflections:			
collected	36488	78493	10165
unique (R_{int})	16691 (0.019)	25055 (0.061)	3586 (0.013)
with I>2σ(I)	14866	16616	3371
R(F) [I>2σ(I)]	0.0473	0.0960	0.0340
wR(F^2) [I>2σ(I)]	0.1292	0.2220	0.0967
R(F) [all data]	0.0524	0.1319	0.0360
wR(F^2) [all data]	0.1336	0.2398	0.0982
Goodness of fit	1.024	1.008	1.060
max/min $\Delta\rho$ (eÅ^{-3})	1.12/−0.53	0.80/−0.43	0.27/-0.16
CCDC numbers	1944084	1944085	1944086

4.8.5 Cubosomes preparation

Cubosomes were initially formulated by dispersing the squaramide receptor in melted MO (37 °C) by using an ultrasonic bath (UP100H by Dr. Hielscher) for 45 min and then adding a water solution of Pluronic F108. This mixture was then homogenized using an ultrasonic processor (UP100H by Dr. Hielscher, cycle 0.9, amplitude 90 %) for 15 min. The sample volume was usually 4 mL with approximately 96.4 wt % of water, 2.97 wt % of MO and 0.3 wt % of Pluronics mixture. The squaramide concentrations inside the cubosome formulations were respectively $7.33 \cdot 10^{-6}$ M (**L13**) and $1.20 \cdot 10^{-6}$ M (**L11**) as determined by Uv- Vis spectroscopy.

4.8.6 Dynamic Light Scattering (DLS)

Particle size and ζ-potential determinations of the nanoparticles were performed with a ZetaSizer Nano ZS (Malvern Instruments, Malvern, U.K.) at a temperature of 25 ± 0.1 °C. Samples were backscattered by a 4 mW He−Ne laser (operating at a wavelength of 633 nm) at an angle of 173°. Diluted samples (1:50) were housed in disposable polystyrene cuvettes of 1 cm optical path length with water as the solvent. At least two independent samples were taken, each of which was measured three to five times. The hydrodynamic diameter distribution is indicated by the PDI (polydispersion index).

4.8.7 Small Angle X-ray Scattering (SAXS)

Synchrotron SAXS experiments were performed at the ID02 beamline at ESRF, Grenoble (France). Samples were enclosed in quartz Mark capillaries, 1 mm thickness. Two-dimensional SAXS patterns were recorded by a fast read-out, low-noise CCD detector (FReLoN); 2D data were radially averaged and standard reduction procedures (subtraction of empty capillary and solvent contribution) were applied. The data are reported here as the absolute scattering cross section $I(q) = d\Sigma/d\Omega(q)$, expressed in cm^{-1}, as a function of q, the modulus of the scattering vector given by $q = 4\pi \sin(\theta)/\lambda$. Here, 2θ is the scattering angle, and λ is the X-ray wave-length which was

0.995 Å. The sample-detector distance was 3 m for SAXS and 20 m for USAXS, giving a total *q* range of 0.0001 − 0.19 $Å^{-1}$ when combined. All measurements were performed at 25 °C. Data reduction and analysis was performed with the Wavemetrics software Igor.

4.8.8 Cell culture

Commercial 293T human kidney embryonic cell line (catalog code HTL03003) and Caco-2 Human Epithelial Colorectal Adenocarcinoma (catalog code HTL97023), were obtained from the Istituto Nazionale per la Ricerca sul Cancro c/o CBA (ICLC, Genova).

The culture medium used was a mixture of minimal essential medium, MEM (EBSS), 10% fetal bovine serum (FBS), 100 units per ml penicillin, 100 mg×mL streptomycin, 2 mM glutamine, and 1% non-essential amino acids. To achieve the experimental conditions, confluent cells were isolated using trypsin/EDTA and cell samples of 2–3 × 10^4 cells per cm^2 were seeded in 35 mm dishes, plated at 37°C, and 5% CO_2. After 24 h of growth with the complete medium, the cells were grown in the presence of different experimental samples: **L13**, and **L11** ligands, cubosomes with and without **L13** and **L11**ligands.

4.8.9 Fluorescence microscopy

Zoe® microscopy was used for live cell imagining in bright field and variable fluorescence wavelengths (blue channel λ_{Ex} 355 ± 40 nm λ_{Em} 433 ± 36; Green channel λ_{Ex} 480 ± 17 λ_{Em} 517 ± 23; Red channel λ_{Ex} 556 ± 20 λ_{Em} 615 ± 61). Olympus BX41 fluorescence microscopy equipped with an appropriate filter for FITC detection (λ_{Ex} 490 nm; λ_{Em} 517 nm) microscopy was used for the fixed cell imagining with 60× enlargement.

4.8.10 Cell membrane staining with PKH26 Red Fluorescent marker

PKH26 Red Fluorescent Cell Linker Kits for General Cell Membrane Labeling was purchased from Sigma Aldrich (Cat. No. MINI26, MIDI26, PKH26GL) and used as

indicated in the manufacturer's user manual. Briefly, cells were suspended in Diluent C and immediately after PKH26 solution in Diluent C was added (final concentration 2 μM).

The PKH26 Fluorescent marker is commercially available as Cell Linker Kits for membrane labeling technology. It is stably incorporated in the membranes as yellow-orange fluorescent dye with long aliphatic tails (PKH26) into lipid regions of the cell membrane The labeling vehicle provided in the kits (Diluent C) is an aqueous solution, which maintains cell viability, and maximize dye solubility and staining efficiency during the labeling process. Diluent C is iso-osmotic for mammalian cells and contains no detergents nor organic solvents, but also lacks physiologic salts and buffers. The appearance of labeled cells may vary from bright and uniform to punctate or patchy, depending on the cell type.

Cells must washed carefully with medium without serum before staining with PKH26.

4.8.11 Cytotoxic activity: Trypan Blue staining

The cytotoxic effect (ID_{50}) of different combinations of **L13** and cubosomes administration were evaluated in non-tumoral 293T cells. Different concentrations of **L13** (0.02 - 497 μM) and cubosomes (16-649 μg/mL) were added to confluent cells and incubated at 37°C for 24 h. The cell viability was evaluated using the Luna^{FL} Cell Counter (www.logosbio.com) as indicated in the manufacturer's user manual. Briefly, cell samples mixed 1 : 1 with 0.2% Trypan Blue solution supplied in the kit reagents, were counted in the Luna cell counting chamber slide within 1–3 minutes. Results were analysed as percent of cell viability in comparison with non-treated control cells. To obtain an accurate cell viability measurement the cell count was repeated at least three times. Moreover, the additional experiment, as a control of automated technique, was prepared. The Trypan Blue solution was added to the treated cells and visual microscopic analysis of live (trypan blue negative) and dead (trypan blue positive) cells was performed in each experimental culture condition.

4.9 References

1. J. L. Sessler, P. A. Gale and Won-Seob Cho, Anion Receptor Chemistry, RSC Pub., 2006
2. C. Caltagirone and P. A. Gale, *Chem. Soc. Rev.*, 2009, **38**, 520-563.
3. P. A. Gale and T. Gunnlaugsson, *Chem. Soc. Rev.*, 2010, **39**, 3595-3596.
4. R. Martínez-Máñez and F. Sancenón, *Chem. Rev.*, 2003, **103**, 4419-4476.
5. M. Wenzel, J. R. Hiscock and P. A. Gale, *Chem. Soc. Rev.*, 2012, **41**, 480-520.
6. C. Caltagirone, P. A. Gale, J. R. Hiscock, S. J. Brooks, M. B. Hursthouse and M. E. Light, *Chem. Comm.*, 2008, 3007-3009.
7. A. Casula, A. Llopis-Lorente, A. Garau, F. Isaia, M. Kubicki, V. Lippolis, F. Sancenón, R. Martínez-Máñez, A. Owczarzak, C. Santi, M. Andrea Scorciapino and C. Caltagirone, *Chem. Comm.*, 2017, **53**, 3729-3732.
8. X. J. Cai, Z. Li and W. H. Chen, *Mini-Rev. Org. Chem.*, 2018, **15**, 148-156.
9. L. A. Marchetti, L. K. Kumawat, N. Mao, J. C. Stephens and R. B. P. Elmes, *Chem*, 2019, **5**, 1398-1485.
10. V. Amendola, G. Bergamaschi, M. Boiocchi, L. Fabbrizzi and M. Milani, *Chemistry - Eur. J.*, 2010, **16**, 4368-4380.
11. J. M. Andrés, A. Maestro, M. Valle and R. Pedrosa, *J. Org. Chem.*, 2018, **83**, 5546-5557.
12. S. Park, J. Uchida, K. Urushibara, H. Kagechika, T. Kato and A. Tanatani, *Chem. Lett.*, 2018, **47**, 601-604.
13. R. Prohens, A. Portell, O. Vallcorba, M. Font-Bardia, A. Bauzá and A. Frontera, *CrystEngComm*, 2018, **20**, 237-244.
14. P. A. Gale, J. T. Davis and R. Quesada, *Chem. Soc. Rev.*, 2017, **46**, 2497-2519.
15. R. B. P. Elmes, P. Turner and K. A. Jolliffe, *Org. Lett.*, 2013, **15**, 5638-5641.
16. A. Danao, V. Ramalingam, V. Ramamurthy and R. S. Muthyala, *J. Photochem. Photob. A: Chemistry*, 2017, **344**, 108-113.
17. X. Bao, X. Wu, S. N. Berry, E. N. W. Howe, Y. T. Chang and P. A. Gale, *Chem. Comm.*, 2018, **54**, 1363-1366.
18. J. I. Lachowicz, G. Picci, P. Coni, V. Lippolis, M. Mamusa, S. Murgia, G. Pichiri and C. Caltagirone, *New J. Chem.*, 2019, **43**, 10336-10342.
19. A. Rostami, A. Colin, X. Y. Li, M. G. Chudzinski, A. J. Lough and M. S. Taylor, *J. Org. Chem.*, 2010, **75**, 3983-3992.
20. M. J. Hynes, *J. Chem. Soc., Dalton Trans.*, 1993, 311-312.
21. X. Mulet, B. J. Boyd and C. J. Drummond, *J. Coll. Int. Sci.*, 2013, **393**, 1-20.

22. S. Biffi, L. Andolfi, C. Caltagirone, C. Garrovo, A. M. Falchi, V. Lippolis, A. Lorenzon, P. Macor, V. Meli, M. Monduzzi, M. Obiols-Rabasa, L. Petrizza, L. Prodi, A. Rosa, J. Schmidt, Y. Talmon and S. Murgia, *Nanotechnology*, 2017, **28**.

23. V. Meli, C. Caltagirone, A. M. Falchi, S. T. Hyde, V. Lippolis, M. Monduzzi, M. Obiols-Rabasa, A. Rosa, J. Schmidt, Y. Talmon and S. Murgia, *Langmuir*, 2015, **31**, 9566-9575.

24. A. Jaszczyszyn and K. Gasiorowski, *Adv. Clin. Exp. Med.*, 2008, **17**, 525-529.

25. V. Fernández-Moreira, J. V. Alegre-Requena, R. P. Herrera, I. Marzo and M. C. Gimeno, *RSC Advances*, 2016, **6**, 14171-14177.

26. S. K. Narasimhan, P. Sejwal, S. Zhu and Y. Y. Luk, *Bioorg. Med. Chem.*, 2013, **21**, 2210-2216.

27. A. Sampedro, R. Villalonga-Planells, M. Vega, G. Ramis, S. Fernández De Mattos, P. Villalonga, A. Costa and C. Rotger, *Bioconj. Chem.*, 2014, **25**, 1537-1546.

28. . R. Casey, S. Grinstein and J. Orlowski, *Nature Reviews Molecular Cell Biology*, 2009, **11**, 50.

29. A. M. Falchi, A. Rosa, A. Atzeri, A. Incani, S. Lampis, V. Meli, C. Caltagirone and S. Murgia, *Tox. Res.*, 2015, **4**, 1025-1036.

Chapter 5

Urea-based Low Molecular Weight Gelators

5 Urea-based Low Molecular Weight Gelators

In this chapter the synthesis, gelation tests and characterization of eight LMWGs (**L17**-**L24** Figure 4) based on the urea moiety scaffold are describe. The bis-urea based gelators **L17**-**L19** are characterised by the presence of three different fluorophores as substituents (quinoline, indole and dansyl derivative for **L17**, **L18**, and **L19**, respectively) in order to design new luminescent materials enable to change their optical properties in the presence of external stimuli or in the presence of other species enable to interact by means non-covalent interactions. Oscillatory stress sweep rheometry results evidenced **L18** in a mixture of DMSO and water as the strongest LMWG. Particularly, the formation of the gel in this medium allowed to perform tests in presence of anion species enable to affect the self-association properties of the compound estabilishing non-covalent gelator-anion interactions. The presence of BzO^- and F^- inhibits the gelation process. An explanation is proposed on the base of the results of ^{1}H-NMR titrations in DMSO d_6 performed in presence of the different anion species tested. The monourea based receptors **L20**-**L24** are characterised by an alkyl chain of different length and different aryl substituents. Particularly, **L20**-**L22** bear a nitrophenyl ring, while **L23**-**L24** are characterised by a naphtyl aromatic group. In this case, the aim was to understand how the different length of the alkyl chain was able to modulate or change the gelation properties of the gelators and, particularly in the case of **L20**-**L22**, a multicomponent systems was able to affect the capability to form gels, to modulate or increase the gelation process or the strength of the gel at least. **L23**-**L24** formed soft gels in apolar solvents like nitrobenzene and chlorobenzene. Particularly, the materials obtained in nitrobenzene are stronger then in chlorobenzene, as suggested by the rheology analysis performed. **L22** formed gels in a polar-like media as ethanol. Interestingly, changes in the mechanic properties as well as in the morphology of the materials obtained in presence of different species (a metal ion or an anion) were suggested by rheology

and SEM analysis. In particular, an increase of the solid-like behaviour was observed moving from the free ligand compound to the three components system (gelator + metal ion + anion).

5.1 Introduction

Gels are everyday materials. Everybody always able to recognize a flexible, soft, solid material.

A vast and diverse array of organic compounds and coordination complexes will form gels by hierarchical self-assembly either because of hydrophobic effects in water or by more directional interactions such as hydrogen bonding in less polar solvents. Some well-known gelators include bis(ureas) and amides,[1] nucleobase-derived compounds, fatty acids, steroids, anthryl derivatives, amino acid derivatives,[2] dendrimers, phthalocyanines and porphyrins.[3] These gelators are normally classified as Low Molecular Weight Gelators (LMWGs).

Attractive features of LMWGs for the scientific community are the reversible nature of the interactions between the gelator molecules, the wide (essentially unlimited) range of solvents that can be gelled and the possibility of tuning the gels' behaviour by introducing responsive or switching functionality either as part of the gelator itself or by an external chemical stimulus such as a change in pH, or addition of molecules or ions that interact with the dynamic gel. Gels derived from LMWGs have been proposed in a range of applications recently summarised by Smith and coworkers[4, 5] and include templation of nanoparticles and nanostructures, drug delivery and wound healing and, recently, as crystal growth media.[6] Gelators are also not limited to single components[7] and can include gelator analogues of co-crystals such as dipyridylurea–carboxylic acid combinations,[8] diamine-linked dendrons, or aminopyrimidine/dialkylbarbituric acid mixtures as well as are having a huge success studies regarding metal-, anion- and salt-containing gelators.[9]

Ureas are an especially versatile class of gelators with well-understood supramolecular chemistry in self-assembly and anion binding. As a result, they represent an excellent example of systems in which a molecular level understanding of intermolecular interactions can translate into interesting new materials science.

The commonly accepted definition of a gel is a material with a continuous structure that is permanent on the analytical timescale and it is solid-like in its rheological behaviour.[10] Gels also comprise two (or more) components such that one component is a dispersion within the other. The inversion tube test (when a container of a gel is upended the material stays where it is) is an example of a simple rheological experiment and it is, in some cases, sufficient to allow us to recognise a gel. However, a more quantifiable test involves the use of a rheometer (Figure 5.1).[13]

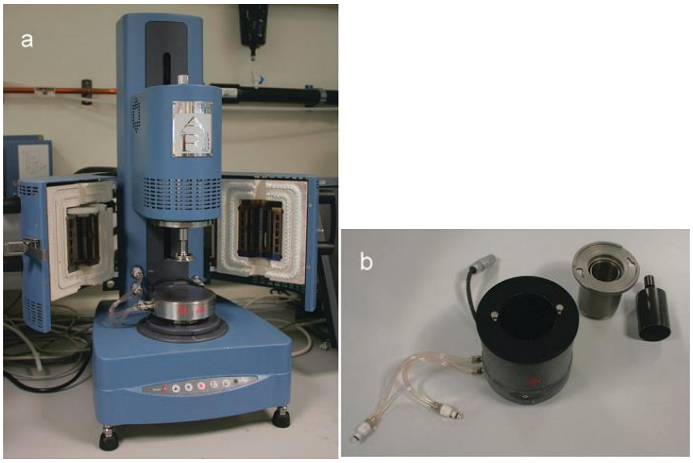

Figure 5.1 (a) TA Instruments AR2000 rheometer with parallel-plate attachment and (b) concentric cylinder couette arrangement useful for the study of relatively weak gels.

Technically, rheology involves the study of the liquids and solids under applied stress conditions where they flow rather than deform in a classical, elastic fashion. Rheology is mostly concerned with materials which, like gels, have a complex structure in which

their flow is not characterised by a single value for their viscosity at constant temperature.

In a rheometer the sample is placed between two parallel flat plates (or a shallow cone and plate), or between two concentric cylinders and the stress is applied by moving one plate or cylinder relative to the other while the resulting strain is measured using a pressure transducer. In the concentric cylinder geometry (Figure 5.1b) the gel is placed within a cylindrical cup (couette) and a second cylinder is introduced such that the sample occupies a small, well-defined space in between the two. One of the cylinders is oscillated at a user-determined rate (the shear rate). This, in turn, pulls the other cylinder round depending on flow characteristics of the intervening gel. The force on the second cylinder is then recorded and translated to a shear stress. In the parallel plate geometry the fluid is placed in between two plates with one applying a shear by oscillating at a constant frequency with increasing applied stress. A frequency-sweep is also possible with constant stress. For weaker gels or those involving volatile solvents the less exposed concentric cylinder geometry is often easier to work with in practice. Temperature sweep experiments also allow the measurement of flow characteristics as a function of temperature allowing a more sophisticated examination of the temperature dependence of the gel–sol transition compared to the simple determination of T_{gel} (the temperature at which the gel–sol transition occurs) by the dropping ball method. The rheological behaviour of a material in response to shear stress can be categorised into solid-like or liquid-like behaviour. Solids eventually resist deformation in response to a continuous weak stress after some deformation. Conversely, liquids eventually flow in response to an applied stress. Complex fluids fall in between these two extremes over a short timescale. In elastic materials the amount of deformation is proportional to applied force (e.g. a rubber band). In viscous materials, however, the deformation rate is proportional to the applied force. Viscoelastic materials have both viscous and elastic characteristics. In molecular terms, we can think of elasticity as arising from features such as chemical bonds stretching in ordered solids along crystallographic planes,

while viscoelasticity is related to diffusion of molecules in an amorphous material. Gels are commonly viscoelastic, but are more solid-like than liquid-like under weak applied stress. Under high stress, a solid will often begin to flow. These materials are referred to as plastic and the point at which they flow is termed the yield stress. For complex fluids the strain they exhibit in response to an applied stress is described by the complex dynamic modulus (G, equation (1)) which divides the behaviour into two components—the elastic storage modulus (G' —the contribution of solid-like behaviour) and the elastic loss modulus (G''—the contribution of viscous or liquid-like behaviour). Both have units of Pascal. For solids the applied stress and resulting strain are in phase and hence application of stress results in immediate strain. For viscous materials, the strain lags behind the stress by a 90° phase difference (δ). The intermediate viscoelastic materials have a strain lag that is somewhere between 0° and 90°.

$$G = G' + iG'' \qquad \text{equation (1)}$$

The storage and loss moduli are related to the quantities σ_0 and ε_0, the amplitudes of stress and strain, respectively, and the phase shift between them (δ) as shown in the equations (2) and (3) reported below:

$$G' = \frac{\sigma_0}{\varepsilon_0}\cos\delta \qquad \text{equation (2)}$$

$$G'' = \frac{\sigma_0}{\varepsilon_0}\sin\delta \qquad \text{equation (3)}$$

The magnitude of G' gives some information about gel strength, although rheological experiments on supramolecular gels are notoriously difficult to reproduce quantitatively. With care, the behaviour and magnitude of the storage and loss moduli, and yield stress as a function of applied stress or oscillatory frequency and

concentration can be modelled mathematically and can give insights into the microstructure of the material.[11, 12] Factors that influence the magnitude of G' are the concentration of gel fibres, the strength of the individual gel fibres and the fibre connectivity (i.e. the number of fibres joined at a given node).

Figure 5.2 illustrates some typical architectures formed through gel formation, which can be broadly classified into several hierarchical levels and several dimensions from zero-dimension (0D) to three-dimension (3D).[13]

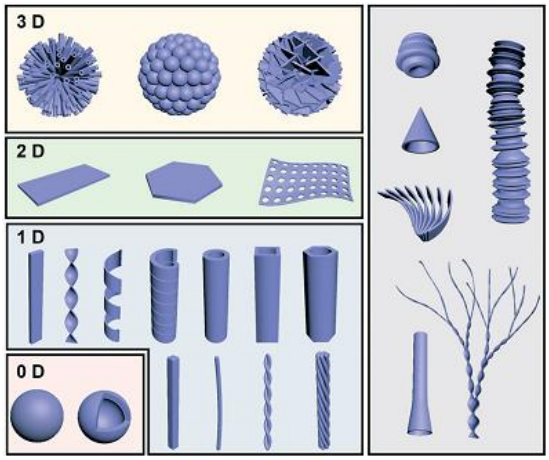

Figure 5.2 Schematic illustration of various nanoarchitectures obtained through supramolecular gelation. Based on the structural features, these basic nanoarchitectures can be classified into different hierarchical orders from zero-dimensional (0D) to three-dimensional (3D). In addition, some special architectonics (right panel) can also be formed *via* the gelation process. Reproduced with permission from ref. 13

One-dimensional (1D) morphologies, including nanofibers, helixes, tubes and their analogue, are the most common structures observed in gels. 0D structures mainly consist of hollow or solid spheres, which are not very common in gels. Two-dimensional (2D) nano/micro-sheets, plate-like morphologies, membranous and porous membrane-like structures can be formed as well during the gelation process. More hierarchical level nano/micro-structures such as flower-like structures usually

composed of dozens of tubes, nanospheres or petals. Besides the above conventional structures, some unique structures such as trumpet-shaped tubes, dendritic nanotwists, nanotrumpets, and toruloid-like nanostructures could be also obtained through gel formation. In this paragraph, several basic nanoarchitectures and their molecular packing are listed in order to explain the relationship between the molecular design and the nanoarchitectures. TEM, SEM and AFM spectroscopies are often used to better understand the different morphologies, structures and architectures of a single gel sample.

Interestingly, achiral gelators could form chiral architectures with an equal or unequal amount of enantiomers.[14] As shown in Figure 5.3, an achiral C_3-symmetric molecule **1** can form supramolecular gels in a mixture of DMF and H_2O.[15] Left (*M*) and right handed (*P*) twists simultaneously formed in an unequal number, resulting in macroscopic chirality without any chiral additives. At the early stages of gelation, one-dimensional helical aggregates with a predominantly *P* or *M* conformation were randomly formed *via* three-fold intermolecular hydrogen bonding and π–π stacking. Once the assemblies with a certain chiral bias start to form, the further growth follows the original chiral conformation, and larger twists with an unequal amount of conformations finally form.

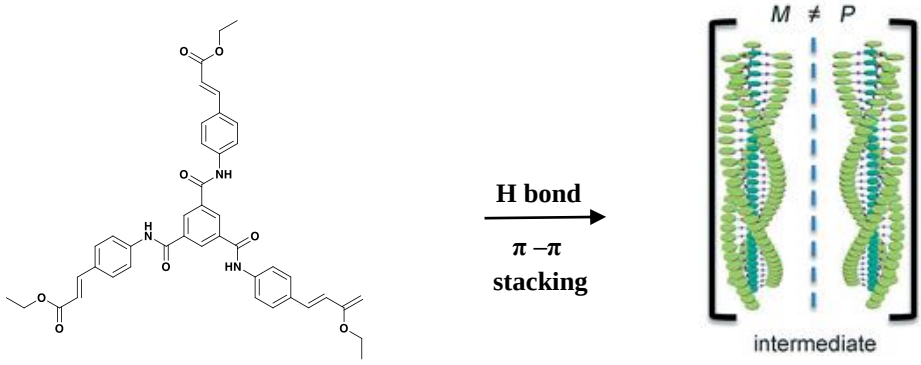

Figure 5.3 Formation of nanotwists by the hierarchical self-assembly of achiral building blocks via gelation. Reproduced with permission from ref. 15

Peptide-amphiphiles, glucolipids, amphiphilic metal complexes, phospholipids, cyclic peptides and bolaamphiphiles have been designed to form organic nanotubes. In Figure 5.4, a C_3-symmetrical glutamic acid ethyl ester gelator **2** is reported. Gelator **2** was found to form hexagonal tubes in a wide range of mixed solvents through supramolecular gelation.[16]

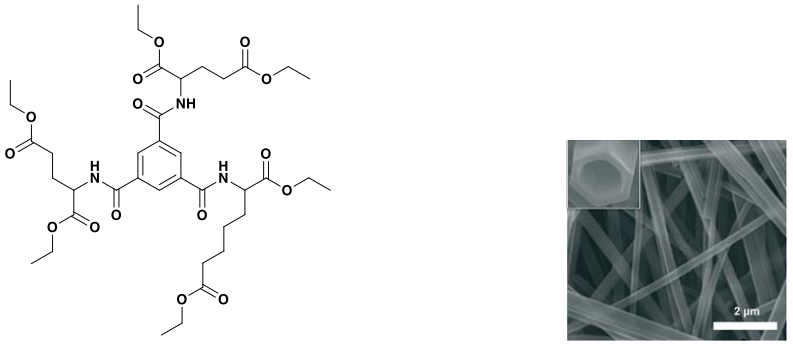

Figure 5.4 Tubular architectures based on glutamic acid-based amphiphilic gelators. Reproduced with permission from ref. 16

Supramolecular gelation is also applied to prepare spherical nanostructures[17] as reported by Bag and coworkers for molecule **3**, an amphiphilic gelator can self-assemble in aqueous media and result in a hydrogel with nanospherical morphologies.[18] The nanosphere is solid with a diameter of 700 ± 100 nm.

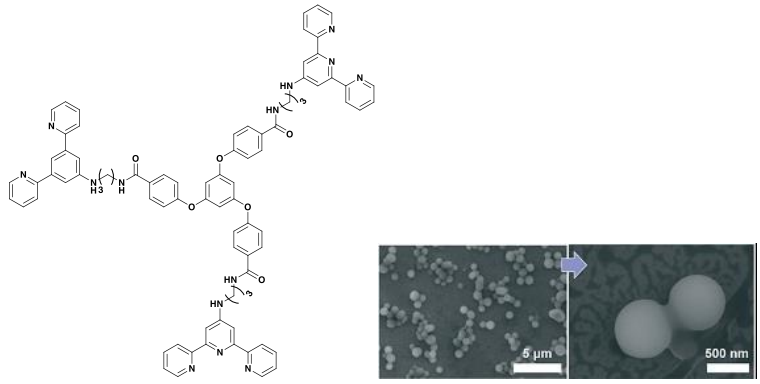

Figure 5.5 Formation of nanotwists by the hierarchical self-assembly of achiral building blocks *via* gelation. Reproduced with permission from ref. 18

A two-step hierarchical self-assembly process was proposed for the formation of this nanosphere. Firstly, the gelator assembles into extended 2D sheets through intermolecular π–π stacking. As time proceeds, the nanosheets tend to minimize their contact with the solvent (H_2O/MeOH) due to the hydrophobic effect. In contrast, the amide groups tend to be exposed to the polar medium due to H-bonding with the solvent.

5.2 Urea-based gelators

We can think about the urea functionality as the molecular equivalent of a Velcro type hook-and-loop fastener[19]Imagine a strip of Velcro with hooks on one side and loops on the other. Since hooks can only bind to loops, such a double-sided strip would readily form directional stacks. The molecular analogy is the urea α-tape motif (Figure 5.6). This key supramolecular interaction that results from urea self-association to form a 6-membered hydrogen bonded ring based on two donors and one carbonyl acceptor, has been used extensively in supramolecular self-assembly.[20]

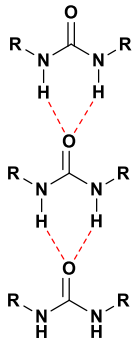

Figure 5.6 α tape motif of a urea based gelator

The parent urea molecule is also well-known for the formation of channel inclusion compounds based on the porous structure of hexagonal β-urea, Figure 5.7a. The channel walls comprise a hydrogen bonded polymer of NH—O=C interactions, in which each molecule both donates and accepts four hydrogen bonds, Figure 5.7b. In urea derivatives, however, hydrogen bonded polymers based on the urea α-tape are common.

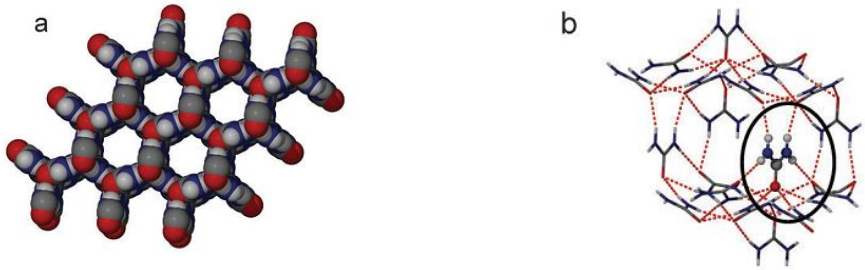

Figure 5.7 (a) Hexagonal channels in β-urea and (b) detail of one molecule in a urea channel showing how it both accepts and donates a total of four hydrogen bonds. [21] Reproduced with permission from ref. 19

It is the strong directionality of such hydrogen bonded chains that leads to the formation of high aspect ratio fibres and (upon physical entanglement) formation of gels. The urea hydrogen bonding tends to give rapid fibril growth in one dimension without significant aggregation in the other two. We can think of bis(urea) gels in terms of a primary structure made up from strands linked by the urea α-tape motif. Groups of strands comprise a secondary structure of fibrils and ultimately bunches of

fibrils (fibres) of relatively uniform diameter. These fibres then tangle and cross-link *via* physical or supramolecular interactions into a tertiary structure to give a 3D solid network.[22] The process is represented schematically in Figure 5.8a[22], and a representative SEM micrograph of a dried gel (xerogel) showing the fibrous structure is shown in Figure 5.8b. [12]

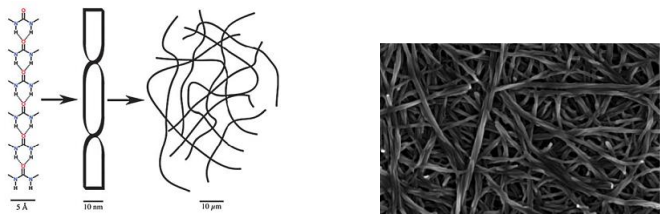

(a) **(b)**

Figure 5.8 (a) the primary, secondary and tertiary structures of a self-assembled physical gel of a urea-based LMWG; Reprinted with permission from 22 Copyright (2004) American Chemical Society (b) SEM image of the xerogel(Reproduced with permission form ref.12)

Gelation process in ureas is usually considered a hierarchical assembly process that generally follows a sequence involving the following steps: [19]

1. dimerization of two individual molecules;
2. oligomer formation by interaction of dimers with further molecules;
3. formation of polymer fibrils of approximately the same width as the molecular building blocks (*ca.* 1–2 nm) by extension of the oligomers;
4. fibre formation by bundling of fibrils (*ca*. 20–50 nm width);
5. interactions of fibres to give an effectively infinite, interconnected network spanning the entire sample (the least well understood aspect of the gelation process);

6. immobilization of the solvent by the fibre network, generally by surface tension effects.

Effective bis(urea) gelators have been prepared based on hydrogen bonded polymers of ureas linked by simple linear chains as in **4**, cyclohexane derivatives as in **5** and geminal bis(ureas) as in **6** (Figure 5.9).[23] These compounds are potent, fully thermoreversible gelators of a wide range of organic solvents ranging from methanol and dimethyl sulfoxide to hydrocarbons, at concentrations below 1 wt%. Modelling suggests a urea α-tape type aggregation mode.

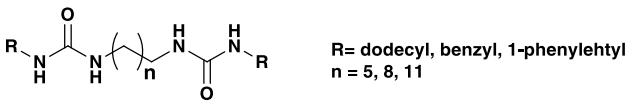

4

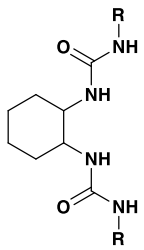

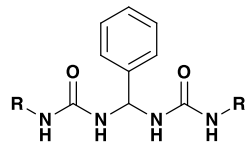

5 **6**

Figure 5.9 Structure of the urea based LMWG **4**, **5** and **6**

Ressouche and coworkers proposed a simple concept of a two component gelling system, where the first component is chosen for its capacity to form rodlike assemblies and the second component contains (i) a sticker for coassembly with the first component and (ii) an oligomer that is rationally chosen to tune the compatibility with the liquid of interest. This concept is successfully illustrated with bis-urea stickers (**7**) that allow the formation of elastic and thermoreversible gels in a large variety of liquids (Figure 5.10).[24]

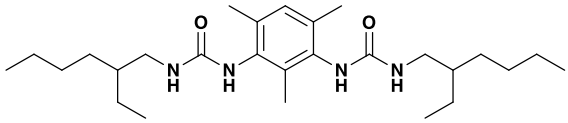

7

Figure 5.10 structure of compound **7** studied by Ressouche and coworkers

Compounds **8** and **9** reported in Figure 5.11 have been described by Paveler and co-workers as good gelators for a range of environmentally polluting liquids, such as petrol and oils, and can form stable gels at less than 1% w/v in certain cases. In particular, the restriction of available hydrogen bonding sites and an increase in steric bulk actually improved gelation properties, through improved solubility in relevant solvents. Further to this, modification of the symmetry, and hence steric hindrance of the aryl group dramatically changed the self-assembly thermodynamics and kinetics, and corresponding gel strengths.[1]

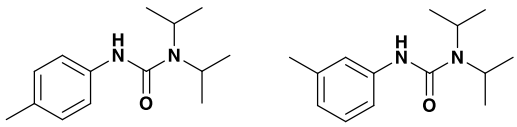

8 **9**

Figure 5.11 Structure of the gelators **8** and **9**

Furthermore, in a more recent study reported by Steed and coworkers with the aim to determine how helix chirality influences the topology of a braid (defined as the crossing pattern of strands) and the connectivity of the gel fibre networks, defined how helical fibrils in gels of pentakis(urea) **10** reported in Figure 5.12 form high-fidelity braids with repeated crossing patterns due to the topological constraints governing interhelical interactions.[25]

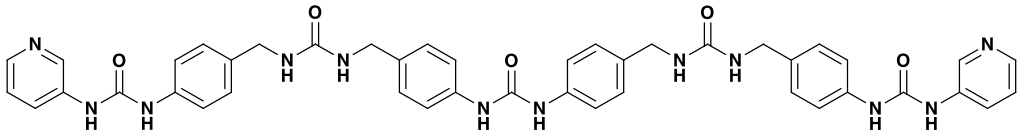

10

Figure 5.12 Structure of the pentakis(urea) **10** LMWG reported by Steed and co-workers

Moreover, they demonstrated that braids of mixed-chirality helices form more varied arrangements of crossings but may also undergo inversions of chirality to generate simple helical bundles. Building on this observation, they have shown that the oligo(urea) assemblies are highly sensitive to chiral amplification, giving rise to helices of a single handedness if the precursor are filtered through a chiral material.

Urea self-association readily leads to versatile fibril formation and hence gelation in a variety of bis and tris(ureas). Urea-anion interactions are also a common supramolecular motif. These anion binding interactions would be expected to be in competition with urea self-association because the anion takes the place of the urea carbonyl as a hydrogen bond acceptor. Hence it should be possible to design urea-based systems in which self-association and anion binding are tensioned against one another to allow the anion binding to modulate the urea self-association and hence the bulk materials behaviour of the gels, particularly their rheology. A series of gelators based on molecular skeleton **11** has been used to test this approach (Figure 5.13). The compounds with an even number of methylene spacer units (n= 2, 4, 6 and 8) act as gelators in solvents such as acetonitrile and chloroform. While BF_4^- had no effect on the observed storage and loss moduli (G' and G''), chloride, bromide and acetate dramatically compromise the gel strength and greatly decrease the values of the moduli. The addition of small amounts of these anions (0.1 equiv. with respect to the gelator concentration) reduces the storage modulus by up to two orders of magnitude depending on the identity of the anion. In addition to the decrease in G',

the anions cause a decrease in the yield stress of the gel, also indicating a weakening of the gel.[26]

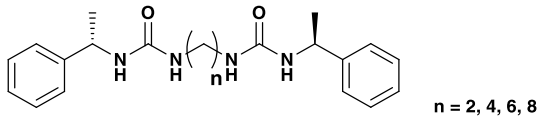

11

Figure 5.13 Structure of urea based LMWG **11** studied for anion tuning

In this chapter, we describe the synthesis, gelation tests and characterization of eight small molecule gelators (**L17**-**L24**) reported in Figure 5.14 based on the urea moiety scaffold. The eight gelators could be divided in three different sub-categories.The bis-urea based gelators **L17**-**L19** have been designed with a spacer unit previously synthesised through a reported procedure[26], and as substituent unit three different fluorophores (quinoline, indole and dansyl derivative for **L17**, **L18**, and **L19**, respectively) in order to design new luminescent materials enable to change their optical properties in the presence of external stimuli or in the presence of other species enable to interact by means non-covalent interactions. The monourea based receptors **L20**-**L24** are characterised by a alkyl chain of different length. Particularly, **L20**-**L22** bear a nitrophenyl ring as a substituent and different alkyl chain (C_n with n = 12, 14 and 16), while **L23**-**L24** are characterised by a naphtyl aromatic group (in order to confer fluorescent properties and enable the possibility to estabilish π-π interactions) and different alkyl chain(C_n with n = 14 and 16). In this case, our interest was to understand how different length of the alkyl chain was able to modulate or change the gelation properties of the gelators and, particularly in the case of **L20**-**L22**, the presence of the electron withdrawing group -NO_2 was able to affect the capability to form gels and how the presence into the system of a third component affine to the nitro group (*i.e*. a metal ion or an anion) could modulate or increase the gelation process or the strength of the gel at least.

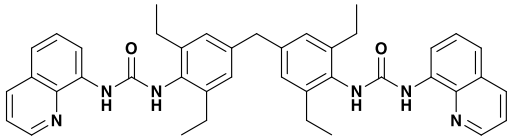

L17

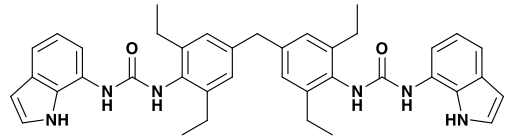

L18

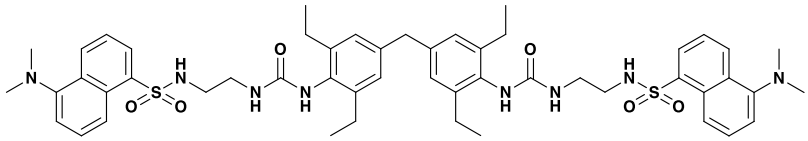

L19

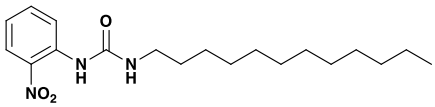

L20

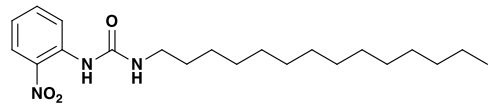

L21

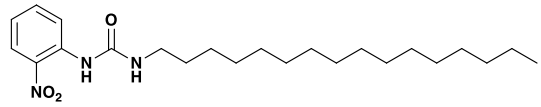

L22

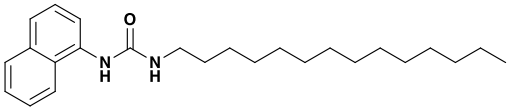

L23

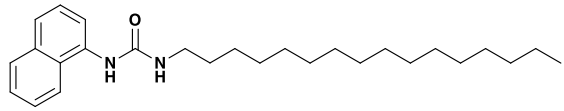

L24

Figure 5.14 Structure of the small molecule gelators studied in this chapter

5.3 Synthesis

Gelators **L17-L24** have been synthesised following the synthetic procedures reported in the experimental section (Paragraph 5.8). In particular, the synthesis of **L17**-**L19** was carried out by reacting the bis-isocyanate bis(3,5-diethyl-4-isocyanatophenyl)methane with the appropriate amine (Scheme 5.1).

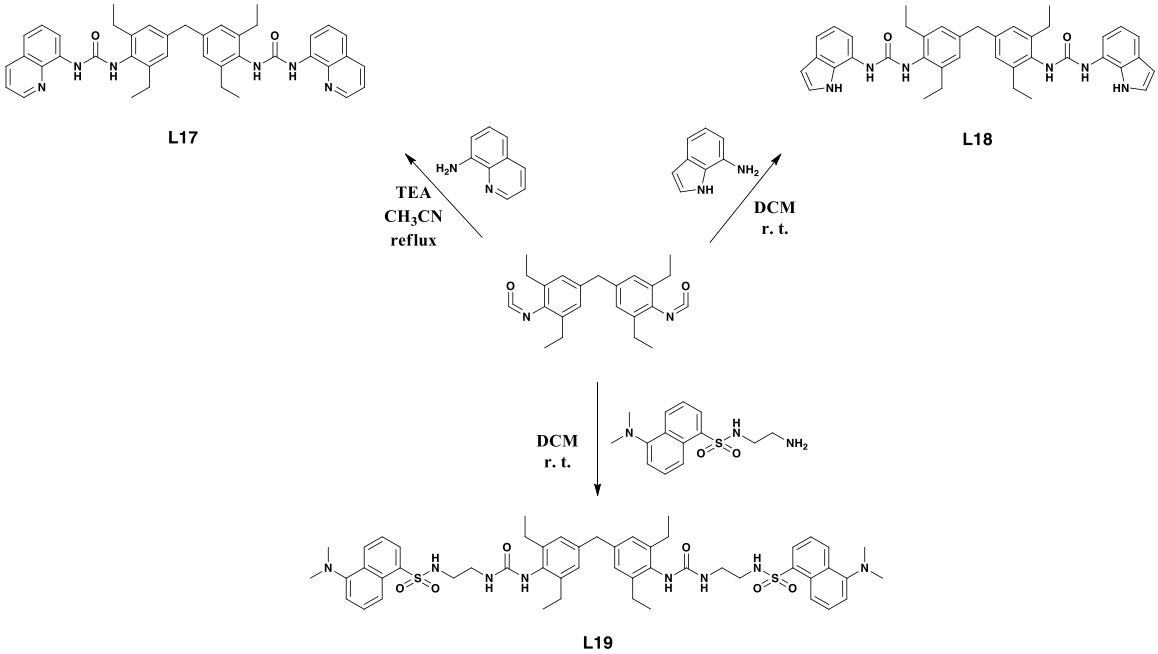

Scheme 5.1 Reaction scheme adopted for the synthesis of **L17**-**L19**.

The synthesis of **L20**-**L24** were carried out by reacting the 2-nitrophenyisocyanate or 1-naphtylisocyanate with the appropriate aliphatic amine as reported in Schemes 5.2 and 5.3.

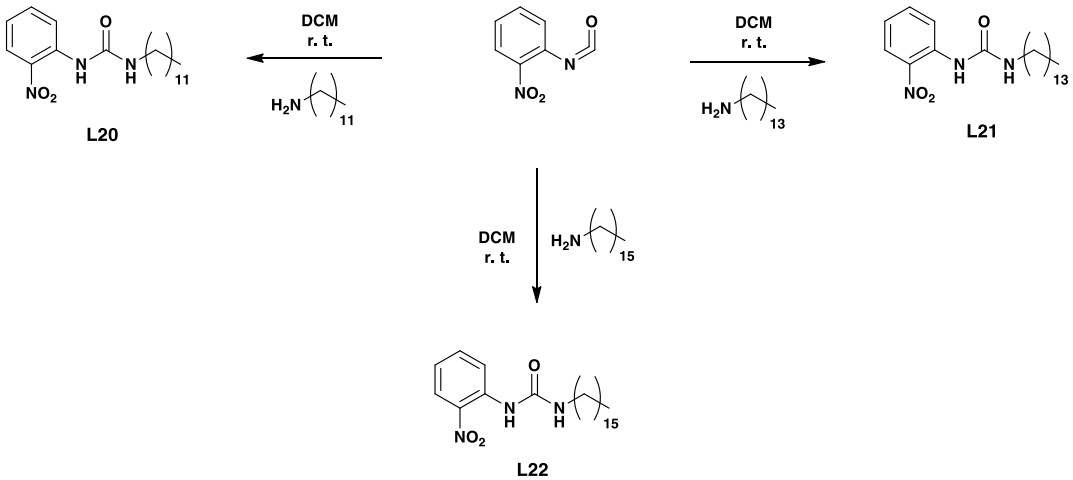

Scheme 5.2 Reaction scheme adopted for the synthesis of **L20**-**L22**

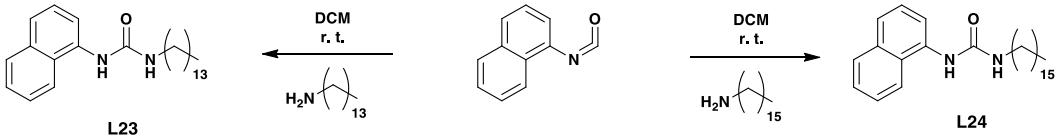

Scheme 5.3 Reaction scheme adopted for the synthesis of **L23**-**L24**

5.4 Preparation of gels from L17-L19 and their characterization

Gelation tests were carried out at different concentrations in a wide range of solvents (nitrobenzene, chlorobenzene, nitromethane, 1,4-dioxane, tetrahydrofuran, acetonitrile, dichloromethane, chloroform, methanol, ethanol, 1-isopropanol, 2-isopropanol, 1-butanone, ethyl acetate, dimethyl sulfoxide, dimethyl sulfoxide:water). Samples were sonicated, then heated gently to dissolve the solid, and subsequently allowed to cool to room temperature. Full results are reported in the Table 5.1.

Table 5.1 Gelation tests of **L17**-**L19** performed at different concentration with different solvents through a heating and cooling cycle.

	$BzNO_2$ (1%w/v)	$BzNO_2$ (0.75%w/v)	$BzNO_2$ (0.5%w/v)	BzCl (1%w/v)	BzCl (0.75%w/v)	BzCl (0.5%w/v)	DMSO:Water (15% water) (2% w/v)	DMSO:Water (20% water) (2% w/v)
L17	no gel	gel	gel	no gel	gel	no gel	no gel	no gel
L18	no gel	no gel	no gel	no gel	no gel	no gel	gel	gel
L19	gel	----	----	no gel	gel	gel	no gel	gel

L17, **L18** and **L19** have been tested with the rest of the solvents resulting unsoluble till 0.25 w/v%

As reported in Table 5.1, **L17-L19** showed low solubility in most of the solvents used. Promising results have been achieved with apolar solvents as nitrobenzene and chlorobenzene for **L17** and **L19**, while in these solvents, **L18** was insoluble. Hence, in

order to increase the solubility and encourage gelation, we decided to conduct the gelation test in a mixture of DMSO and water at different volume ratios. Under these experimental conditions, we were able to obtain a gel for **L18** in a mixture of DMSO/water (with a 15%v/v water). The same experimental conditions were applied also for **L17** and **L19** using different mixtures DMSO/H_2O.

As a result, we managed to obtained material that qualitatively appeared to be a gel only with **L19** (in a mixture DMSO/H_2O at 20%v/v water), whereas upon the addition of water at different ratios a precipitate of **L17** has been observed, suggesting no tendency to form a gel in these experimental conditions.

Samples, were inverted to test whether they resisted flow due to gravity, indicative of supramolecular gelation. This observations is colloquially referred to as the vial inversion test. In Figure 5.15 pictures of the tests are reported showing gel-like properties at naked eye.

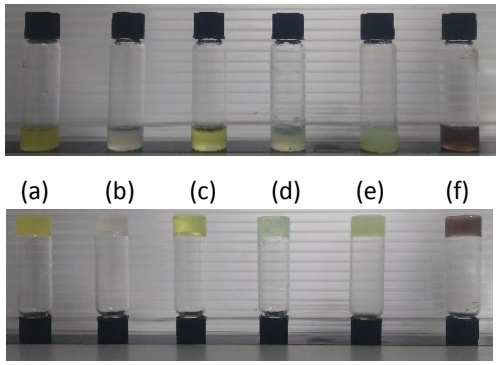

Figure 5.15 Images of the inversion tube test for the LMWG **L17**-**L19** in different solvents; (a) **L17** in nitrobenzene (0.75% w/v); (b) **L17** in chlorobenzene (0.75% w/v); (c) **L19** in nitrobenzene (1% w/v); (d) **L19** in chlorobenzene (0.75% w/v); (e) **L19** (2% w/v) in a mixture of DMSO/H_2O (20%v/v H_2O); (f) **L18** (2% w/v) in a mixture of DMSO/H_2O (15%v/v H_2O)

Once prepared, gels were characterised by oscillatory stress sweep rheometry to probe their viscoelastic properties in all solvents in which gels were formed. The solid-like character of the materials was confirmed by the fact that the G' (storage

modulus) remains significantly higher than the viscous modulus G'' up to the yield stress of the gel, the point at which the gels are sheared and form a viscous solution.

Then, the samples were dried at 70°C into the oven to obtain the xerogels and scanning electron spectroscopy (SEM) were used to capture the morphology of the xerogels obtained.

Since gels of **L17** and **L19** were achieved both in the same solvents, we were able to compare the properties of the two materials. The oscillator sweep results for **L17** and **L19** in nitrobenzene and chlorobenzene are presented in Figure 5.16. These results suggested the relatively weaker nature of the gels of **L17** compared to those of **L19** in both the solvents. Indeed, this is evident in the fairly lower value of G' of ca 1000 Pa for **L17** compared to the ca. 10000 Pa for **L19** at low stress in nitrobenzene.

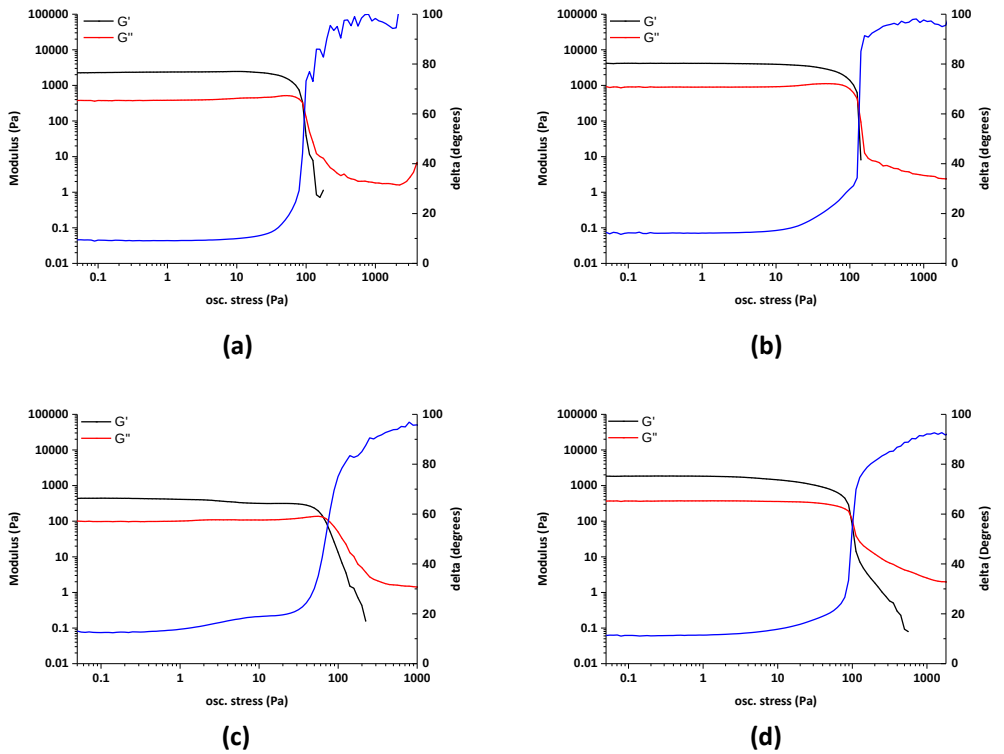

Figure 5.16 Stress-sweep rheology for LMWG **L17** in (a) nitrobenzene and (b) chlorobenzene; for **L19** in (c) nitrobenzene and (d) chlorobenzene. The solid-like

nature of the gel is evidenced by the fact that G'>>G'' and the phase difference is about 10 until the point where the gel yields.

Furthermore, the lower yield stress, that is estimated as the point where the storage and loss moduli cross over, around 80 Pa for **L17** compared to ca 100 Pa in the case of **L19**, in nitrobenzene, confirms the trend.

The rheology results achieved in chlorobenzene confirm the same trend as in nitrobenzene and allow us to identify **L19** as the best LMWG of the two. Particularly, the lower values of G' (*ca.* 1000 Pa for **L19** and ca. 700 Pa for **L17**) for both the gelators suggested a weaker nature of the gels in chlorobenzene compared to nitrobenzene. However, this value remains higher compared to the viscous modulus G''(ca 300 Pa), indicative of a very soft gel, at the boundary of being a supramolecular gel or a viscous liquid.

Indeed, one of the proofs characterising the strength of a gel are the values of the storage modulus G' (the highest the value, the more the material is solid-like) and the ratio between the storage and the viscous moduli G'/G'', that should be (for stable and 'hard' materials) around one order of magnitude of difference. The observed values of the G' and G'' moduli and, moreover, the values of the ratio G'/G'' suggested the formation of soft gels for both compounds. In the case of **L17** and **L19** the ratio G'/G'' was between 7 and 8 (nearly an order of magnitude difference), suggesting the soft nature of our materials. To further support the hypothesis of a solid-like behaviour, we consider also the lag phase, which is the phase between the applied stress and the shear stress. This value would be zero for an ideal solid while it would be 90 for an ideal Newtonian liquid.

L17 and **L19** oscillator sweep results showed a value of the lag phase close to zero and low shear stresses, thus suggesting that the two materials are viscoelastic solids. These values rise as the network is sheared and the gel breaks before eventually rising to *ca.* 90-100.

Beyond the mechanical properties, the presence of a network is a key requirement for supramolecular gelation.[13] The presence of a highly entangled network was observed using SEM (Figure 5.17)

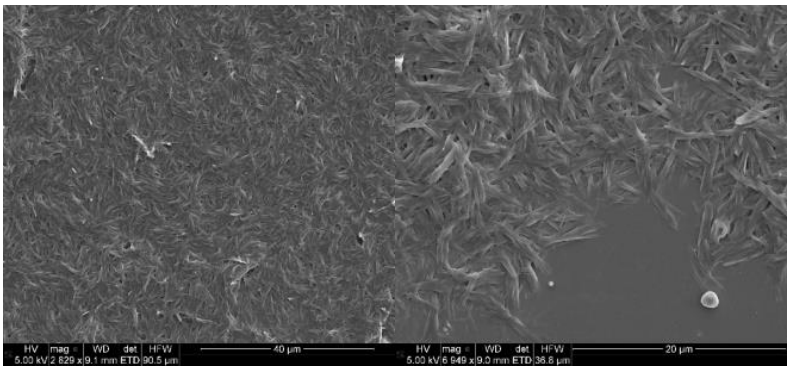

(a)

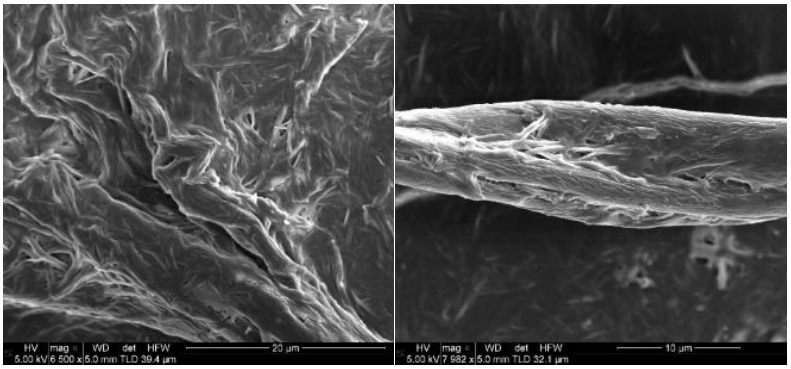

(b)

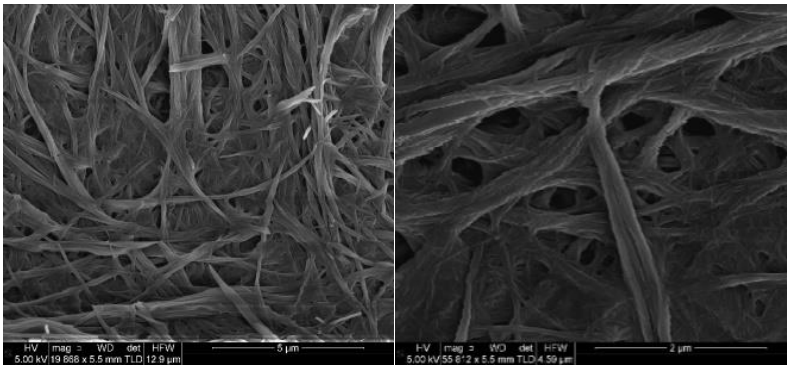

(c)

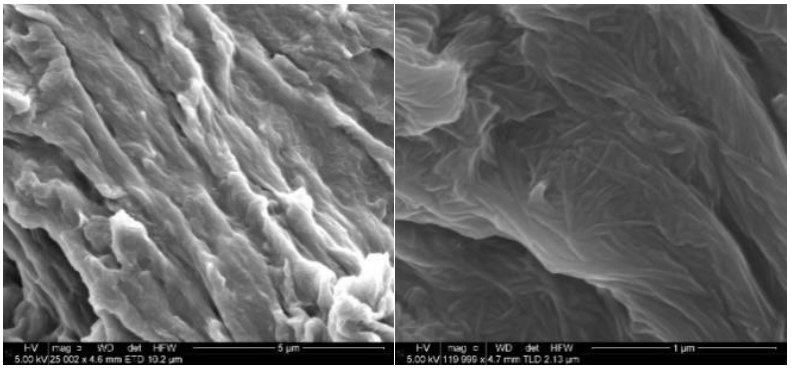

(d)

Figure 5.17 SEM images of **L17-L19** xerogel at different concentrations % w/v at different magnifications. (a) xerogel of **L19** at 1% w/v in nitrobenzene; (b) xerogel of **L19** at 0.75% w/v in chlorobenzene; (c) xerogel of **L17** at 0.75% w/v in nitrobenzene and (d)) xerogel of **L17** at 0.75% w/v in chlorobenzene.

As reported in Table 5.1, **L18** formed gels only in a mixture of DMSO/water (15% v/v water). **L18** was insoluble in most of the solvents used, precipitating in the presence of nitrobenzene, chlorobenzene, 1, 4-dioxane. The gelation in polar solvents like DMSO gave us the opportunity to perform the gelation experiments in the presence of different anion species and to investigate if the interaction LMWG-anion could modulate the properties of the materials. The oscillator sweep results presented in Figure 5.18 demonstrated that the **L18** gel in DMSO/water mixture as the strongest obtained. Indeed, the storage modulus G' is ca 33000 Pa, suggesting the high strength of the material. G' is more than one order of magnitude higher than the loss modulus, and the yield stress value is also quite high (ca 1000 Pa). Furthermore, the low lag phase near zero confirm a solid-like behaviour of the gel in this solvent mixture.

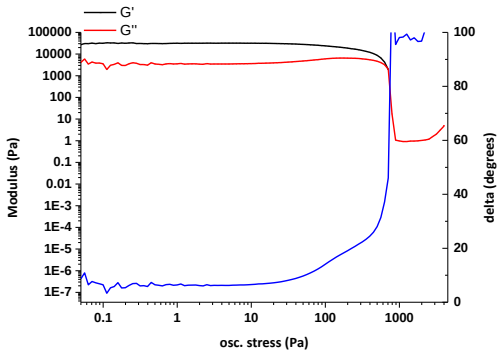

Figure. 5.18 Stress-sweep rheology for gel obtained with **L18** in a mixture of DMSO: H_2O (15% v/v water)

In Figure. 5.19 the SEM images of the xerogel of **L18** achieved after drying it at 70°C for two days are reported. Unfortunately, the presence of two high-temperature boiling solvents in the mixture (with a relevant difference in the boiling temperatures) prevented the removal of both solvents at the same time making hard to extract information regarding the real morphology of the material.

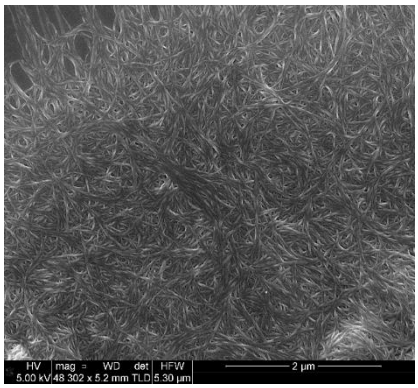

Figure 5.19 SEM image of **L18** xerogel at 2% w/v at high magnification that show a thick three-dimensional network of nanofibers.

Oscillatoratory stress sweep results for the gels of **L18** and **L19** obtained in DMSO/water mixture were compared (Figure 5.20). The weaker nature of the gel of **L19** compared to that of **L18** can be easily observed. Indeed, the value of the storage

modulus G' of ca 10000 Pa is quite lower compared to that of the gel of **L18** with a storage modulus of *ca.* 33000 Pa.

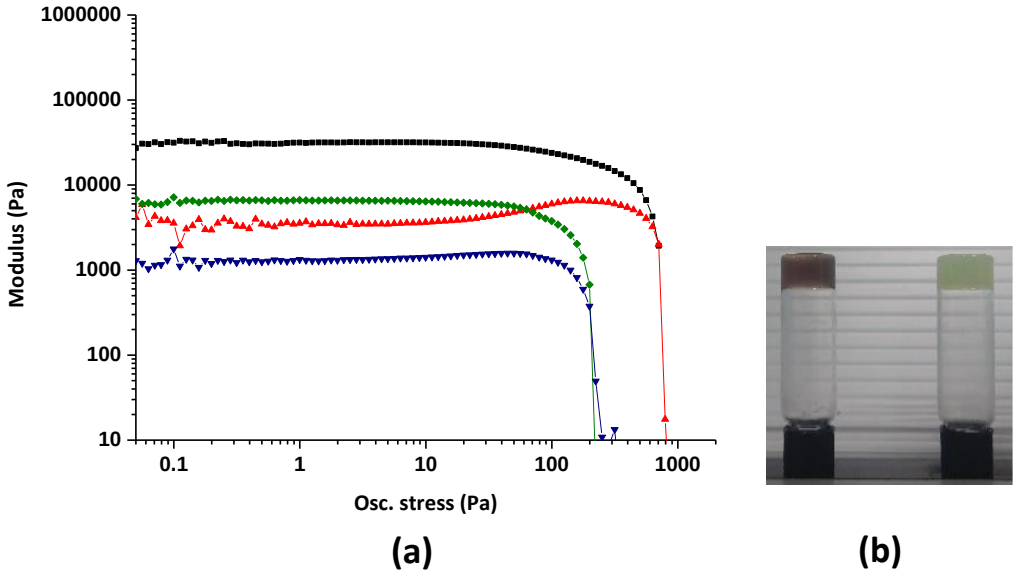

Figure 5.20 Stress-sweep rheology for gel **L18** and **L19** at 2% w/v in different mixtures of DMSO/ H_2O; G' and G'' are represented in black (squares) and red (up triangles) respectively for **L18** and in green (diamonds) and blue (down triangles) for **L19** (b) inversion tube test for the gels of **L18** and **L19** at 2% w/v in different mixtures of DMSO/ H_2O

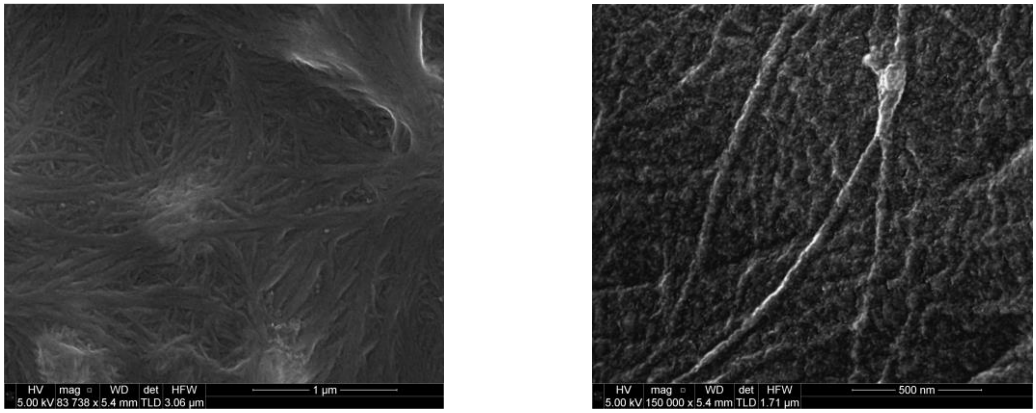

(a) **(b)**

Figure 5.21 SEM images of **L19** xerogel at 2% w/v at different magnifications.

In an attempt to elucidate the interactions involved in the formation of the gels, ATR FT-IR and pXRD analysis on gelator powder and xerogels were performed. Unfortunately, both spectroscopic techniques were ineffective because of the noise and the low intensity of the characteristic bands in the case of the IR spectroscopy, and the lack of diffraction pattern in the case of the pXRD difractograms for all the three small gelators.

5.5 Anion tuning of the gelation properties of L18

As already mentioned in Paragraph 5.1, the urea self-association could be modulated by the presence of a third component within the gel system, represented in our specific case by an anion species. Indeed, the potential host-guest interactions could modulate the self-association properties of the compounds and, hence, the bulk material behaviour of the gels, particularly the rheology and, specifically in a fluorescent system, its own emission properties. Hence, in order to test this approach, gelation tests on LMWG **L18** in the presence of different anion species (in a 1:1 ratio with respect to the gelator) added as tetrabutylammonium salts (Cl^-, BzO^-, $H_2PO_4^-$, F^-) were performed using the same solvent mixture and the same concentration

described above. The inversion tube test for the gelation experiments performed are reported in Figure 5.22.

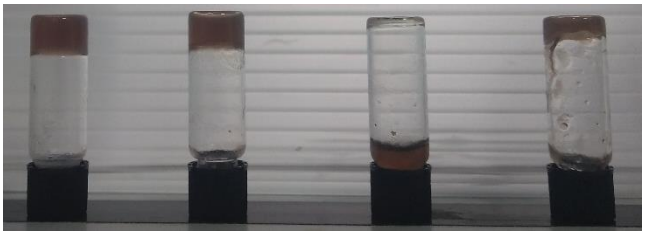

(a) (b) (c) (d)

Figure 5.22 Inversion tube test for the **L18** gels in presence of a 1:1 ratio of different anion species as tetrabutylammonium salts; (a) TBACl; (b) $TBAH_2PO_4$; (c)TBAF; (d)TBABzO at 2% w/v in DMSO/ H_2O (15% v/v water).

It is possible to observe that the presence of chloride and dihydrogen phosphate does not appear to affect the gelation process, whereas the addition of benzoate and, moreover, fluoride results in the breakdown of the gel.

Therefore, in order to explain this behaviour anion-binding studies were conducted by means of ^{1}H-NMR titrations using DMSO-d_6/0.5% water as a solvent. Stability constants from the obtained ^{1}H-NMR titration curves were calculated by fitting the data to a 1:2 (receptor:anion) binding model using WinEQNMR[27] as shown in Table 5.2 and 5.3

Table 5.2 Association constants (K_a/M^{-1}) for the formation of the 1:2 adducts of **L18** (monitoring the downfield shift of the NH signal attributed to the indole moiety) with anions added as tetrabutylammonium salts in DMSO-d_6/0.5% water at 300 K. All errors estimated to be ≤15%.

	F^-	**Cl^{--}**	**BzO^-**	**$H_2PO_4^-$**
L18	Deprot.	<10	9198	9309

As shown in Table 5.2 the formation of a H-bond interaction between the anion guests and the indole NH of **L18** can be observed. However, by monitoring the H-bond formation following the downfield shift of one of the N-H peaks, attributed to the urea moiety, we were able to measure a weaker interaction between **L18** and $H_2PO_4^-$ species compared to BzO^-, as suggested by the association constant values reported in Table 5.3.

Importantly, in the absence of the information on the competitive self-association of the free ligand that should take place in the beginning of the gelation process, we could only hypothesise the mechanism of the inhibition of the gelation process caused by different anion species. As reported in Tables 5.2 and 5.3, upon the addition of fluoride the deprotonation of **L18** was observed. Deprotonation should inhibit the self-association of the compound due to the absence of the NH protons of the urea moiety and for this reason, the gel might not form. The association constant value for both the NH protons suggested how cooperative H-bonding between the indole and the urea NHs with BzO^- anion might prevent gelation by hampering the formation of the urea α-tape. On the other hand, in the case of dihydrogen phosphate the H-bond formed between the anion and the indole NH is stronger than that between the anion and the urea NH, thus a lower degree of cooperativity can be hypothesised in this case. In other words, although the indole moiety is strongly interacting with the anion, the urea moiety should be available to trigger the dimerization process for the gel formation.

Table 5.3 Association constants (K_a/M^{-1}) for the formation of the 1:2 adducts of **L18** (monitoring the downfield shift of the one of the NH signal attributed to the urea moiety) with anions added as tetrabutylammonium salts in DMSO-d_6/0.5% water at 300 K. All errors estimated to be≤15%

	F^-	Cl^{--}	BzO^-	$H_2PO_4^-$
L18	deprot[a]	<10	10080	3494

5.6 Preparation of gels from L20-L24 and their characterization

A family of long alkyl chain urea-based compounds as small gelators **L20-L22** have been synthesised following the synthetic procedure reported in the experimental section (paragraph 5.8). These compounds are distinguished by the presence of an alkyl chain of different length and by the presence of a nitro group in *ortho* position as substituent on the aromatic rings of the different ligands. Our interest was to design a system enable to interact by means of non-covalent interactions in solution forming oligomers solid-like materials, and moreover to tune their properties in presence of different species enable to interact with a moiety of the molecule.

In particular, the aim of this part of the work was to study the tendency of these compounds to form supramolecular metallogels due to the presence of a metal cation, like copper (added as a chloride hydrate salt), into the system. In literature several example of supramolecular metallogel, of urea based gelators are reported, but there are really few examples of metallogel formed from nitrourea based gelator.

In theory, we supposed that the assembly of the nitrophenyl urea could be partially inhibited by the formation of an intramolecular hydrogen bond between the nitro group and one of the urea NH proton. The addition of copper should disfavour the intramolecular H-bond between the nitro group and the NH by the coordination of the metal ion and thus improve the self-assembly process.

Furthermore, the addition of an anion with good affinity for copper should be able to further tune the properties of the system.

Gelation tests on compounds **L20-L22** were carried out at different concentrations in a wide range of solvents (nitrobenzene, chlorobenzene, nitromethane, 1,4-dioxane, tetrahydrofuran, acetonitrile, dichloromethane, chloroform, methanol, ethanol, 1-isopropanol, 2-isopropanol, 1-butanone, ethyl acetate, dimethyl sulfoxide, dimethyl sulfoxide:water). Samples were sonicated, then heated gently to dissolve the solid, and subsequently allowed to cool to room temperature. Full results are presented in the Table 5.4.

Table 5.4 Gelation tests of **L20-L22** performed at 1% w/v in different solvents.

	$BzNO_2$ (1% w/v)	**BzCl (1% w/v)**	**Toluene (1% w/v)**	**EtOH (1% w/v)**
L20	no gel	no gel	no gel	no gel
L21	no gel	no gel	no gel	no gel
L22	no gel	gel	ppt	gel

L_{20}-L_{22} have been tested with the rest of the solvents detecting no gel formation

As reported in Table 5.4, only in the case of **L22** gels were obtained, specifically in chlorobenzene and ethanol. The results obtained in polar solvents like ethanol are particularly interesting because the solubilization of metal salts and anion species (added as tetrabutylammonium salt) is favoured in such solvents. Hence, in order to examine how the absence of a metal cation firstly, and then the presence of a third component represented by an anion species was able to modulate the behavior of the LMWG **L22**, we decided to perform the gelation tests in the same conditions in the presence of these species. The results of the performed tests are reported in Table 5.5 and evidence the gelation for all the made attempts.

Table 5.5 Gelation tests of **L22** performed at 1% w/v in ethanol.

	Free ligand	**$CuCl_2 \cdot 2H_2O$ (0.5:1)**	**$CuCl_2\ 2H_2O$ (1:1)**	**$CuCl_2\ 2H_2O$ (2:1)**	**$CuCl_2\ 2H_2O$ + TBAAcO**
L22	gel	gel	gel	gel	gel

Tests have been performed also with **L_{20}-L_{21}** detecting no gel formation

In order to investigate the morphology of the gels obtained in presence of different components, the gel samples were dried at 70°C into the oven to obtain the xerogels, and then SEM was used to capture the morphology of the gels obtained (Figure 5.23). The images of the free ligand (Figure 5.23a) showed a rod-shaped nature of the gel fibres, whereas the contrast of the images suggested a slight precipitate on the fibres. It appears that moving from the free ligand to the other two multicomponent samples, especially in presence of a 1:1:1 ratio of hydrate $CuCl_2$ and TBAAcO, wider sheet-shaped structures perhaps indicating more lateral association, are observed.

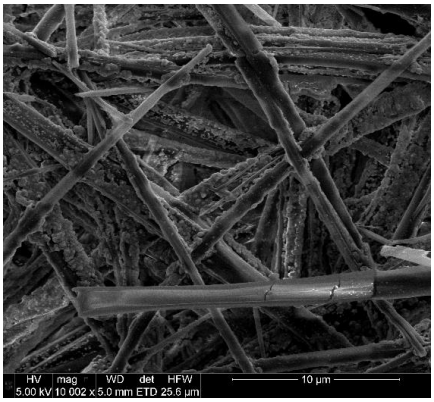
HV mag WD det HFW
5.00 kV 10 002 x 5.0 mm ETD 25.6 µm
10 µm

(a)

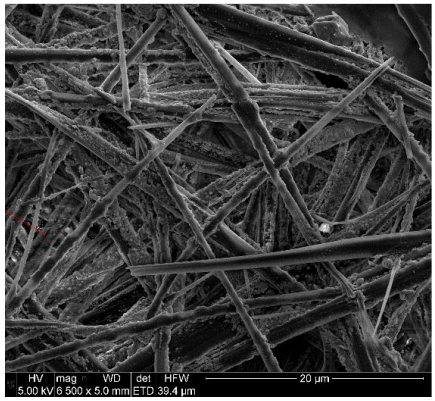
HV mag WD det HFW
5.00 kV 6 500 x 5.0 mm ETD 39.4 µm
20 µm

(b)

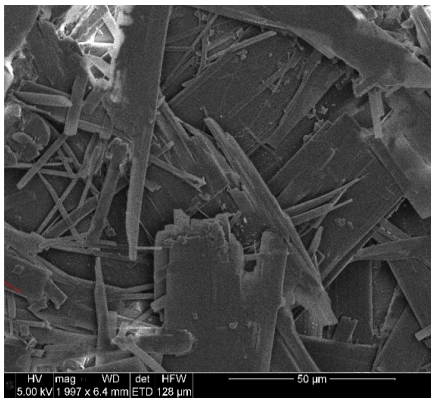
HV mag WD det HFW
5.00 kV 1 997 x 6.4 mm ETD 128 µm
50 µm

(c)

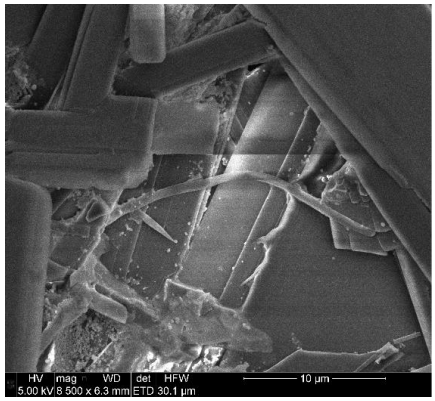
HV mag WD det HFW
5.00 kV 8 500 x 6.3 mm ETD 30.1 µm
10 µm

(d)

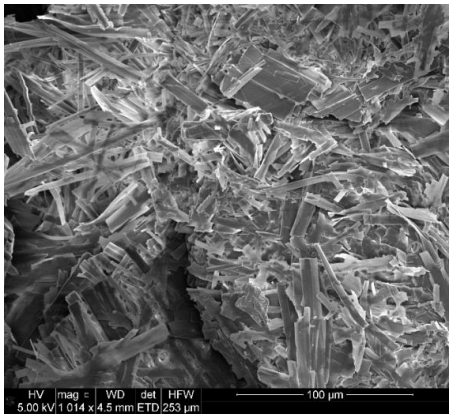

(e)

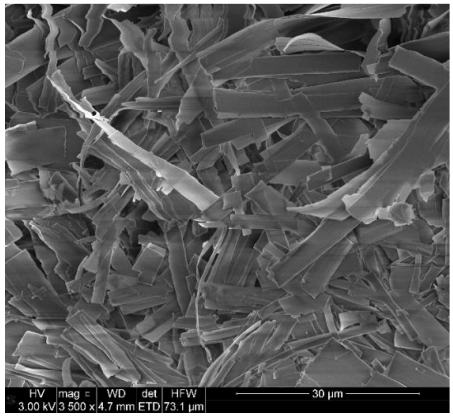

(f)

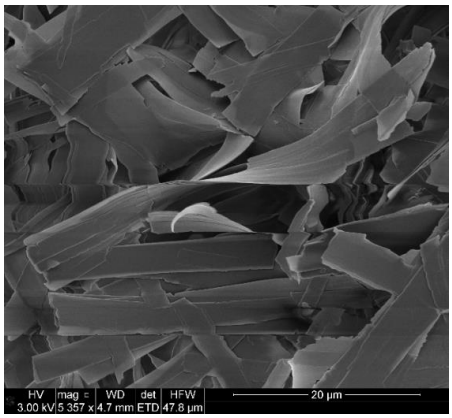

(g)

Figure 5.23 SEM images of **L22** xerogel at 1% w/v at different magnifications and in presence of different components: (a) and (b) **L22** as a free ligand; (c) and (d) **L22** at 1% w/v in presence of a 1:1 ratio of hydrate $CuCl_2$; (e), (f) and (g) **L22** at 1% w/v in presence of a 1:1:1 ratio of hydrate $CuCl_2$ and TBAAcO.

Gels of **L22** were characterised by oscillatory stress sweep rheometry to probe their viscoelastic properties in ethanol (Figure 5.24). The solid-like character of the materials was manifest in the fact that the G' (storage modulus) remains well higher than the viscous modulus G'' up to the yield stress of the gel. The value of the storage modulus G' (ca 10000 Pa), the ratio G'/G'', the yield stress, as well as the lag phase, suggested similar solid like behaviour for the gels of **L22** as the free ligand (Figure 5.24 a), in the presence of 1 equivalent of hydrate $CuCl_2$ (Figure 5.24b) and in the presence

of 1 equivalent of hydrate $CuCl_2$ and one equivalent of TBAAcO (Figure 5.24c). In particular, although the value of the storage modulus should highlight a solid nature of the gels, the ratio between the two moduli and the lag phase indicate a soft nature of the materials.

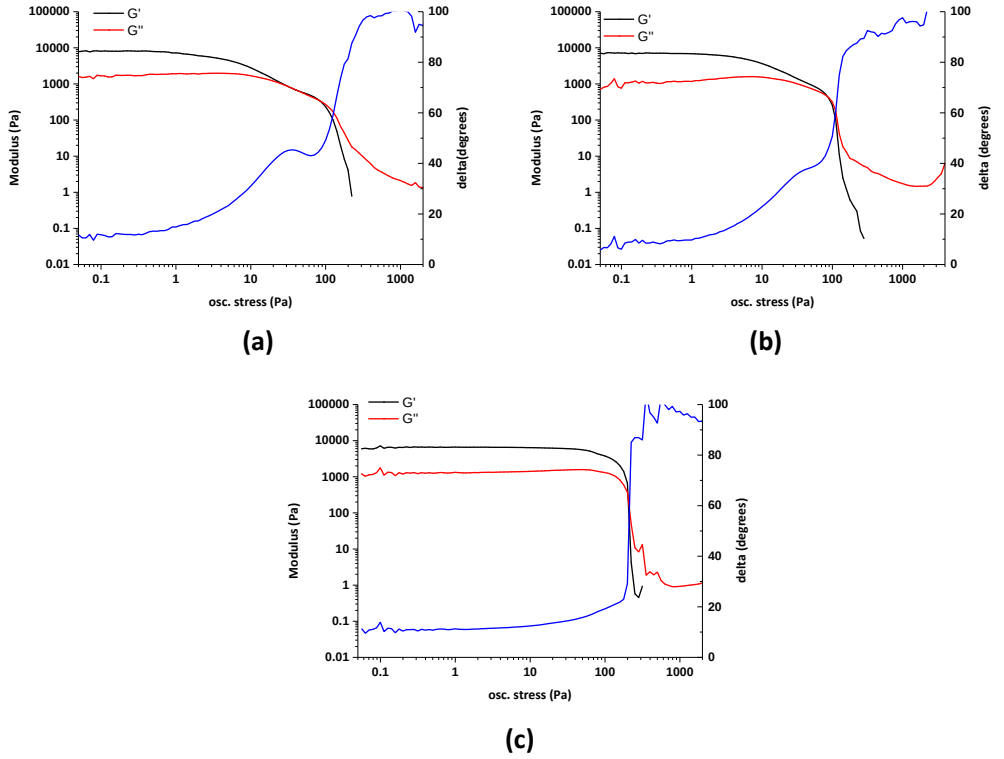

Figure 5.24 Stress-sweep rheology for (a) gel **L22** as a free ligand at 1% w/v**;** (b) **L22** at 1% w/v in presence of a 1:1 ratio of hydrate $CuCl_2$; (c) **L22** at 1% w/v in presence of a 1:1:1 ratio of hydrate $CuCl_2$ and TBAAcO.

As shown in Figure 5.24 the rheology results for **L22** as free ligand (Figure 5.24 a) describe a quite soft material, as evidenced by the trend of the phase lag that increases just at a value of 20 Pa of shear stress. Although the value of the storage modulus is quite high (ca 10000 Pa) and higher than the loss/viscous modulus, the ratio between them is not too high and considering also the low value of the yield stress, these results suggest a weak solid-like behaviour of the gel of **L22**, that could

be expressed in a soft nature of the material obtained. Upon the addition of a second component, the copper (II) cation (added as hydrate chloride salt), the sweep oscillatory stress at the same experimental conditions suggested an increase of the solid-like behaviour of the material, as indicated by of the lag phase trend and by the yield stress value (Figure 5.24b). In fact, as presented in the rheology graph recorded for the free ligand we observed a first crosspoint between the two moduli G' and G'' at *ca* 20 Pa indicating a quite weak resistance to the stress applied to the material. Moreover, upon the addition of the metal cation component, we could observe an increase of the crosspoint, at around 100 Pa. Further a change in the lag phase trend, that still suggest a soft nature of our material, but with an increased solid-like behaviour. Finally, under the same experimental conditions in the presence of three component (**L22**, $CuCl_2 \cdot H_2O$ and TBAAcO in 1:1:1 molar ratio) the sweep rheology results revealed a material with higher solid-like behaviour compared to the other obtained for the single component and two components systems (Figure 5.24c). Indeed, the sample still display a quite high value of the storage modulus G', higher than the loss/viscous modulus G''. Interestingly, a linear value of the lag phase during the shear stress application and a higher value of the yield stress are observed, suggesting a further increase of the solid-like properties of the system in the presence of three components.

In the attempt to justify the different behaviours described by the rheology, the three samples were dried at 70°C into the oven to obtain the xerogels and then powder X-ray diffraction and ATR FT-IR analysis have been conducted. The ATR-FT IR spectrum and the diffractogram of free **L22** as a powder were also recorded. The ATR-FT-IR for the single sample and the overlapping graph with the three systems (single, two and three components systems) are reported in Figure 5.25. We were able to observe the appearance of a new band at 1184 cm^{-1} in the two components system (**L22** + $CuCl_2 \cdot H_2O$, 1:1 molar ratio) and the broadening of the –NH stretching band at 3300 cm^{-1}, suggesting some interaction between the two species. However, in the three components system (**L22**, $CuCl_2 \cdot H_2O$ and TBAAcO in 1:1:1 molar ratio the

disappearance of the band at 1184 cm^{-1} was detected, suggesting a change in the Cu(II)- **L22** interaction observed in the previous spectrum. Indeed, the ATR-FTIR spectrum of the three components system is similar to the spectrum of **L22** as free ligand xerogel and **L22** as powder.

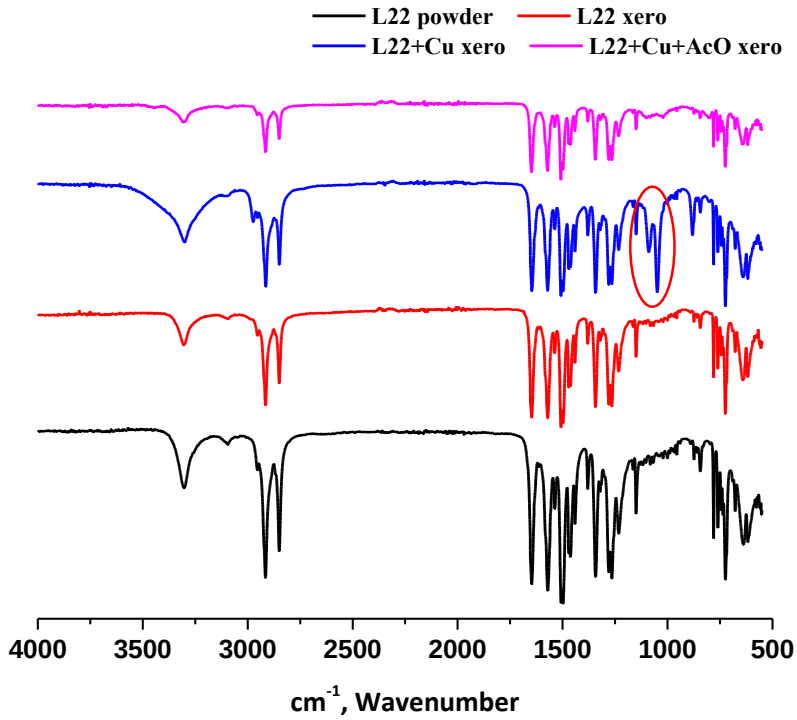

Figure 5.25 FT-ATR-IR specta of **L22** as a powder(black), the xerogels of free ligand (red) and in presence of a 1:1 ratio of $CuCl_2 \cdot H_2O$ (blue)and in presence of a 1:1:1 ratio of $CuCl_2 \cdot H_2O$ and TBAAcO (magenta).

The overlapping PXRD pattern for the four systems studied is reported in Figure 5.26. As shown in the graph, no appreciable variation was detected in the diffractograms of the different xerogel samples, suggesting that the presence of the metal ion and the anion, and the xerogel form of **L22** do not affect the diffraction pattern of the gelator.

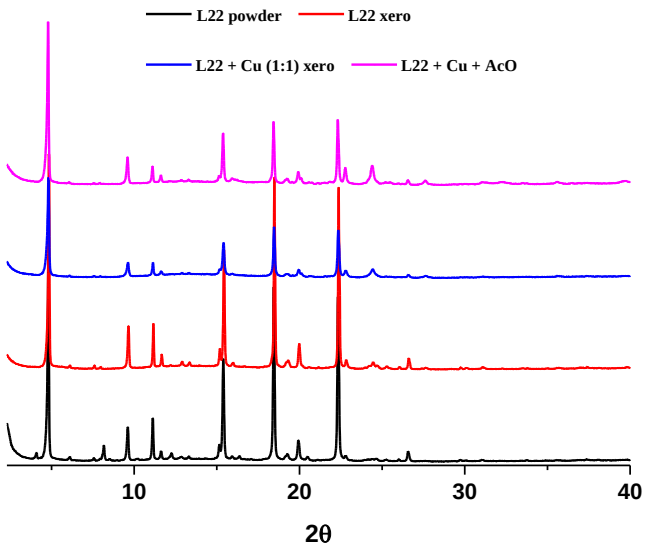

Figure 5.26 Stack Plot of the PXRD pattern of **L22** as a powder(black), the xerogels of free ligand (red)and in presence of a 1:1 ratio of $CuCl_2 \cdot H_2O$ (blue)and in presence of a 1:1:1 ratio of $CuCl_2 \cdot H_2O$ and TBAAcO(magenta)

Furthermore, in order to better understand the behaviour of **L22** we decided to synthesise a simpler model molecule **A** (namely 1-isopropyl-3-(2-nitrophenyl)urea and reported in Figure 5.27) with higher solubility in the wide range of solvents used and then, in theory, easier to crystallize.

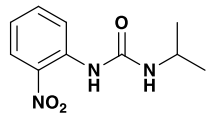

A

Figure 5.27 structure of the model molecule **A**

A was synthesised following the procedure reported by Perveen *et al.* [28] and described in Scheme 5.5

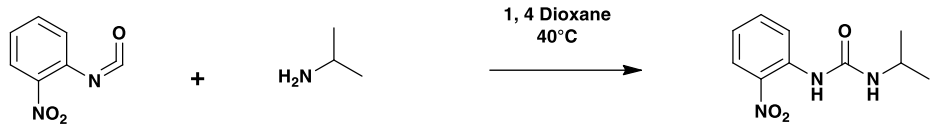

Scheme 5.5 Reaction scheme adopted for the synthesis of **A**

Several crystallization attempts using different techniques in a wide range of solvents were carried out. The crystallization experiments performed in methanol are reported in Table 5.6

Table 5.6 Crystallization experiments of model molecule performed methanol. Samples were sonicated, then heated gently to dissolve the solid, and subsequently allowed to cool to room temperature

	Solvent	**Method**	**Results**
Free ligand	methanol	Slow evaporation	Single crystals
$CuCl_2 \cdot 2H_2O$ (0.5:1)	methanol	Slow evaporation	In progress
$CuCl_2 \cdot 2H_2O$ (1:1)	methanol	Slow evaporation	In progress
$CuCl_2 \cdot 2H_2O$ (2:1)	methanol	Slow evaporation	In progress
$CuCl_2 \cdot 2H_2O$ + TBAAcO	methanol	Slow evaporation	In progress
$CuCl_2 \cdot 2H_2O$ + TBAAcO	methanol	Slow evaporation	In progress
TBAAcO	methanol	Slow evaporation	In progress

As reported in Table 5.6 we are still working in order to obtain results enable to describe the behaviour of the system. However, at the moment we were able to obtain the crystal structure of the free ligand from methanol through slow evaporation of the solvent. The results confirmed our hypothesis about the presence of an intramolecular hydrogen bond O=N-O---H-N (2.162Å) between the nitrogroup in *ortho* position on the aromatic ring and the –NH proton of the closer urea moiety.

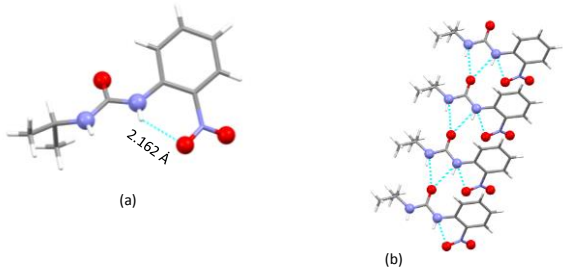

Figure 5.28 (a) Crystal structure of **A** and (b) portion of the crystal packing.

Gelation tests on LMWGs **L23-L24** were carried out at different concentrations in a wide range of solvents ($BzNO_2$, CH_3NO_2, BzCl, Dioxane, THF, CH_3CN, CH_2Cl_2, CH_3Cl, MeOH, EtOH, 1-isopropanol, 2-isopropanol, butanone, EtOAc, DMSO, DMSO:water). Samples were sonicated, then heated gently to dissolve the solid, and subsequently allowed to cool to room temperature. Full results are tabulated in the Table 5.7.

Table 5.7 Gelation tests of **L23-L24** performed at 1% w/v with different solvents. temperature

	$BzNO_2$ (2% w/v)	**BzCl (2% w/v)**	**CH_3NO_2 (2% w/v)**	**Toluene (2% w/v)**	**Dioxane (2% w/v)**
L23	Ppt	Ppt	Ppt	Ppt	Ppt
L24	gel	gel	Ppt	Ppt	Ppt

L23 and **L24** has been tested with the rest of the solvents detecting no gel formation and precipitation of the gelators up to the 1% w/v.

As reported in Table 5.7, only **L24** formed gels at the conditions used in nitrobenzene and chlorobenzene whereas, at the same conditions with the rest of the solvents selected, a precipitation of the compound at higher than 1% w/v concentration or no gelation at lower than that concentration were detected. Firstly, inversion tube test response was performed. Pictures of the tests are reported In Figure 5.29 revealing first gel-like property which we could evaluate.

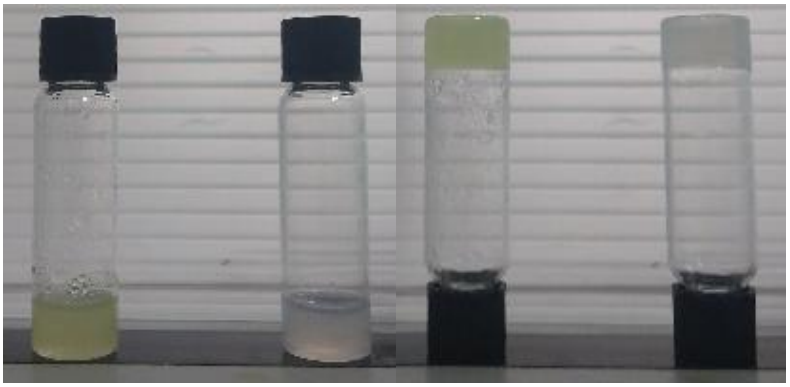

(a) (b)

Figure 5.29 images of the inversion tube test for the LMWG **L24** in (a) nitrobenzene and (b) chlorobenzene at 2% w/v

Once prepared, the sample were at 70°C into the oven to obtain the corresponding xerogels, and then SEM has been used to capture the structure/morphology of the gels obtained (Figure 5.29) An entangle network of fibres can be identify. Although could be hard to compare and to associate the images of the xerogels obtained with the rheology results, it is interesting to notice how the fibres of **L24** in nitrobenzene (Figure 5.29a) appears more define and more solid compared to chlorobenzene (Figure 5.29b), as suggested even by the magnification of the imagine we needed to appreciate the sample details.

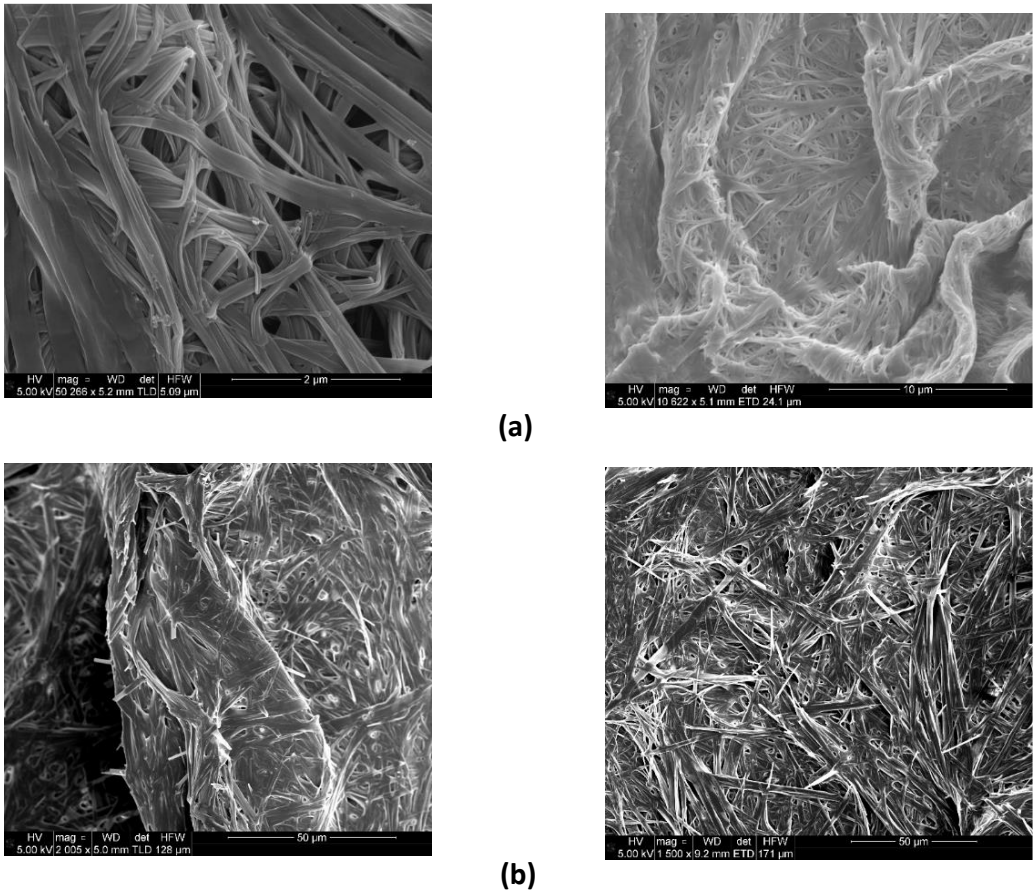

Figure 5.30 SEM images of **L24** xerogel at 2% w/v in (a) nitrobenzene and in (b) chlorobenzene at different magnifications

Gels of **L24** were characterised by oscillatory stress sweep rheometry to probe their viscoelastic properties in both solvents it formed gels.(Figure 5.30) The solid-like character of the materials is manifest in the fact that the G' (storage modulus) remains well higher than the viscous modulus G'' up to the yield stress of the gel. The value of the storage modulus G' (ca 10000 pa in both the solvents), the ratio between the storage and the loss/viscous moduli, the yield stress higher than 100 pa but quite similar for both the materials, as well as the lag phase, although not zero but lower than 20 degrees suggested similar solid-like behaviours for the two gels of **L24** obtained. Therefore, although the value of the storage modulus should highlight a

solid-like nature of the gels, the ratio between the two moduli and the lag phase suggest a quite soft nature of the materials.

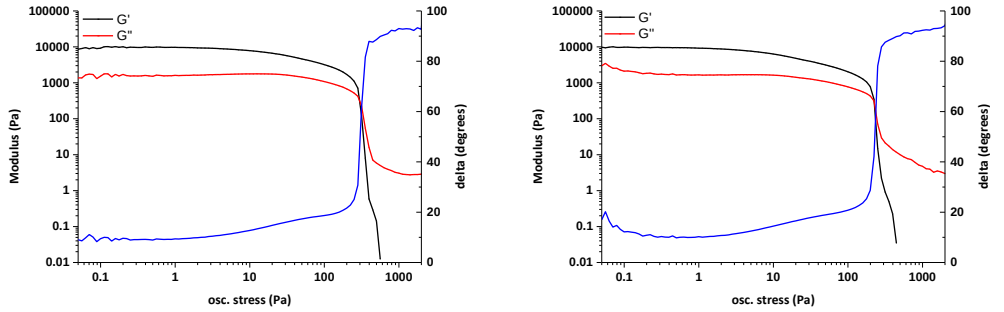

Figure 5.31 Stress-sweep rheology for LMWG **L24** in (a) nitrobenzene and (b) in chlorobenzene at 2% w/v.

5.7 Conclusions

In conclusion, we developed two novel families of LMWGs: the bis urea-based **L17**-**L19** bearing fluorophore units and the long alkyl chain urea-based **L20**-**L24** bearing different aryl units as a substituents. The rheology results demonstrate that **L18** exhibits the strongest solid-like properties when prepared in a mixture of DMSO/water with the 15% v/v of water. Particularly, inhibition tests performed in this media demonstrates that the presence of BzO^- and F^- inhibits the gelation process. ^{1}H-NMR titrations in DMSO d_6 performed in presence of the different anion species tested suggests a cooperative H-bonding between the indole and the urea NHs with BzO^- whereas a lower degree of cooperativity was observed in the case of $H_2PO_4^-$ with a stronger H-bond due to the indole NH with respect to the urea NH. We hypothesise that, in the case of dihydrogen phosphate, the urea moiety should be available to trigger the dimerization process for the gel formation.

L22 formed gels in a polar-like media as ethanol. Interestingly, changes in the mechanic properties as well as in the morphology of the materials obtained in presence of different

species (a metal ion or an anion) were suggested by rheology and SEM analysis. In particular, an increase of the solid-like behaviour was observed moving from the free ligand compound to the three components system (gelator + metal ion + anion).

5.8 Experimental part

All reactions were performed in oven-dried glassware under a slight positive pressure of nitrogen. ^{1}H-NMR (300 MHz) and ^{13}C NMR (100 MHz) spectra were determined on a 300 MHz Bruker. Chemical shifts for 1H NMR are reported in parts per million (ppm), calibrated to the residual solvent peak set, with coupling constants reported in Hertz (Hz). The following abbreviations are used for spin multiplicity: s = singlet, d = doublet, t = triplet, m = multiplet . Chemical shifts for 13C NMR are reported in ppm, relative to the central line of a septet at δ = 39.52 ppm for deuteriodimethyl sulfoxide. Infrared All solvents and starting materials were purchased from commercial sources where available. Proton NMR titrations were performed by adding aliquots of the putative anionic guest (as the TBA salt, 0.075 M) in a solution of the receptor (0.005M) in DMSO-d6/0.5% water to a solution of the receptor (0.005M).

FT-IR spectra of all solids were taken in the lab on a Perkin-Elmer Spectrum 100 Series spectrometer. Oscillatory stress sweep experiments were performed between 0.1 – 1000 Pa at a constant frequency of 1 Hz on a TA instruments AR 2000 rheometer equipped with a rough plate geometry. When preparing the sample, 2 ml of gelator solution was transferred to a sealed glass cylinder on the lower plate. The gels were allowed 30 minutes to equilibrate before the geometry was lowered onto the sample at a pre-determined gap of 2.2-2.5 mm, and the glass cylinder gently removed before running the experiment. Single crystal data was collected at 120.0(2) K on a Bruker D8Venture diffractometer (PHOTON-100 CMOS detector, IμSmicrosource, focusing mirrors, MoKα, λ = 0.71073Å) and processed using Bruker APEX-II software. The temperature of the samples was maintained by the Cryostream (Oxford Cryosystems) open-flow nitrogen cryostat. The structure was solved by direct method and refined by full-matrix least squares on F2 for all data using Xseed and SHELXTL software. SEM samples were dried in

vacuo for two days, and coated with 2 nm of platinum of chromium using a Cressington 328 Ultra High Resolution EM Coating System.

5.8.1 Synthesis

1,1'-(methylenebis(2,6-diethyl-4,1-phenylene))bis(3-(quinolin-8-yl)urea) (**L17**)

To a stirred solution of 8-aminoquinoline (1 equiv) and triethylamine (1 equiv) in CH_3CN a solution of bis(3,5-diethyl-4-isocyanatophenyl)methane (1 equiv) in CH_3CN (5 mL) was added dropwise. The solution was heated at 70° C and stirred for 24h. When the reaction was cooled, a precipitate was observed and isolated by filtration. The solid was further washed with dichloromethane (3x5 mL), and dried under reduced pressure to remove the residual solvent obtaining the product as crude white solid. Y = 41%; ^{1}H-NMR (300 MHz, , 298 K), δ_H: 9.74(s, 1H) 8.91(d, 1H), 8.52 (d, 1H), 8.36(t, 1H), 7.64(m, 2H), 7.50(s, 2H), 7.03(dd, 1H), 3.70(s, 1H), 2.65(q, 4H), 1.34(t, 6H)^{13}C-NMR 13.43, 42.74, 43.85, 118.63, 120.65, 123.87, 124.68, 125,47, 127,42, 133.12, 134.45, 135.95, 136.86, 137.73, 141.45, 144.53, 153.44

1,1'-(methylenebis(2,6-diethyl-4,1-phenylene))bis(3-(1H-indol-7-yl)urea) (**L18**)

To a stirred solution of 7-aminoindole (1 equiv) in CH_2Cl_2 the bis(3,5-diethyl-4-isocyanatophenyl)methane (1 equiv) was added. The solution was kept stirring at room tempetature for 24h. when the reaction was stopped, a precipitate was observed and isolated by filtration. The solid was further washed with dichloromethane (3x5 mL), and dried under reduced pressure to remove the residual solvent obtaining the product as crude grey solid. Y = 85%; ^{1}H-NMR (300 MHz, , 298 K), δ_H: 10.68(s, 1H), 8.66(broad, 1H), 7.68 (s, 1H), 7.30(s, 1H), 7.24(d, 1H), 7.10(d, 1H), 7.03(s, 2H), 6.89(t, 1H), 6.40(s, 1H), 3.87(s, 1H), 2.60(q, 4H), 1.14(t, 6H)^{13}C-NMR 13.43, 27.92, 42.74, 103.57, 125.34, 125,47, 132.06 133.45, 153.50

N,N'-(((((methylenebis(2,6-diethyl-4,1-phenylene))bis(azanediyl))bis(carbonyl))bis(azanediyl)bis(ethane-2,1-diyl))bis(5-(dimethylamino)naphthalene-1-sulfonamide (**L19**)

To a stirred solution of N-(2-aminoethyl)-5-(dimethylamino)naphthalene-1-sulfonamide (1 equiv) in CH_2Cl_2 the bis(3,5-diethyl-4-isocyanatophenyl)methane (1 equiv) was added. The solution was kept stirring at room tempetature for 24h. when the reaction was stopped, a precipitate was observed and isolated by filtration. The solid was further washed with dichloromethane (3x5 mL), and dried under reduced pressure to remove the residual solvent obtaining the product as crude yellow solid. Y = 81%; ^{1}H-NMR (300 MHz, , 298 K), δ_H: 8.46(d, 1H), 8.26(d, 1H), 8.09 (d, 1H), 8.07(broad, 1H), 7.58(q, 2H), 7.40(s, 1H), 7.25(d, 1H), 6.91(s, 2H), 6.06 (broad, 1H) 3.78(s, 1H), 3.03(dd, 2H), 2.82(s, 6H), 2.76(dd, 2H), 2.40(q, 4H), 1.00(t, 6H)^{13}C-NMR 13.43, 27.92, 37.8, 41.77, 42.74, 43.85, 112.9, 116,7, 123.37, 125,05, 125,47, 128,7, 132.2, 132.8, 133.45, 135.95, 137.78, 141.78, 144.6, 156.98

General procedure for urea long alkyl chain based LMWG **L20-L22**

To a stirred solution of 2-nitrophenylisocyanate (1 equiv) in CH_2Cl_2 a solution of the amine (1 equiv) in CH_2Cl_2 (5 mL) was added dropwise. The solution was kept stirring at room tempetature for 24h. Then the solvent was removed under reduced pressure and the product purified through chromatography column (Hex:EtAcO 4:1) isolating a crude yellow solid.

1-dodecyl-3-(2-nitrophenyl)urea (**L20**)

Y= 87% mp = 135°C ^{1}H-NMR (400 MHz, , 298 K, $CDCl_3$), δ_H: 9.78(s, 1H), 8.68 (dd, 1H), 8.18 (dd, 1H), 7.59(t, 2H), 7.03(t, 2H), 4.95(s, 1H), 3.30(t, 2H), 1.59(q, 2H), 1.33 (m, 22H), 0.88(t, 3H)^{13}C-NMR 155.2,139.9, 138.6,128.3,124.0, 123.9,110.2, 34.56, 32.30, 31.99, 31.93, 29.5, 25.32, 16.8 IR: ν_{CO} =1522, ν_{NH} = 3331 cm^{-1}

1-tetradecyl-3-(2-nitrophenyl)urea (**L21**)

Y= 97.5% mp = 155°C ^{1}H-NMR (400 MHz, , 298 K, $CDCl_3$), δ_H: 9.78(s, 1H), 8.68 (dd, 1H), 8.18 (dd, 1H), 7.59(t, 2H), 7.03(t, 2H), 4.95(s, 1H), 3.23(t, 2H), 1.59(q, 2H), 1.25 (m, 22H), 0.88(t, 3H)^{13}C-NMR 155.2,139.9, 138.6,128.3,124.0, 123.9,110.2, 34.56, 32.30, 31.99, 31.93, 29.52, 25.32, 16.73 IR: ν_{CO} =1522, ν_{NH} = 3331 cm^{-1}

1-hexadecyl-3-(2-nitrophenyl)urea (**L22**)

54% mp = 253°C ^{1}H-NMR (400 MHz, , 298 K, $CDCl_3$), δ_H: 9.78(s, 1H), 8.68 (dd, 1H), 8.18 (dd, 1H), 7.59(t, 2H), 7.03(t, 2H), 4.95(s, 1H), 3.33(t, 2H), 1.61(q, 2H), 1.37 (m, 24H), 0.91(t, 3H)^{13}C-NMR 156.69, 138.6, 128.3,124.0, 123.9, 110.2, 34.56, 32.30, 31.99, 31.93, 29.5, 25.32, 16.34 IR: ν_{CO} =1522, ν_{NH} = 3331 cm^{-1}

General procedure for urea long alkyl chain based LMWG **L23-L24**

To a stirred solution of 1-naphtylisocyanate (1 equiv) in CH_2Cl_2 a solution of the amine (1 equiv) in CH_2Cl_2 (5 mL) was added dropwise. The solution was kept stirring at room tempetature for 24h and a precipitate was observed. Then the solid was filtrated and washed with dichloromethane (3x5mL). Then the solid was dried under reduced pressure to remove the residual solvent collecting the product as crude white solid.

1-tetradecyl-3-(naphthalen-1-yl)urea (**L23**)

Y= 80.0% mp = 144°C ^{1}H-NMR (400 MHz, , 298 K, $CDCl_3$), δ_H: 10.12(s, 1H), 8.13 (s, 1H), 7.78 (dd, 1H), 7.63(dd, 1H), 7.44(m, 2H), 7.38 (m, 3H), 3.06(t, 2H), 1.61(q, 2H), 1.37 (m, 20H), 1.00(t, 3H)^{13}C-NMR 156.55, 137.06, 135.29, 129.25, 126.14, 125.44, 124.77, 124.45, 123.46, 40.44, 31.64, 29.49, 29.06, 28.98, 22.93, 14.01, IR: ν_{CO} =1522, ν_{NH} = 3331 cm^{-1}

1-hexadecyl-3-(naphthalen-1-yl)urea (**L24**)

Y= 85.5% mp = 152°C ^{1}H-NMR (400 MHz, , 298 K, $CDCl_3$), δ_H: 10.15(s, 1H), 8.10 (s, 1H), 7.78 (dd, 1H), 7.63(dd, 1H), 7.44(m, 2H), 7.38 (m, 3H), 3.03(t, 2H), 1.58(q, 2H), 1.41 (m,

24H), 0.96(t, 3H)^{13}C-NMR 156.55, 137.06, 135.29, 129.25, 126.14, 125.44, 124.77, 124.45, 123.46, 40.44, 31.64, 29.49, 29.06, 28.98, 22.93, 14.01, IR: ν_{CO} =1522, ν_{NH} = 3331 cm^{-1}

5.8.2 ^{1}H-NMR titrations

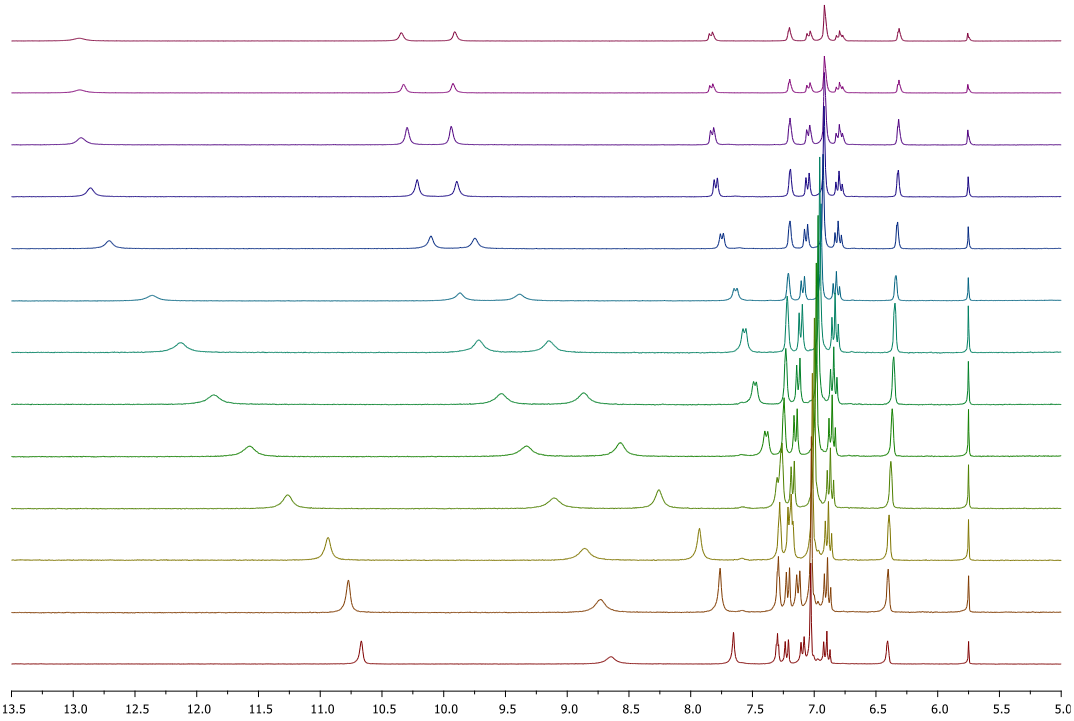

Figure 5.32 Stack plot of the ^{1}H-NMR spectra of **L18** (0.005 M) upon addition of increasing amount of $TBAH_2PO_4$ (0.075 M) in DMSO-d_6.

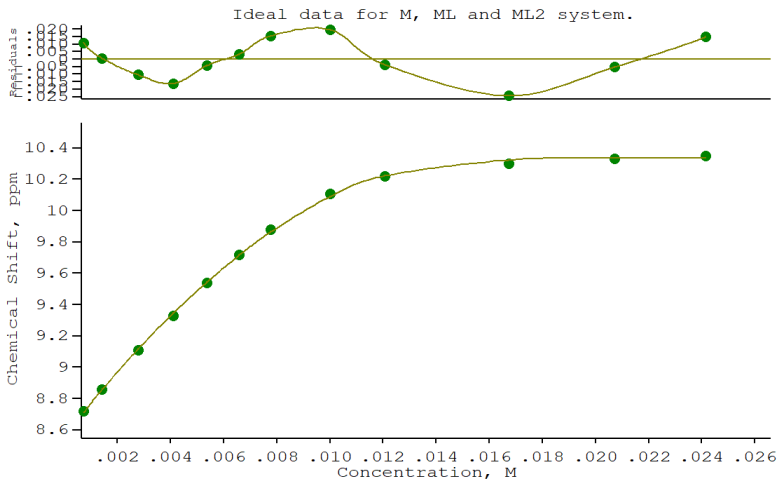

Calculations by WinEQNMR2 Version 2.00 by Michael J. Hynes

Program run at 15:09:28 on 10/31/2019

Ideal data for M, ML and ML2 system.

IDEAL DATA TAKEN FROM ACTUAL FIT of JIMMY1.FIT

Reactions: M + L = ML (beta1 = K1); M + 2L = ML2 (beta2 = K1K2)

Theoretical: k1=39.75, k1k2 =289.07 del ML = -27.83, del ML2 = -82.29

File prepared by M.J. Hynes october 22 2000 (Shift is on 119Sn)

Equilibrium constants are floating point numbers

NO. A PARAMETER DELTA ERROR CONDITION DESCRIPTION

1 1 1.28489E+02 1.000E-01 1.484E+02 1.803E+03 BETA1

2 1 4.48958E+05 2.000E+00 5.506E+04 1.809E+00 BETA2

3 1 8.52693E+00 1.000E+00 2.111E-02 5.162E+00 Sn SHIFT

4 1 1.25705E+01 1.000E-01 3.380E+00 1.958E+03 Sn(L) SHIFT

5 1 1.03092E+01 5.000E-01 2.870E-02 1.344E+01 Sn(L)2 SHIFT

0RMS ERROR = 1.69E-02 MAX ERROR = 2.42E-02 AT OBS.NO. 10

RESIDUALS SQUARED = 2.00E-03

RFACTOR = 0.1328 PERCENT

Figure 5.33 ^{1}H-NMR titration of **L18** with $TBAH_2PO_4$ in DMSO-d_6 following the NH proton attributed to the urea moiety

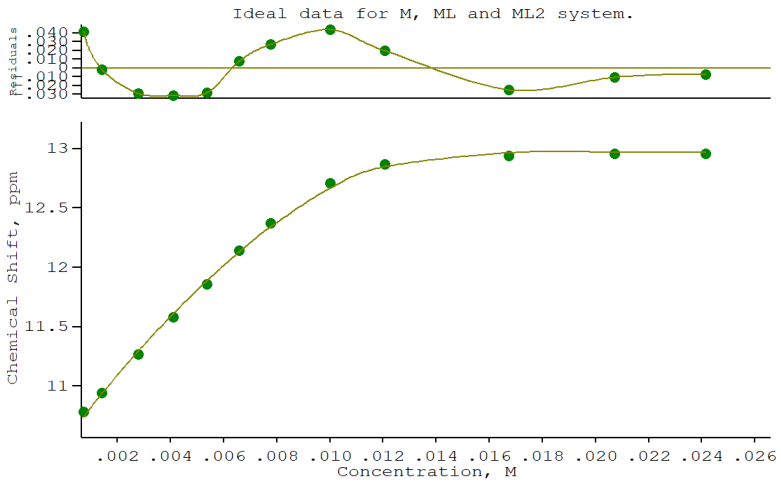

Calculations by WinEQNMR2 Version 2.00 by Michael J. Hynes

Program run at 15:10:28 on 10/31/2019

Ideal data for M, ML and ML2 system.

IDEAL DATA TAKEN FROM ACTUAL FIT of JIMMY1.FIT

Reactions: M + L = ML (beta1 = K1); M + 2L = ML2 (beta2 = K1K2)

Theoretical: k1=39.75, k1k2 =289.07 del ML = -27.83, del ML2 = -82.29

File prepared by M.J. Hynes october 22 2000 (Shift is on 119Sn)

Equilibrium constants are floating point numbers

NO.	A	PARAMETER	DELTA	ERROR	CONDITION	DESCRIPTION
1	1	7.06895E+01	1.000E-01	2.460E+02	6.595E+03	BETA1
2	1	6.58082E+05	2.000E+00	9.872E+04	1.404E+00	BETA2
3	1	1.04873E+01	1.000E+00	4.205E-02	5.008E+00	Sn SHIFT
4	1	1.98216E+01	1.000E-01	2.722E+01	6.846E+03	Sn(L) SHIFT
5	1	1.29336E+01	5.000E-01	4.828E-02	1.007E+01	Sn(L)2 SHIFT

0RMS ERROR = 3.44E-02 MAX ERROR = 4.40E-02 AT OBS.NO. 8

RESIDUALS SQUARED = 8.29E-03

RFACTOR = 0.2165 PERCENT

Figure 5.34 ^{1}H-NMR titration of **L18** with $TBAH_2PO_4$ in DMSO-d_6 following the NH proton attributed to the indole moiety

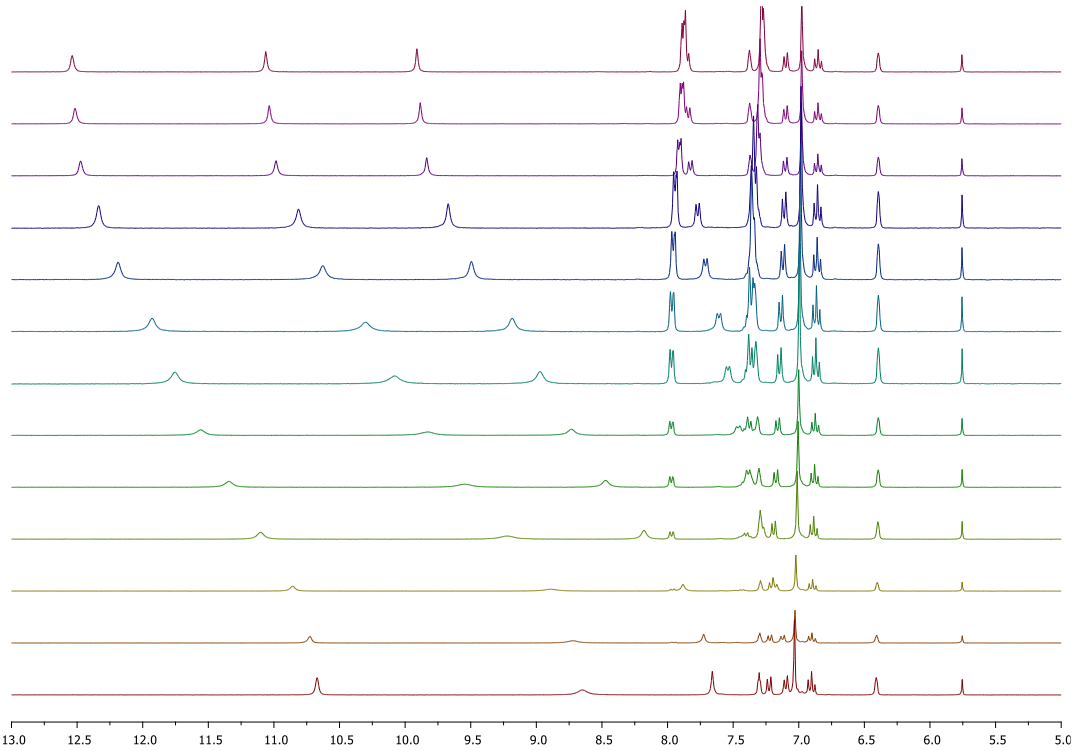

Figure 5.35 Stack plot of the ^{1}H-NMR spectra of **L18** (0.005 M) upon addition of increasing amount of TBABzO (0.075 M) in DMSO-d_6.

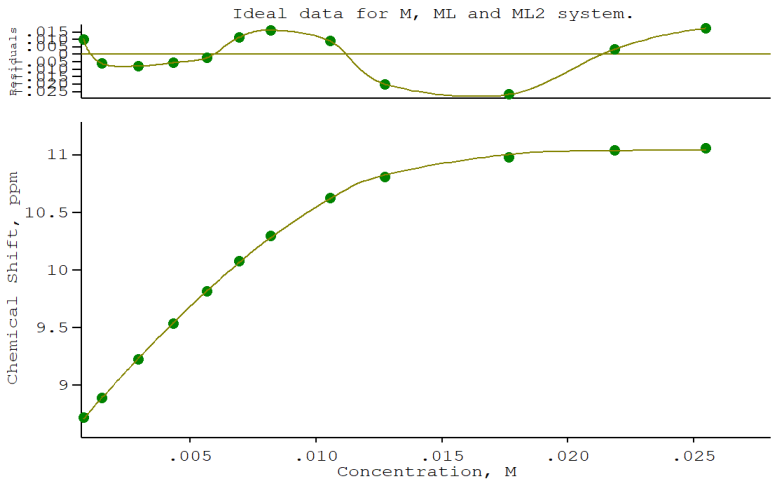

Calculations by WinEQNMR2 Version 2.00 by Michael J. Hynes

Program run at 15:11:51 on 10/31/2019

Ideal data for M, ML and ML2 system.

IDEAL DATA TAKEN FROM ACTUAL FIT of JIMMY1.FIT

Reactions: M + L = ML (beta1 = K1); M + 2L = ML2 (beta2 = K1K2)

Theoretical: k1=39.75, k1k2 =289.07 del ML = -27.83, del ML2 = -82.29

File prepared by M.J. Hynes october 22 2000 (Shift is on 119Sn)

Equilibrium constants are floating point numbers

NO. A PARAMETER DELTA ERROR CONDITION DESCRIPTION

1 1 3.13555E+01 1.000E-01 9.346E+01 1.151E+04 BETA1

2 1 3.16038E+05 2.000E+00 5.369E+04 1.598E+00 BETA2

3 1 8.50694E+00 1.000E+00 2.156E-02 5.330E+00 Sn SHIFT

4 1 1.92993E+01 1.000E-01 2.807E+01 1.209E+04 Sn(L) SHIFT

5 1 1.10216E+01 5.000E-01 3.583E-02 2.076E+01 Sn(L)2 SHIFT

0RMS ERROR = 1.75E-02 MAX ERROR = 2.68E-02 AT OBS.NO. 10

RESIDUALS SQUARED = 2.15E-03

RFACTOR = 0.1323 PERCENT

Figure 5.36 ^{1}H-NMR titration of **L18** with TBABzO in DMSO-d_6 following the NH proton attributed to the urea moiety

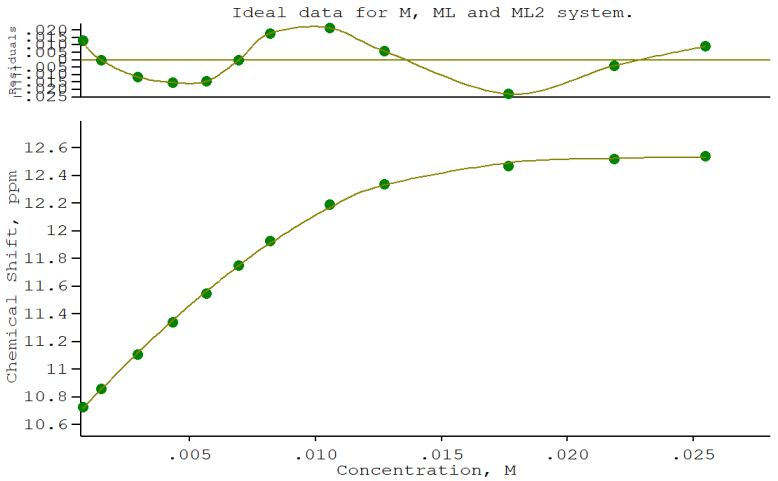

Calculations by WinEQNMR2 Version 2.00 by Michael J. Hynes

Program run at 15:12:57 on 10/31/2019

Ideal data for M, ML and ML2 system.

IDEAL DATA TAKEN FROM ACTUAL FIT of JIMMY1.FIT

Reactions: M + L = ML (beta1 = K1); M + 2L = ML2 (beta2 = K1K2)

Theoretical: k1=39.75, k1k2 =289.07 del ML = -27.83, del ML2 = -82.29

File prepared by M.J. Hynes october 22 2000 (Shift is on 119Sn)

Equilibrium constants are floating point numbers

NO.	A	PARAMETER	DELTA	ERROR	CONDITION	DESCRIPTION
1	1	2.28975E+01	1.000E-01	9.317E+01	1.858E+04	BETA1
2	1	2.10614E+05	2.000E+00	4.082E+04	2.424E+00	BETA2
3	1	1.05619E+01	1.000E+00	2.497E-02	7.446E+00	Sn SHIFT
4	1	2.12775E+01	1.000E-01	3.908E+01	1.924E+04	Sn(L) SHIFT
5	1	1.25068E+01	5.000E-01	3.723E-02	2.084E+01	Sn(L)2 SHIFT

0RMS ERROR = 1.77E-02 MAX ERROR = 2.30E-02 AT OBS.NO. 10

RESIDUALS SQUARED = 2.19E-03

RFACTOR = 0.1145 PERCENT

Figure 5.37 ^{1}H-NMR titration of **L18** with TBABzO in DMSO-d_6 following the NH proton attributed to the indole moiety

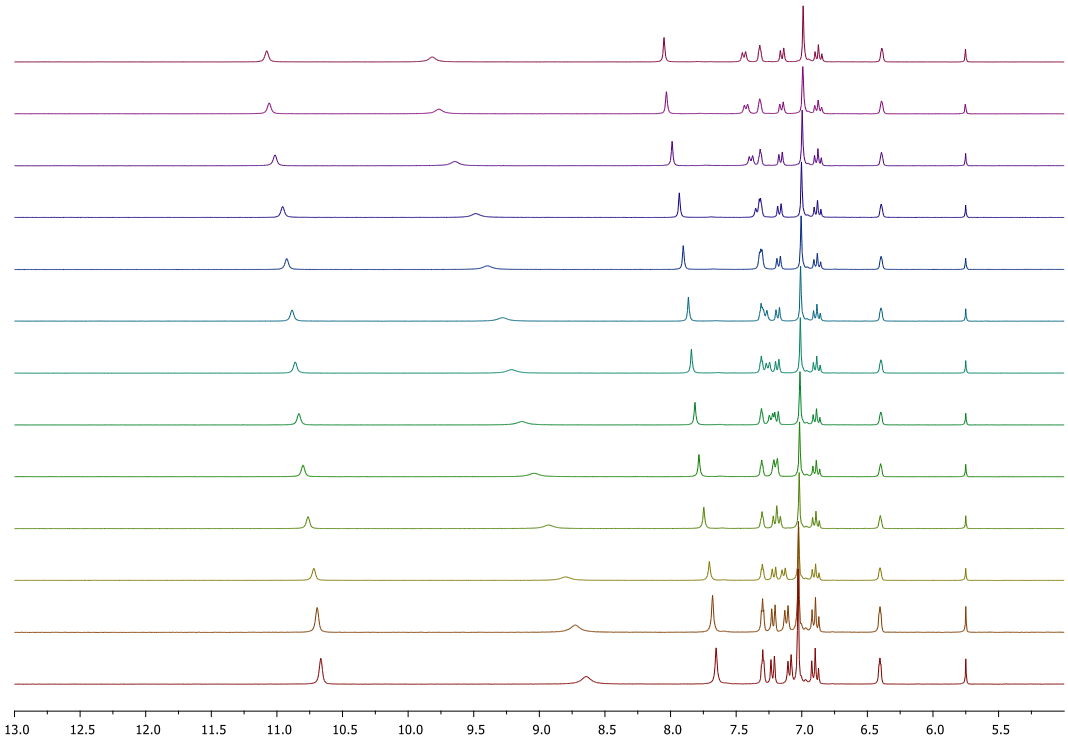

Figure 5.38 Stack plot of the ^{1}H-NMR spectra of **L18** (0.005 M) upon addition of increasing amount of TBACl (0.075 M) in DMSO-d_6.

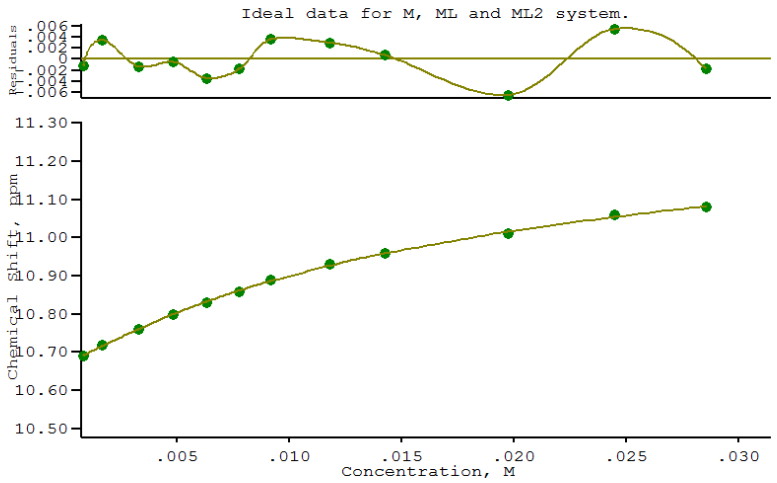

Calculations by WinEQNMR2 Version 2.00 by Michael J. Hynes

Program run at 15:31:24 on 10/31/2019

Ideal data for M, ML and ML2 system.

IDEAL DATA TAKEN FROM ACTUAL FIT of JIMMY1.FIT

Reactions: M + L = ML (beta1 = K1); M + 2L = ML2 (beta2 = K1K2)

Theoretical: k1=39.75, k1k2 =289.07 del ML = -27.83, del ML2 = -82.29

File prepared by M.J. Hynes october 22 2000 (Shift is on 119Sn)

Equilibrium constants are floating point numbers

NO. A PARAMETER DELTA ERROR CONDITION DESCRIPTION

1 1 8.47228E+01 1.000E-01 1.107E+02 1.022E+04 BETA1

2 1 9.49590E+01 2.000E+00 3.390E+03 1.549E+05 BETA2

3 1 1.06637E+01 1.000E+00 4.315E-03 5.374E+00 Sn SHIFT

4 1 1.12297E+01 1.000E-01 5.119E-01 2.991E+04 Sn(L) SHIFT

5 1 1.27706E+01 5.000E-01 4.851E+01 1.000E+05 Sn(L)2 SHIFT

0RMS ERROR = 4.26E-03 MAX ERROR = 6.45E-03 AT OBS.NO. 10

RESIDUALS SQUARED = 1.27E-04

RFACTOR = 0.0299 PERCENT

Figure 5.39 ^{1}H-NMR titration of **L18** with TBACl in DMSO-d_6 following the NH proton attributed to the urea moiety

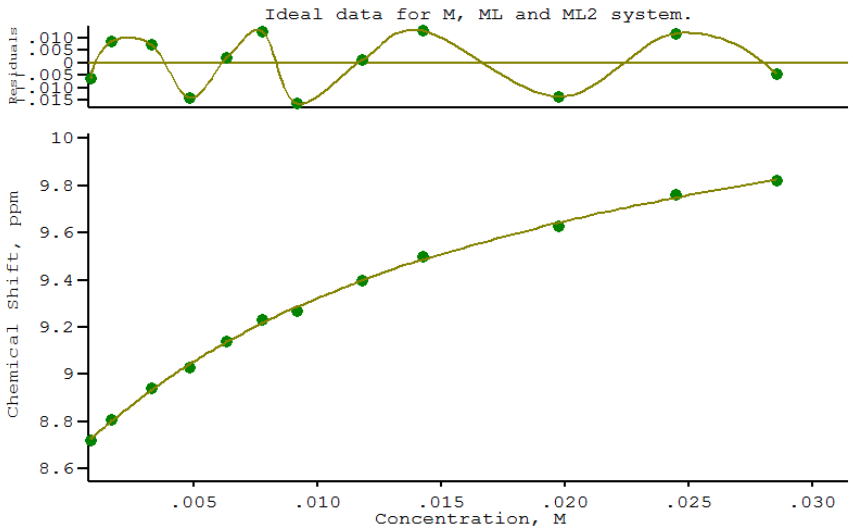

Calculations by WinEQNMR2 Version 2.00 by Michael J. Hynes

Program run at 15:43:59 on 10/31/2019

Ideal data for M, ML and ML2 system.

IDEAL DATA TAKEN FROM ACTUAL FIT of JIMMY1.FIT

Reactions: M + L = ML (beta1 = K1); M + 2L = ML2 (beta2 = K1K2)

Theoretical: k1=39.75, k1k2 =289.07 del ML = -27.83, del ML2 = -82.29

File prepared by M.J. Hynes october 22 2000 (Shift is on 119Sn)

Equilibrium constants are floating point numbers

NO.	A	PARAMETER	DELTA	ERROR	CONDITION	DESCRIPTION
1	1	1.09533E+02	1.000E-01	5.813E+01	8.258E+02	BETA1
2	1	9.52041E+01	2.000E+00	6.843E+02	1.297E+04	BETA2
3	1	8.64413E+00	1.000E+00	1.393E-02	4.859E+00	Sn SHIFT
4	1	1.00619E+01	1.000E-01	4.164E-01	2.413E+03	Sn(L) SHIFT
5	1	1.88615E+01	5.000E-01	5.880E+01	1.021E+04	Sn(L)2 SHIFT

0RMS ERROR = 1.36E-02 MAX ERROR = 1.65E-02 AT OBS.NO. 7

RESIDUALS SQUARED = 1.30E-03

RFACTOR = 0.1121 PERCENT

Figure 5.40 ^{1}H-NMR titration of **L18** with TBACl in DMSO-d_6 following the NH proton attributed to the indole moiety

5.9 References

1. W. J. Peveler, H. Packman, S. Alexander, R. R. Chauhan, L. M. Hayes, T. J. Macdonald, J. K. Cockcroft, S. Rogers, D. G. A. L. Aarts, C. J. Carmalt, I. P. Parkin and J. C. Bear, *Soft Matt.*, 2018, **14**, 8821-8827.
2. S. M. Hashemnejad and S. Kundu, *Langmuir*, 2017, **33**, 7769-7779.
3. J. Ruíz-Olles and D. K. Smith, *Chem. Sci.*, 2018, **9**, 5541-5550.
4. D. B. Amabilino, D. K. Smith and J. W. Steed, *Chem. Soc. Rev.*, 2017, **46**, 2404-2420.
5. P. R. A. Chivers and D. K. Smith, *Nature Rev. Mat.*, 2019, **4**, 463-478.
6. J. Buendía, E. Matesanz, D. K. Smith and L. Sánchez, *CrystEngComm*, 2015, **17**, 8146-8152.
7. A. R. Hirst and D. K. Smith, *Chemistry – Eur. J.*, 2005, **11**, 5496-5508.
8. N. N. Adarsh, D. K. Kumar and P. Dastidar, *Tetrahedron*, 2007, **63**, 7386-7396.
9. M.-O. M. Piepenbrock, G. O. Lloyd, N. Clarke and J. W. Steed, *Chem. Rev.*, 2010, **110**, 1960-2004.
10. P. J. Flory, *Faraday Disc. Chem. Soc.*, 1974, **57**, 7-18.
11. G. A. Buxton and N. Clarke, *Phys. Rev. Lett.*, 2007, **98**, 238103.
12. C. E. Stanley, N. Clarke, K. M. Anderson, J. A. Elder, J. T. Lenthall and J. W. Steed, *Chem. Comm.*, 2006, 3199-3201.
13. Y. Sang and M. Liu, *Mol. Sys. Des. & Eng.*, 2019, **4**, 11-28.
14. J. Sun, Y. Li, F. Yan, C. Liu, Y. Sang, F. Tian, Q. Feng, P. Duan, L. Zhang, X. Shi, B. Ding and M. Liu, *Nature Comm.*, 2018, **9**, 2599.
15. Z. Shen, T. Wang and M. Liu, *Angew. Chem. Int. Ed.*, 2014, **53**, 13424-13428.
16. H. Cao, P. Duan, X. Zhu, J. Jiang and M. Liu, *Chemistry – Eur. J.*, 2012, **18**, 5546-5550.
17. B. G. Bag and R. Majumdar, *Chem. Rec.*, 2017, **17**, 841-873.
18. P. Sutar and T. K. Maji, *Chem. Comm.*, 2016, **52**, 13136-13139.
19. J. W. Steed, *Chem. Soc. Rev.*, 2010, **39**, 3686-3699.

20. J. Bernstein, R. E. Davis, L. Shimoni and N.-L. Chang, *Angew. Chem. Int. Ed. Engl.*, 1995, **34**, 1555-1573.
21. K. D. M. Harris, *Supramol. Chem.*, 2007, **19**, 47-53.
22. L. A. Estroff and A. D. Hamilton, *Chem. Rev.*, 2004, **104**, 1201-1218.
23. F. S. Schoonbeek, J. H. van Esch, R. Hulst, R. M. Kellogg and B. L. Feringa, *Chem. – Eur. J.*, 2000, **6**, 2633-2643.
24. E. Ressouche, S. Pensec, B. Isare, G. Ducouret and L. Bouteiller, *ACS Macro Letters*, 2016, **5**, 244-247.
25. C. D. Jones, H. T. D. Simmons, K. E. Horner, K. Liu, R. L. Thompson and J. W. Steed, *Nature Chem.*, 2019, **11**, 375-381.
26. M.-O. M. Piepenbrock, G. O. Lloyd, N. Clarke and J. W. Steed, *Chem. Comm.*, 2008, 2644-2646.
27. M. J. Hynes, *J. Chem. Soc., Dalton Trans.*, 1993, 311-312.
28. S. Perveen and S. Mustafa, *J. Chem. Soc. Pak.*, 2013, **35**, 1605-16013.

Appendix A

Selenoureas for anion binding as molecular logic gates

Appendix A

A.1 Introduction

Classic molecular logic gates are based on molecules which are able to perform a logic operation when one (or more) chemical process acts as input and one (or more) easily detectable analytical signal acts as output. The first pioneering works in this field were reported by Aviram[1]and de Silva[2] almost 30 years ago. In particular, de Silva *et al.*, realised that the binary notation, zeros and ones, and the principles of Boolean language, could be applied to chemical systems and they reported the first molecular logic AND gate using protons and sodium ions as chemical inputs and fluorescence as optical output.[2] Since then, many examples of molecular logic gates have been developed and the complexity of the realized logic functions has dramatically increased.[3-8] Most of the described molecular logic gates are based on fluorescent chemosensors because the "OFF" or "ON" fluorescent status can be straightforwardly translated into the "0" or "1" Boolean operations. Nevertheless, Keinan *et al*. demonstrated that chemical shift and peak integration in ^{1}H-NMR spectra can be efficiently used as measurable parameters to develop an infochemical device able to perform three different operations, i) text encoding, ii) encryption of 21-digit binary numbers and their addition and subtraction, and iii) encryption of 21-digit decimal numbers.[9] Jurczak proposed a novel strategy for the classification of guest chirality based on the combination of artificial neural networks and anion-receptor chemistry using ^{1}H-NMR spectroscopy.[10]

Urea and thiourea moieties have been widely used for the design of artificial receptors for anion binding and sensing.[11-13] Recently, Caltagirone *et al*. proposed for the first time selenoureas as a new binding motif for anion recognition and sensing.[14] Normally, ureas and thioureas act, at least in solution, as bidentate ligands for anions forming eight-membered ring with oxoanions or six-membered rings with spherical anions such as halides,[15, 16] while , to the best of our knowledge, stable mono-coordinated adducts

are unknown. Following our interest in the development of selenourea-based receptors for anion binding, we designed and synthesised a new family of aromatic selenoureas **AL1**-**AL3** and we compared their anion binding properties with those of the corresponding thioureas (**AL4**-**AL6**) and ureas (**AL7**-**AL9**) using ^{1}H-NMR spectroscopy in DMSO-d_6 (Figure. A1). We wanted to explore the possibility for selenoureas of forming mono-coordinated adducts in solution along with classic bi-coordinated ones and, therefore, the possibility to construct molecular logic gates based on the nature of the adduct formed, as illustrated hereinafter.

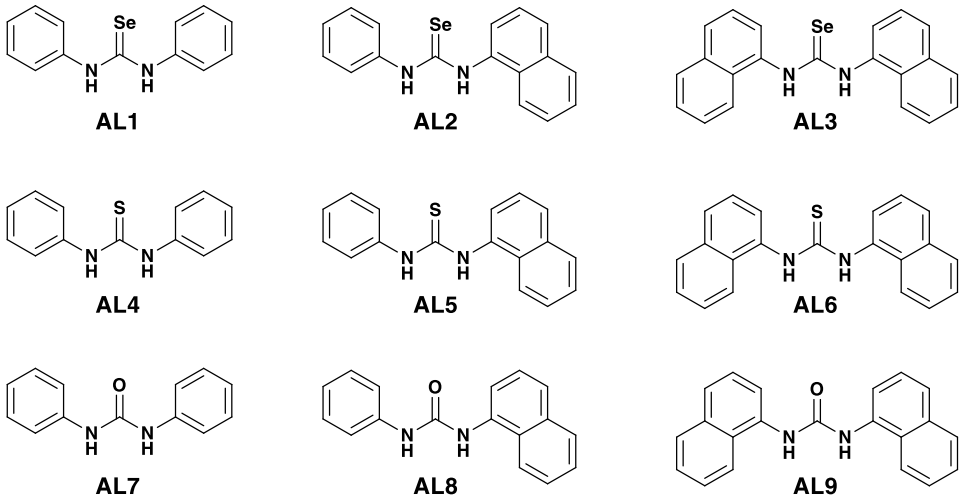

Figure A1 Receptors presented in the appendix

A.2 Results and discussion

The synthesis of the selenoureas **AL1-AL3** is based on the reaction of phenyl isoselenocyanate (for **AL1**) or 1-naphtyl isoselenocyanate (for **AL2** and **AL3**) with aniline (for **AL1** and **AL2**) and 1-naphtylamine (for **AL3**) in a 1:1 mixture of dry DCM and EtOH under inert atmosphere in the dark at room temperature to give the desired product in good yields (84%, 79%, and 55%, for **AL1**, **AL2**, and **AL3**, respectively, see paragraph A4 for synthetic details).

The synthesis of the isoselenocyanates was previously reported by Fernández-Bolaños et al.[17] Receptors **AL4**-**AL9** were already described in the literature.[18-22]

In order to evaluate the anion binding modes of **AL1**-**AL3**, as well as those of the other receptors, ^{1}D-NMR titrations in DMSO-d_6 were performed with chloride, dihydrogenphosphate, acetate, and benzoate as their tetrabutylammonium salts. Resonances due to the selenourea NHs protons were found to shift from 10-11 ppm to higher frequencies as a consequence of the anion coordination event. Additionally, the appearance of multiple resonances in the range 10-12 ppm and of new resonances both in the aromatic range and at lower frequencies (5-6 ppm), was observed in a number of instances, suggesting the presence of more than one adduct species in solution. In order to rationalize this behaviour and to assign the new resonances, both 1D and 2D-NMR experiments were carried out in DMSO-d_6, starting from the case of the structurally asymmetric L2 and acetate as guest anion species. This prototypical study case was chosen because during the titration, for a relatively wide range of anion added equivalents, four 1H singlets were simultaneously present in the 10-12 ppm range together with two new singlets in the 5-6 ppm range (Figure A2a and paragraph A4 Figure A4 for a complete stack-plot).

Due to the asymmetric structure of **AL2** the two signals observed at ~10 ppm in the free receptor are due to the two selenourea NHs protons. After the coalescence regime at the beginning of the titration, up to six different singlets attributable to NHs protons were observed (Figure A2a) which could be categorized into three couples of resonances on the basis of their frequency: high (>10.5 ppm), intermediate (9.5-10.5 ppm) and low (4.5-6.0 ppm) (Fig. A5). g-COSY, TOCSY and ROESY were carried out on **AL2** in DMSO-d_6 in the presence of 2.5 equivalents of acetate (in this condition all the six singlets were well-resolved, see paragragh A4 and Figure A5 for the 2D-NMR description) with the aim of identifying all the species present in solution. From the results of these experiments, we concluded that three different adduct species were present in solution: a bi-coordinated and two different mono-coordinated adducts of **AL2** with acetate as shown in Figure 2. Attribution of the NHs signals for the two mono-

coordinated adducts, which are marked in red and blue in Figure 2, is inherently ambiguous, but it is important to stress here that the presence of the bi-coordinated adduct is clearly demonstrated by the presence of resonances above 11 ppm, while the presence of mono-coordinated species is unambiguously supported by resonances in the 4.5-6.0 ppm range. Among the two signals assigned to each mono-coordinated adduct, the one at higher frequency (10-10.5 ppm) is attributed to the selenourea NH proton coordinating the anion, the one at the lower frequency is attributed to the non-coordinating NH (paragraph A4 Fig. A6).

This interpretation is also strongly supported by a previous study reported by Roberts et al.[23] on the interaction of simple urea, thiourea, 1,1-dimethylurea and 1,1-dimethylthiourea with acetate. It was demonstrated that the resonance frequency of the urea protons depended on their localization in space with respect to the chalcogen, with cis NH protons characterized by a remarkably lower frequency than trans NH protons.

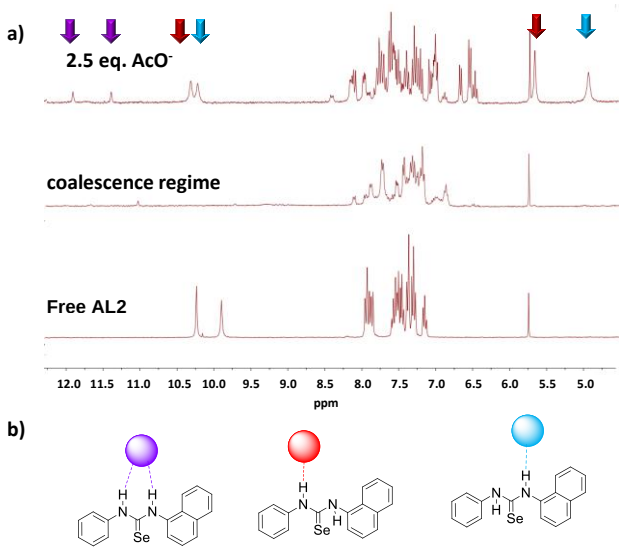

Figure A2 a) ^{1}H-NMR spectra of free **AL2**, upon addition of 0.5 equivalents of TBAAcO tetrabutylammonium acetate), and in the presence of 2.5 equivalents of TBAAcO in DMSO-d_6; b) structures of the proposed mono and bi-coordinated adducts. Colour

code: purple indicates bi-coordinated adduct, red and light blue indicate mono-coordinated adducts and the corresponding ^{1}H-NMR signals.

At room temperature, rotation around C-N bonds was fast enough to observe only a single time averaged resonance but, by decreasing the temperature, the two separate signals were visible in the spectrum, after the coalescence regime was overcome.[23] It was also demonstrated that by moving from oxygen to sulfur, the coalescence temperature increased as well as the frequency separation between cis and trans NH proton signals.[23] Our results seem to be consistent with this evidence and show that the trends (coalescence temperature and frequency separation) on changing the chalcogen continue also by moving further along the 16 group down to selenium. In fact, even increasing the temperature up to 330 K to speed up the rotation around the C-N bonds, we did not reach the coalescence regime for **AL2** (it should also be noted that our substituents in the selenourea moiety are bulkier than Robert methyls).

After these findings, we moved on to evaluate the effect of the chalcogen on the binding modes by using the asymmetric receptors **AL2**, **AL5**, and **AL8** and acetate as anion (see paragraph A4 Figure. A4 and A7). In the case of **AL8**, upon addition of increasing amounts of acetate, the usual progressive shift of the two NHs signals was previously reported,[21] which clearly indicated the formation of a bi-coordinated adduct and the fast (on the NMR time scale) exchange rate between the adduct and the free receptor. In the case of **AL5**, the behaviour appeared the same (Figure A7) but the system immediately showed a coalescence regime, indicating that the exchange rate significantly decreased when compared to **AL8**. As reported above, in the case of the **AL2** (Figure A4), we observed the formation of both the bi- and mono-coordinated adducts in equilibrium with a slow exchange rate. In the light of the above-mentioned evidence from the literature (and the correlations we found with substituents' size in the receptors as reported hereinafter), the observed differences between **AL8**, **AL5**, and **AL2**, could be reasonably explained considering the increasing size of the Van der Waals radius of the chalcogen, which could change the rotation barrier around the C-N

bonds following the order **AL2**>**AL5**>**AL8**. The effect of the chalcogen on the binding modes was also confirmed in the case of the symmetric diphenyl-substituted **AL1**, **AL5**, and **AL7** (Figure A8).

We then evaluated the role of the anion size and geometry on the coordination modes of selenoureas **AL1**-**AL3** by comparing chloride, dihydrogenphosphate, acetate, and benzoate. Results obtained for the prototypical case of **AL2** are summarised in Table A1 and in the stack plots in the paragraph A.4 (Fig. A9). Results for **AL1** and **AL3** are shown in Figs. A12 and A13, respectively.

Table A1 Type of adducts observed for **AL2** in presence of different anions in DMSO-d_6

Anion	Mono-coordination	Bi-coordination
Cl^-	✗	✓
$H_2PO_4^-$	✗	✓
AcO^-	✓	✓
BzO^-	✓	✓

In the case of the relatively small and spherical chloride anion, the usual progressive shift of the two selenourea NHs to higher frequency was observed only at high anion equivalents added, indicating a low binding affinity. No coalescence regime was observed, while the resonance shift presumably reflected the fast exchange rate between the free receptor and the bi-coordinated adduct.

In the case of dihydrogenphosphate, after a first coalescence regime the two signals reappeared in the spectrum but located at lower frequency than those of the free receptor. Upon addition of further increasing amounts of anion, the progressive shift of the two NHs was observed, up to frequency values higher than those observed for the free receptor. This peculiar behaviour can be explained with a fast exchange rate between the two possible mono-coordinated species and the bi-coordinated adduct. The absence of resonances in the 4.5-6.0 ppm range, characteristic of mono-coordinated adducts, showed that the bi-coordinated species is the dominating one, to which dihydrogenphosphate anion can evolve very rapidly from any of the two mono-coordinated forms. This is absolutely reliable if one considers the tetrahedral geometry of the anion. The presence of four oxygen atoms pointing to different directions should

be able to facilitate the second coordination event even if the receptor adopts a "distorted" non-planar conformation.

The observation of distinct resonances for both mono- and bi-coordinated adducts in the case of the Y-shape anions acetate and benzoate reflected the slower exchange rate between the different species formed in solution. The bulky selenium atom in the receptor should limit rotations around the C-N bonds, thus limiting the accessible conformations. As a consequence, the complementarity between the directionality of the two NHs hydrogen bond donors and the Y-shape of these anions is more difficult to be achieved when selenoureas are compared to ureas and thioureas (see Figure A10). The bulkier benzoate, indeed, formed only one of the two possible mono-coordinated adducts with **AL2** because of its increased steric hindrance, which determined the preferential coordination direction on the less cluttered phenyl side of the receptor.

Finally, we evaluated the effect of the substituents size in the receptors on the anion binding ability of selenoureas **AL1**-**AL3**, by using acetate as prototypical anion. The results are summarised in Table A2 and in the stack plots in the paragraph A4 (Figures. A12 and A13).

Table A1 Type of adducts observed for **AL1-AL3** in presence of acetate in DMSO-d_6

Receptor	Mono-coordination	Bi-coordination
AL1	✓	✓
AL2	✓	✓
AL3	✓	✗

Both in the case of the di-phenyl (**AL1**) and phenyl-naphthyl (**AL2**) substituted receptors, resonances corresponding to both mono- and bi-coordinated adducts were observed, with the difference in the total number of NH singlets simply due to the symmetry of the receptor itself (Fig. A9a and A9b). Differently, in the case of 1,3-dinaphtylselenourea **AL3** we observed only the mono-coordinated species (Fig. A11c). In the light of all the collected evidence, this difference is clearly due to the increased

steric hindrance provided by the two aryl substituents, making the formation of the bi-coordinated adduct particularly unfavourable. We performed 1H-NMR titrations also with receptors **AL4**-**AL9** and all the anions considered and we observed only the formation of the bi-coordinated adducts. It is worth noticing that we did not observed any relevant variation in the Uv-Vis and the fluorescent properties of receptors **AL1**-**AL3** upon addition of the anions investigated.

The results obtained can be summarised in a truth table (Table A3) where the input are i) the nature of the chalcogen (0, 1, 2 for oxygen, sulphur and selenium, respectively), ii) the steric hindrance of the aryl substituents at the urea moiety (0, 1, and 2 for diphenyl, phenyl-naphtyl, and di-naphtyl, respectively), and iii) the geometry of the anion (0, 1, 2, 3, for spherical chloride, tetrahedral dihydrogenphosphate, Y-shape acetate, and bulky Y-shape benzoate, respectively), while the output are the type of adducts formed identified on the base of 1H-NMR signals (0, 1, 2, for only mono-coordinated, both mono- and bi-coordinated, and only bi-coordinated, respectively).

Table A3 truth table based on the interaction between receptors and anions investigated in this appendix

Input			Output [d]
Chalcogen[a]	Substituents [b]	Anion shape[c]	
0	0, 1, 2	0,1, 2,3	2
1	0, 1, 2	0,1, 2,3	2
2	0	0	2
2	0	1	2
2	0	2	1
2	0	3	1
2	1	0	2
2	1	1	2
2	1	2	1
2	1	3	0
2	2	0	2
2	2	1	2
2	2	2	0

[a]Ternary input: 0, oxygen; 1, sulfur; 2, selenium.
[b]Ternary input: 0, di-phenyl; 1, phenyl-naphthyl; 2, di-naphthyl.
[c]Quaternary input: 0, spherical; 1, tetrahedral; 2, small Y-shaped; 3, bulky Y-shaped.
[d]Ternary output: 0, only mono-coordination; 1, both mono- and bi-coordination; 2, only bi-coordination.

It is clear, that only selenoureas are able to give multiple response depending on the anion and on the aryl substituents considered. The output type in Table A3 can be easily determined using the flowchart in Figure A3, which also provides the basis to implement the automatic NMR spectral analysis for the interactions of the receptors and anions investigated in the paper.

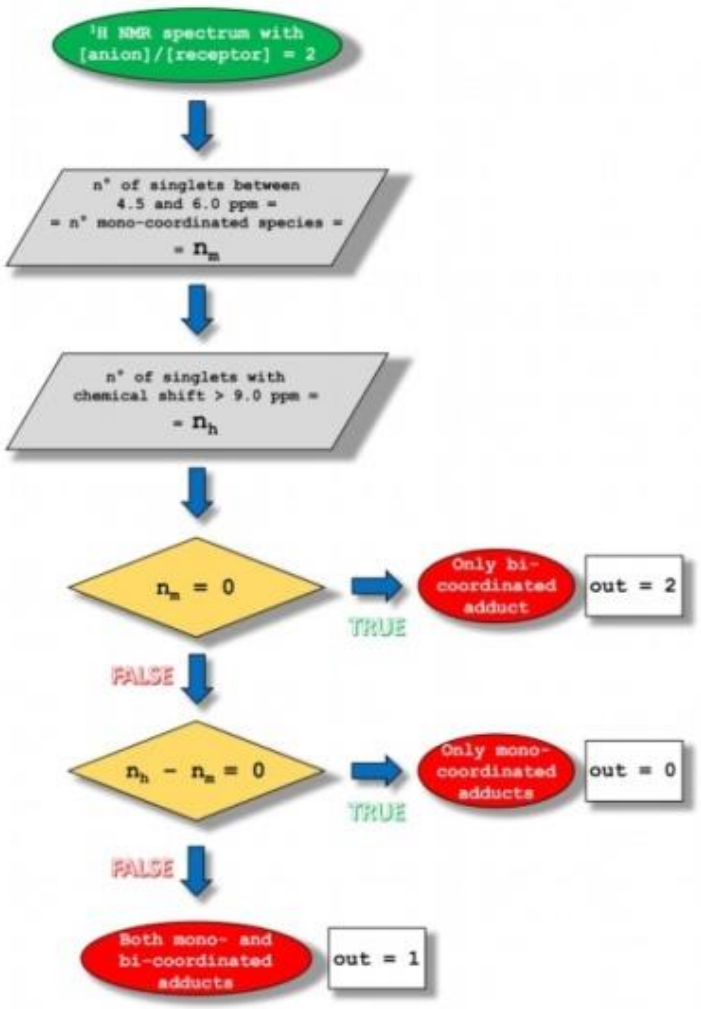

Figure A3 Explicative flowchart to implement automatic spectra analysis of the receptors **AL1**-**AL3** in the presence of Cl^-, $H_2PO_4^-$, CH_3COO^- and Ph-COO^-.

A.3 Conclusions

In conclusion, we showed that when compared to ureas and thioureas, selenoureas appear to be more versatile receptors for anion binding, capable of forming at room temperature in solution both mono- and bi-coordinated adducts depending on the geometry of the bound anion and the steric hindrance exerted by the chalcogen itself and the substituents on the urea moiety. This is reflected also on the increase of the

NMR coalescence temperature that facilitate the easy detection of the mono-coordinated adduct in solution at room temperature. As a consequence, on using i) the steric hindrance of the aryl substituents in selenoureas, and ii) the geometry of the anion guest as inputs, a molecular logic gate can be easily developed following 1H-NMR signals of the adducts formed as chemical outputs.

The investigated series of selenoureas/anions thus, represents, to the best of our knowledge, the first example of molecular logic gate using the urea– based receptors for anions, that performs a ternary logic operation based on a 1H-NMR easy to read response.

A.4 Experimental part

^{1}H NMR spectra were recorded on Bruker Avance-300 spectrometer with 300 MHz Larmor frequency at 300 K. Chemical shifts are reported in parts per million (ppm), referenced to the residual solvent peak. All solvents and starting materials were purchased from commercial sources where available. ^{1}H NMR titrations were performed by adding aliquots of a stock solution of the anionic guest (as tetrabutylamonium (TBA) salt, 0.075 M) to a solution of the receptor (0.005M) in DMSO-d_6. 2D NMR spectra acquisition was performed at 300K with an Agilent UNITY INOVA spectrometer operating at a ^{1}H frequency of 500 MHz. A ^{1}H(90°) pulse of 6.6 μs (90°) was applied over a spectral window of 8000 Hz, with 1 s recycle delay. Homonuclear gCOSY was collected by sampling each of the 256 increments with 2048 complex points. The same was carried out for TOCSY and ROESY by applying the mlev17 spin-lock scheme with 80 and 200 ms mixing time, respectively. Mass spectra (CI, EI, FAB and LSI) were recorded on Kratos MS-80-RFA and Micromass AutoSpec-Q mass spectrometers with a resolution of 1000 or 10,000 (10% valley definition). For the FAB and LSI spectra, ions were produced by a beam of xenon atoms and Cs^+ ions, respectively, by using 1-thioglycerol as matrix and NaI as additive. TLC was performed on aluminum pre-coated sheets (E. Merck Silica Gel 60 F_{254}); spots were visualized under UV light, by charring with 10% H_2SO_4 in EtOH. Column chromatography was

performed with E. Merck Silica Gel 60 (40–63 mm). All the reactions and purifications involving organoselenium derivatives were carried out in the darkness by using aluminium foil.

Synthesis of AL1

A solution of isoselenocyanatobenzene (0.200 g, 1.098 mmol) in dry DCM (2mL) was added dropwise to a solution of aniline (0.102 g, 1,098 mmol) in ethanol absolute (2mL) in the darkness under Ar. The mixture was stirred for 4h at room temperature and then it was filtered to give the desired compound as white solid. Yield 84 %(0,255 g, 0,927 mmol). ^{1}H-NMR (300 MHz,DMSO-d_6, 298K): δH: 10.14 (s, 1H); 7.41-7.31 (m, 8H); 7.15 (t, 7.1, Hz, 2H). ^{13}C-NMR (75.5 MHz, DMSO-d_6, 298 K), δC: 179.40, 140.06, 128.92, 125.54, 125.22. ESI m/z 299.0051 $[M+Na]^+$.

Synthesis of AL2

A solution of 1-isoselenocyanatonaphtalene (0.200 g, 0,862 mmol) in dry DCM (2mL) was added dropwise to a solution of aniline (0.102 g, 0,862 mmol) in ethanol absolute (2mL) in the darkness under Ar. The mixture was stirred for 4h at room temperature and then it was filtered to give the desired compound as white solid. Yield 79 % (0,220 g, 0,676 mmol).^{1}H-NMR (300 MHz,DMSO-d_6, 298K): δH: 10.28 (s, 1H); 9.94 (s, 1H); 7.99-7.88 (m, 3H); 7.63-7.46 (m, 4H); 7.38 (d, J= 7.2 Hz, 2H); 7.30 (t, J= 7.8 Hz, 2H); 7.15 (t, J= 7.2 Hz, 1H). ^{13}C-NMR (75.5 MHz, DMSO-d_6, 298 K), δC: 180.30, 140.28, 136.07, 134.46, 130.35, 128.88, 128.58, 127.74, 126.75, 126.63, 126.22, 126.18, 125.95, 123.76. ESI m/z 349.0210 $[M+Na]^+$.

Synthesis of AL3

A solution of 1-isoselenocyanatonaphtalene (0.200 g, 0,862 mmol) in dry DCM (2mL) was added dropwise to a solution of naphthalenamine (0.123 g, 0,862 mmol) in ethanol absolute (2mL) in the darkness under Ar. The mixture was stirred for 4h at room temperature and then it was filtered to give the desired compound as white solid. Yield 55 % (0.178 g, 0,474mmol).^{1}H-NMR (300 MHz,DMSO-d_6, 298K): δH: 10.14 (s, 1H); 7.95

(d, J= 7.9, Hz, 2H); 7.91-7.87 (m, 1H); 7.64-7.51 (m, 4H); 7.42-7.33 (m, 4H); 7.21 (t, 7.2 Hz, 1H). ^{13}C-NMR (75.5 MHz, DMSO-d_6, 298 K), δC: 181.30, 136.28, 134.40, 130.66, 128.53, 127.83, 126.77, 126.68, 126.62, 126.17, 123.78. ESI m/z 399.0367 $[M+Na]^+$.

Discussion of 2D-NMR experiments

In the gCOSY spectrum, no correlation (scalar coupling) was found among the six singlets indicated by arrows in Fig. A5, confirming their multiplicity. The analysis revealed eight different spin systems comprising three aromatic protons each. One additional spin system could not be accurately identified together with several resonances belonging to other spin systems as illustrated in Fig. S3, because of resonances partial overlap with insufficient spectral resolution. TOCSY and ROESY spectra confirmed the correlation between the NH proton signals and the different aromatic spin systems identified in the gCOSY. By taking all the results together into consideration, including frequency order and range for each of the spin systems, the assignments shown in Fig. S3 emerged, indicating the co-existence of three different species in the solution. The only ROEs (dipolar interaction) among HN protons was found for the two with the highest frequency, namely, at 11.65 and 11.15 ppm, clearly indicating that these belonged to the same species. Such a through-space direct interaction between two protons indicates that they are relatively still over time in close proximity with each other (usually at a distantce < 5Å). This led to their attribution to the bi-coordinated adduct, since the interaction with the anion is expected to keep the two NHs directed towards the same direction and to shift their resonance frequency to rather high values. As far as the remaining NH signals are concerned, they were categorized into two couples, one at intermediate frequencies (at 10.11 and 10.04 ppm) and the other at low frequencies (at 4.97 and 5.67 ppm). As already discussed in the main paper, on the basis of the work by Roberts and co-workers it was possible to attribute these to coordinating and non-coordinating NHs in two different mono-

coordinated adducts. In one of the latter, the NH on the phenyl side interacted with the acetate anion while the other NH pointed to the opposite direction, thus, towards the side of the chalcogen atom. In a second mono-coordinated adducts, the NH on the naphthyl side interacted with the anion, while the other NH pointed to the chalcogen side. This interpretation is bolstered by evidence from the literature and explains the large difference in frequency among the NHs.

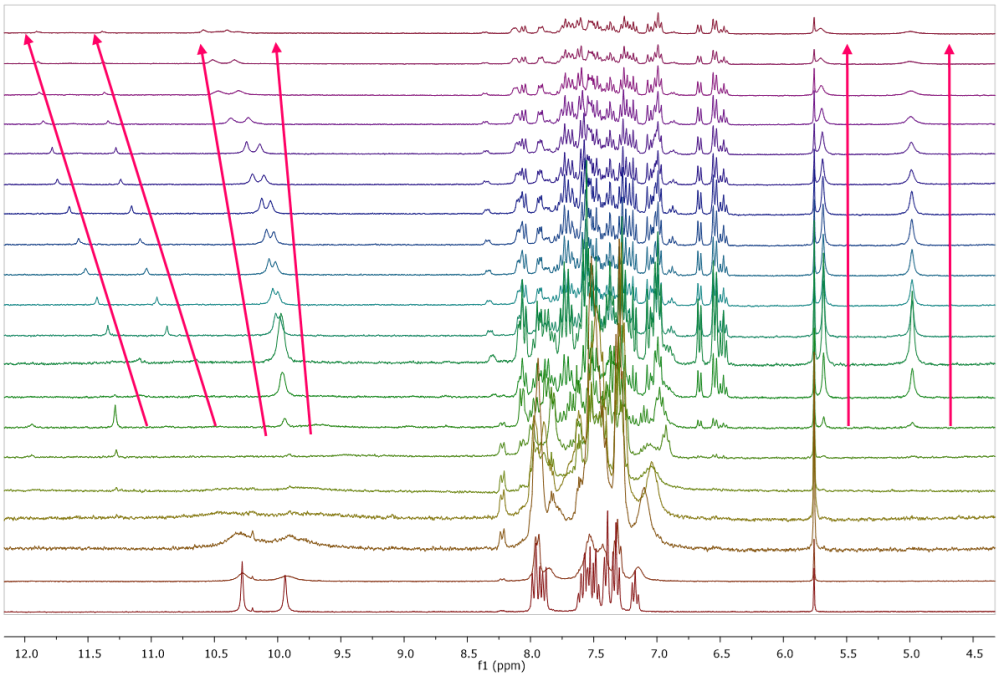

Figure A4 Titration of **AL2** (0.005M) with acetate as TBA salt (0.075M) in DMSO-d_6.

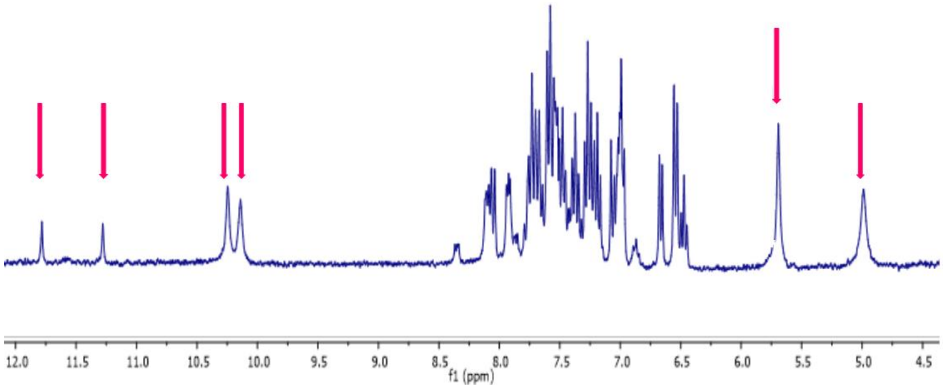

Figure A5 Spectrum of L2 (0.005M) in the presence of 2.5 equivalents of acetate as TBA salt (0.075M) in DMSO-d_6

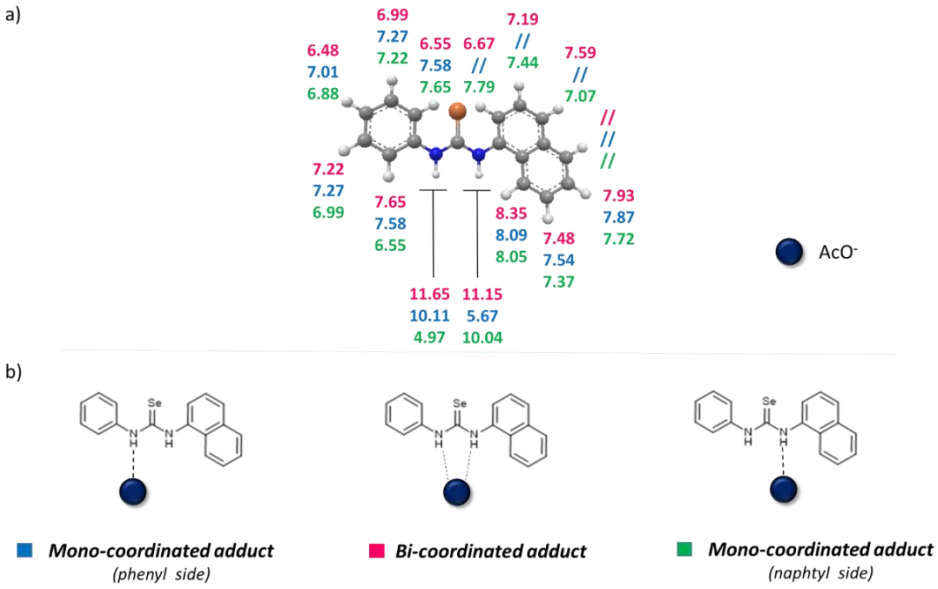

Figure A6 a)^{1}H-NMR frequencies attribution of receptor **AL2** in the presence of 2.5 equivalents of TBAAcO in DMSO-d_6 and b) structures of the hypothesised mono and bi-coordinated adducts with acetate.

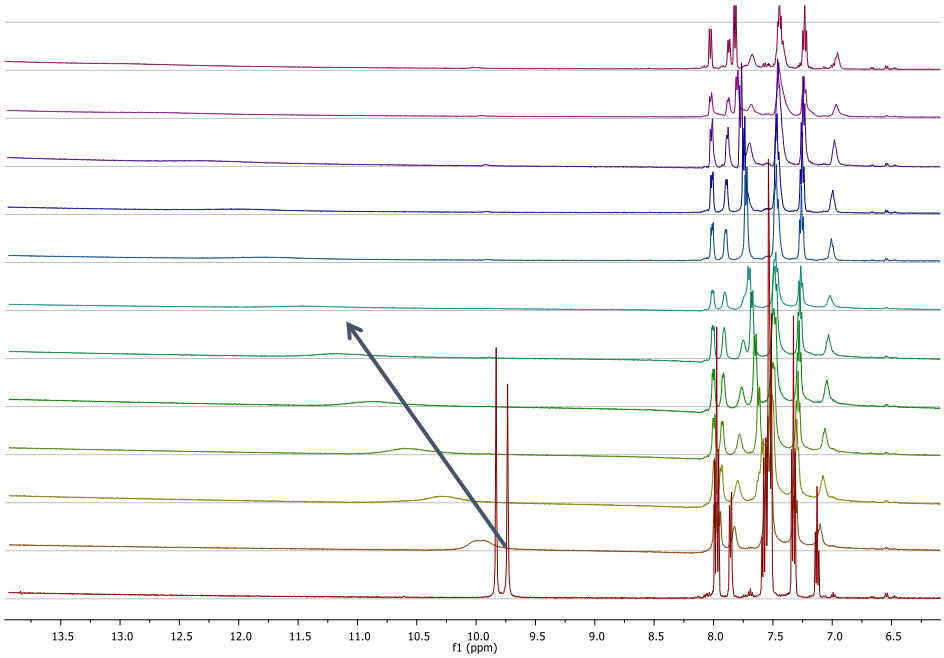

Figure A7 Stack plot of the titrations of **AL5** (0.005M) with TBAAcO (0.075M) (in DMSO-d_6.

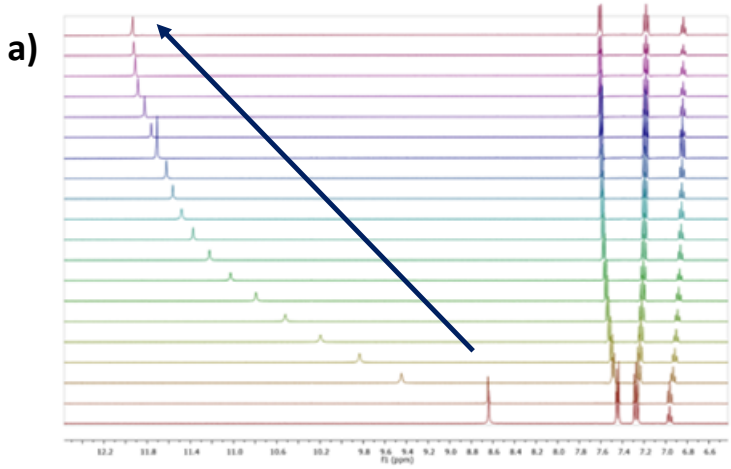

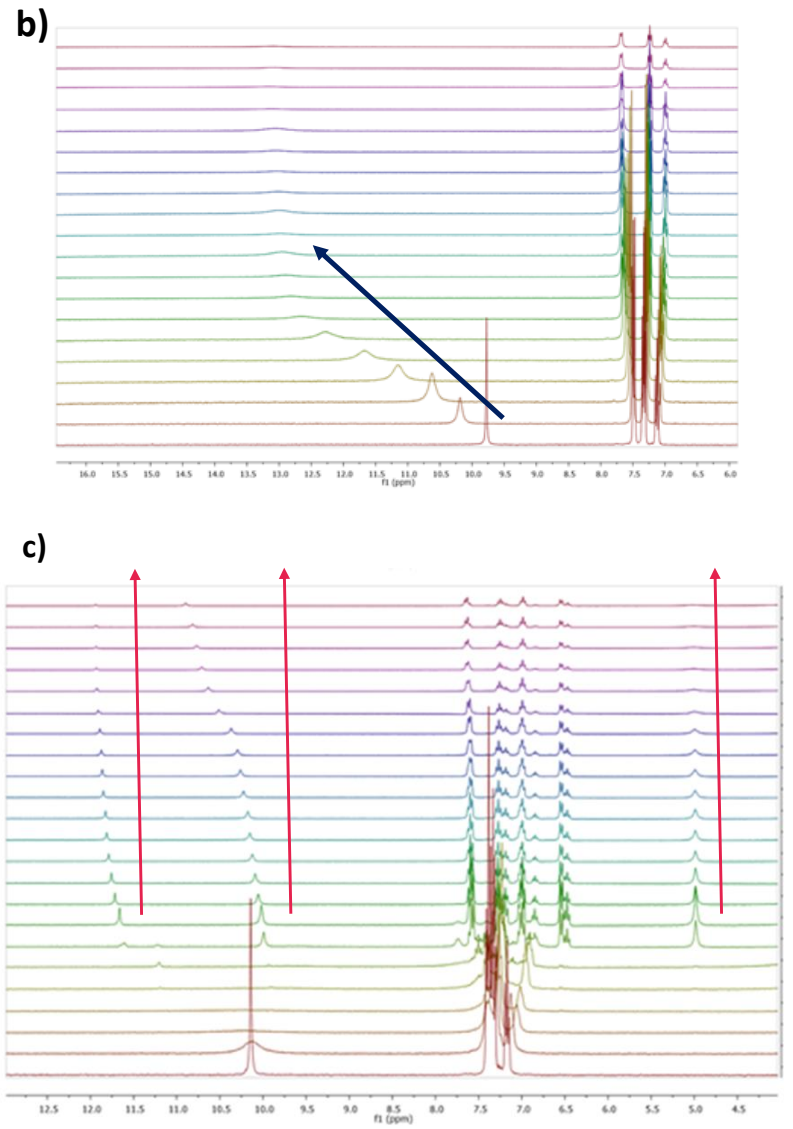

Figure A8 Stack plots of the titrations of **AL4**, **AL7**, and **AL1** (0.005M) with TBAAcO (0.075M) (a, b and c for the titration of **AL4**, **AL7**, and **AL1**, respectively) in DMSO-d_6.

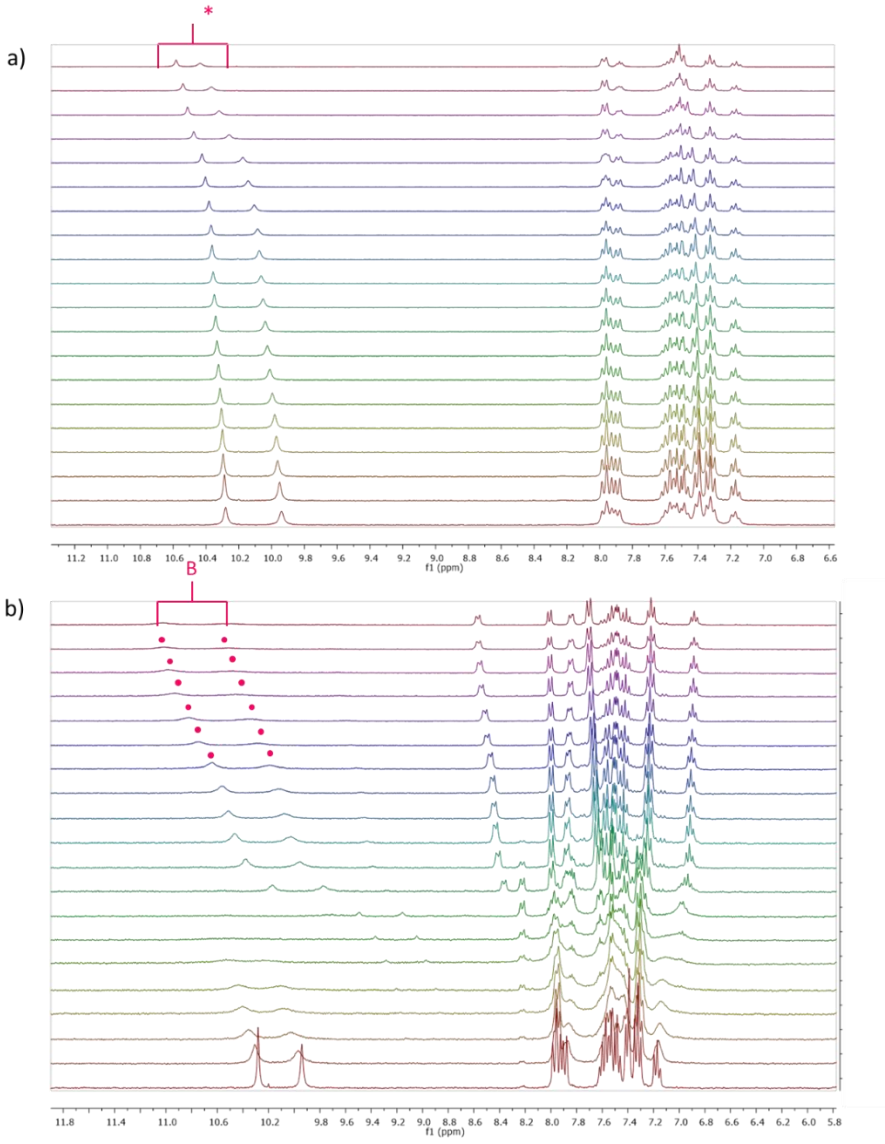
a)
*
11.2 11.0 10.8 10.6 10.4 10.2 10.0 9.8 9.6 9.4 9.2 9.0 8.8 8.6 8.4 8.2 8.0 7.8 7.6 7.4 7.2 7.0 6.8 6.6
f1 (ppm)
b)
B
11.8 11.4 11.0 10.6 10.2 9.8 9.6 9.4 9.2 9.0 8.8 8.6 8.4 8.2 8.0 7.8 7.6 7.4 7.2 7.0 6.8 6.6 6.4 6.2 6.0 5.8
f1 (ppm)

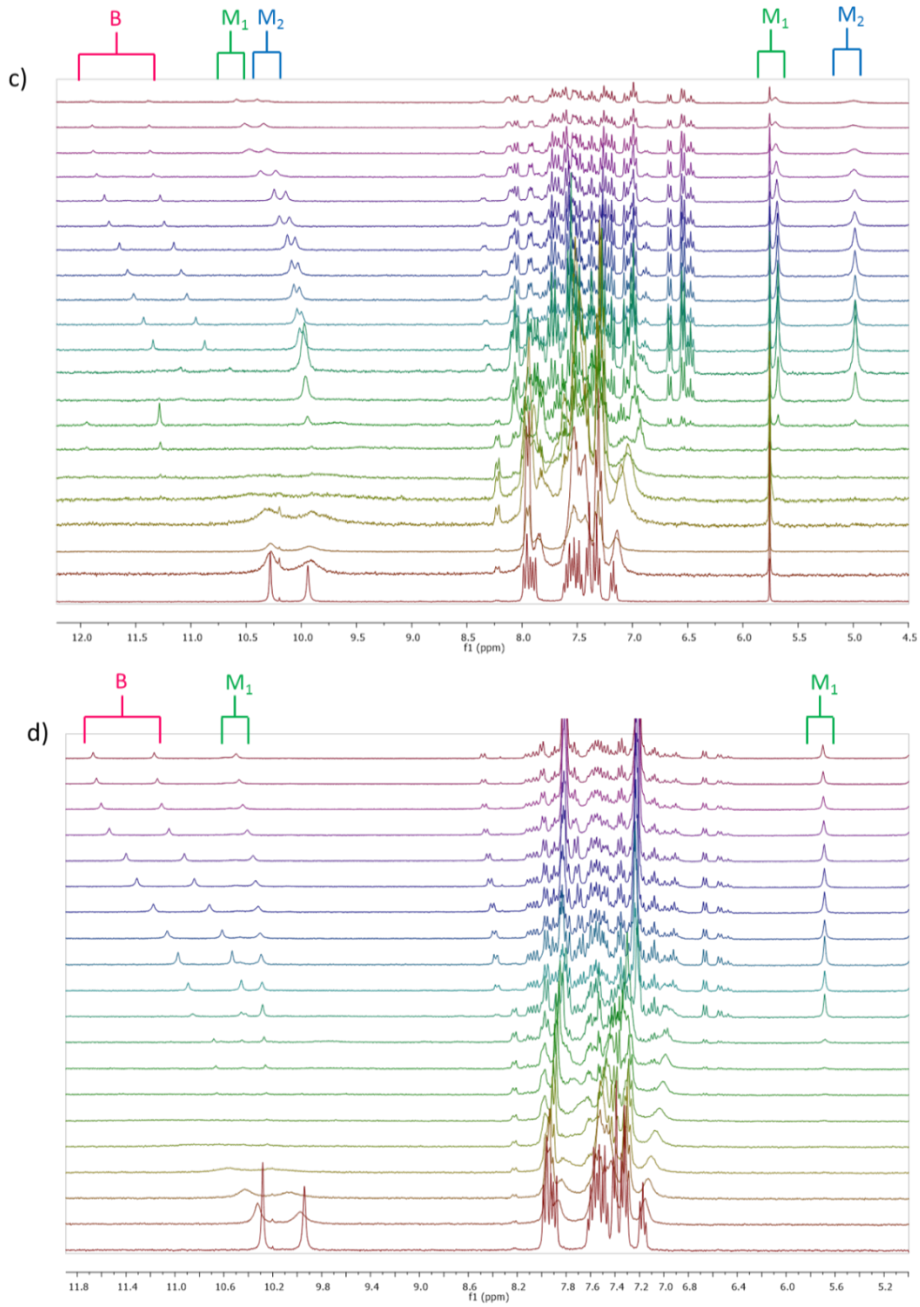

Figure A9 Titration in DMSO-d_6 of **AL2** (0.005M) with Cl^-, $H_2PO_4^-$, AcO- and BzO^- (figure a, b, c and d respectively) as TBA salt (0.075M). The label B, M1 and M2 indicate the bi-coordinated adduct and the two mono-coordinated forms, respectively. *In Figure b the presence of poorly visible peaks is indicated by red dots.

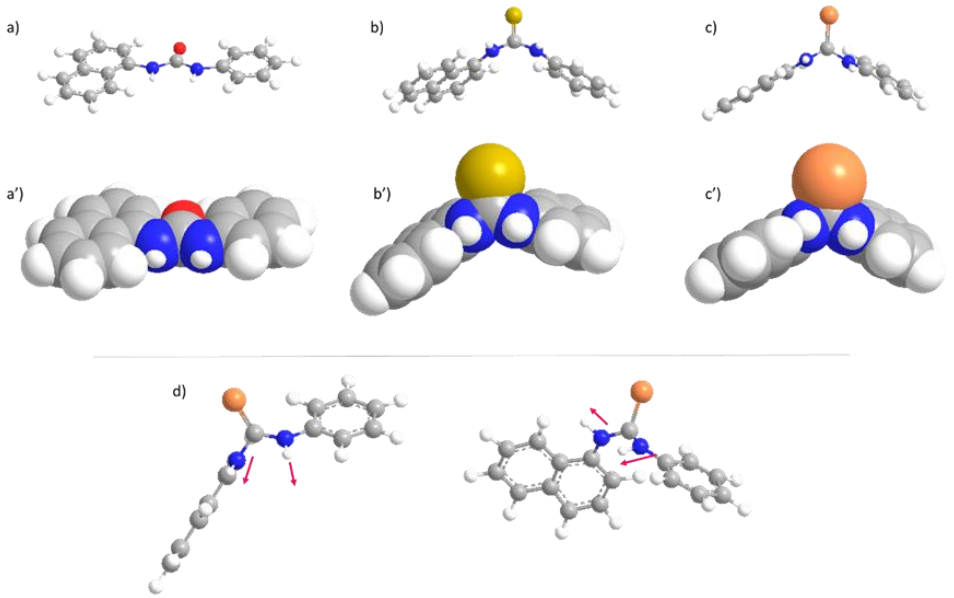

Figure A10 Balls and sticks and space fill representations of the 1-naphtyl-3phenyl urea (a and a'), thiourea (b and b') and selenourea (c and c') and NH hydrogen bonding directionality (d) in the case of 1-naphtyl-3phenyl selenourea obtained using ChemBio3D (12.0 Version) software.

a)

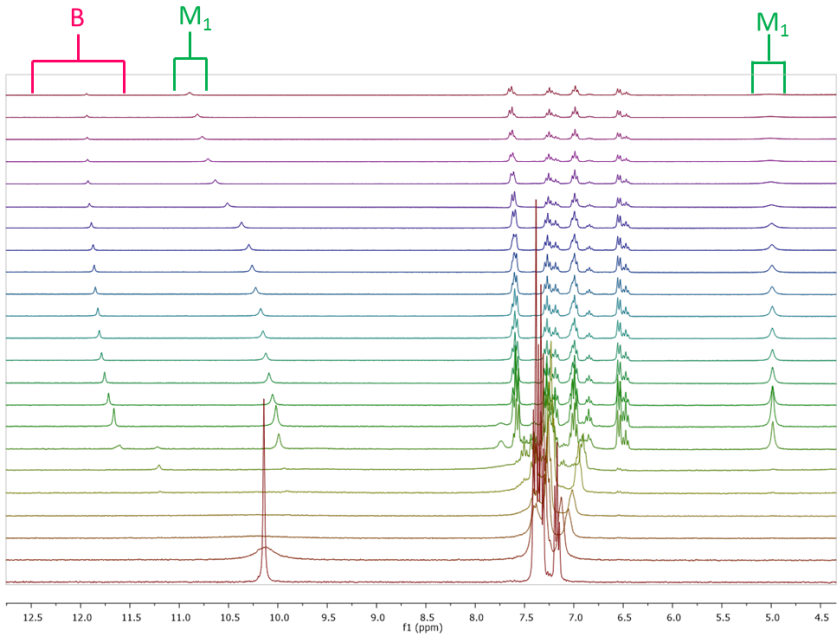
B
M1
M1
12.5 12.0 11.5 11.0 10.5 10.0 9.5 9.0 8.5 8.0 7.5 7.0 6.5 6.0 5.5 5.0 4.5
f1 (ppm)

b)

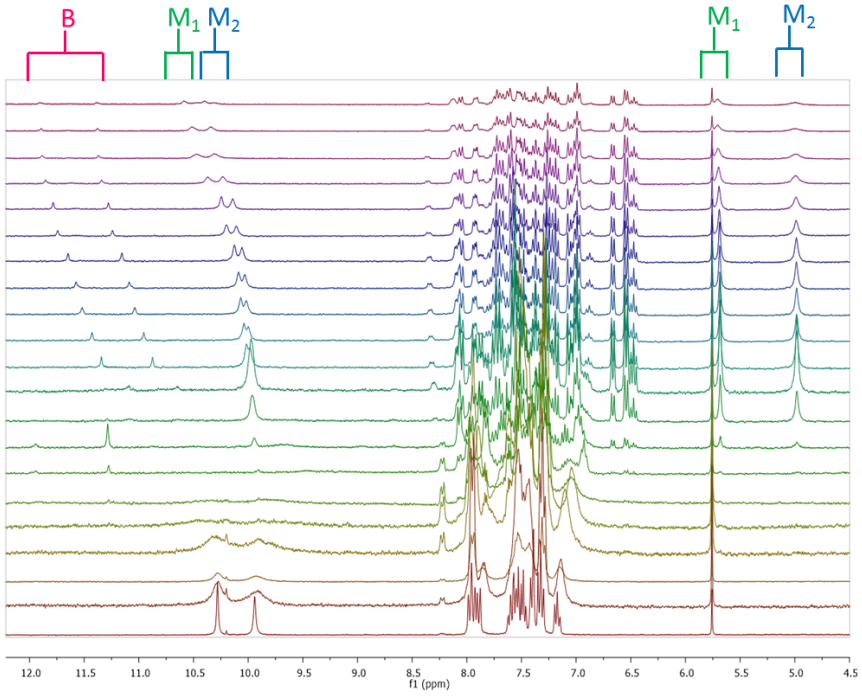
B
M1
M2
M1
M2
12.0 11.5 11.0 10.5 10.0 9.5 9.0 8.5 8.0 7.5 7.0 6.5 6.0 5.5 5.0 4.5
f1 (ppm)

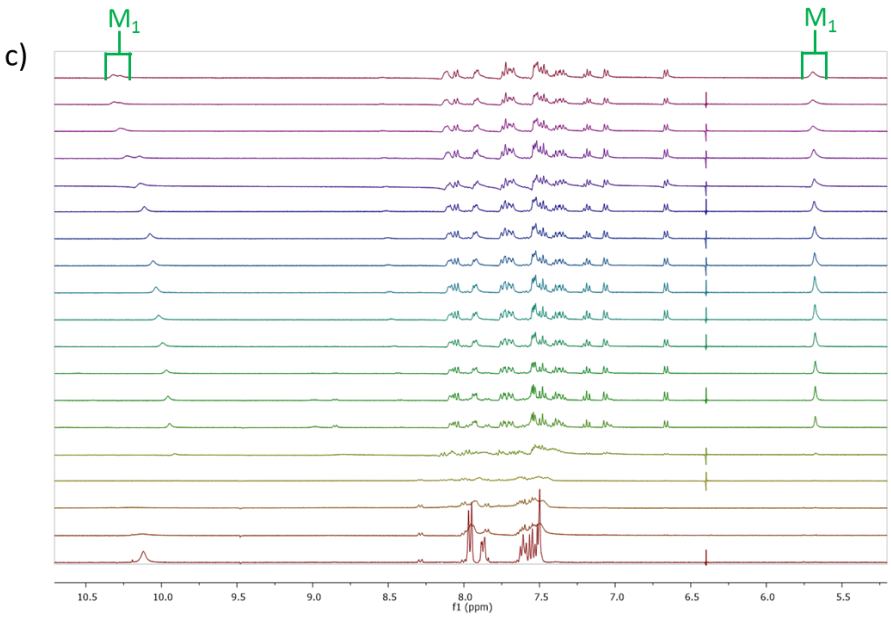

Figure A11 Stack plots of the Titrations of **AL1**, **AL2** and **AL3** (0.005M) (figure a, b and c, respectively) with acetate as TBA salt (0.075M) in DMSO-d_6

a)

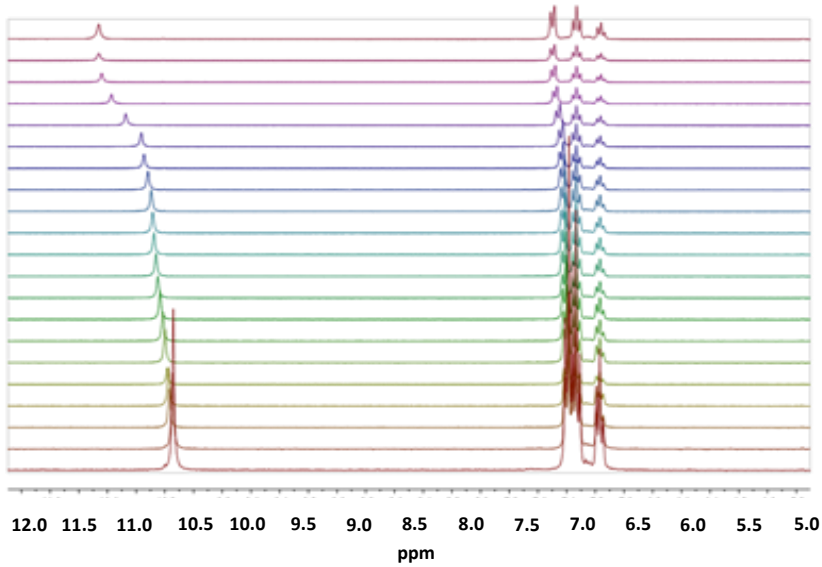
12.0 11.5 11.0 10.5 10.0 9.5 9.0 8.5 8.0 7.5 7.0 6.5 6.0 5.5 5.0
ppm

b)

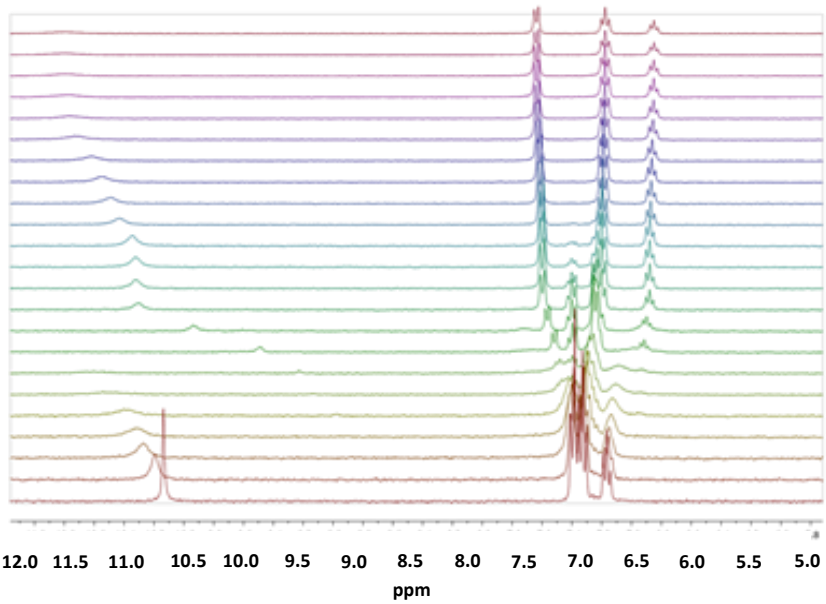
12.0 11.5 11.0 10.5 10.0 9.5 9.0 8.5 8.0 7.5 7.0 6.5 6.0 5.5 5.0
ppm

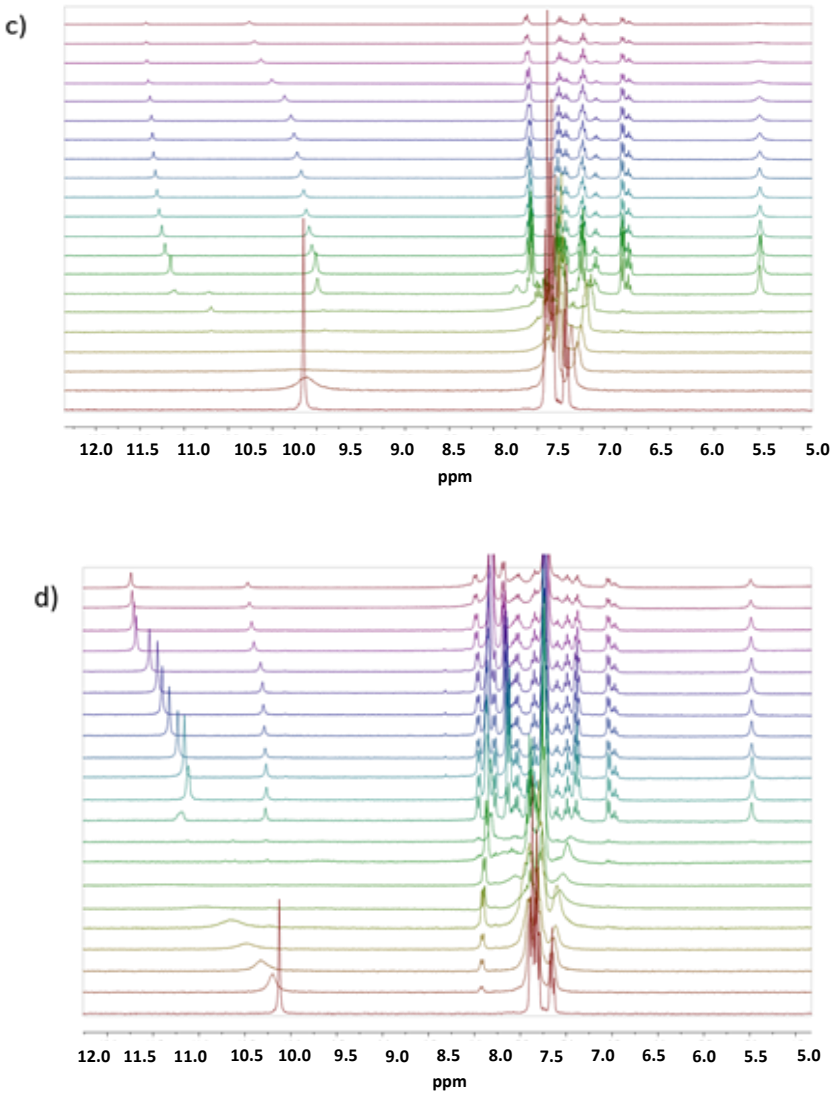

Figure A12. Changes in the ^{1}H-NMR spectra of **AL1** (0.005M) upon addition of increasing amounts of Cl^- (a), $H_2PO_4^-$ (b), AcO^- (c) and BzO^- (d) (0.075M) in DMSO.

a)

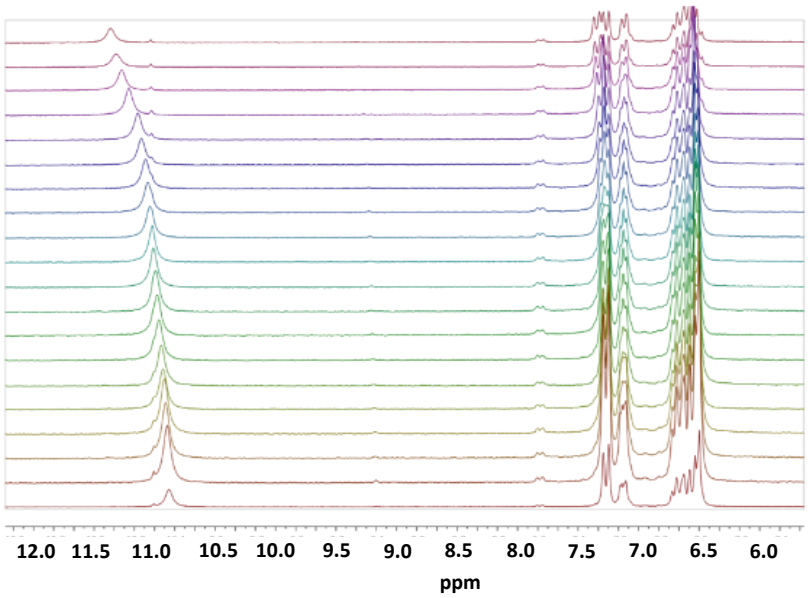
12.0 11.5 11.0 10.5 10.0 9.5 9.0 8.5 8.0 7.5 7.0 6.5 6.0
ppm

b)

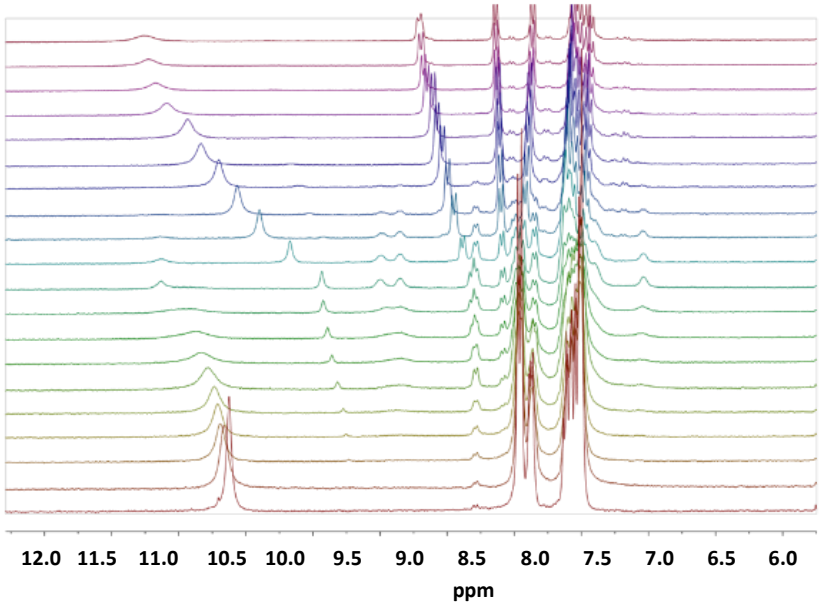
12.0 11.5 11.0 10.5 10.0 9.5 9.0 8.5 8.0 7.5 7.0 6.5 6.0
ppm

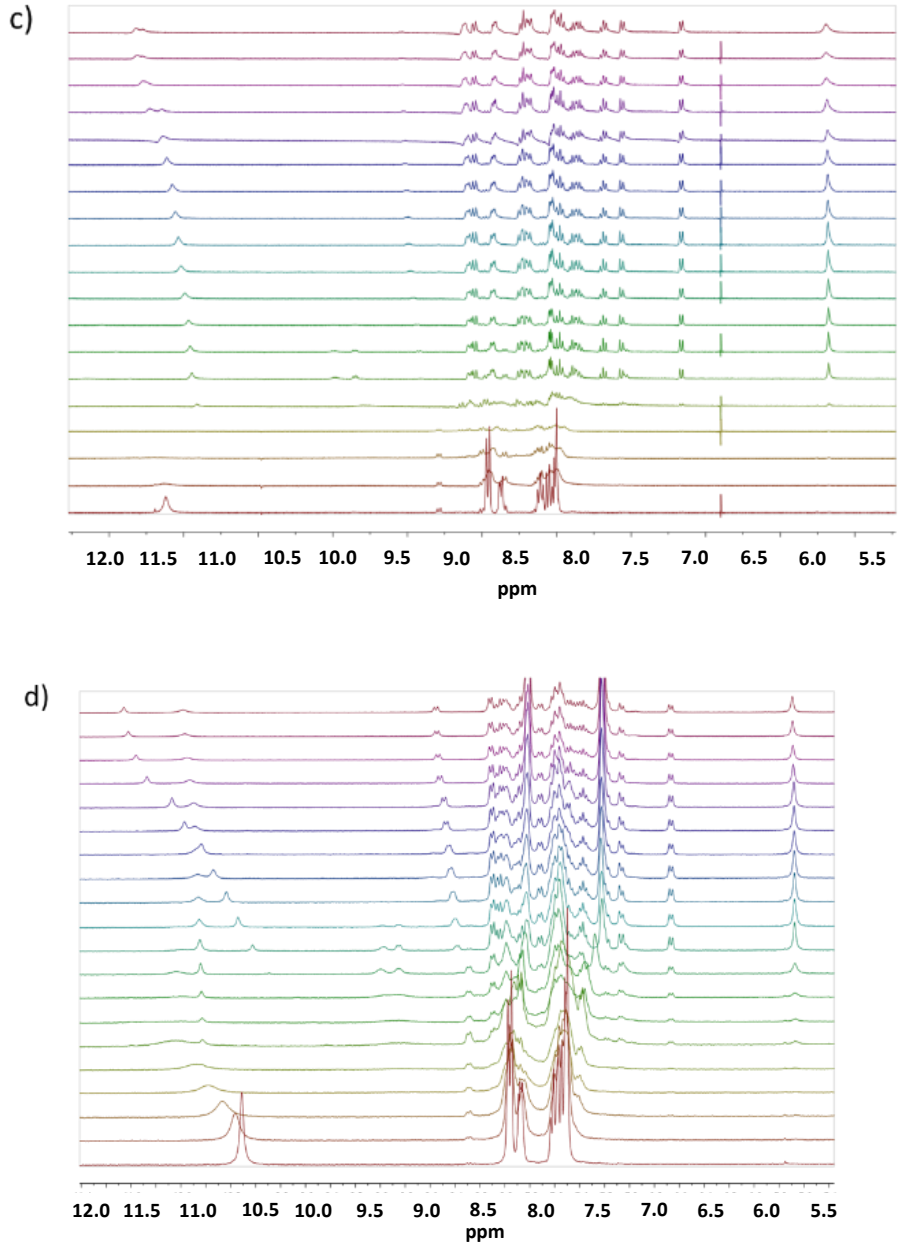

Figure A13. Changes in the ^{1}H-NMR spectra of **AL3** (0.005M) upon addition of increasing amounts of Cl^- (a), $H_2PO_4^-$ (b), AcO^- (c) and BzO^- (d) (0.075M) in DMSO. In the case of BzO-, we observed an exception: the high frequency NHs resonances due to the bi- and mono- coordinated adducts inverted along the titration.

A.5 References

1 A. Aviram, *J. Am. Chem. Soc.*, 1988, **110**, 5687-5692.
2. P. A. de Silva, N. H. Q. Gunaratne and C. P. McCoy, *Nature*, 1993, **364**, 42-44.
3. J. Andréasson and U. Pischel, *Chem. Soc. Rev.*, 2015, **44**, 1053-1069.
4. A. Credi, *Angew. Chem. – Int. Ed.*, 2007, **46**, 5472-5475.
5. B. Daly, J. Ling and A. P. de Silva, *Front. Chem. Sci. Eng.*, 2014, **8**, 240-251.
6. A. P. De Silva and N. D. McClenaghan, *Chem. -Eur.. J.*, 2004, **10**, 574-586.
7. Madhuprasad, M. P. Bhat, H. Y. Jung, D. Losic and M. D. Kurkuri, *Chem – Eur. J.*, 2016, **22**, 6148-6178.
8. U. Pischel, *Austr. J. Chem.*, 2010, **63**, 148-164.
9. T. Ratner, O. Reany and E. Keinan, *ChemPhysChem*, 2009, **10**, 3303-3309.
10. J. M. Granda and J. Jurczak, *Chem. – Eur. J.*, 2014, **20**, 12368-12372.
11. N. Busschaert, C. Caltagirone, W. Van Rossom and P. A. Gale, *Chem. Rev.*, 2015, **115**, 8038-8155.
12. P. A. Gale and C. Caltagirone, *Chem. Soc. Rev.*, 2015, **44**, 4212-4227.
13. P. A. Gale and C. Caltagirone, *Coord. Chem. Rev.*, 2018, **354**, 2-27.
14. A. Casula, A. Llopis-Lorente, A. Garau, F. Isaia, M. Kubicki, V. Lippolis, F. Sancenón, R. Martínez-Máñez, A. Owczarzak, C. Santi, M. Andrea Scorciapino and C. Caltagirone, *Chem. Comm.*, 2017, **53**, 3729-3732.
15. V. Amendola, L. Fabbrizzi and L. Mosca, *Chem. Soc. Rev.*, 2010, **39**, 3889-3915.
16. A.-F. Li, J.-H. Wang, F. Wang and Y.-B. Jiang, *Chem. Soc. Rev.*, 2010, **39**, 3729-3745.
17. J. G. Fernández-Bolaños, Ó. López, V. c. Ulgar, I. Maya and J. Fuentes, *Tetrahedron Lett.*, 2004, **45**, 4081-4084.
18. N. Busschaert, I. L. Kirby, S. Young, S. J. Coles, P. N. Horton, M. E. Light and P. A. Gale, *Angew. Chem. – Int. Ed.*, 2012, **51**, 4426-4430.
19. P. P. Deohate, J. P. Deohate and B. N. Berad, *Asian J. Chem.*, 2004, **16**, 255-260.
20. S. A. Kadam, K. Haav, L. Toom, T. Haljasorg and I. Leito, J*. Org. Chem.*, 2014, **79**, 2501-2513.
21. S. A. Kadam, K. Martin, K. Haav, L. Toom, C. Mayeux, A. Pung, P. A. Gale, J. R. Hiscock, S. J. Brooks, I. L. Kirby, N. Busschaert and I. Leito, *Chem. – Eur. J.*, 2015, **21**, 5145-5160.
22. A. Tarai and J. B. Baruah, *J. Mol. Struct.*, 2015, **1091**, 147-151.
23. K. A. Haushalter, J. Lau and J. D. Roberts, *J. Am. Chem. Soc.*, 1996, **118**, 8891-8896.

Appendix B

Reverse Hexagonal Liquid Crystalline Dispersion for Theranostic Cancer Treatments: An in-vitro Study

Appendix B

B.1 Introduction

The scenario of dispersed lipid liquid crystalline phases for biomedical applications is dominated by lamellar phase dispersions, namely, liposomes. Indeed, they have been widely studied as model membranes,[1, 2] templates,[3] and transporters for drugs.[4] From a clinical perspective, this huge effort of research has translated into several marketed liposomal formulations, mainly for anticancer applications (Doxil, Caelyx, and Myocet are liposome systems used for Kaposi's sarcoma, ovarian cancer, and multiple myeloma).[5] Remaining in the lipid liquid crystalline phases arena, aqueous dispersions of reverse bicontinuous cubic phases, commonly known as cubosomes, were, in the past, deeply investigated from a physicochemical point of view,[6, 7, 8, 9] and more recently proposed for biomedical uses.[10, 11] Hexosomes, dispersions of the reverse hexagonal phase, represent another example of liquid crystalline structure into nanoparticles. They are constituted of water cylinders surrounded by lipid monolayers and packed in a two-dimensional hexagonal arrangement. Similarly to cubosomes, hexosomes can be prepared by dispersion in a multiphase region, where the liquid crystalline phase coexists with water. Although a variety of lipids can form reverse hexagonal phases, they (also in excess of water) are often thermodynamically stable only at high temperature, as found in the monoolein (MO)/water or phytantriol (PHYT)/water binary phase diagrams.[12, 13] The formation of this phase at room temperature generally requires the presence of a lipophilic molecule (e.g., oleic acid, OA) that may alter the MO or PHYT effective packing parameter, causing the reverse bicontinuous cubic to reverse hexagonal phase transition.[14, 15] In addition, several examples in the literature described how appropriate modification of the PHYT chain can lead to the formation of a hexagonal structure.[16, 17, 18]

The colloidal stability of hexosomes (and cubosomes as well) is achieved by the action of stabilizing polymers. These polymers may have a role in reducing the rapid

clearance of the nanoparticles from the bloodstream by plasma proteins, but their primary function is promoting steric stabilization against aggregation. The most diffuse polymers used for such purpose are Pluronics, especially F127 and F108, which differ for the HLB (Hydrophilic-Lipophilic Balance) value, lower for F127.[19] Other stabilizing agents are also employed, such as DSPE-PEG_{2000}[20] and Citrem.[21]

Hexosomes of various compositions were studied as drugs nanocarriers. For instance, the release of Irinotecan (a water-soluble anticancer drug) from oleyl glycerate-based hexosomes was reported,[22] and MO/OA-based hexosomes were proposed for oromucosal delivery of progesterone and for improving skin penetration of a model protein (Cyclosporin A).[23, 24] More recently, hexosomes based on diethylenetriamine pentaacetic acid and PHYT, able to complex Gd(III) and targeted with an α-Flag antibody fragment for antigen recognition, were developed as MRI imaging tool.[17] To the same aim, nitroxide-loaded MO-based hexosomes were designed. *In-vivo* MRI imaging tests were conducted on mice using these nanoparticles to investigate the biodistribution of the system after intravenous administration.[25] Cancer cell-targeted hexosomes were also engineered as potential theranostic platform by simultaneously combining the therapeutic action of Camptothecin, and the fluorescence imaging functionality of a pyrene-modified BODIPY.[26]

Docetaxel (DTX) is an important chemotherapeutic agent against many locally advanced and metastatic cancers. However, clinical applications are drastically limited by its low water solubility and lack of targeting, which leads to several side effects due to acute toxicity to normal tissues. During the last decade, several drug delivery systems have been developed to improve DTX water solubility and reduce toxicity, including polymeric and lipid nanocarriers.[27]

In this context, we present here a MO-based hexosomes formulation loaded with DTX, and stabilized in water by a mixture of commercial, Rhodamine-conjugated, and folate-conjugated Pluronic F108. This innovative system was developed with the aim to enhance aqueous solubility and bioavailability of DTX by means of its encapsulation

in the stable liquid crystalline structure of hexosomes with long circulating properties. Indeed, the prepared hexosomes were sufficiently large to avoid a rapid renal clearance while their nanostructure was enclosed within a highly flexible and hydrophilic polymeric layer of Pluronic F108, which should confer them stealth properties, thus avoiding opsonisation and consequent clearance from the bloodstream. Further, to make them suitable as both therapeutic and diagnostic tool in cancer treatment, hexosome particles were functionalized with targeting and imaging moieties, namely folic acid and Rhodamine. Folate was selected as a tumor-targeting ligand since it is a small, non-toxic, non-immunogenic molecule, whose receptors are often over-expressed in tumor cells.

DTX-loaded hexosomes were characterized for size, morphology, and structural features, while the drug stability in the liquid crystalline matrix was evaluated by *in-vitro* release studies. Finally, HeLa cells were used to assess cytotoxicity and cellular uptake.

B.2 Results and discussion

Hexosomes physicochemical and photophysical characterization

Figure B1 is a cryo-TEM image representative for the hexosome formulation investigated here. The examination of this image reveals several spherical and quasi-spherical nanoparticles showing an inner structure denoted by the hexagonal motifs and curved striations that are commonly observed in liquid crystalline nanoparticles characterized by the reverse hexagonal symmetry. Such striations are very likely related to the configuration adopted by the water tubules to better stabilize the nanostructure.[28]

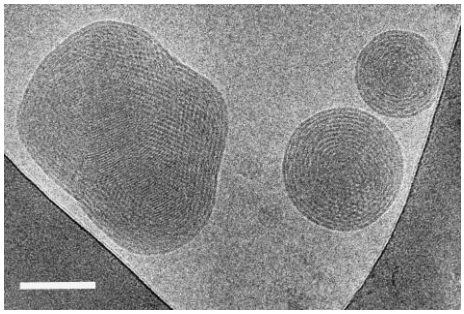

Figure B1. Cryo-TEM image of the hexosome formulation stabilized using a 60/20/20 mixture of commercial PF108, folate-conjugated, and rhodamine-conjugated PF108, and loaded with Docetaxel. Bar is 100 nm.

Size and structural features of the hexosomes were studied by DLS and SAXS. Moreover, since this formulation is proposed for theranostic nanomedicine, it seemed important investigating its stability at different temperatures. Results are reported in Figure B2 and Table B1.

Table B1. Hexosomes lattice parameters (a), radius of the water channels (r_w), average hydrodynamic radius (R_h), and polydispersity index (PdI) at different temperatures.

T (°C)	a (Å)	r_w (Å)	R_h (nm)	PdI
25	60.0 ± 0.1	31.0 ± 0.1	109	0.12
37	58.1 ± 0.1	30.0 ± 0.1	106	0.16
50	56.3 ± 0.1	29.0 ± 0.1	104	0.12
10	---	---	105	0.27
25	60.4 ± 0.2	31.1 ± 0.1	---	---

37	59.1 ± 0.1	30.5 ± 0.1	---	---

SAXS experiments proved the hexagonal inner structure of the formulation. Indeed, the diffraction pattern at 25 °C (Figure B2) is characterized by three Bragg peaks in a *q* ratio of 1:√3:2, consistent with the reverse hexagonal phase.

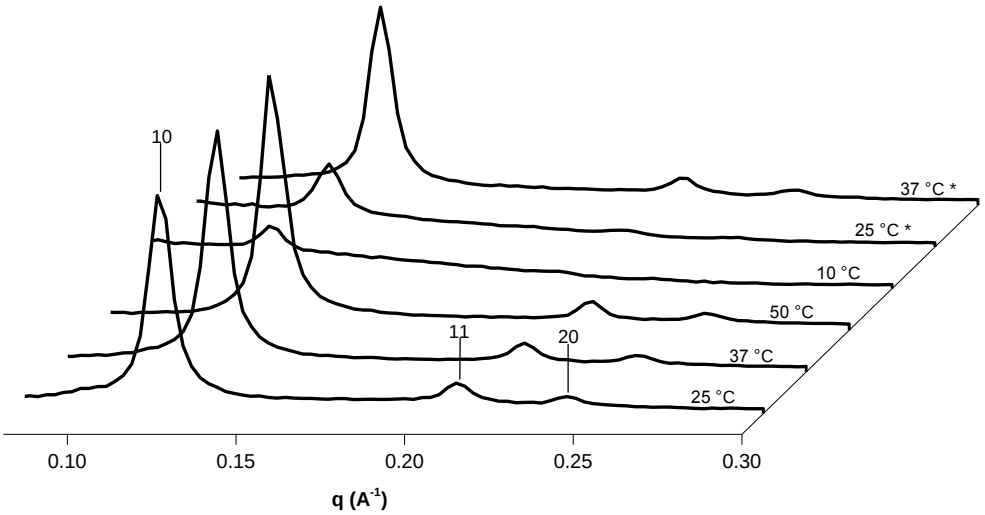

Figure B2. SAXS diffraction pattern recorded at different temperatures of the same hexosome formulation described in Figure B1. The Miller indices are reported on top of the corresponding Bragg peaks.

Table B1 reports the lattice parameter, *a,* obtained from the SAXS experiments as well as the calculated radius of the water channels, r_w, (see the Materials and Methods section). These experiments were performed with the following temperature cycle: 25, 37, 50, 10, 25, and 37 °C. Basically, the reverse hexagonal nanostructure was observed at all the investigated temperatures, though a slight decrease of the lattice parameter was detected as the temperature is increased. Such a behavior, already reported in the literature, is related to the greater disorder of the monoolein alkyl chains at higher temperatures, which brings to a higher negative curvature of the lipid/water interface.[29] However, it should be noticed that the intensity of the diffraction pattern collected at 10 °C is greatly reduced compared to that obtained at

the higher temperatures, so that the reflections corresponding to the 11 and 20 planes almost vanished. This fact suggests some kind of alteration of the sample in terms of aggregation of the nanoparticles, or the loss of the symmetry of their inner phase.

The DLS results reported in Table A1 demonstrate that the formulation is essentially not sensitive to the temperature variations, since the nanoparticles average size and polydispersity index (PdI) did not change increasing the temperature from 25 to 37 to 50 °C. At the same time, the huge increase in the PdI recorded at 10 °C supports the idea that aggregation of the nanoparticles occurred at this temperature. Remarkably, the nanostructural features as determined by SAXS are recovered after return to room temperature.

Rhodamines belong to the family of the xanthene dyes. Due to strong absorption in the visible region, high fluorescence quantum yield (Φ = 0.95 in EtOH for Rhodamine 6G),[30] as well as good optical and thermal stability, they have been extensively employed as lasing media in liquid and solid-state dye lasers. However, the self-assembly aggregation process between individual dye molecules often minimizes the performance efficiency.[31] Although for some applications Rhodamines are used in the free form, often the probes must be modified *via* synthetic path, and the absorption and emission properties can be strongly influenced by substituents in the xanthene skeleton.[32]

The photophysical properties of PF108-R were investigated in our previous work.[33] In chloroform and water PF108-R shows the same strong absorption at 560 nm, with a shoulder at 522 nm. The emission band generated at 584 nm in chloroform, upon excitation at 522 nm, undergone a red-shift in water at 594 nm, as result of the increased polarity of the medium. The measured quantum yields (0.16 and 0.58, in water and chloroform, respectively) show that Pluronic conjugation has a negative effect on the emission efficiency of the dye (for its precursor Rhodamine B, Φ = 0.31 in water[34] and Φ = 0.65 in basic EtOH).

The hexosome formulation was characterized from the photophysical point of view after 1:100 dilution in water (Figure A3). Upon excitation at 522 nm a band centred at 583 nm arises. Considering the closeness to the emission band of PF108-R in chloroform, the conjugated stabilizer is probably embedded in the poly(ethyleneoxide) corona surrounding hexosomes, thus experiencing quite an apolar environment. By setting the emission wavelength to 620 nm, the recorded excitation spectrum overlaped the absorption spectra of PF108-R in chloroform and in water.

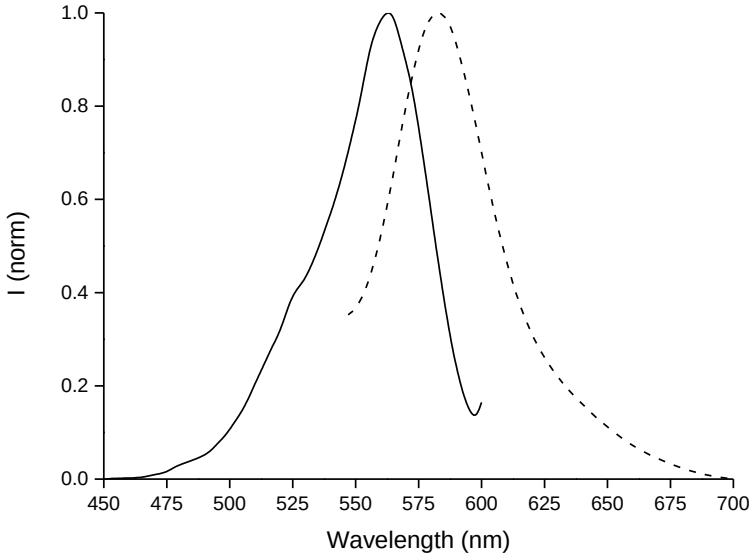

Figure B3. Normalized emission (solid line, λ_{exc} = 522 nm) and excitation (dashed line, λ_{em} = 620 nm) spectra of the aqueous hexosome formulation stabilized using a PF108/PF108-FA/PF108-R = 60/20/20 (wt %).

In-vitro release study

The *in-vitro* release study was carried out to assess both the stability of the drug in the liquid crystalline matrix and the ability of the carrier to release the incorporated

drug at a suitable rate. DXT release is supposed to occur only from the lipid phase because of the poor water solubility of this drug. To evaluate the *in-vitro* DXT release from the hexosome formulation, the infinite dose technique was used by applying a large amount of formulation (200 µL) on the membrane surface. The use of an infinite dosing prevents drug depletion from the donor compartment during the experiment, thus ensuring a constant driving force for the release process, and gives steady-state conditions. The drug percentage released from the hexosomes as a function of time during 8 h, is reported in Figure B4.

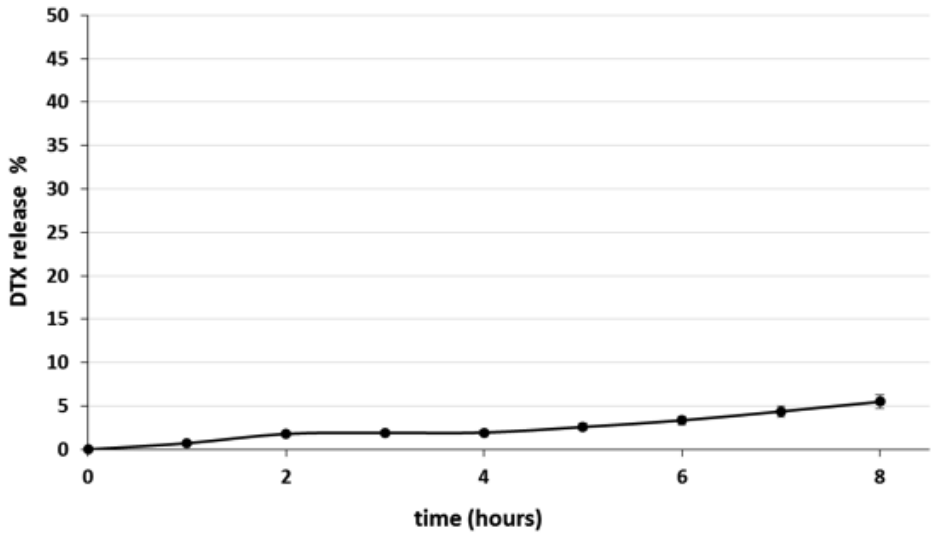

Figure B4. Release profile of Docetaxel (DTX) from hexosomes at 37 °C as a function of time.

As it can be seen from the graph, the drug release exhibited a linear profile characterized by a very slow and continuous release rate. Such behavior is remarkable, since it differentiates this formulation from others of the same kind, commonly characterized by an initial burst release.[35] After the 8 h experiment only 6% of the applied dose was recovered from the receptor compartment, thus demonstrating stable entrapment of the drug into the hexosome formulation. DTX

recovery from the donor and receptor compartment was always more than 95–97% of the applied dose, and DLS analyses did not show any significant alteration in hexosome size and polydispersity after an 8 h experiment. This studied period gives significant information to predict the stability during the distribution process, since *in-vivo* study with monoolein-based liquid crystalline nanoparticles demonstrated a high accumulation of carrier systems to tumor mass after less than 8 h.[35]

HeLa cell imaging and cytotoxic activity

Investigation of the hexosomes internalization within HeLa cells was conducted by fluorescence microscopy.

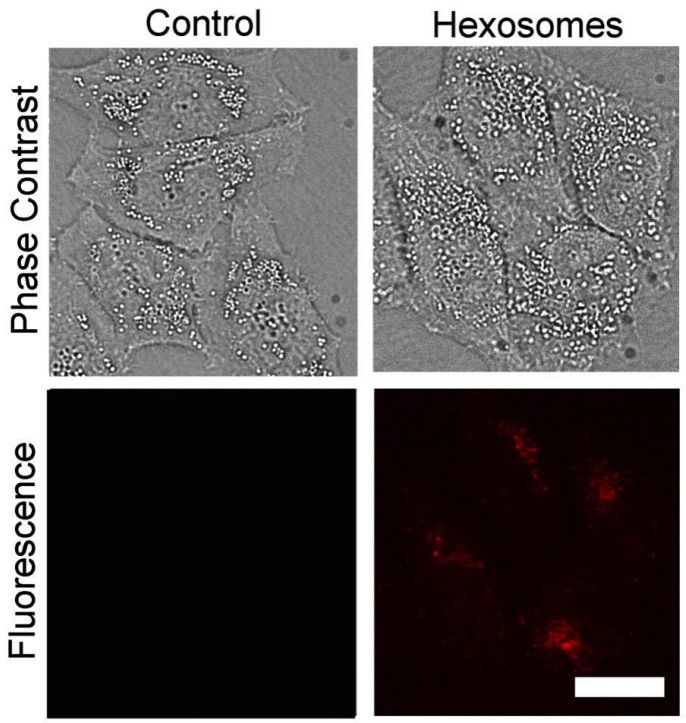

Figure B5. Fluorescence microscopy of living HeLa cells treated with hexosomes not carrying the drug (incubation for 4 h) showing a diffuse cytoplasmic fluorescence in treated cells indicating nanoparticles uptake. Scale bar = 20 µm.

As can be noticed in Figure B5, while no fluorescence was detected in untreated-control cells, a faint diffuse fluorescence was observed within the cellular cytoplasm after 4 h incubation with the fluorescent hexosomes (not loaded with the drug). Differently from other fluorescent microscopy experiments performed on HeLa cells using similar liquid crystalline formulations,[36] here it was not possible assessing a specific compartmentalization of the dye. This fact may be related to the nature of the dye used. Indeed, while hydrophobic dyes loaded into liquid crystalline nanoparticles invariably localize in the lipid droplets (dynamic storage organelles representing intracellular reservoir of apolar lipids) after release from the nanoparticles within the cells, here the surfactant nature of the dye (conjugated to the Pluronic) probably allowed its more extensive distribution in the cytoplasmic membranes, thus leading to the observed lack of a definite localization.

The amount of MO, OA (expressed as mg/mL of dispersion), and DTX (μg/mL) in different hexosome formulations was monitored by HPLC-DAD. The formulations analyzed were: the hexosome formulations stabilized either with the mixture PF108/PF108-FA (HEX) or with the mixture PF108/PF108-FA/PF108-R (HEX-R), and the latter formulation also loaded with DTX (HEX-R/DTX).

Monoolein content in HEX, HEX-R, and HEX-R/DTX formulations was found to be 31.4 ± 2.9 mg/mL, while OA concentration measured in the same series of nanoparticle formulations was 3.8 ± 0.3mg/mL.

The HEX-R/DTX formulation was found loaded with 203.7 ± 27.28 μg/mL of drug, with a DTX/MO molecular ratio of 1/6.5 The encapsulation efficacy (EE%) was 68 ± 9%.

These formulations were tested for cytotoxicity (MTT assay) in HeLa cells. Figure B6 shows the viability, expressed as % of the control, induced in HeLa cancer cells after 4 h of incubation in the presence of the nanoparticle formulations at concentration of 2 μL/mL of medium (corresponding to 63 μg/mL of MO).

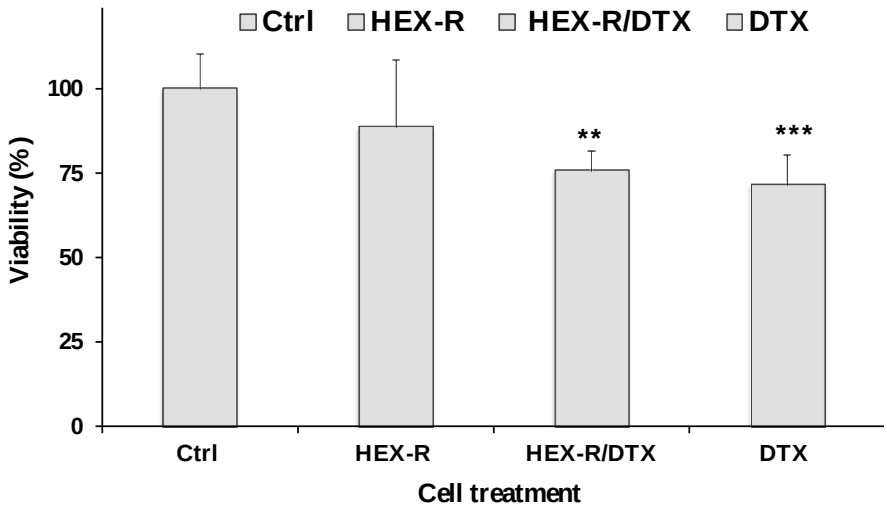

Figure B6. Viability, expressed as % of the control, induced in HeLa cells by incubation for 4 h in the presence of different type of hexosome formulations (HEX-R, and HEX-R/DTX, see the text) and Docetaxel (DTX). Drug concentration in the HEX-R/DTX formulation (0.5 μM) is 20-fold lower than in DTX solution (10 μM). Results are expressed as a mean ± standard deviation (SD) of four independent experiments involving quadruplicate analyses for each sample (n = 4). *** = $P < 0.001$; ** = $P < 0.01$ versus Ctrl, and data were analyzed using one-way ANOVA.

The cytotoxic effect of DTX 10 μM was also determined at 4 h-incubation for comparison. Treatment with HEX-R formulations did not induce significant reduction in cell viability, in comparison with control cells (Ctrl, not treated with nanoparticles). Differently, the incubation with HEX-R/DTX particles induced a statistically significant decrease in HeLa cell viability (24% of reduction) with respect to the control due to the presence of the anticancer drug. A significant cytotoxic effect (28% reduction in cell viability) was also observed in cells treated with a 10 μM solution of the antitumor drug. Remarkably, the HeLa cell treatment with DTX-loaded hexosomes (DTX dose of approximately 0.5 μM) induced a cytotoxic effect comparable to that of the antitumor drug tested at much higher (20-fold) concentration.

B.3 Conclusions

In this paper we investigated monoolein-based nanoparticles, known as hexosomes, characterized by a core made by a liquid crystalline reverse hexagonal phase. It was demonstrated that hexosomes can be loaded with Docetaxel, a highly hydrophobic anticancer drug, and stabilized by a mixture of commercial and derivatized Pluronics conjugated to fluorescent (Rhodamine) and cancer cells targeting (folate residues) moieties while keeping unaltered the specific liquid crystalline features of their inner nanostructure. The high stability of this formulation was also demonstrated by release experiments, showing a very slow and continuous profile without initial burst release of the drug. In addition, cytotoxicity tests proved the efficacy of this formulation against HeLa cells, being 20-fold more active than the Docetaxel administered in solution. These results confirm that hexosomes are a most promising and useful platform for theranostic nanomedicine.

B.4 Materials and methods

Materials

Monoolein (MO, 1-monooleoylglycerol, RYLO MG 19 PHARMA, glycerol monooleate, 98.1 wt %) was kindly provided by Danisco A/S, DK-7200, Grinsted, Denmark. Pluronic F108 (PF108, PEO132-PPO50-PEO132), Docetaxel (≥ 97%), oleic acid (OA, 99%), acetonitrile (≥ 99.9%), ethanol (≥ 99.8%), and acetic acid (≥ 99.7%) were purchased from Sigma-Aldrich. Distilled water passed through a Milli-Q water purification system (Millipore) was used to prepare the samples. The syntheses of PF108-FA and PF108-R have been reported elsewhere.[26]

Hexosomes preparation and characterization

MO-based hexosomes were prepared and stabilized by dispersing the appropriate amount of MO and OA in water solution of a mixture of Pluronic F108, folate-conjugated and Rhodamine-conjugated F108 (PF108/PF108-FA/ PF108-R), using an

ultrasonic processor UP100H by Dr. Hielscher, cycle 0.9, amplitude 90 %, for 10 min. PF108/PF108-FA/PF108-R ratio was 80/20/0 and 60/20/20 respectively for not fluorescently marked hexosomes (HEX) and for Rhodamine marked hexosomes (HEX-R). Docetaxel doped hexosomes (HEX-R/DTX) were obtained by dispersing the drug in the melted lipids with the help of an ultrasonic bath before mixing with the Pluronics solution. The sample volume was usually 4 mL with approximately 96.4 wt % of water, 2.97 wt % of MO, 0.33 wt % of OA and 0.3 wt % Pluronics mixture.

Dynamic light scattering (DLS) measurements for the determination of the nanoparticles size and polydispersity index were performed at 10, 25, 37, and 50 °C using a light scattering goniometer instrument (3D LS Instruments, Fribourg, Switzerland), which was equipped with a 35 mW He-Ne laser light source (wavelength of 632.8 nm). The characterization of the nanoparticles internal structure at 10, 25, 37, and 50 °C was carried out by small angle x-ray scattering (SAXS) using a Ganesha 300XL (SAXSLAB ApS, Skovlunde, Denmark). The scattering data was collected over a q range of $0.014 < q\ (Å^{-1}) < 0.753$, where the magnitude of the scattering vector, q, is defined as $q = (4\pi/\lambda)\sin(\theta/2)$, where θ is the scattering angle. Water channels radii of the reverse hexagonal phase were calculated using the relation $r_w = a(1 - \phi_{lip})^{1/2}(\sqrt{3}/2\pi)^{1/2}$, where a is the lattice parameter obtained from the SAXS analysis and ϕ_{lip} is the volume fraction of the dispersed phase. Samples were equilibrated during 1 h at the measurement temperature prior performing the 2 h experiment. The morphology of the nanoparticles was observed by cryo-TEM at 120 kV acceleration voltage using an FEI Tecnai T12 G^2 transmission electron microscope at about -175 °C in the low-dose imaging mode to minimize electron-beam radiation-damage. Images were digitally recorded with a Gatan US1000 high-resolution CCD camera.

Photophysical measurements

Hexosome dispersions were diluted with Milli-Q water (1:100) before performing the photophysical measurements. The emission and excitation spectra were recorded

with a PerkinElmer LS 55 spectrofluorimeter. The fluorescence quantum yield on PF108-R was determined by using Rhodamine 6G dissolved in EtOH as the reference standard (Φ_{ref} = 0.95). The absorption spectra were recorded on a Thermo Nicolet Evolution 300 spectrophotometer.

Drug release experiments

DTX release from the hexosomes under investigation was measured through regenerated cellulose membranes using Franz-type diffusion cells (LGA, Berkeley, CA). The cellulose membrane was moistened by immersion in water for 1 hour at room temperature before being mounted in Franz-type diffusion cells. Diffusion surface area and receiving chamber volume of the cells were, respectively, 0.75 cm^2 and 5.5 mL. The receptor was filled with water/ethanol (50/20 v/v) for ensuring pseudo-sink conditions by increasing active compound solubility in the receiving phase. The receiving solution was constantly stirred and thermostated at 37 °C. 200 μL of formulation were applied on the membrane surface under non-occlusion conditions and the experiments was run for 8 hours. At intervals, the receptor phase was withdrawn and replaced with an equal volume of receiving solution pre-equilibrated to 37 °C. The receptor phase samples were analyzed by the HPLC method described below to determine DTX content. At the end of the experiments, samples of the hexosomes applied on the membrane surface were withdrawn and analyzed to determine particle size and polydispersity index. Experiments were performed in triplicate.

Determination of MO, OA and DTX content in hexosomes

After loading with DTX the hexosomes dispersion was purified from the non-encapsulated drug by dialysis: 2 mL were loaded into a dialysis tubing cellulose membrane (14 kDa MW cut-off) and dialyzed against water (1 L) for 2 hours (by replacing water after 1 hour) at 25 °C.

Aliquots (10 µL) of the dialyzed nanoparticle preparations were dissolved in 300 µL of CH_3CN with 0.14 % CH_3COOH (v/v). The samples were vortexed to get a clear solution, and aliquots (20 µL) were injected into the Agilent Technologies 1100 liquid chromatograph equipped with a diode array detector (DAD) (Agilent Technologies, Palo Alto, CA). Analyses of MO and OA (detected at 200 nm), and Docetaxel (at 230 nm) in hexosome dispersions were carried out with a XDB–C_{18} Eclipse (150 × 4.6 mm, 3.5 mm particle size) (Agilent Technologies) equipped with a Zorbax XDB–C_{18} Eclipse (12.5 × 4.6 mm, 5 mm particle size) guard column (Agilent Technologies), with a mobile phase of $CH_3CN/H_2O/CH_3COOH$ (75/25/0.12, v/v/v), at a flow rate of 2.3 mL/min. The temperature of the column was maintained at 37 °C. Recording and integration of the chromatogram data was carried out through an Agilent OpenLAB Chromatography data system. The identification of lipid components and drug was made using standard compounds and conventional UV spectra. Calibration curves of all of the compounds were constructed using standards and were found to be linear, with correlation coefficients > 0.995.

Drug encapsulation efficacy (EE%) was calculated by the following equations: EE% = (weight of the drug in nanoparticles)/(weight of the feeding drug) × 100%. Data were expressed as a mean ± standard deviation (SD) of three independent experiments involving duplicate analyses for each sample.

Cell Culture

HeLa cells (ATCC collection) were grown in phenol red-free Dulbecco's modified Eagle's medium (DMEM, Molecular Probes, USA) with high glucose, supplemented with 10% (v/v) fetal bovine serum, penicillin (100 U/mL) and streptomycin (100 µg/mL) (Invitrogen) in 5% CO_2 incubator at 37 °C. For live cell imaging, HeLa cells were seeded in 35 mm dishes and experiments were carried out two days after seeding when cells had reached 90% confluency. Liquid crystalline nanoparticles were added to the cells at a concentration of 1:500 (2 µL in 1 mL of fresh medium) and incubated

at 37 °C for 4 h. Fresh serum-free medium was used to remove the extracellular particle suspension before imaging session.

Fluorescence microscopy

Light microscopy observations were made using a Zeiss (Axioskop) upright fluorescence microscope (Zeiss, Oberkochen, Germany) equipped with 10x, 20x and 40x/0.75 NA water immersion objectives and a HBO 50 W L-2 mercury lamp (Osram, Berlin, Germany). Twelve-bit-deep images were acquired with a monochrome cooled CCD camera (QICAM, Qimaging, Canada). For observation of dye fluorescence, filters were: ex 546 ± 6, em 620 ± 60. Digital images were obtained with Image Pro Plus software (Media Cybernetics, Silver Springs, MD).

Cytotoxic activity (MTT assay)

The cytotoxic effect of hexosome formulations was evaluated in HeLa cells by the MTT assay. HeLa cells were seeded in 24-well plates at density of 3×10^4 cells/well in 500 µL of serum-containing media. Experiments were carried out two days after seeding when cells had reached 90% confluence. The different formulations were added to the cells at concentration of 1:500 (2 µL in 1 mL of serum-free medium) and incubated at 37 °C for 4 h. The effect of Docetaxel 10 µM (specifically, 1 µL of a 10 mM solution of Docetaxel in DMSO was added to 1 mL of serum-free medium) on HeLa cell viability was also tested for comparison at the same incubation time. A 50 µL portion of MTT solution (3-(4,5-dimethylthiazol-2-yl)-2,5-diphenyltetrazolium bromide) (5 mg/mL in H_2O), was then added and left for 2 h at 37 °C. The medium was aspirated, 500 µL of DMSO was added to the wells, and color development was measured at 570 nm with an Infinite 200 auto microplate reader (Infinite 200, Tecan, Austria). The absorbance is proportional to the number of viable cells. Results are shown as percent of cell viability in comparison with non-treated control cells. Data

were expressed as a mean ± standard deviation (SD) of three independent experiments involving quadruplicate analyses for each sample.

Statistical analysis

Evaluation of statistical significance of differences was performed using Graph Pad INSTAT software (GraphPad software, San Diego, CA, USA). Comparison between groups was assessed by one–way analysis of variance (One–way ANOVA) followed by the Bonferroni Multiple Comparisons Test.

B5 References

1 Cuomo, F., Ceglie, A., Lopez, F., *J. Colloid Interface Sci*. 2012, **365**, 184–190.

2 Edidin, M.,. *Annu. Rev. Biophys. Biomol. Struct.* 2003, **32**, 257–283.

3 Cuomo, F., Lopez, F., Ceglie, A., *Adv. Colloid Interface Sci*. 2014, **205**, 124–133.

4 Cho, K., Wang, X., Nie, S., Chen, Z., Shin, D.M.,. *Clin. Cancer Res.* ,2008, **14**, 1310–1316.

5 Al-Jamal, W.T., Kostarelos, K., *Acc. Chem. Res.*,2011, **44**, 1094–1104.

6 Gustafsson, J., Ljusberg-Wahren, H., Almgren, M., Larsson, K., *Langmuir*, 1997 **13**, 6964–6971.

7 Gustafsson, J., Ljusberg-wahren, H., Almgren, M., *Langmuir* 1996, **12**, 4611–4613. doi:10.1021/la960318y

8 Monduzzi, M., Ljusberg-Wahren, H., Larsson, K., *Langmuir*, 2000, **16**, 7355–7358. doi:10.1021/la0000872

9 Neto, C., Aloisi, G., Baglioni, P., Larsson, K., *J. Phys. Chem. B*, **1999**, 103, 3896–3899.

10 Azmi, I.D., Moghimi, S.M., Yaghmur, A., *Ther. Deliv.*, 2015, **6**, 1347–1364.

11 Mulet, X., Boyd, B.J., Drummond, C.J., *J. Colloid Interface Sci.*, 2013, **393**, 1–20.

12 Barauskas, J., Landh, T., *Langmuir*, 2003, **19**, 9562–9565.

13 Qiu, H., Caffrey, M., *Biomaterials*, 2000, **21**, 223–234.

14 Nilsson, C., Østergaard, J., Larsen, S.W., Larsen, C., Urtti, A., Yaghmur, A., *Langmuir*, 2014, **30**, 6398–6407.

15 Wibroe, P.P., Mat Azmi, I.D., Nilsson, C., Yaghmur, A., Moghimi, S.M., *Biol. Med.*, 2015, **11**, 1909–1914.

16 Fong, C., Weerawardena, A., Sagnella, S.M., Mulet, X., Waddington, L., Krodkiewska, I., Drummond, C.J., *Soft Matter*, 2010, **6**, 4727–4741.

17 Moghaddam, M.J., de Campo, L., Hirabayashi, M., Bean, P.A., Waddington, L.J., Scoble, J.A., Coia, G., Drummond, C.J., *Biomater. Sci.*, 2014, **2**, 924–935.

18 Moghaddam, M.J., de Campo, L., Waddington, L.J., Drummond, C.J., *Soft Matter*, 2010, **6**, 5915.

19 Chong, J.Y.T., Mulet, X., Waddington, L.J., Boyd, B.J., Drummond, C.J., *Soft Matter*, 2011, **7**, 4768.

20 Zeng, N., Hu, Q., Liu, Z., Gao, X., Hu, R., Song, Q., Gu, G., Xia, H., Yao, L., Pang, Z., Jiang, X., Chen, J., Fang, L., 2012. *Int. J. Pharm.*, 2012, **424**, 58–66.

21 Nilsson, C., Edwards, K., Eriksson, J., Larsen, S.W., Østergaard, J., Larsen, C., Urtti, A., Yaghmur, A., *Langmuir*, 2012, **28**, 11755–11766.

22 Boyd, B.J., Whittaker, D. V., Khoo, S.M., Davey, G., *Int. J. Pharm.*,2006, **318**, 154–162.

23 Lopes, L.B., Ferreira, D.A., De Paula, D., Garcia, M.T.J., Thomazini, J.A., Fantini, M.C.A., Bentley, M.V.L.B., *Pharm. Res.*, 2006, **23**, 1332–1342.

24 Swarnakar, N.K., Jain, V., Dubey, V., Mishra, D., Jain, N.K., *Pharm. Res*., 2007,

24, 2223–2230.

25 Bye, N., Hutt, O.E., Hinton, T.M., Acharya, D.P., Waddington, L.J., Mo, B.A., Wright, D.K., Wang, H.X., Mulet, X., Muir, B.W., *Langmuir*, 2014, **30**, 8898−8906.

26 Caltagirone, C., Arca, M., Falchi, A.M., Lippolis, V., Meli, V., Monduzzi, M., Nylander, T., Rosa, A., Schmidt, J., Talmon, Y., Murgia, S., *RSC Adv*., 2015, **5**, 23443–23449.

27 Zhao, P., Astruc, D., *ChemMedChem*, 2012, **7**, 952–972.

28 Sagalowicz, L., Michel, M., Adrian, M., Frossard, P., Rouvet, M., Watzke, H.J., Yaghmur, A., De Campo, L., Glatter, O., Leser, M.E., *J. Microsc*., 2006, **221**, 110–121.

29 Nakano, M., Sugita, A., Matsuoka, H., Handa, T., *Langmuir*, 2001, **17**, 3917–3922.

30 Kubin, R.F., Fletcher, A.N.,. Fluorescence Quantum Yields of Some Rhodamine 1982, **27**, 455–462.

31 Kazakevicĭus, A., Peckus, D., Boiko, O., Valkunas, L., Leonenko, E., Telbiz, G., Gulbinas, V., *J. Phys. Chem. C*, 2015, **119**, 19126–19133.

32 Gonçalves, M.S.T., Gonçalves, M.S.T., *Chem. Rev.*, 2009, **109**, 190–212.

33 Meli, V., Caltagirone, C., Falchi, A.M., Hyde, S.T., Lippolis, V., Monduzzi, M., Obiols-Rabasa, M., Rosa, A., Schmidt, J., Talmon, Y., Murgia, S., *Langmuir*, 2015, **31**, 9566–9575.

34 Magde, D., Rojas, G.E., Seybold, P.G., *Photochem. Photobiol*., 1999, **70**, 737–744.

35 Jain, V., Swarnakar, N.K., Mishra, P.R., Verma, A., Kaul, A., Mishra, A.K., Jain, N.K., *Biomaterials*, 2012, **33**, 7206–7220.

36 Falchi, A.M., Rosa, A., Atzeri, A., Incani, A., Lampis, S., Meli, V., Caltagirone, C., Murgia, S., *Toxicol. Res*., 2015, **4**, 1025–1036.

Appendix C

Multifunctional cubic liquid crystalline nanoparticles for chemo- and photodynamic synergistic cancer therapy

Appendix C

C.1 Introduction

Bicontinuous cubic liquid crystalline nanoparticles, universally known as cubosomes, represents a very peculiar class of soft matter-based material that differentiates from their lamellar counterpart, the liposomes. In cubosomes, the three dimensional arrangement of the lipid bilayer is folded in space on an infinite periodic minimal surface of cubic symmetry and separates two interwoven water channels,[1,2] resembling that of the bicontinuous cubic bulk phases.[3,4] In addition, since the lipid matrix completely fills the inner portion of the nanoparticles, compared to single-bilayer liposomes cubosomes offer a larger (up to three times) hydrophobic volume, at the same time exposing to water only 60 % of their surface with respect to that of liposomes.[5] Such characteristics made cubosomes extremely interesting for pharmaceutical applications as drug delivery vehicles.[6,7] Therefore, cubosomes have been largely explored in nanomedicine, and numerous articles have been published discussing their potential for the topical,[8–10] enteral,[11–14] or parenteral[15–21] administration of drugs. Particularly, cubosomes can be designed to simultaneously transport imaging agents and therapeutic agents, so they can be effectively used in theranostic nanomedicine.[22–24] Although numerous investigations demonstrated that cubosomes may be somewhat cytotoxic, and some types of cubosome formulations were also shown to induce hemolysis,[25,26] they can be formulated and administered at a non-toxic concentration still useful for medical purposes. By contrast, only few in vivo experiments were performed so far, and much more are needed to fully understand the relevance of this kind of nanoparticles in medical applications.[10,27–30]

Among many therapeutic procedures approved by US FDA, Photodynamic Therapy (PDT) has been proven as an interesting and emerging tool for cancer treatment, since its first application. PDT is a minimally invasive approach that can be safely combined

with other antitumor treatments, such as chemotherapy, radiotherapy, and surgery.[31] It requires a photosensitizer molecule (PS), light and oxygen. After injection of the PS into the blood stream and its accumulation into the target tissues, light irradiation (600 - 800 nm) is applied. After absorption of light and intersystem crossing, the PS in the excited triplet state can transfer its energy to molecular oxygen O_2 (Type II process), giving highly cytotoxic $^1O_2$ or it can react with surrounding biomolecules by electron or proton transfer (Type I process) leading to radical species that further react with oxygen to generate Radical Oxygen Species (ROSs).[32] The effects of the treatment are first the direct tumor cell death, a microvascular damage and latter an inflammatory reaction that can lead to a development of systemic immunity.[33] The literature most reported structures for a PS is the tetrapyrrolic macrocycle due to its high absorption peak in the optical window of tissue, no dark toxicity and relatively rapid clearance from healthy tissues.[34–37] Recent papers showed how a two-photon photosensitizer for PDT connected to one or two GdDOTA-based complexes could be used as a theranostic tool in PDT and MRI, giving low dark toxicity and promising results on HeLa cells.[38,39]

Enhancing the accumulation of the PS in the target tumor cells is one of the most important aims in PDT. Using nanoparticles, soft or hard matter based, represent a strategy to achieve this goal; many examples for tumortropic active- and passive-targeted lipid-based and polymeric nanoparticles has been reported in the last decades, showing how the high loading efficiency and the flexibility of the nanoparticles can improve the biodistribution, the blood circulation time of the photosensitizer, and the efficacy of PDT.[40–42]

Cubosomes were recently proven useful in PDT. Indeed, polymer-free cubosomes proposed for topical applications were loaded with a photosensitizer and used for bioimaging PDT of skin malignant melanoma cells. With respect to the free photosensitizer, a superior cytotoxic effect was detected when the latter was encapsulated within the cubosomes.[9] Here, a multifunctional fluorescent cubosome formulation was engineered for cancer PDT and chemotherapy after parenteral

administration. Particularly, a newly synthesized fluorescent PS was conjugated to the block copolymer used to stabilize the nanoparticles in water, while Docetaxel, an antineoplastic drug, was encapsulated within the nanoparticles.

It deserves noticing that grafting imaging/therapeutic molecules to the cubosome surface instead of encapsulating them between the lipid bilayer could be an effective strategy to avoid the phase transition of the inner phase, taking into account that lipid self-assembly processes are delicately poised and can be easily altered by inserting molecules within the lipid palisade.

C.2 Synthesis

To simultaneously provide cubosomes with both imaging and therapeutic properties, Docetaxel (DTX) was loaded within the lipid bilayer, while the PS **DPP-ZnP-NH_2**[38] was covalently linked to the block copolymer PF108 typically used to stabilize cubosomes in water. This PS was chosen because of its fluorescent and PDT features.[37,43]

After activation of the PF108 with carbonyldiimidazole, an addition-elimination reaction with **DPP-ZnP-NH_2** was performed in DMSO to obtain the conjugate **PF108-(DPP-ZnP)$_2$** (Scheme C1).

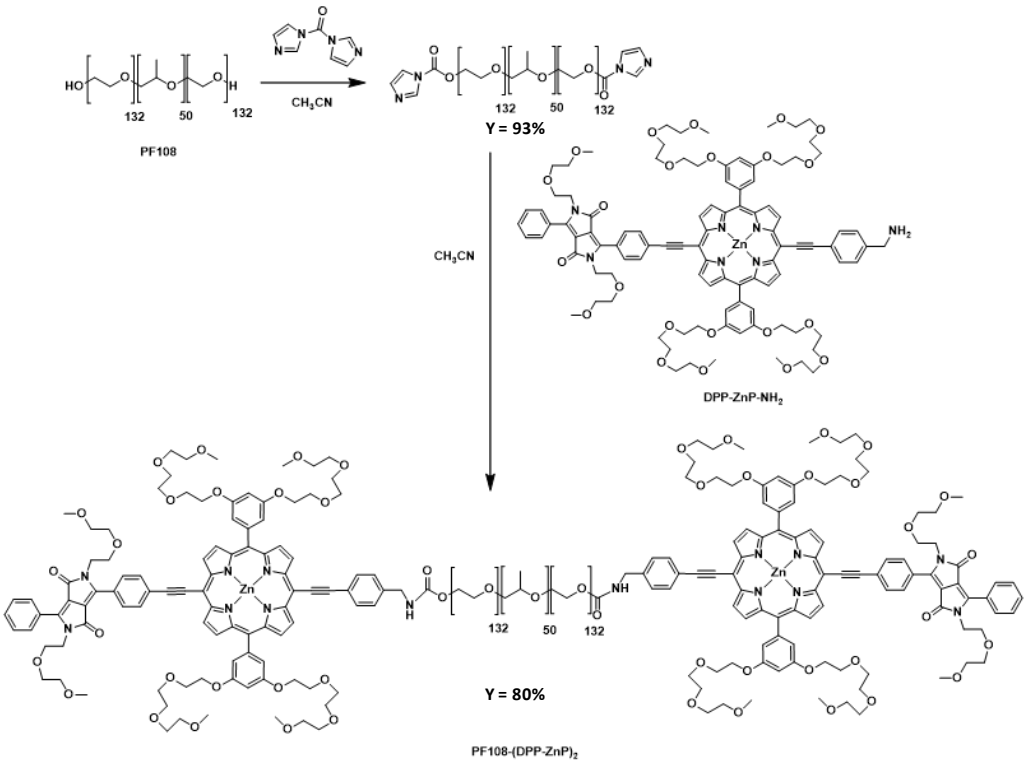

Scheme C.1 Synthetic scheme for PF108-(DPP-ZnP)$_2$

C.3. Physicochemical characterization of the cubosome formulation.

Cubosomes loaded with DTX in the lipid bilayer were prepared, as reported in the Materials and Methods section, using monoolein as molecular building block and stabilizing the dispersion in water by 40 % of **PF108-(DPP-ZnP)$_2$** and 60 % of classical PF108. The concentrations of DTX and PS in such formulation were 1.1 mM and 140 μM, respectively. The 35/65 40/60 ratio among the conjugated and non-conjugated Pluronic was used to allow a proper stabilization of the nanoparticles in water. Indeed, when 100 % of the newly synthesized stabilizer was used, the formulation promptly phase separates.

Cubosomes morphology was evaluated by Cryo-TEM (Figure C1). The nanoscopic inspection of the formulation disclosed the presence of polydisperse cubic and round shaped nanoparticles characterized by the dense inner lipid matrix usually shown by cubosomes. Analysis of Cryo-TEM picture in Figure C1, also revealed the presence of unilamellar vesicles, as frequently observed in cubosomes formulations.

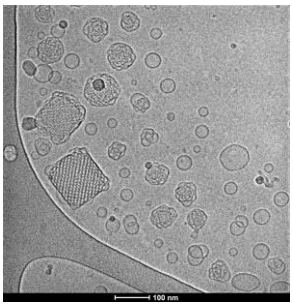

Figure C1 Cryo-TEM image of the cubosomes formulation stabilized with 40% of PF-108-(DPP-ZnP)$_2$ and 60% of PF108

According to DLS experiments, the cubosomes average hydrodynamic diameter, polydispersity index, and ζ-potential were found equal to 159 nm, 0.20, and −21.9 mV, respectively. These values are well within the range typically found for this kind of formulations.[44–46]

The inner bicontinuous cubic structure of the nanoparticles was definitely proven by SAXS analysis. Particularly, the SAXS diffractogram is characterized by the superimposition of two patterns originated by two different cubic bicontinuous liquid crystalline phases, one belonging to the Pn3m space group, the other to the Im3m. The coexistence of these two phases was already reported in literature. It is worth recalling here that, according to the monoolein/water binary phase diagram, at room temperature excess of monoolein in water originates only the Pn3m phase, and the presence of the Im3m phase in this system can be ascribed to the interaction of the block copolymer with the lipid bilayer. In a seminal work, Nakano demonstrated that

the Im3m phase growths at the expense of the Pn3m phase as the Pluronic content (PF127 in that case) is increased.[47] On the basis of that observation he suggested that the Im3m nanostructure originates by the incorporation of the surfactant in the bilayer. From the Bragg peaks detected in SAXS experiments on our nanoparticles, the calculated lattice parameters were 136.8 ± 0.2 and 100.1 ± 0.2 Å for, respectively, the Im3m and the Pn3m phases, while the calculated radius of the water channels were 24.8 ± 0.1 and 22.8 ± 0.1 Å.

These values are in good agreement with those typically found in similar systems, evidencing that the tiny amount of DTX added and the conjugation of the PS to the PF108 (rather than encapsulating it in the nanoparticles) did not provoke modifications of the original cubosome nanostructure.

C.4 Cellular imaging and cytotoxic activity

The PS **DPP-ZnP-NH$_2$** conjugated to PF108 in the cubosomes formulation is fluorescent, thus allowing cell localization studies. Cells were incubated with the cubosome formulation at a concentration of C_{500} (the original formulation was diluted 500 times) for 4 h. One hour before the acquisition of the images, Hoescht 33258, Mitotracker green or Lysotracker blue were also added (Figure C2).

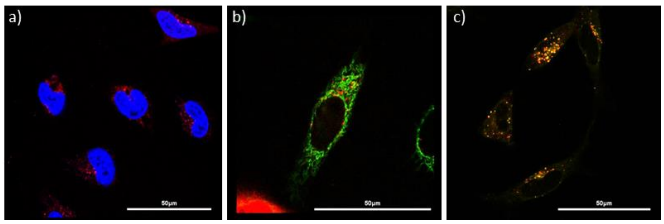

Figure C2 Confocal fluorescence images of HeLa cells after 4 h incubation with cubosome formulation (C_{500}) detected by its red fluorescence (λ_{ex}: 488 nm, λ_{em}: 700–800 nm) ; the cells are costained with (a) Hoechst 33258 (λ_{ex}: 405 nm, λ_{em}: 425–500 nm), (b) Mitotracker green (λ_{ex}: 488 nm, λ_{em}: 500–600 nm), and (c) Lysotracker blue (λ_{ex}: 405 nm, λ_{em}: 425–500 nm). Scale bar: 50 µm.

A colocalization between the Lysotracker blue and cubosomes fluorescence in lysosomes was observed. This lysosomal localization was also observed by other groups for this type of surfactant.[48] Quite surprisingly, a colocalisation between the fluorescence of the mitotracker and the cubosomes was also detected, suggesting mitochondria as extra targeting site. Remarkably, localization studies performed with PF85 (having a structure analogue to PF108) linked to a fluorophore (tetramethylrhodamine) also showed mitochondria localization.[49]

DTX is an antineoplastic drug that causes cell death acting on the microtubular network that prevents cell division,[50] and it was already demonstrated that dispersing DTX in a cubosomes formulation increase its cytotoxicity of about one order of magnitude with respect to the molecularly dispersed drug.[5] As PDT does not induce anticancer resistance and could be useful in killing localized resistant cells, a cubosome formulation was engineered, carrying both DTX and a PS with the aim of providing a synergic toxic effect in cancer cell killing.[51]

The cytotoxicity studies here performed were realized on HeLa cells after 4h incubation at a concentration of cubosomes between C_{5000} and C_{50}, corresponding to a concentration of **DPP-ZnP-NH$_2$** between 0.04 μM and 3.8 μM and of DTX between 0.21 μM and 21 μM. The cell viability was evaluated with an MTT test (Figure C3).

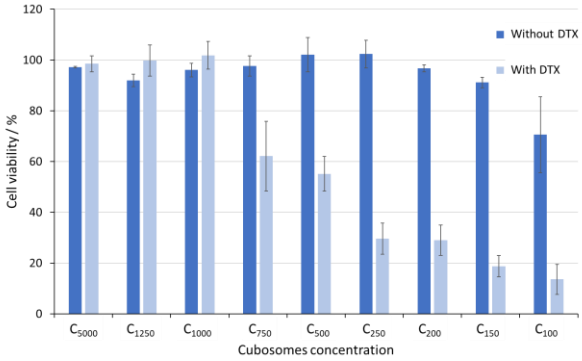

Figure C3 Cytotoxicity induced on Hela cells by cubosome formulation with PF108-(DPP-ZnP)$_2$ and with or without DTX, after 4 h incubation. The index numbers correspond to the dilution factor of the original formulation.

Cubosome formulation stabilized with **PF108-(DPP-ZnP)$_2$** and incorporating DTX became toxic for a concentration of C_{750} and the IC_{50} was estimated between C_{750} and C_{500}. It is interesting to note that cubosomes without DTX are not toxic at these concentrations suggesting that toxicity derived from the drug and not from the PS. This finding is in good agreement with results previously obtained. It was reported a toxicity of 30 % for a DTX concentration of 0.8 μM after 4 h incubation in HeLa cells.[5] In the present study, the cubosomes induced 40 % of cell death at a concentration of DTX of 1.4 μM.

The studies of phototoxicity induced by monophotonic excitation were performed on HeLa cells after incubation with a dispersion of cubosomes formulation stabilized with **PF108-(DPP-ZnP)$_2$** with or without DTX**.** Cells were incubated at C_{750}, corresponding to a concentration of 0.25 μM for the PS and of 1.4 μM for the DTX, for 4 h. The cells were then irradiated at 660 nm for 1 h with a fluence rate of 36 mW/cm². Cell viability was evaluated 24 h after the irradiation with MTT test (Figure C4).

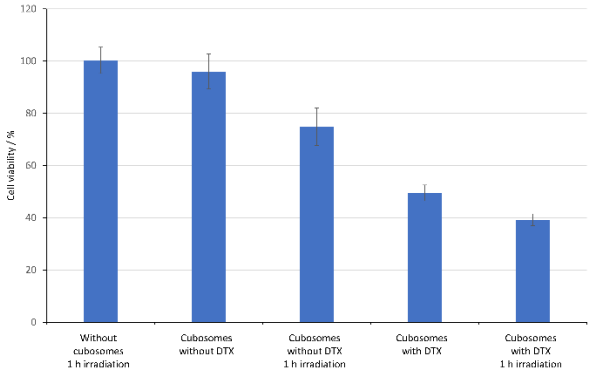

Figure C4 Phototoxicity on HeLa cells incubated 4 h with a cubosome formulation with PF108-(DPP-ZnP)$_2$ and with or without DTX, after 1h irradiation at 660 nm at 36 mW/cm². Cell viability was evaluated 24 h after the irradiation.

According to the results obtained from this experiment, cubosomes formulation stabilized with **PF108-(DPP-ZnP)$_2$** without DTX did not induce any toxic effect, while irradiation of the same formulation with a high light dose of 130 J/cm² caused a phototoxicity at around 20 %. It must be noticed that such light dose did not induced cell death. When the cubosomes were loaded with DTX, the toxicity increased reached about 50 %, while irradiation of cubosomes incorporating DTX caused a further slight increase of the toxicity up to 60 %, showing some additive effect among the photosensitizer and DTX in cell killing.

C.5 Conclusions

With the aim of engineering a multifunctional cubosomes formulation useful for imaging and therapeutic applications, a fluorescent PS, **DPP-ZnP-NH$_2$**, was conjugated to the block copolymer PF108 used to stabilize the nanoparticles against phase separation. Moreover, Docetaxel, an antineoplastic drug, was loaded within the lipid bilayer to induce higher cell death exploiting possible synergic toxic effects. The physicochemical characterization demonstrated that a stable cubosomes formulation was obtained by using a mixture of the newly synthesized **PF108-(DPP-ZnP)$_2$** and the commercial PF108 in a 40/60 ratio. Interestingly, after incubation with HeLa cells, the imaging experiments evidenced a localization of the fluorescence in lysosomes and mitochondria, while a slight but significant synergic effect in increasing cytotoxicity was observed when Docetaxel containing cubosomes incubated with HeLa cells were also irradiated to induce the monophotonic excitation of the photosensitizer.

On the whole, these results suggest the proposed fluorescent formulation possesses some potential in combined chemo- and photodynamic therapy of cancer.

C.6 Experimental part

Materials

Monoolein (MO, 1-monooleoylglycerol, RYLO MG 19 PHARMA, glycerol monooleate, 98.1 wt %) was kindly provided by Danisco A/S, DK-7200, Grinsted, Denmark. Pluronic

F108 (PF108, PEO132-PPO50-PEO132) was purchased from Sigma Aldrich, and Docetaxel (DTX) from TCI Europe. Distilled water was used to prepare the sample and for the dilution after passing through a Milli-Q water-purification system (Millipore).
All the materials were used without further purification. Compound DPP-ZnP-NH_2 and the CDI-Activated Pluronic F108 (F108-CDI) were prepared according to the literature.[38,52]

Synthesis of the conjugate PF108-$(DPP\text{-}ZnP)_2$

To a solution of Pluronic F108-CDI (0.16g, 0.011 mmol) in dry acetonitrile (10 mL) DPPZn-NH_2 (40 mg, 0.022mmol) was added and the mixture was kept stirring under nitrogen atmosphere in the dark for 24h. Then, the solution was concentrated and recrystallized in diethyl ether. The product was dried under reduced pressure and collected as a green powder. Yield: 80% ^{1}H NMR (500 MHz, DMSO-d_6 , 298 K): δ_H 1.05 (d, J = 6 Hz, 3H×50,–CH_3 of PPO), 2.65−2.75 (m, 2H×2 protons adjacent to the terminal amine), 2.96 (q, J = 6 Hz, 2H×2 protons adjacent to the amide bond), 3.185-3.646 (m, peg chain), 3.47−3.54 (m, 3H×50, 4H× 264,–CH_2–$CH(CH_3)$–O–of PPO and–CH_2–CH_2–O–of PEO), 7.00 (ar-H), 7.04 (ar-H), 7.35 (ar-H), 7.63 (ar-H), 8.26 (ar-H), 8.93 (d, pyr), 9.75 (d, pyr), 12.09 (-NH).

Cubosomes preparation

Cubosomes were prepared by melting MO at 37 °C and then adding the appropriate amount of an aqueous solution of the stabilizers (PF108/PF108-(DPP-ZnP), molar ratio 60/40). Finally, the mixture was homogenized using an UP100H ultrasonic processor developed by Hiescher (cycle 0.9, amplitude 90%) for 5, 3, and 2 min cycles. Cubosomes loaded with DTX were obtained by dispersing the drug in the melted MO with the help of an ultrasonic bath before adding the Pluronics solution. the cubosome formulation used for the cellular studies was usually 2 mL with approximately 96.4 wt % water, 3.3 wt % MO, and 0.3 wt % of the Pluronics mixture

Dialysis and encapsulation efficiency

The cubosomes dispersion loaded with the drug was purified from the non-encapsulated DTX by dialysis as follows: 2 mL of cubosomes dispersion were loaded into a dialysis tubing cellulose membrane (14 kDa MW cutoff, purchased by Sigma-Aldrich) and dialyzed against 2 L of water for 2 h at room temperature, replacing the water after 1 h. The encapsulation efficiency (EE%) of DTX was determined by UV-Vis spectroscopy after the disruption of cubosomes with ethanol reading the absorption of the DTX at 283 nm in a Thermo Nicolet Evolution 300 UV-Vis Spectrophotometer.

Small Angle X-ray scattering (SAXS)

SAXS patterns were recorded using a S3-MICRO SWAXS camera system (HECUS, X-ray Systems, Graz, Austria). The Cu K_α wavelength (1.542 Å) was provided by a GeniX-X-ray generator (50 kV and 1 mA). A 1D-PSD-50M system (HECUS, X-ray Systems, Graz, Austria) containing 1024 channels (54.0 μm) was used for the detection of scattered X-rays in the small angle region. The working q range was $0.003 \leq q \leq 0.6$ ($Å^{-1}$), where $q = 4\pi\sin(\theta)\lambda^{-1}$ is the scattering vector. Thin-walled (2 mm) glass capillaries were filled with the cubosomes dispersions. The SAXS patterns were recorded for 2 h. The camera volume was kept under vacuum during the measurements to minimize scattering from air. Silver Behenate ($CH_3{-}(CH_2)_{20}{-}COOAg$, d spacing value of 58.38 Å) was used as standard to calibrate the angular scale of the measured intensity.

The lattice parameter, a, for the bicontinuous cubic phases was calculated using the relation

$$a = d\,(h^2 + k^2 + l^2)^{1/2} \qquad (1)$$

where $d = 2\pi/q$ and h, k, and l are the Miller indices. The water channel radii (r_W) of the cubic phases were calculated by the equation

$$r_W = [(A_0/{-}2\pi\chi)^{1/2}a] - L_{MO} \qquad (2)$$

where L_{MO} is the length of the monoolein hydrophobic chain (17 Å), while A_0 and χ are, respectively, the surface area and the Euler characteristic of the IPMS geometries

(Pn3m, A_0 = 1.919, χ = −2; Im3m, A_0 = 2.345, χ = −4). The length for the MO used in this study was originally calculated in the binary MO/water system.[53] Herein, it is assumed this value does not vary significantly due to the presence of the Pluronics mixture at the interface.

Dynamic Light Scattering (DLS)

Each sample was diluted 1:50 in Milli-Q water prior to any measurements. The mean hydrodynamic diameter (D_h) and polidispersity index (PdI) of cubosomes were determined by DLS using a Nano Series Zetasizer from Malvern Instruments (Worcestershire, U.K.) at 173° in optically homogeneous square polystyrene cells. The measurements were performed at 25 °C and obtained as an average of three runs with at least 10 measurements.

The ζ-potential of the nanoparticles was measured using the micro-electrophoretic method by the Malvern Zetasizer Nano ZS apparatus. Each value was obtained as an average of three subsequent runs of the instrument at 25 °C, with at least 20 measurements.

Cell culture and MTT cell viability test

HeLa cells were cultured at 37 °C in DMEM complete culture medium containing phenol red with 5% CO_2. They were seeded and maintained in 25 mL Falcon culture flask or multi well

LabTek (Lab-Tek® II) culture flasks. Cell viability was assessed in pentaplicate by adding a solution of 3-(4,5-dimethyl-2-thiazolyl)- 2,5-diphenyl-2H-tetrazolium bromide (50 μL of a 5 mg mL^{-1} solution in DMEM by well). After an incubation period of 45 minutes, the media was removed and replaced by DMSO (150 μL). The absorbance was measured using the Safas Xenius spectrofluorimeter 96 well plates reader at 550 nm.

Dark cytotoxicity

HeLa cells were seeded in 96 wells culture plates. After one day, the cells were incubated with different concentrations of cubosomes with or without DTX ($C_{5000} - C_{100}$ refers to concentration obtained from the original formulation with the index number representing the dilution factor). After 4 h incubation the cell viability was assessed using the MTT test described above.

Phototoxicity tests

One-photon phototoxicity tests were performed as described in the literature using a homemade apparatus[39,43] with 800 mA high power LED Deep Red (640–660 nm) (FutureEden™) adapted for Corning® 96 well special optic plates. HeLa cells were seeded in these plates for 24 h and incubated with a cubosomes solutions (C750) with or without DTX for 4 h. The medium was replaced by new DMEM free of cubosomes and the plates were irradiated for 1 h at a light power of 36 mW/cm². The LEDs power was measured with a Thorlabs PM100D powermeter. The cell viability was then assessed 24 h after irradiation using the MTT test previously described.

C.8 References

1 H. M. G. Barriga, M. N. Holme and M. M. Stevens, *Angew. Chemie - Int. Ed.*, 2019, **58**, 2958–2978.

2 X. Mulet, B. J. Boyd and C. J. Drummond, *J. Colloid Interface Sci.*, 2013, **393**, 1–20.

3 K. Larsson, *Nature*, 1983, **304**, 664.

4 S. Murgia, S. Lampis, P. Zucca, E. Sanjust and M. Monduzzi, *J. Am. Chem. Soc.*, 2010, **132**, 16176–84.

5 V. Meli, C. Caltagirone, A. M. Falchi, S. T. Hyde, V. Lippolis, M. Monduzzi, M. Obiols-Rabasa, A. Rosa, J. Schmidt, Y. Talmon and S. Murgia, *Langmuir*, 2015, **31**, 9566–9575.

6 I. D. Azmi, S. M. Moghimi and A. Yaghmur, *Ther. Deliv.*, 2015, **6**, 1347–1364.

7 Z. Karami and M. Hamidi, *Drug Discov. Today*, 2016, **21**, 789–801.

8 L. Boge, K. Hallstensson, L. Ringstad, J. Johansson, T. Andersson, M. Davoudi, P. T. Larsson, M. Mahlapuu, J. Håkansson and M. Andersson, *Eur. J. Pharm. Biopharm.*, 2019, **134**, 60–67.

9 U. Bazylińska, J. Kulbacka, J. Schmidt, Y. Talmon and S. Murgia, *J. Colloid Interface Sci.*, 2018, **522**, 163–173.

10 S. Salah, A. A. Mahmoud and A. O. Kamel, *Drug Deliv.*, 2017, **24**, 846–856.

11 C. von Halling Laier, B. Gibson, M. van de Weert, B. J. Boyd, T. Rades, A. Boisen, S. Hook and L. H. Nielsen, *Int. J. Pharm.*, 2018, **550**, 35–44.

12 Z. Liu, L. Luo, S. Zheng, Y. Niu, R. Bo, Y. Huang, J. Xing, Z. Li and D. Wang, *Int. J. Nanomedicine*, 2016, **11**, 3571–3583.

13 S. B. Rizwan, W. T. McBurney, K. Young, T. Hanley, B. J. Boyd, T. Rades and S. Hook, *J. Control. Release*, 2013, **165**, 16–21.

14 Y. S. R. Elnaggar, S. M. Etman, D. A. Abdelmonsif and O. Y. Abdallah, *Int. J. Nanomedicine*, 2015, **10**, 5459–5473.

15 M. Godlewska, A. Majkowska-Pilip, A. Stachurska, J. F. Biernat, D. Gaweł and E. Nazaruk, *Electrochim. Acta*, 2019, **299**, 1–11.

16 S. Akbar, A. Anwar, A. Ayish, J. M. Elliott and A. M. Squires, *Eur. J. Pharm. Sci.*, 2017, **101**, 31–42.

17 E. Nazaruk, A. Majkowska-Pilip and R. Bilewicz, *Chempluschem*, 2017, **82**, 570–575.

18 M. Szlezak, D. Nieciecka, A. Joniec, M. Pękała, E. Gorecka, M. Emo, M. J. Stébé, P. Krysiński and R. Bilewicz, *ACS Appl. Mater. Interfaces*, 2017, **9**, 2796–2805.

19 J. Zhai, R. Suryadinata, B. Luan, N. Tran, T. M. Hinton, J. Ratcliffe, X. Hao and C. J. Drummond, *Faraday Discuss.*, 2016, Ahead of Print.

20 M. J. Kim and D. Y. Lee, *Macromol. Res.*, 2016, **24**, 197–204.

21 S. Murgia, A. M. Falchi, V. Meli, K. Schillén, V. Lippolis, M. Monduzzi, A. Rosa, J. Schmidt, Y. Talmon, R. Bizzarri and C. Caltagirone, *Colloids Surfaces B Biointerfaces*, 2015, **129**, 87–94.

22 S. Aleandri, D. Bandera, R. Mezzenga and E. M. Landau, *Langmuir*, 2015, **31**, 12770–12776.

23 C. Caltagirone, A. M. Falchi, S. Lampis, V. Lippolis, V. Meli, M. Monduzzi, L. Prodi, J. Schmidt, M. Sgarzi, Y. Talmon, R. Bizzarri and S. Murgia, *Langmuir*, 2014, **30**, 6228–6236.

24 S. Deshpande, E. Venugopal, S. Ramagiri, J. R. Bellare, G. Kumaraswamy and N. Singh, *ACS Appl. Mater. Interfaces*, 2014, **6**, 17126–17133.

25 J. Barauskas, C. Cervin, M. Jankunec, M. Špandyreva, K. Ribokaitė, F. Tiberg and M. Johnsson, *Int. J. Pharm.*, 2010, **391**, 284–291.

26 J. C. Bode, J. Kuntsche, S. S. Funari and H. Bunjes, *Int. J. Pharm.*, 2013, **448**, 87–95.

27 X. Shi, T. Peng, Y. Huang, L. Mei, Y. Gu, J. Huang, K. Han, G. Li, C. Hu, X. Pan and C. Wu, *Pharm. Dev. Technol.*, 2017, **22**, 322–329.

28 N. Tran, N. Bye, B. A. Moffat, D. K. Wright, A. Cuddihy, T. M. Hinton, A. M. Hawley, N. P. Reynolds, L. J. Waddington, X. Mulet, A. M. Turnley, M. C. Morganti-Kossmann and B. W. Muir, *Mater. Sci. Eng. C*, 2017, **71**, 584–593.

29 S. Biffi, C. Garrovo, P. Macor, C. Tripodo, S. Zorzet, E. Secco, F. Tedesco and V. Lorusso, *Mol. Imaging*, 2008, **7**, 272–282.

30 C. Nilsson, B. Barrios-Lopez, A. Kallinen, P. Laurinmäki, S. J. Butcher, M. Raki, J. Weisell, K. Bergström, S. W. Larsen, J. Østergaard, C. Larsen, A. Urtti, A. J. Airaksinen and A. Yaghmur, *Biomaterials*, 2013, **34**, 8491–8503.

31 Agostinis Patrizia; Berg Kristian; Cengel Keith A.; Foster Thomas H. ; Girotti Albert W.; and Gollnick Sandra O.; Hahn Stephen M.; Hamblin Michael R. Juzeniene Asta; Kessel David; Korbelik Mladen; Moan Johan; Mroz Pawel; Nowis Dominika; Piette Jacques; Wilson Brian C.; Jakub Golab, *CA. Cancer J. Clin.*, 2011, **61**, 250–281.

32 C. S. Foote, *Science (80-.).*, 1968, **162**, 963–970.

33 J. S. Dysart and M. S. Patterson, *Phys. Med. Biol.*, 2005, **50**, 2597–2616.

34 R. R. Allison and C. H. Sibata, *Photodiagnosis Photodyn. Ther.*, 2010, **7**, 61–75.

35 B. Chen, T. Roskams and P. A. M. de Witte, *Photochem. Photobiol.*, 2002, **76**, 509.

36 F. Bolze, S. Jenni, A. Sour and V. Heitz, *Chem. Commun.*, 2017, **53**, 12857–12877.

37 J. Schmitt, V. Heitz, A. Sour, F. Bolze, H. Ftouni, J. F. Nicoud, L. Flamigni and B. Ventura, *Angew. Chemie - Int. Ed.*, 2015, **54**, 169–173.

38 J. Schmitt, V. Heitz, A. Sour, F. Bolze, P. Kessler, L. Flamigni, B. Ventura, C. S. Bonnet and É. Tõth, *Chem. - A Eur. J.*, 2016, **22**, 2775–2786.

39 J. Schmitt, S. Jenni, A. Sour, V. Heitz, F. Bolze, A. Pallier, C. S. Bonnet, É. Tóth and B. Ventura, *Bioconjug. Chem.*, 2018, **29**, 3726–3738.

40 D. K. Chatterjee, L. S. Fong and Y. Zhang, *Adv. Drug Deliv. Rev.*, 2008, **60**, 1627–1637.

41 H. Gong, Z. Dong, Y. Liu, S. Yin, L. Cheng, W. Xi, J. Xiang, K. Liu, Y. Li and Z. Liu, *Adv. Funct. Mater.*, 2014, **24**, 6492–6502.

42 S. S. Lucky, K. C. Soo and Y. Zhang, *Chem. Rev.*, 2015, **115**, 1990–2042.

43 S. Jenni, A. Sour, F. Bolze, B. Ventura and V. Heitz, *Org. Biomol. Chem.*, 2019, **17**, 6585–6594.

44 A. M. Falchi, A. Rosa, A. Atzeri, A. Incani, S. Lampis, V. Meli, C. Caltagirone and S. Murgia, *Toxicol. Res.*, 2015, **4**, 1025–1036.

45 E. Jabłonowska, E. Nazaruk, D. Matyszewska, C. Speziale, R. Mezzenga, E. M. Landau and R. Bilewicz, *Langmuir*, 2016, **32**, 9640–9648.

46 C. Montis, B. Castroflorio, M. Mendozza, A. Salvatore, D. Berti and P. Baglioni, *J. Colloid Interface Sci.*, 2015, **449**, 317–326.

47 M. Nakano, A. Sugita, H. Matsuoka and T. Handa, *Langmuir*, 2001, **17**, 3917–3922.

48 N. Rapoport, A. Marin, Y. Luo, G. D. Prestwich and M. Muniruzzaman, *J. Pharm. Sci.*, 2002, **91**, 157–170.

49 D. Y. Alakhova, N. Y. Rapoport, E. V Batrakova, A. A. Timoshin, S. Li, D. Nicholls, V. Y. Alakhov and A. V Kabanov, *J. Control. Release*, 2010, **142**, 89–100.

50 P. Zhao and D. Astruc, *ChemMedChem*, 2012, **7**, 952–972.

51 M. Gary-Bobo, O. Hocine, D. Brevet, M. Maynadier, L. Raehm, S. Richeter, V. Charasson, B. Loock, A. Morère, P. Maillard, M. Garcia and J.-O. Durand, *Int. J. Pharm.*, 2012, **423**, 509–515.

52 C. Caltagirone, A. M. Falchi, S. Lampis, V. Lippolis, V. Meli, M. Monduzzi, L. Prodi, J. Schmidt, M. Sgarzi, Y. Talmon, R. Bizzarri and S. Murgia, *Langmuir*, 2014, **30**.

53 M. Briggs, J.; Chung, H.; Caffrey, *J. Phys. II*, 1996, **6**, 723–751.

Summarizing, this PhD project has led to the development of novel Supramolecular Architectures based on weak interactions for various purposes.

In particular, we have demonstrated that selenoureas are versatile receptors for anion binding, capable of forming at room temperature in solution both mono- and bi-coordinated adducts. The increase of the NMR coalescence temperature (when comparing with analogous ureas and thioureas) facilitates the easy detection of the mono-coordinated adduct in solution at room temperature. As a consequence, on using i) the steric hindrance of the aryl substituents in selenoureas, and ii) the geometry of the anion guest as inputs, a molecular logic gate can be easily developed following ^{1}H-NMR signals of the adducts formed as chemical outputs. In the case of the bis-selenoureas receptors, the higher affinity towards the anion guests observed compared to the analogous bis-ureas was attributed by the presence of selenium on the receptor structure.

More classic anion-binding motifs described in this PhD thesis are isophthalamides and dipicolinepamides. We have demonstrated that the presence of perfluorophenyl substituents cause the formation of non-symmetric adducts. The study of the crystal structures of the receptors demonstrate that the steric hindrance of the halogens influence the accessibility of the isophtalamide or dipicoline amide NHs, thus modulating the affinity towards the anions. We have also shown that the same receptors are able to bind anions can work as synthetic anion transporters through lipid vesicles.

We have also described the excellent anion binding properties of the bis-indolyl squaramide receptor also in aqueous media. Transport studies showed that this system is able to mediate chloride efflux through phospholipidic membranes with a low EC_{50} value. Moreover, the bis-quinoline and bis-naphthyl-squaramides, due to their fluorescent properties, were used as cell imaging agents both in cancer and non-cancer cells.

Two novel families of ureas that work as LMWGs have been studied and materials with interesting rheological properties were obtained. We demonstrated that by using metal cations or anions we were able to modulate the gels formation.

As a side project we have also developed two interesting platforms for nanomedicine applications using monoolein-based nanoparticles (cubosomes and hexosomes) by loading them with a rhodamine derivative or by functionalizing their surface with a porphyrine as imaging agents and Docetaxel as therapeutic antineoplastic drug .


Giacomo Picci gratefully acknowledges Sardinian Regional Government for the financial support of her/his PhD scholarship (P.O.R. Sardegna F.S.E. - Operational Programme of the Autonomous Region of Sardinia, European Social Fund 2014-2020 - Axis III Education and training, Thematic goal 10, Investment Priority 10ii), Specific goal 10.5.